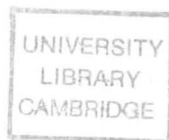


PhD 15884

FRICITION AND LUBRICATION
IN METAL ROLLING

Michael Patrick Forbes Sutcliffe



A dissertation submitted to the University of Cambridge
for the Degree of Doctor of Philosophy

Jesus College

July 1989

PREFACE

I am most grateful to my supervisor Professor K.L. Johnson for all his support and guidance, and should like to thank my 'contacts' at Alcan Int. Ltd., Mr. I.G. Calderbank and Dr. K.W. Waterson, for their help and encouragement. I am most grateful for the use of Alcan's experimental mill and for the practical help provided by Dr. Waterson with the rolling experiments.

I am particularly indebted to Mr. G. Ryder who manufactured the specimens and who patiently and skilfully prepared the discs used in the experiments and am most grateful to Reading University for the loan of the tungsten carbide discs used in the experiments of chapter 2.

The financial support from the Science and Engineering Research Council and Alcan International Ltd. through a C.A.S.E. award is gratefully acknowledged. Finally I should like to thank all those who have helped and supported me in other ways during the course of my research.

This dissertation describes research work carried out by the author and includes nothing that is the outcome of work done in collaboration.

No part of this thesis has been, or is being, submitted to any other University for any degree or any other qualification.

The thesis contains 213 pages.

M.P.F. Sutcliffe

Michael P.F. Sutcliffe
Cambridge, July 1989.

FRICITION AND LUBRICATION IN METAL ROLLING

M.P.F. Sutcliffe

Summary

This dissertation is concerned with the physical processes which determine friction and lubrication in metal rolling in the mixed lubrication regime, with particular attention paid to the conditions encountered when rolling aluminium foil.

Two areas of relevance to the analysis of the rolling process are initially investigated. Firstly, the rheological properties of a typical aluminium foil rolling oil at high pressures and shear rates have been measured using a disc machine. The behaviour of the oil was found to be well described by the Eyring viscous model, at the shear rates and pressure likely to be found in metal rolling. Secondly, the deformation of asperities when the bulk material is deforming has been examined. The theory developed here was found to agree reasonably with experiments.

The results of these investigations are used in the analysis of lubrication in metal rolling, considering the hydrodynamic buildup of oil pressure in the entry region and the crushing of the asperities both in the entry region and at the beginning of the work zone. The contact between roll and strip is divided into two regions, that under the asperities and that in the intervening valleys. Calculations for conditions appropriate to strip and foil rolling give the proportion of the two types of contact and the film thicknesses in each region.

Measurements of film thicknesses with an experimental mill in a regime where roughness is unimportant were not found to agree well with an existing simple theory of lubrication. This was ascribed to uneven lubrication in the experiments. After taking this into account, the experiments in a regime where roughness was important were found to agree reasonably with the theory developed here.

The effect of roughness on traction is measured in a disc machine with elastic contacts. Its behaviour is found to be determined by the bulk properties of the lubricant at the pressures and strain rates under the asperities.

Theory and experiments presented in this dissertation lead to a greater understanding of the physical processes determining friction in metal rolling in the mixed lubrication regime. Film thicknesses and friction coefficients may now be estimated with more confidence (in metal rolling)

CONTENTS

Preface	
Summary	
Notation	

Chapter 1 INTRODUCTION	1
1.1 Lubricant properties	2
1.2 Surface finish	3
1.3 Models of rolling	4
1.3.1 Smooth rolls and strip	4
1.3.2 Rough rolls and strip	5
1.3.3 Thermal effects	7
1.4 Mechanisms of friction in rolling	8
1.4.1 Boundary lubrication	8
1.4.2 Metal-to-metal contact	9
1.4.3 Micro-plasto-hydrodynamic lubrication	10
1.4.4 Lubricant entrapment	11
1.5 Traction in a mixed lubrication regime	12
1.5.1 Elastic contacts	12
1.5.2 Friction in metal rolling	14
1.6 Measurements of film thickness in rolling	15
Chapter 2 MEASUREMENTS OF THE RHEOLOGY OF A FOIL ROLLING LUBRICANT	17
2.1 Introduction	17
2.2 The disc machine	19
2.3 Deduction of rheological properties	20
2.4 Results	21
Chapter 3 SURFACE ASPERITY DEFORMATION IN METAL FORMING PROCESSES	24
3.1 Introduction	24
3.2 Transverse roughness	25
3.2.1 Theory	25
3.2.2 Experiments - transverse roughness	32
3.2.3 Results	33
3.2.4 Transverse random rough surfaces	35

CONTENTS

Preface

Summary

Notation

Chapter 1 INTRODUCTION	1
1.1 Lubricant properties.....	2
1.2 Surface finish	3
1.3 Models of rolling	4
1.3.1 Smooth rolls and strip.....	4
1.3.2 Rough rolls and strip	5
1.3.3 Thermal effects.....	7
1.4 Mechanisms of friction in rolling.....	8
1.4.1 Boundary lubrication.....	8
1.4.2 Metal-to-metal contact.....	9
1.4.3 Micro-plasto-hydrodynamic lubrication.....	10
1.4.4 Lubricant entrapment	11
1.5 Traction in a mixed lubrication regime.....	12
1.5.1 Elastic contacts	12
1.5.2 Friction in metal rolling	14
1.6 Measurements of film thickness in rolling	15
Chapter 2 MEASUREMENTS OF THE RHEOLOGY OF A FOIL ROLLING LUBRICANT	17
2.1 Introduction	17
2.2 The disc machine	19
2.3 Deduction of rheological properties	20
2.4 Results.....	21
Chapter 3 SURFACE ASPERITY DEFORMATION IN METAL FORMING PROCESSES	24
3.1 Introduction	24
3.2 Transverse roughness.....	25
3.2.1 Theory	25
3.2.2 Experiments - transverse roughness.....	32
3.2.3 Results.....	33
3.2.4 Transverse random rough surfaces	35

3.3	Longitudinal roughness	36
3.3.1	Theory	36
3.3.2	Experiments – longitudinal roughness	38
3.3.3	Results	39
3.3.4	Longitudinal random rough surfaces	41
3.4	Conclusions	41

**Chapter 4 FILM THICKNESSES AND TRACTION IN ROLLING
— THEORY**

		43
4.1	Introduction	43
4.2	Film thicknesses in the valleys	45
4.2.1	Calculation of the oil pressures	45
4.2.2	Roughness model	47
4.2.3	Roll shape	48
4.2.4	Without bulk deformation	49
4.2.5	Bulk deformation	50
4.2.6	Calculation method	52
4.3	Dimensional analysis	54
4.4	Results of valley film thickness calculations	58
4.5	Comparison with Sheu's theory	62
4.6	Film thicknesses in the regions of close contact	63
4.7	Results of the film thickness calculations for foil rolling	68
4.8	Traction curves for foil rolling conditions	70
4.9	Conclusions	73

**Chapter 5 EXPERIMENTAL MEASUREMENTS OF FILM
THICKNESS IN ROLLING**

		75
5.1	Experimental setup	75
5.1.1	Rolling mill	75
5.1.2	Materials	75
5.1.3	Oil	76
5.1.4	Experimental method	77
5.1.5	Operating conditions	79
5.2	Experimental corrections to the film thickness	79
5.2.1	Effect of starvation on film thickness	79
5.2.2	Effect of limited oil drop size on side leakage	81
5.2.3	Effect of thick films on the contact arc length	82
5.3	Film thickness measurements at large Λ ratios	83

5.4	Film thicknesses with rough contacts	86
5.5	Results.....	88
5.6	Conclusions	89
Chapter 6 MEASUREMENT OF TRACTION IN A MIXED LUBRICATION EXPERIMENT		91
6.1	Introduction	91
6.2	Experimental setup	92
6.2.1	Discs	92
6.2.2	Operating Conditions.....	93
6.3	Results.....	94
6.3.1	Smooth discs	94
6.3.2	Rough discs	95
6.4	Deduction of experimental film thicknesses.....	96
6.4.1	With uniform pressure ($\Lambda > 2$)	96
6.4.2	With no pressure in the valleys ($\Lambda \leq 0.88$).....	98
6.4.3	Results of film thickness deductions.....	99
6.5	Theoretical film thicknesses.....	101
6.5.1	With uniform pressure ($\Lambda > 2$)	101
6.5.2	With no pressure in the valleys ($\Lambda \leq 0.88$).....	102
6.5.3	Results of theoretical film thickness calculations.....	103
6.6	Conclusions	105
Chapter 7 CONCLUSIONS.....		107
7.1	Recommendations for future work	110
7.1.1	Thermal analysis	110
7.1.2	The geometry of rolls with thin foil	111
7.1.3	Breakdown of lubrication	111
7.1.4	Measurements of friction in rolling.....	112
Appendix A	Asperity crushing calculations for the new velocity field	113
Appendix B	Asperity crushing results with Wilson and Sheu's velocity field.....	116
Appendix C	Estimating the area of contact ratio in the traction experiments for $\Lambda \leq 0.88$	117
Appendix D	Effect of non-Newtonian flow on oil side leakage	118
Appendix E	Central film thicknesses in elliptical contacts	119
E.1	Comparison of different calculations with Hooke's analysis	122
E.2	Deducing film thicknesses for the disc experiments	128
References	130	

NOTATION

a	half width of indenter (chapter 3).
a, a_0	semi-axis of Hertz contact ellipse in entraining direction or semi-width of line contact.
a_1	constant dependent on the ellipticity ψ (appendix E).
A	(= a/c in chapter 3), real area of contact ratio.
b	length of arc of contact in rolling (chapters 4 and 5).
b	semi-axis of Hertz contact ellipse in transverse direction (appendix E).
c	half indenter spacing (chapter 3).
c_0	half indenter spacing before bulk straining.
c	group determining piezo- or isoviscous behaviour (see equation E.1).
C_L	thermal correction to Wilson and Walowit film thickness.
C_m	correction factor for a thermal Reynolds equation.
d	depth of perturbed velocity field (chapter 3).
d	half the peak to peak height of asperities (chapter 6).
d_0	initial combined r.m.s. roughness of rolls and strip (chapters 4 and 5).
d_1	height of asperities (chapter 6, see figure 6.6).
D	= d/c , dimensionless depth of perturbed field.
E'	$1/E' = \frac{1}{2} \{ (1 - \nu_1^2)/E_1 + (1 - \nu_2^2)/E_2 \}$, equivalent elastic modulus.
$f()$	a function of ().
F	change in end force needed for bulk deformation.
$F/2ka$	dimensionless change in end force — transverse roughness.
$F/2kc^2$	dimensionless change in end force — longitudinal roughness.
G	elastic shear modulus (chapter 2).
G	= $\alpha E'$, material parameter (appendix E).

h	height of Hill forging field (chapter 3).
h	film thickness.
h	central film thickness (appendix E).
\bar{h}	mean film thickness over whole contact, at the end of the asperity crushing process, assuming that the film under the contacts is negligible.
\bar{h}_t	as above, but including the asperity film thicknesses.
h_a	film thickness under the asperities.
h_d	Dowson and Toyoda smooth film thickness (equation 2.6).
\bar{h}_e	measured mean film thickness at exit from bite.
h_i	film thickness at start of integration for asperity film calculations.
h_s	theoretical smooth film thickness including thermal effects and roll curvature.
$h_{*\infty}$	theoretical isothermal smooth film thickness with a curved inlet and no starvation.
\bar{h}_v	mean film thickness of the valley regions.
h_w	Wilson and Walowitt smooth film thickness (equation 4.20).
H	$= h(\alpha\eta_0 u)^{-2/3} Re^{-1/3}$, dimensionless film thickness (appendix E).
H_0	half the depth of a ridged block (chapter 3).
k	thermal conductivity of oil.
$2k$	plane strain yield strength of workpiece.
l	width of valley regions in integration distance Δl .
m	length of wedge entraining region in asperity film calculations.
L	thermal loading parameter.
n	a typical hydrodynamic length for piezoviscous contacts (see equation E.4).
p, \bar{p}	(mean) pressure.
p_0	maximum Hertzian pressure.

p_0	mean pressure under indenter (chapter 3).
$P_d/2kc^2\dot{\epsilon}_z$	dimensionless power dissipation.
P_d	power dissipated per half indenter spacing c per unit length in the z direction down to a depth d .
q	reduced pressure.
ΔQ	reduced pressure parameter in asperity film calculations.
R_0, R	roll or disc radius.
R'_e	$= R/2$, effective radius of curvature in entraining direction.
t_1, t_2	initial and final strip thicknesses.
u, \bar{u}	$= (u_1 + u_2)/2$, mean entraining velocity.
Δu	$= (u_1 - u_2)$ relative sliding speed.
U	$= u\eta_0/(E'R_e)$, velocity parameter (appendix E).
v, v_0	(initial) volume of oil drop (chapter 5).
v_a	downwards velocity of indented surface.
v_f	$= (v_a - v_v)$, flattening velocity.
v_s	sideways velocity of material midway between indenters.
v_v, \bar{v}_v	(mean) downwards velocity of free surface.
w	width of oil patch (chapter 5).
w	load, for point contacts.
w'	load per unit length of contact, for line contacts.
W	$= w/(E'R_e^2)$, load parameter (appendix E).
W	$= v_f/c\dot{\epsilon}$, dimensionless flattening and bulk strain velocity parameter.
x	axis in entraining direction.
x	distance from the indenter centre line perpendicular to the indenter axis and the normal to the surface (chapter 3).
y	axis in transverse direction.

y	distance normal to surface from the boundary of local deformation (chapter 3).
z	direction parallel to indenter axis (chapter 3).
α	pressure viscosity coefficient in Barus equation.
β	temperature viscosity coefficient.
γ	ratio of roughness correlation lengths in entraining and transverse directions ($\gamma = \infty$ for longitudinal roughness).
$\dot{\gamma}$	shear strain rate.
$\dot{\gamma}_e$	measured nominal shear strain rate in rough disc experiments.
$\dot{\gamma}_s$	nominal shear strain rate based on smooth conditions.
δ	separation distance between centre lines of roll and original strip roughness.
$\varepsilon_x, \dot{\varepsilon}_x$	nominal bulk strain and strain rate — transverse roughness.
$\dot{\varepsilon}_x, \dot{\varepsilon}_y$	variable strain rates in the x and y directions — longitudinal roughness.
$\dot{\varepsilon}_z$	strain rate parallel to indenter axis; zero for transverse roughness, constant for longitudinal roughness.
η	oil viscosity.
η_0	viscosity at ambient pressure.
θ	slope of serrations on ridged surface (chapter 3).
θ	angle between rolls and centreline of strip.
θ_0	as above, but at point where the strip first deforms in bulk.
λ	characteristic roughness wavelength for valley film calculations.
λ_a	characteristic width of asperities for asperity film calculations.
λ	wavelength of asperities (chapter 6).
λ	numerical factor in equation E.2 (appendix E).
Λ	ratio of film thickness to roughness height.
Λ	$= h_d/d$, based on a smooth film thickness (chapter 6).

Λ_r	$= \bar{h}/d_0$, based on a rough mean film thickness.
Λ_s	$= h_s/d_0$, based on a smooth film thickness.
μ	coefficient of friction.
ν	ratio of the width to the length of an entraining wedge.
ν	Poisson's ratio.
ρ_0, ρ_1, ρ_2	hydrostatic pressures — transverse roughness.
$\bar{\sigma}_a$	mean end stress on the perturbed region of deformation — transverse roughness.
σ_b	end stress on the unperturbed region of deformation.
σ_e	end stress across BG in figure 3.2 for $\rho_0 = 0$.
σ_y	plane strain yield stress of strip.
$\bar{\sigma}$	mean tensile end stress on block.
τ	shear stress.
τ_0	Eyring shear stress.
τ_n	nominal shear stress.
$\bar{\tau}$	mean shear traction on indented surface — transverse roughness.
ϕ	fan angle in slip-line field for transverse roughness (chapter 3).
ϕ	angle between valley bottoms and centreline of strip (chapter 4).
ψ	$= b/a$, ellipticity ratio.

Subscripts.

*	conditions where the pressure gradient is zero.
a	under the asperities.
R	refers to roll.
S	refers to strip.
v	in the valleys.

Λ_r	$= \bar{h}/d_0$, based on a rough mean film thickness.
Λ_s	$= h_s/d_0$, based on a smooth film thickness.
μ	coefficient of friction.
ν	ratio of the width to the length of an entraining wedge.
ν	Poisson's ratio.
ρ_0, ρ_1, ρ_2	hydrostatic pressures — transverse roughness.
$\bar{\sigma}_a$	mean end stress on the perturbed region of deformation — transverse roughness.
σ_b	end stress on the unperturbed region of deformation.
σ_e	end stress across BG in figure 3.2 for $\rho_0 = 0$.
σ_y	plane strain yield stress of strip.
$\bar{\sigma}$	mean tensile end stress on block.
τ	shear stress.
τ_0	Eyring shear stress.
τ_n	nominal shear stress.
$\bar{\tau}$	mean shear traction on indented surface — transverse roughness.
ϕ	fan angle in slip-line field for transverse roughness (chapter 3).
ϕ	angle between valley bottoms and centreline of strip (chapter 4).
ψ	$= b/a$, ellipticity ratio.

Subscripts.

*	conditions where the pressure gradient is zero.
a	under the asperities.
R	refers to roll.
S	refers to strip.
v	in the valleys.

CHAPTER 1

INTRODUCTION

In metal rolling processes, lubricants are applied to keep the surfaces of roll and workpiece separated by a film of solid or fluid. This serves two primary purposes. Firstly the lubricant will generally have a relatively low shear stress compared with the workpiece, so that the friction forces generated by shearing of the lubricant will be lower than by shearing of the workpiece itself. Lower loads will then be needed to deform the workpiece. Secondly, damage to the surface of the workpiece will be reduced as the surfaces are kept apart. The lubricant may act as a coolant. In metal working, the heat generated by deformation work is often considerable and this rôle can be of crucial importance.

This dissertation is applicable to friction in a general metal rolling process, but particular attention has been paid to friction in rolling aluminium foil where the friction and lubrication conditions are especially critical. This is confirmed by Cheng [15], who discusses the practical requirements of an aluminium foil rolling lubricant and is demonstrated in a theoretical analysis of foil rolling by Fleck and Johnson [33].

The considerable rôle of lubrication in foil rolling is illustrated by a technique used industrially to control the gauge of the foil. Increasing the load in foil rolling has little effect on the reduction of the foil, because of the elasticity of the rolls. However, by increasing the rolling speed, the friction conditions in the bite are changed due to the hydrodynamic entrainment of the lubricant, thus producing a change in the reduction in foil thickness taken. Indeed, if different lubricant/coolant flow rates are applied across the width of the roll, the differential cooling rates lead to differences in temperature across the width of the roll. Different friction conditions which result can be used to control the reduction and shape variations across the width of the foil. The need for increasingly fine control of both gauge and shape in foil rolling, as well as the demands for greater speeds and hence increased productivity has led to the development of automatic gauge control systems, which control the coolant flow patterns in response to measured differences in shape across the width.

The friction conditions in metal rolling are determined by three constraints.

- i) The finish is generally required to be bright, with a limit on the number of surface defects (e.g. pin holes in foil). When the surfaces are completely separated by the lubricant, the surface of the strip roughens as it is elongated, forming hydrodynamic pits. Only by having close contact between the surfaces of the strip and the roll can a bright surface without excessive pitting be produced.
- ii) Sufficient lubricant must be applied to prevent excessive friction and to reduce damage to the strip and roll surfaces.
- iii) There must be adequate friction to prevent 'skidding' between the roll and the strip.

Where surface quality is a consideration, these requirements generally dictate that there must be some close contact between the roll and strip, but also some hydrodynamic action, giving what is termed mixed lubrication. Lubricant properties, surface finish and overall models of rolling are now discussed in more detail.

1.1 Lubricant properties

The shear behaviour of mineral oils used in rolling is approximated by a Newtonian viscosity at low pressures and strain rates, but this is no longer adequate at higher pressures and strain rates. There are two main techniques to measure the oil properties at high pressures. The first method, notably used by Bair and Winer [7, 6], is to conduct traction tests inside a specially constructed pressure vessel. Alternatively oil properties can be deduced from measurements of traction in the nip of a lubricated concentrated contact. This latter method has been used by Evans and Johnson [27, 28], who made extensive measurements in a disc machine for a variety of oils. Although the disc machine has its disadvantages, it is simple to use and is the only way of making measurements at high shear rates.

The results of these two measurement techniques lead to a constitutive model for mineral oils. The oil may behave as a viscous fluid, with non-Newtonian behaviour becoming significant at a characteristic shear stress, as a plastic solid with a critical shear stress or as an elastic solid at high enough shear rates.

1.2 Surface finish

There are two competing effects which will determine the topography of the strip or foil surface.

- i) Reid and Schey [76] and Ratnagar *et al.* [75] show that hydrodynamic pits are formed transverse to the rolling direction when the film thickness is much more than the initial roughness. A similar type of roughening is found in a tensile test, where individual grains can deform differently depending on their orientation with respect to the straining direction. Thomson [96] shows how hydrodynamic roughening in a thick film rolling operation is related to the nature of the grain structure and the deformation history of the workpiece. Wilson [112] investigates an extra mechanism to enhance this roughening in lubricated rolling. He shows that an instability in the hydrodynamic pressure encouraging formation of these pits can arise where there are differences in yield stress in the strip due, presumably, to the grain structure.
- ii) Soft asperities on the workpiece will be crushed by the hard roll asperities where the film thickness is much less than the roughness. When the underlying material is not deforming in bulk the amount of crushing is limited [16], but it is enhanced where the bulk material is deforming leading to a growth of the contact areas. This aspect of the problem is investigated in chapter 3 where the background is introduced. Friction behaviour will be dependent only on this growth of contact areas where hydrodynamic action is not found and the lubrication is due to boundary additives. Stephenson [90] has included this type of friction in a rolling analysis and Wilson [111] has derived friction laws for a variety of asperity geometries where there is no hydrodynamic effect.

In most metal rolling processes, including foil rolling, there is a need for a good surface finish, so it is important that hydrodynamic roughening is not allowed to take place to any great extent. The film thickness separating the strip and roll must be of the same order or less than the height of the roughness on the surfaces and some contact and crushing of the asperities will take place. With a substantial degree of contact between the roll and the strip, the smooth finish of the roll is then imprinted on the foil. Figures 1.1a and b show electron micrographs of a plastic replica taken from a roll used in aluminium foil rolling and the surface of a piece of aluminium foil

produced industrially. The asperities run circumferentially round the roll, due to the grinding process used to produce the roll surface finish. There is slight hydrodynamic roughening on the foil surface, but the structure of the roughness is basically the longitudinal ground pattern of the rolls. The extent of this pitting will depend on the conditions in which the strip has been rolled and where other constraints override the need for good surface finish the amount of pitting might be increased. A greater degree of hydrodynamic pitting was found in some of the experiments of chapter 5 with thicker films. Figures 5.14b and c show electron micrographs of these surfaces. Individual slip bands can be observed in the micrograph of figure 5.14c with rolled lead.

This imprinting of the roll pattern onto the foil is used in foil rolling where, by reducing the roughness of the ground roll surfaces used in the pass schedule, the roughness of the foil is progressively reduced.

The quality of the strip and in particular the tendency for it to form pin holes will be affected by these hydrodynamic pits, but the generation of oil pressure and friction may not be greatly affected.

1.3 Models of rolling

1.3.1 Smooth rolls and strip

A first approximation to the friction conditions may be made by estimating the film thicknesses for smooth rolls and strip. Work by Wilson and Walowit [107] for smooth rolls has been extended by Wilson and Murch [108] and Dow *et al.* [20] to include thermal effects in the inlet. Wilson and Mahdavian [110] found that a similar thermal calculation for film thicknesses in hydrostatic extrusion agreed reasonably with measured film thicknesses (although the scatter in results was large), even when the thermal correction was very large.

These analyses assume that the geometry of the inlet can be approximated by a straight wedge and that the roll is rigid. Walowit (see [100]) has assessed the effect of including the curvature of the roll in the inlet. Where the elastic deformation of the roll is moderate, this can be modelled by using a slightly increased roll radius given by Hitchcock (see [79]). However, Atkins [3] has directly calculated the effect of the pressures under the contact on the roll shape in the inlet. The elastic deflections

considered appear to be relatively small, but he concludes that, even here, Hitchcock's flattening formula is not very good at estimating the change in inlet geometry.

Where the elastic deflections become large compared with the strip thickness, as is the case in foil rolling, the calculation of the roll geometry becomes rather involved. A parallel can be drawn between thin foil rolling and elastohydrodynamic lubrication (EHL) [23], where the deflections of the roll are greater than the oil film thickness. In EHL, the coupled elastic and hydrodynamic equations must be considered together to find the oil film thickness. Because the elastic deflections are large, there exists a large flat region with a pressure distribution close to Hertzian. Only at the inlet and exit do the film shape and pressure deviate from this distribution. The additional complication of the plasticity of the interposing foil makes the equivalent calculation in foil rolling even more formidable. Fleck and Johnson [33] have simplified the elastic behaviour of the roll using an 'elastic mattress' model to illustrate the effects that may be found. However, Mear and Zhang [64] solve numerically the coupled elastic equations for the roll deflections and the elastic and plastic equations for the foil and find significant differences in the details of the film shape in the nip.

1.3.2 Rough rolls and strip

The effect of roughness on the film generation can be assessed by Λ , the ratio of the mean film thickness to the roughness. The smooth calculations will be good where Λ is greater than about 3 but where this is less than 3 they will no longer be accurate. The buildup of oil pressure for smooth contacts is governed by the Reynolds equation. A number of authors have made attempts to extend this equation for rough contacts. In general these assume a roughness distribution and contact geometry appropriate for less severe contacts. For example, Baglin [5] by an approximate analysis and Tønder and Christensen [92] by numerical solution of the hydrodynamic equations for a fixed film shape, consider the effect of regular longitudinal grooves on the buildup of pressure.

Patir and Cheng [70, 71] find flow factor corrections to the smooth Reynolds equation to describe the effects of roughness. They use numerically generated Gaussian distributions of roughness with different degrees of directionality of the roughness lay with respect to the entraining direction. Although their work is valuable in understanding the effects of roughness orientation on the Reynolds equation, it is derived for

cases where the contact between the two surfaces is small. The numerical results may not be accurate for the situation in metal rolling where the contact is significant. In rolling, the nature of the roughness, made up of a pronounced longitudinal structure punctuated by hydrodynamic pits, is not typical of the Gaussian roughness used in their analysis. The effects of pits on the pressure buildup is much less marked than peaks in a Gaussian roughness, so that these transverse features will not generate the same increase in pressure gradients found by Patir and Cheng for transverse or isotropic roughness. The most critical part of the pressure buildup is when there is significant contact between the strip and roll. Because of the longitudinal nature of the roll and strip roughness, the valleys will then be separated by the contacts at the asperity peaks and the channels formed by the valleys will not be well modelled by Patir and Cheng's roughness.

Only a few attempts have been made to include the effects of roughness in a lubrication calculation. Tsao and Sargent [97, 99] and Tsao and Tong [98] attempt to include the effects of roughness in a simple inlet analysis, although it is probable that their models will not reflect very closely the effects of roughness on the pressure buildup or the contact between roll and strip. A simpler form of the averaged Reynolds equation method to that used by Patir and Cheng has been applied by Sargent and Tsao [80] to find the oil film thickness in a rolling situation using an inlet analysis. They assume a 'micro-elastohydrodynamic' (micro-EHD) film thickness under the contacts to cope with the part of the inlet where there is 'contact' between the strip and the roll. This is not entirely consistent as micro-EHD implies significant pressure differences between the contacts and the valleys, which are not allowed in the averaged Reynolds equation approach, but was used to simplify the analysis.

Sheu [88] has treated the problem of rolling lubrication in depth in a recent dissertation. He considers the effect of roughness on the film thickness, both in the inlet and at the beginning of the zone where the strip deforms. The pressure gradient is calculated assuming Patir and Cheng's flow factor method.

The second important consideration when including roughness in calculations of the lubrication conditions is the influence of the substrate, which is deforming in the nip, on the surface asperity deformations and the growth of the area of contact in a bulk deforming region. Sheu's analysis of strip rolling appears to be the only previous

calculation which has introduced this aspect of the surface asperity deformation in metal working into a lubrication analysis.

1.3.3 Thermal effects

Wilson and Mahdavian [109] derive a thermal Reynolds equation which can in principle be used both in the inlet and the work zones. However, the complications that are involved in a rigorous thermal analysis of the work zone in mixed lubrication have probably not been modelled in sufficient detail to make this or any other thermal analyses accurate enough to estimate thermal effects on the traction in the nip in mixed lubrication rolling with confidence. The effect of the different thermal conductivities of the lubricant, the roll and the workpiece and oxide films that will be present on the surfaces will all be important. Heat generation in the workpiece and in the lubricant separating roll and strip must be balanced by heat flow both conducted into the roll and convected out with the strip. The exact balance between all these competing effects will be very process dependent and only a full analysis will avoid over-simplifying the problem.

A number of papers outline the different thermal effects that must be considered.

- i) Mahdavian and Wilson [61] examine in detail the variation in temperature across a full oil film in the work zone with constant strip and roll temperatures. They show that differences in the strip and roll temperatures and the effect of shear heating in the oil have a significant effect on the friction and lubricant flow in the work zone. The shearing of the oil is concentrated closer to the hotter surface, where the viscosity is less.
- ii) Rashid and Seifrig [73, 74] analyse conduction and convection in an elastohydrodynamic contact with surface layers of different conductivities.
- iii) Johnson and Tanner [94] calculate workpiece temperatures due to deformation work where conduction to the rolls is negligible.
- iv) Patula [72] calculates roll temperature distributions when the heat input from the workpiece is known. He shows that the roll temperatures in the nip are significantly raised only in a small surface layer, which can then adequately be cooled by the lubricant coolant applied on the roll surfaces at the entry side of the bite.

v) It will probably be instructive to apply the flash temperature concept first proposed by Blok [10] to the tops of the asperity peaks where the friction forces would be highest, to ascertain whether the temperatures here would build up appreciably. Again the details would be strongly influenced by the assumed conductivity of the surface layers separating the roll and strip.

Lahoti *et al.* [58] have taken into account items iii) and iv) in combining the heat generation in the nip due to mechanical work with the heat conduction and convection away from the nip using a numerical approximation.

The calculations of film thicknesses and contact area presented in this dissertation will be little affected by changes in the temperature in the bite, but the estimated traction forces may be affected through the change in viscosity of the oil. Although a full thermal analysis of the work zone has not been performed in this dissertation, the information about the friction conditions in the bite necessary for this is included.

1.4 Mechanisms of friction in rolling

The contact in mixed lubrication is generally divided into two regions with different friction characteristics. In the valleys regions the friction is taken as hydrodynamic, dependent on the oil properties and sliding rate. Under the regions of close contact, a number of mechanisms have been proposed which may determine the traction behaviour.

1.4.1 Boundary lubrication

The simplest approximation assumes that boundary lubrication prevails. Evidence for some action of boundary additives is strong. Cheng [15] finds that the reduction taken in experiments rolling $30\mu\text{m}$ foil was reduced from 61% with a 10% additive concentration to 39% without additives, although his experiments were performed at a relatively slow speed of 1.2 m/s so that they will not have the same lubrication conditions as industrial foil rolling. In addition the formation of a herringbone pattern on the foil which arises from an instability in the rolling process related to the friction in the bite, can be prevented by control of the additive concentration [15, 21]. Chambat *et al.* [13] show that the polar additives react with the aluminium in cold rolling to

produce soaps. During rolling, fresh metal surface is produced as the strip elongates and this reactive surface will promote the chemical adhesion of the polar molecules to the surface.

While Langmuir (see [105]) showed that even a mono-molecular layer of a boundary additive is sufficient to reduce friction between metals, it is more likely that a film of boundary additive will build up on the roll surface. Briscoe *et al.* [12] have made a thorough study of the shear strength of calcium stearate, stearic acid and some polymers at the pressures found in metal working, which may be used to estimate the traction forces under a boundary friction contact. They find that shear strength changes little with the thickness of the boundary film, or with the sliding speed and that it is approximately constant at very low pressures, but increases greatly with the contact pressure at metal working pressures.

1.4.2 Metal-to-metal contact

In some contacts the action of the boundary additives may break down. Evidence of this is provided by the way that new rolls used in aluminium foil mills soon acquire a blueish sheen, which is found to be a soft layer including aluminium and aluminium oxide. Similarly, in hot rolling of aluminium, the aluminium metal adhering to the roll must be brushed off continuously to prevent an excessive layer building up. This metallic pickup is typical of situations where there is metal-to-metal contact between the surfaces. Bowden and Tabor [105] show that boundary additives are most effective in preventing the seizure and metal-to-metal contact which is the cause of this pickup. It may be that the primary rôle of the additives is to reduce this breakdown in lubrication.

1.4.3 Micro-plasto-hydrodynamic lubrication

Recent advances in EHL have shown that even under regions of close contact it is sometimes possible to maintain a continuous film of the bulk fluid. Kaneta and Cameron [52], using optical interferometry, have observed films less than 40 nm thick in experiments in which model asperities of chromium were sputtered onto a steel ball. Calculations by, for example, Karami *et al.* [55] and Seabra and Berthe [84], show how the film thicknesses under the contact areas can be calculated from the elastic and hydrodynamic equations. Evidence for a type of micro-plasto-hydrodynamic lubrication in metal working is provided by Mizuno and Okamoto [67] and Mizuno and Hasegawa [66]. They first compressed some rough copper sheets between rough platens to trap oil on the surfaces and measured the friction stress as the sheet was pulled between the platens. If the friction is due to boundary additives on the areas of contact, it should be independent of the sliding speed. However, Mizuno and Okamoto found that the friction does change with the sliding speed. Figure 1.2 shows their results. The area of contact ratio was 0.8. When the product of speed V and viscosity η is below 100 Pa mm, the friction stress is independent of sliding speed — the friction is presumably due to shearing of the boundary molecules. Above this value, the friction increases with sliding speed suggesting that hydrodynamic action is changing the friction conditions. By assuming that this friction is all due to shearing of the bulk fluid under the contact areas, a film thickness can be inferred. Where ηV equals 100 Pa mm the film thickness is estimated as 8 nm, while for $\eta V = 1000$ Pa mm it has increased to 53 nm. The friction is not taking place while the metal is being deformed in bulk, although conditions are reasonably close to those found in rolling, with an enhanced contact area and pressurisation of the oil.

The calculation of film thickness under individual asperities has recently received some attention. Fowles [36] has investigated the film thickness under elastic asperities assuming a Newtonian viscosity. Non-Newtonian properties of the oils at the high pressures and shear rates under the asperities may affect the film thicknesses generated. Sheu and Wilson [87, 106] include the effect of the limiting shear stress found in lubricants at high pressures and shear rates on the inlet pressure buildup. They use a simple rigid geometry, which is probably appropriate for transverse roughness in metal working. The non-Newtonian properties of typical fluids will also affect the side

leakage of oil away from asperity contacts where there is relative sliding. Johnson and Higginson [50] included the limiting shear stress in a theoretical model of side leakage which demonstrated this effect and observed a thinning of the oil films due to enhanced side leakage in a simple traction experiment. Even when the limiting shear stress is not reached, it is possible that the reduction in effective viscosity found at high shear rates may reduce the film thicknesses generated under the asperities, either by a reduction in pressure buildup in the inlet, or by enhanced side leakage under the contact.

An interesting analysis by Sinha *et al.* [89] attempts to combine the rheology of lubricant additives with the roughness of the strip to calculate traction forces in a mixed lubrication regime. Although this is an attractive proposition, it is not clear if the model of the lubricant rheology is more representative of lubricant conditions in a rough contact or if the considerable extra complexity is justified by the need to measure a range of additive properties. However this type of analysis does offer scope for addressing the cross-over between hydrodynamic and boundary lubrication.

1.4.4 Lubricant entrapment

Many authors suggest that lubrication is controlled by trapping of oil in the hydrodynamic pits or transverse valleys found in some metal working situations [32, 65, 67, 81]. The suggestion is that the surfaces are in intimate contact around the edges of the pits and that the oil inside them then becomes trapped. This model of the film thicknesses and lubrication may be appropriate for conditions where there is only a small film thickness and the only roughness present is because of these pits. In these circumstances Kudo *et al.* [56] show that this oil may subsequently be squeezed out due to hydrodynamic action, acting as a reservoir to help the lubrication in the bite. Although this mechanism can occur where the roughness is predominantly transverse and where the hydrodynamic action is small, it is not likely that this mechanism will be significant in most rolling processes where the roughness is mostly longitudinal, except for the hydrodynamic pits. Where there is a significant hydrodynamic action (which will be the case where hydrodynamic pits are being formed) the film thickness will be of the order of the roughness of the roll and strip. These pits cannot then be treated as isolated trapped pits in the lubricated valley areas since there is a significant film thickness surrounding them. Under the areas of contact it may be that this mechanism

of entrapment does serve to enhance the lubrication there. However, it is doubtful whether the pits will become completely trapped here either. It is more likely that considerable leakage of oil sideways out of the transverse grooves into the adjoining valleys will occur as the contact areas are crushed down.

1.5 Traction in a mixed lubrication regime

Although the effects of roughness on lubrication will differ in several ways between elastic and metal rolling contacts, some features will be common. In particular, the onset of mixed lubrication can be measured in both cases by Λ , the ratio of the mean film thickness to the roughness. To identify the likely traction behaviour for a mixed lubrication contact, it is important to have some idea of the mechanism of lubrication. The traction behaviour can then be determined using the appropriate shear stress laws (e.g. Newtonian lubrication, non-linear viscosity, boundary friction).

1.5.1 Elastic contacts

Most of the basic experimental and theoretical work on traction in mixed lubrication has been concerned with elastic contacts.

Bair and Winer [8] have described three separate regimes of traction in an experiment with steel discs lubricated by a variety of oils. They distinguish between traction regimes on the basis of the measured shear stress at a specific slip ratio.

- i) $\Lambda > 15$: they find that the traction is determined by the viscous properties of the oils that they used.
- ii) $1 < \Lambda < 15$: the traction is determined by the plastic shearing of the fluid at these high shear rates.
- iii) $\Lambda < 1$: the traction is greater than the plastic strength of the bulk lubricant, but determined by the strength of the boundary films adsorbed onto the surfaces.

Evans and Johnson [27] distinguish between regimes by comparing traction curves obtained at different Λ ratios. As the contact pressure under the contacts increases the shear behaviour of the bulk lubricant there changes, thus modifying the shape of the

traction curve. The effects of roughness on the traction behaviour can be summarised by three regimes.

- i) $\Lambda > 5$: they found no influence of roughness.
- i) $0.5 < \Lambda < 5$: the shear traction became increasingly determined by the shear property of the oil under the asperities.
- i) $\Lambda < 0.5$: they found that boundary lubrication prevailed.

Results are expressed in terms of Λ , but this alone cannot describe the 'severity' of the contact. For example, if we consider a crowned disc as one of a row of asperities then we can define a Λ ratio as the ratio of the film thickness under the disc to the amplitude of the crown. This Λ ratio can be very much less than one without exhibiting the traction behaviour found in other contacts with small Λ . In a less extreme example, the amplitude or the wavelength of the roughness and the extent to which it can be squashed down elastically will determine the severity of the contact conditions.

In both the sets of experiments described above, the traction behaviour is determined not only by the Λ ratio, giving the effect of roughness on the films generated, but also by the type of shear behaviour of the oil under the asperities or in the valleys (the 'regimes of traction' for smooth contacts described by Evans and Johnson [27]). Thus the change in traction behaviour that Bair and Winer find for $\Lambda = 15$ is not a change in the effects of roughness on the contact, but a change in the bulk behaviour of the oil. The roughness itself plays no rôle in the shear behaviour with these films. Similarly the details of the traction at small Λ ratios will depend on the shear behaviour of the oil at these shear rates.

If regimes of *traction* for rough contacts are required then the approach of Bair and Winer will be dependent on the individual properties of the oil and the type of roughness considered. While the ground surfaces and gear oils that they use may be relevant to many situations, they will not necessarily be applicable to more unusual situations.

Finally the breakdown of the hydrodynamic fluid film occurs at different values of Λ , about 1 with Bair and Winer, but at 0.5 for the experiments of Evans and Johnson. The film thickness under the asperities, which probably determines most accurately the transition to boundary lubrication, depends not only on the Λ ratio but also on the

geometry and elasticity of the asperities.

A recent thesis by Schipper [83] addresses the transitions of lubricated contacts, He attempts to define regimes of traction using only one variable, so that results must be interpreted according to the oil rheology and contact geometry that he uses.

Although the transitions found are useful guides for gear and traction engineers, the exact nature of the transitions will not necessarily be similar in other applications. Here it will be important to identify first the effects of the roughness on the oil film thicknesses under the asperities and in the valleys. After assessing whether full film lubrication will occur, the traction curves can then be found using the shear behaviour of the oil or boundary film at the film thicknesses and shear rates calculated.

1.5.2 Friction in metal rolling

Measurements of friction on a rolling mill are not easy and, because of the complexities of the friction process, interpretations of measurements with mixed lubrication can be difficult. Experimental measurements of friction on a disc machine or on an experimental rolling mill can only be extrapolated with confidence to industrial rolling mills where there is a good understanding of the friction mechanisms involved in each case.

There is a reversal in the direction of relative sliding between the roll and the strip through the bite in most rolling operations, so that measurements of the net traction only give the difference between two opposing friction forces. Direct measurements of the pressure changes in the bite have been made using vapour deposited transducers on the rolls [53], while transducers embedded in the rolls have also been used to measure the friction forces [1, 59, 101]. Although the experimental technique is not easy, Al-Salehi *et al.* claim good reproducibility for their results with embedded transducers using thick strip. Like other friction measurements these are difficult to interpret without a good understanding of the contact conditions. They report typical coefficients of friction between 0.06 and 0.1, but since they find no difference with and without lubrication, these results will not be typical of situations where hydrodynamic action is important.

Several experimenters [60, 65, 76] rely on measurements of the relative speeds of the strip and roll at exit to deduce friction properties in the bite, using rolling analyses by, for example, Ford [see 79] which relate the slip ratio to the friction coefficient. Tsao

and Sargent [99] show that estimates of friction using this method may not always be accurate. Average results of this kind cannot discriminate the details of the friction which will change through the bite in response to changes in pressure and sliding speed, although they may give some indication of the friction conditions in the bite.

Sargent and Stawson [84] describe a set of experiments to evaluate cold rolling lubricants. They conclude that derived coefficients of friction are not always a good indicator of the ability of the lubricant to enable high reductions, but that the energy consumed by the mill when rolling does relate well to the known mill performances.

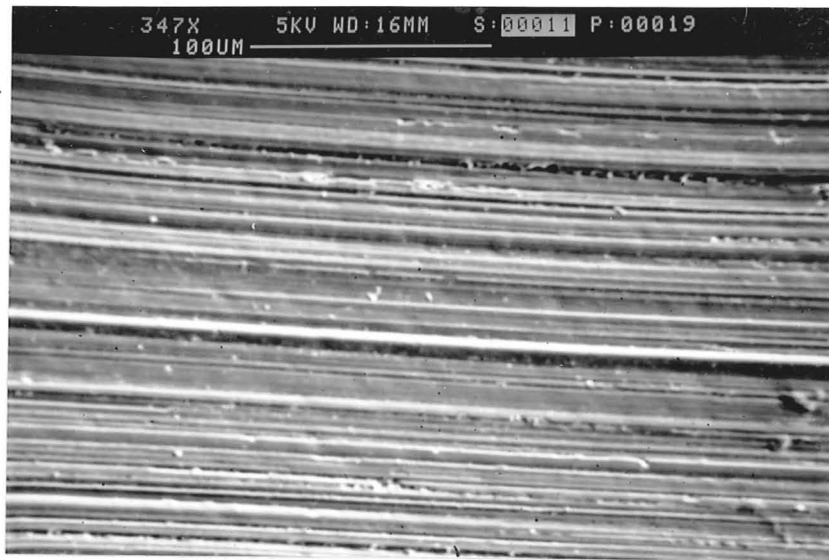
1.6 Measurements of film thickness in rolling

Direct measurements of film thickness in metal rolling are sparse. The technique used commonly in elastohydrodynamics of measuring the resistance or capacitance between the lubricated surfaces cannot work in the mixed lubrication regime because of the asperity contacts [76]. The only technique to have been used appears to be that of Azushima [4], in which he measures the area that a weighed drop of oil covers after rolling, to deduce the mean film thickness of the oil film. This technique has been applied by Tsao and Wilson [100] in the thick film regime and by Sheu [88] in the mixed lubrication regime.

Sheu and others have studied some of the problems associated with modelling friction and lubrication in metal rolling, but the details of the lubrication process and the effect of the various parameters involved on friction are still not clear. It is the object of this thesis to examine some of the physical processes determining friction conditions in metal rolling. In chapter 2, the properties of a base oil used in aluminium foil rolling are measured at the high pressures and shear rates relevant to metal working. Chapter 3 presents a new analysis of the way that asperities are crushed in metal working. This is relevant not only to rolling, but also to other metal working processes. The results of these chapters are used in chapter 4 to calculate theoretical film thicknesses in metal rolling. A distinction is drawn in the analysis between strip rolling, where the elastic distortions of the roll are small and thin foil rolling, where the shape of the roll is dominated by elasticity. However, the theoretical results show that the film

thicknesses and ratio of the areas of close contact to the total surface area can be related to the operating conditions in a similar way in both cases. The film thickness and area of contact ratio calculations are used to give traction curves for foil rolling. Experiments on a small scale mill to validate the calculations of film thicknesses for strip rolling are described in chapter 5. Finally, friction measurements in the mixed lubrication regime, but with no bulk plastic deformation of the surfaces, are presented in chapter 6. Despite the significant differences between this experiment and metal rolling conditions, it is hoped to demonstrate that, in this experiment at least, friction can be estimated reliably from calculations of the film thicknesses under the asperities using the appropriate rheological properties of the oil at the pressures and strain rates there.

a)



b)

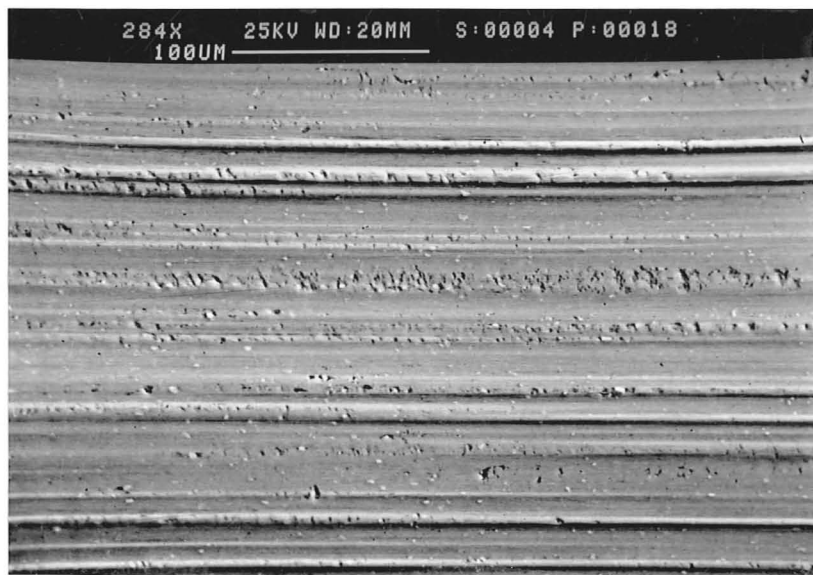


Figure 1.1 Micrographs of a) Roll replica, b) Foil surface.

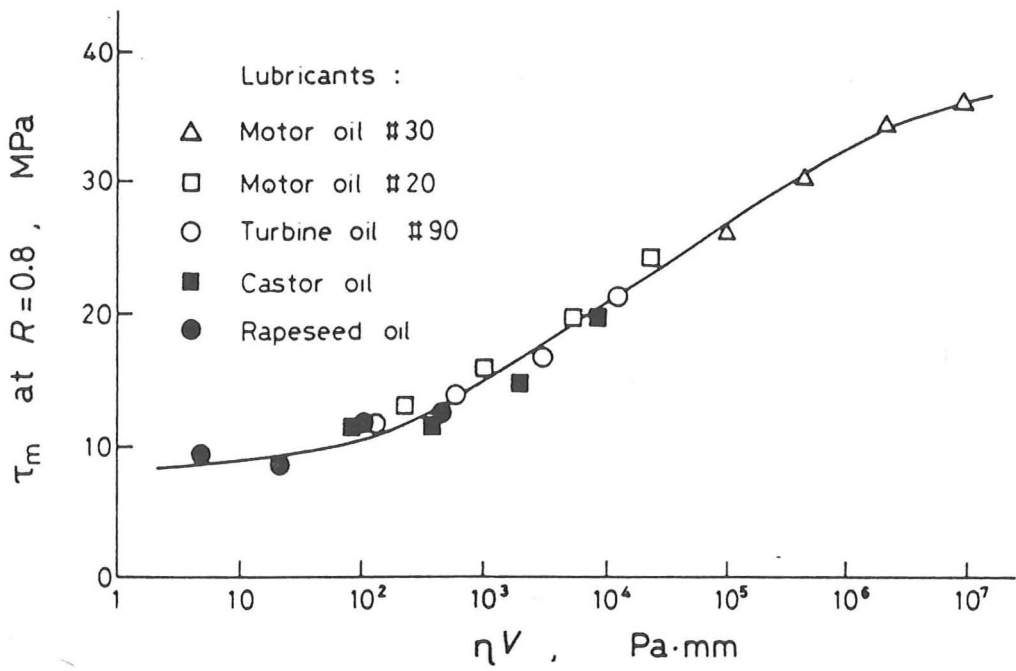


Figure 1.2 The dependence of traction stress on sliding speed in a mixed lubrication experiment (from [67]).

CHAPTER 2

MEASUREMENTS OF THE RHEOLOGY

OF A FOIL ROLLING LUBRICANT

2.1 Introduction

A prerequisite in determining the friction conditions in metal rolling will be some knowledge of the rheological properties of the lubricants used in rolling at the pressures in the bite. For the low pressures at the entry to the bite of elastohydrodynamic and foil rolling contacts, the rheology of the oil may be approximated by a Newtonian viscosity η with an exponential increase in viscosity with pressure p given by the Barus equation

$$\eta = \eta_0 e^{\alpha p} \quad \{2.1\}$$

where η_0 is the viscosity at ambient pressure and α is the pressure viscosity coefficient. This behaviour determines the film thicknesses generated in the contacts. The traction characteristics are determined, however, by the rheology of the oil in the nip.

Evans and Johnson [27, 28] have investigated the properties of a variety of lubricants and constructed a map to delineate which of these factors will influence the traction over a range of conditions. Measurements were made in a disc machine which can measure the viscosity at the high pressures and shear rates required. This chapter describes experiments using the disc machine to derive the rheological properties of a base lubricant, Somentor 31, used in the rolling of aluminium foil. Somentor 31 is a mainly paraffinic kerosine mineral oil with a carbon chain length of approximately 14 and a molecular weight of about 200. No additives were added to the lubricant. Table 2.1 gives the low pressure viscosities as measured in an Amsterdam viscometer [19]. The values of α , the pressure viscosity index, which are included in table 2.1 were averaged over the pressure range 0–100MPa. The thermal conductivity of the oil in the nip was assumed to be the same as that of HVI 650, which, after allowing for the increase in conductivity with pressure [77], is 0.25 W/mK [30].

Evans and Johnson list several effects which may account for the non-linear traction characteristics found in elastohydrodynamic contacts.

i) Shear heating of the oil. In order to eliminate the effect of shear heating in these experiments and identify the non-Newtonian properties of the oil, a correction is made for shear heating in the bite to give isothermal traction curves.

ii) A non-linear relationship between strain rate and shear stress, iii) viscoelasticity and iv) plastic behaviour at a critical shear stress. Evans and Johnson find that the relationship between the shear stress τ and the strain rate $\dot{\gamma}$ in the oil is well described by the non-linear Maxwell model

$$\dot{\gamma} = \frac{\dot{\tau}}{G} + \frac{\tau_0}{\eta} \sinh\left(\frac{\tau}{\tau_0}\right) \quad \{2.2\}$$

with a limiting shear stress τ_c . The oil's properties, the elastic shear modulus G , the Newtonian viscosity η and the Eyring shear stress τ_0 at which non-Newtonian effects become significant are dependent on the pressure and the temperature.

The disc machine is not suitable for measuring the elastic shear modulus, but Evans and Johnson suggest that, as a first approximation this may be estimated as $G = 3\bar{p}$ for mineral oils. They find that the transition between elastic and viscous behaviour is controlled by the Deborah number $= \eta\bar{u}/Ga_0$, where $\bar{u} = (u_1 + u_2)/2$ is the mean rolling speed of the discs and a_0 is the Hertz semi-contact length. Due to the very low viscosity of Somentor 31, the Deborah number will always be small in these experiments and in rolling practice and the traction curves will always be in the viscous regime. For example, using the approximation for G given above, the maximum value of Deborah number in the disc experiments is 0.03. The elastic term $\dot{\tau}/G$ is not then applicable.

(v) Non-equilibrium behaviour of the oil in the contact. No difference was found by Evans and Johnson or in the experiments described in this chapter between traction tests at different speeds. This shows that a transient behaviour in which the oil does not have time to respond to changes in pressure going through the nip does not account for the non-linear behaviour observed. In these experiments the transit times were between 15 and 30 μs ; the time scale in rolling will be much greater, so that transient effects cannot be expected there.

2.2 The disc machine

The details of the disc machine and its operation are described elsewhere [30].

The discs are loaded together using dead weights and the speeds of the two discs measured by counting the passage of holes drilled in thin discs mounted on each shaft. The discs are driven independently to control the sliding speed in the contact. Lubricant was fed onto the discs from a drip supply through a very fine filter to eliminate any contaminating dirt. Small heating elements on the sides of the discs controlled the temperature of the disc surfaces which was monitored using thermocouples trailing on each disc surface. The rise in temperature in the nip due to shear heating was estimated using the method described by Evans and Johnson [28]. By carefully monitoring this correction and the measured surface temperatures, isothermal traction curves were obtained. The maximum thermal correction used was 2°C, because of the uncertainties in this calculation, and the resulting difference between the estimated nip temperature and the nominal temperature was at most 1°C.

The traction force was measured using a strain gauge torquemeter mounted on one of the drive shafts. Because there was a set of bearings between the torquemeter and the contact, the measured friction included some bearing friction. To compensate for this friction, which made up a large proportion of the measured traction in some tests, traction measurements were taken both where the disc with the torquemeter mounted on its shaft was being driven and driving. The point at which there was no sliding between the discs could be estimated with a good degree of accuracy assuming that the traction curve was symmetrical. The measured friction was then taken to be solely due to bearing friction.

Initial experiments used hardened steel discs. However, because Somentor 31 has a very low viscosity, the film separating the discs was very small. The very smooth surface finish required to provide the full film lubrication which is needed to avoid any effects of roughness in the traction measurements was not maintained for any length of time. By using tungsten carbide discs this problem was avoided. Even if there were occasions when contact between the discs occurred, they did not scuff and lose their surface finish. The effective elastic modulus E' for the tungsten carbide was 767 GPa [45]. Due to the high elastic modulus of the tungsten carbide discs the contact was much smaller than with the steel discs and this, combined with the low viscosity of

the oil, meant that traction measurements were made at the limit of the torquemeter's sensitivity. This accounts for the greater than normal scatter in the traction curves, particularly at the lower pressures.

The discs were 75.7mm in diameter with a face width of 19mm. They were polished to a 0.006 μm c.l.a finish and after grinding and polishing had a 0.05 μm crown across the face. The shape of the contact was checked by loading the discs together with a thin copper-coated steel shim between them. The influence of the disc roughness on the traction may be neglected as the minimum oil film thickness in the experiments was 0.07 μm . A high concentricity of the discs was found essential to prevent excessive vibration. This was monitored by examining the output from the torquemeter on an oscilloscope to find the variation in the torque due to the dynamic loading of the discs.

2.3 Deduction of rheological properties

For smooth line contacts in the elastohydrodynamic regime, the mean shear stress and the strain rate in the high pressure region in the nip can be estimated with confidence using well established theory. Traction measurements in a disc machine can then be used to deduce the high pressure properties of the oil. For these heavily loaded contacts, the semi contact width is given by the Hertz width a_0

$$a_0 = \left(\frac{4w'R'_e}{\pi E'} \right)^{1/2} \quad \{2.3\}$$

where w' is the load per unit length of contact, $R'_e = R/2$ is the effective radius of curvature in the entraining direction and $E' = \frac{1}{2} \{ E_1/(1 - \nu_1^2) + E_2/(1 - \nu_2^2) \}^{-1}$ is the effective elastic modulus. The mean pressure \bar{p} in the nip is

$$\bar{p} = \frac{w}{2a_0} \quad \{2.4\}$$

and the mean shear stress τ in the oil is

$$\tau = \mu\bar{p} \quad \{2.5\}$$

where μ is the traction coefficient.

For the conditions of these experiments the central film thickness may be estimated using the formula of Dowson and Toyoda [22]

$$h_d = 2.43R'_e \left(\frac{\alpha\eta_0\bar{u}}{R'_e} \right)^{0.69} (\alpha E')^{0.07} (\alpha\bar{p})^{-0.20} \quad \{2.6\}$$

This formula was derived from calculations assuming steel discs; the film thickness will be slightly less for tungsten carbide discs. Because of their higher elastic moduli the tungsten carbide discs will have higher pressures, giving a greater compression of the oil in the bite, where the other dimensionless operating groups are the same. A correction has been made for this amounting at most to 8%, following the method of appendix E.

The mean oil strain rate in the nip is then

$$\dot{\gamma} = \Delta u / h_d$$

where Δu is the relative sliding speed of the discs.

If the oil behaves as an Eyring viscous fluid then, at sufficiently high shear stresses, the logarithm of the strain rate is linearly related to the shear stress, with the slope giving the Eyring shear stress τ_0 . The Newtonian viscosity η can be found in two ways; either from the slope of the shear stress–strain rate curve at small strains or from the traction curve at large strains once τ_0 has been determined¹.

2.4 Results

Measurements were taken at three mean Hertz pressures of 625, 945 and 1510MPa and at temperatures of 40 and 80°C.

The measured strain rate–shear stress relationships are given in figures 2.1–2.5. The large scatter in the results at small strain rates in figures 2.1, 2.3, 2.4 and 2.5 is due to errors in accounting for the bearing friction. This problem is not important in estimating the small strain rate viscosity, since it is only the slope of the curve at this position which is important and not the exact position of the zero. This is demonstrated in figure 2.2, where the two halves of the traction curve have been plotted and the small strain viscosity fit included. The relationship between shear stress and strain rate was found to be typical of an Eyring fluid. For the measurements at 625 MPa and 80°C, it

¹ The process of assuming an average pressure and viscosity for the lubricant in the high pressure region of the contact is used with a good degree of success in conventional disc experiments. In the Newtonian regime the shear stress varies exponentially with pressure for a given strain rate making averaging of the traction over the contact dubious. However, when operating in the Eyring regime, the shear stress is linearly related to the pressure at a constant strain rate so that averaging becomes more reasonable.

was not possible to go sufficiently far into the non-linear region to deduce a high strain rate viscosity or Eyring shear stress without excessive shear heating in the nip. The low and high strain rate viscosities and the deduced Eyring shear stresses are shown in figures 2.6 and 2.7.

The viscosities at low and high shear strain rates are derived independently. It is rather surprising that these measurements should agree so well. Because of the averaging of the traction and pressure over the contact, the mean viscosity in the small strain rate Newtonian region should significantly overestimate the actual viscosity at the mean pressure while the high strain rate data should give a reasonable averaging process.

Evans and Johnson find that the limiting shear stress τ_c is approximately proportional to the mean pressure for mineral oils. In none of the above measurements up to a shear stress/normal pressure ratio of 68/1510 MPa ($\mu=0.045$) was a limiting shear stress observed.

There is no significant difference between measurements at speeds of 3.96 and 9.91m/s at 1510MPa and 40°C (figure 2.6), showing that transient effects in the nip are not important in these measurements.

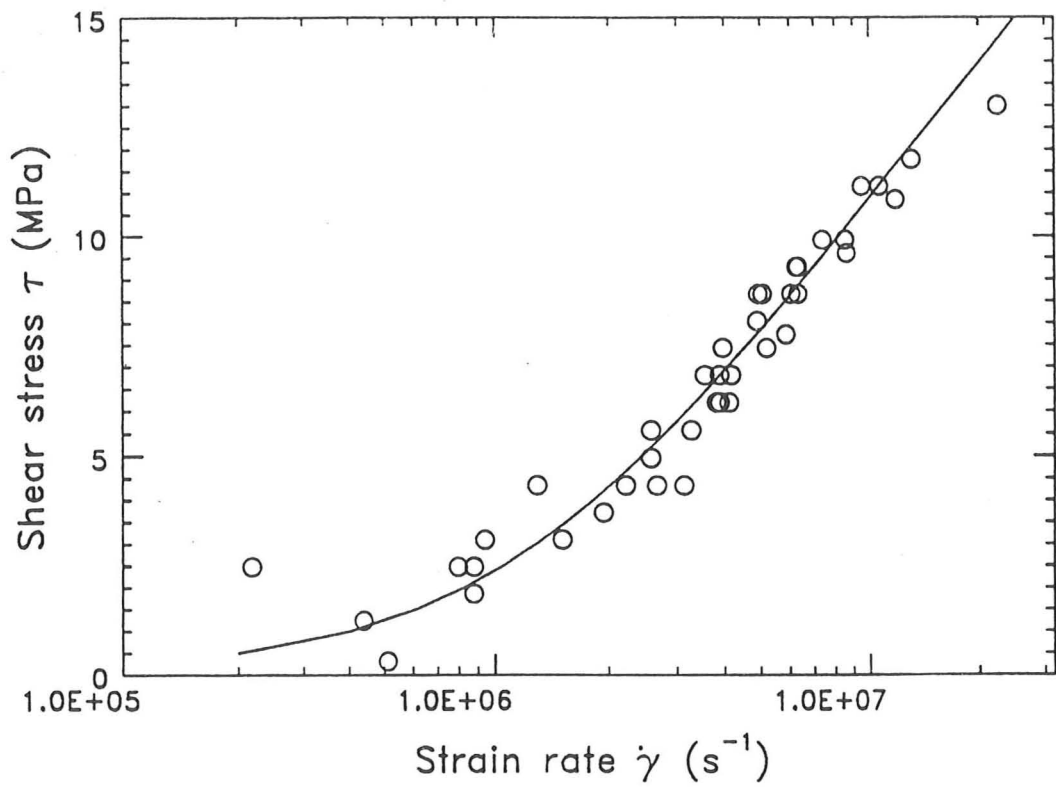
Roelands [78] gives a form of equation for mineral oils which has been found in some cases to give a good extrapolation from relatively low pressure viscometer measurements to those at higher pressures. The low pressure viscosity measurements given in table 2.1 have been used in reference [19] to derive a Roelands fit to the results for Somentor 31, which is a mineral oil. This fit underestimates the viscosity at high pressures. It may be that measurement problems encountered with the Amsterdam viscometer at the higher pressures contributed to this. Figure 2.7 shows that there is a reduction in α with pressure for Somentor 31, which is typical for mineral oils.

Eyring shear stress values are similar to those found by Evans and Johnson for the mineral oil HVI 650. They found a slight increase in τ_0 with temperature. In these experiments there is a slight drop in Eyring stress with temperature at 1510MPa. However, errors in estimating τ_0 from the slope of the traction curves are of the same order as the small rise with temperature expected. The rise in Eyring stress with pressure found here is similar to the increase that Evans and Johnson found for HVI 650 (see figure 6.5). The Eyring stress has been related to the activation volume of the molecule(s)

which are moving in the shearing motion [45]. The higher values of τ_0 observed with Somentor 31 than with HVI 650 are as expected given the smaller relative molar weight of Somentor 31 of 200 compared with the value of 800 given by Tevaarwerk [95] for Vitrea 79, a very similar oil which HVI 650 replaces.

Table 2.1 Low pressure viscosity and pressure viscosity coefficient of Somentor 31, from [19].

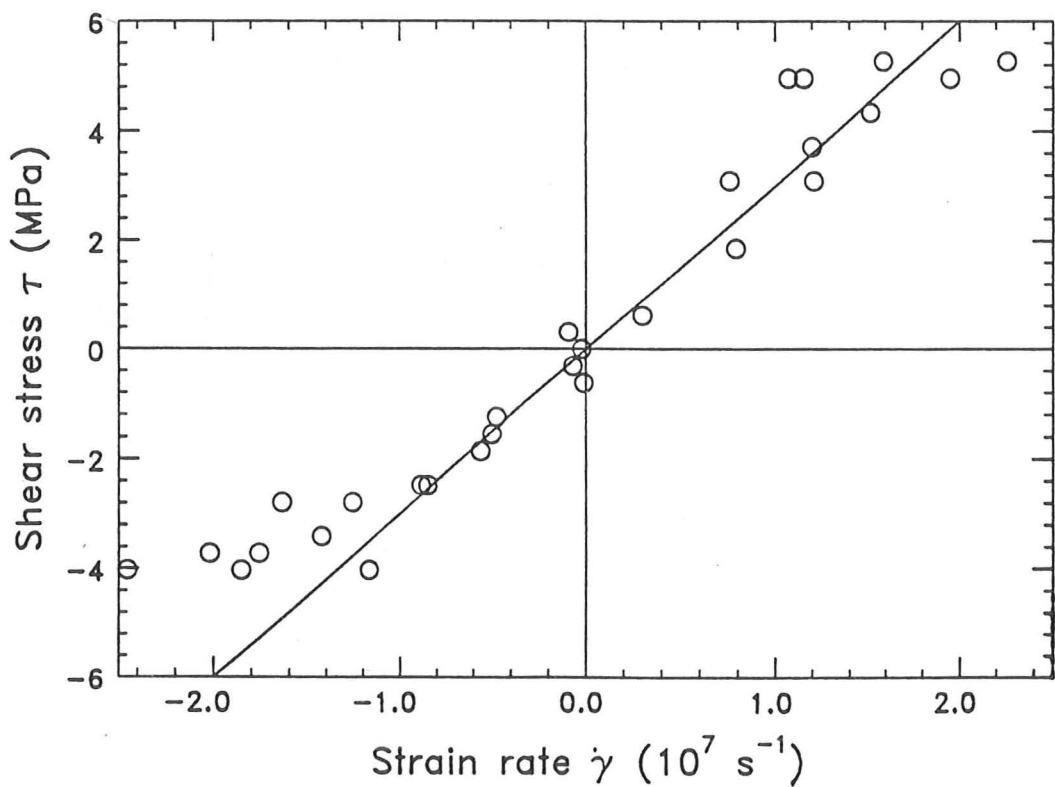
Temperature	40°C	60°C	100°C
Pressure (MPa)	Viscosity (mPas)		
0	1.409	1.033	0.632
25	1.905	1.386	0.844
50	2.481	1.784	1.080
75	3.157	2.192	1.342
100	3.985	2.699	1.625
α ($10^{-9}\text{m}^2/\text{N}$)	10.40	9.60	9.44



KEY

Eyring fit; $\tau_0=4.5$ MPa, $\eta=2.5$ Pas

Figure 2.1 Traction curve; $\bar{p} = 625$ MPa at 40°C.



KEY

Newtonian fit; $\eta=0.33$ Pas

Figure 2.2 Traction curve; $\bar{p} = 625$ MPa at 80°C.

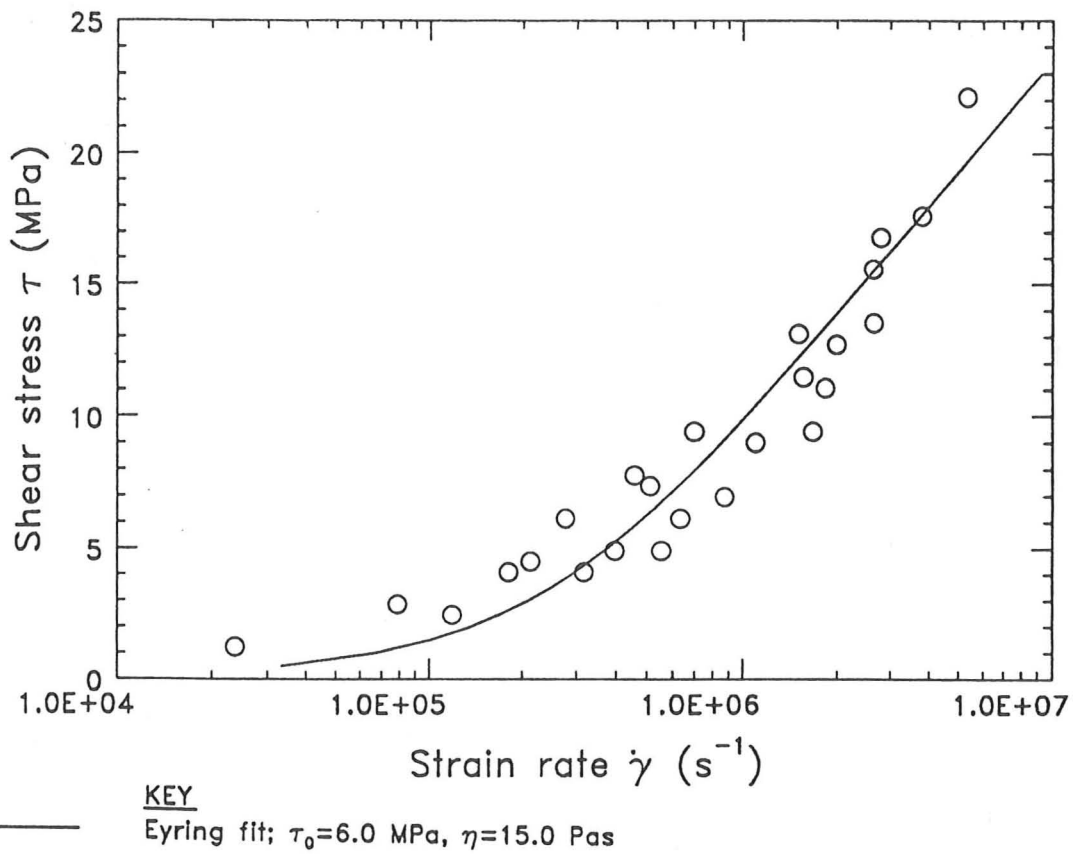


Figure 2.3 Traction curve; $\bar{p} = 945$ MPa at 40°C .

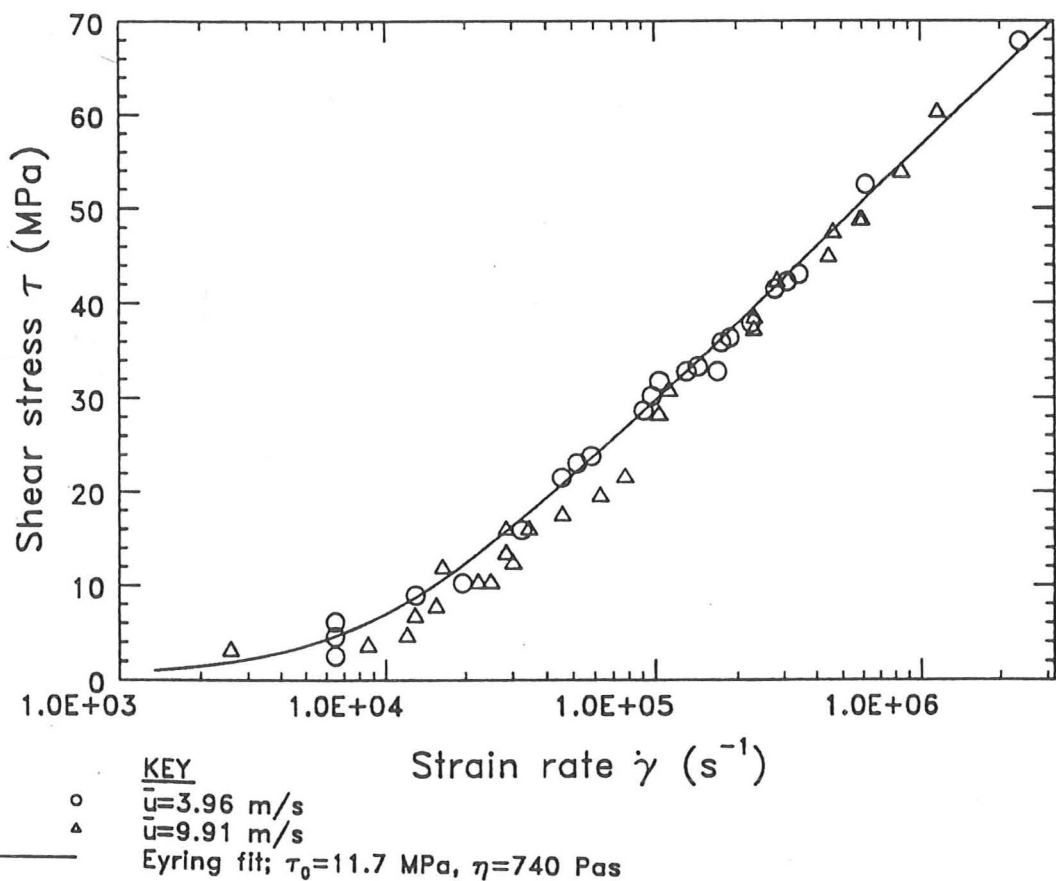
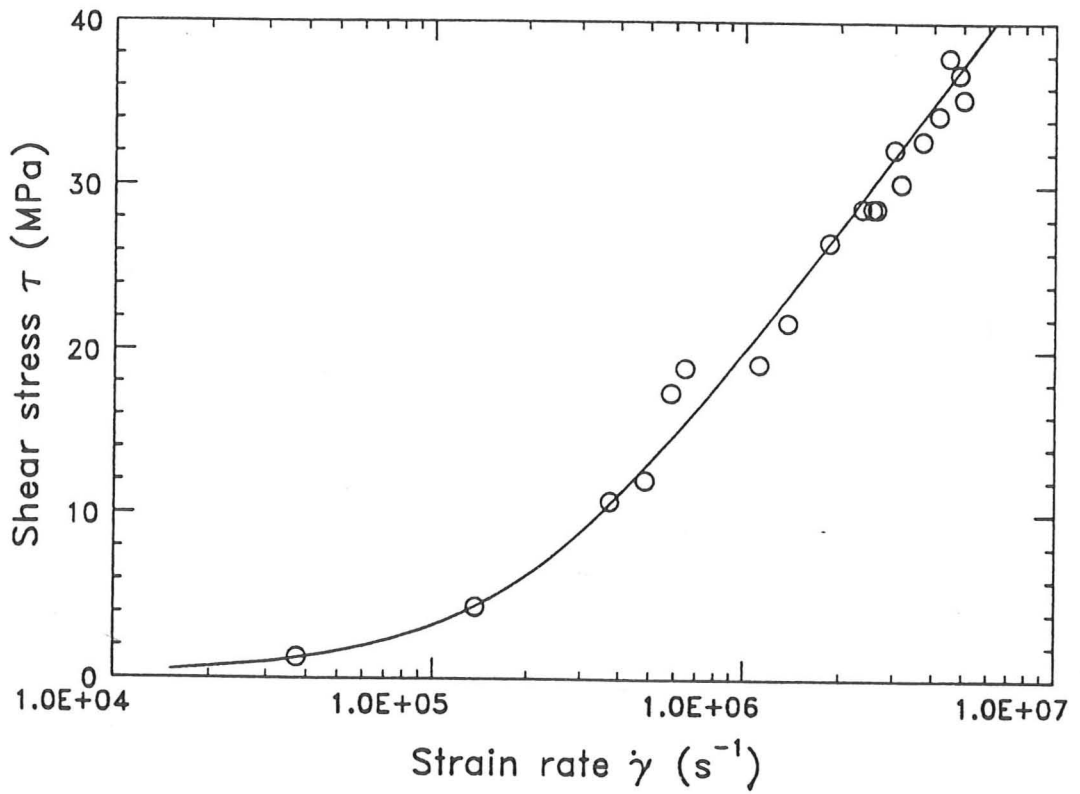


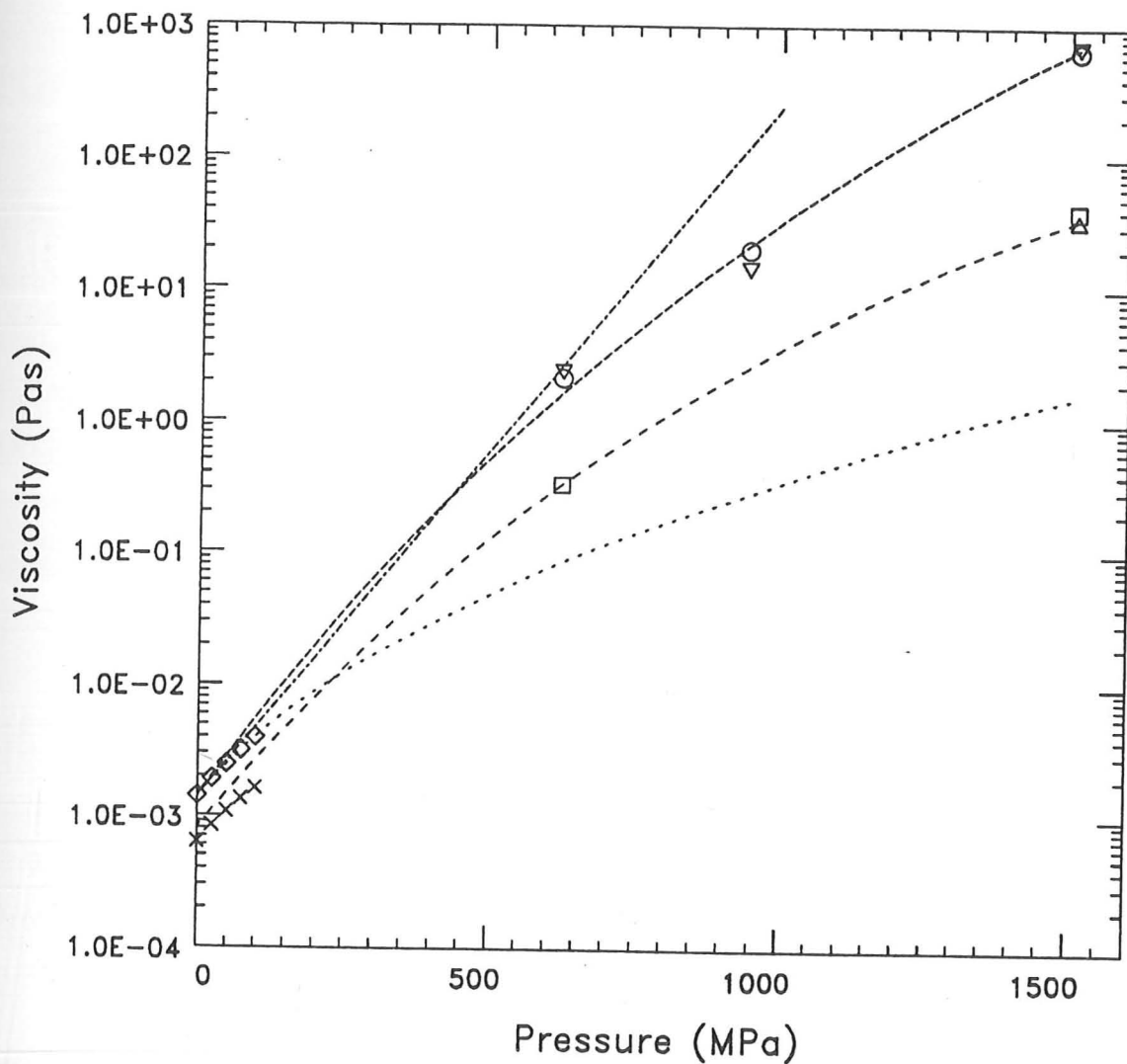
Figure 2.4 Traction curve; $\bar{p} = 1510$ MPa at 40°C .



KEY

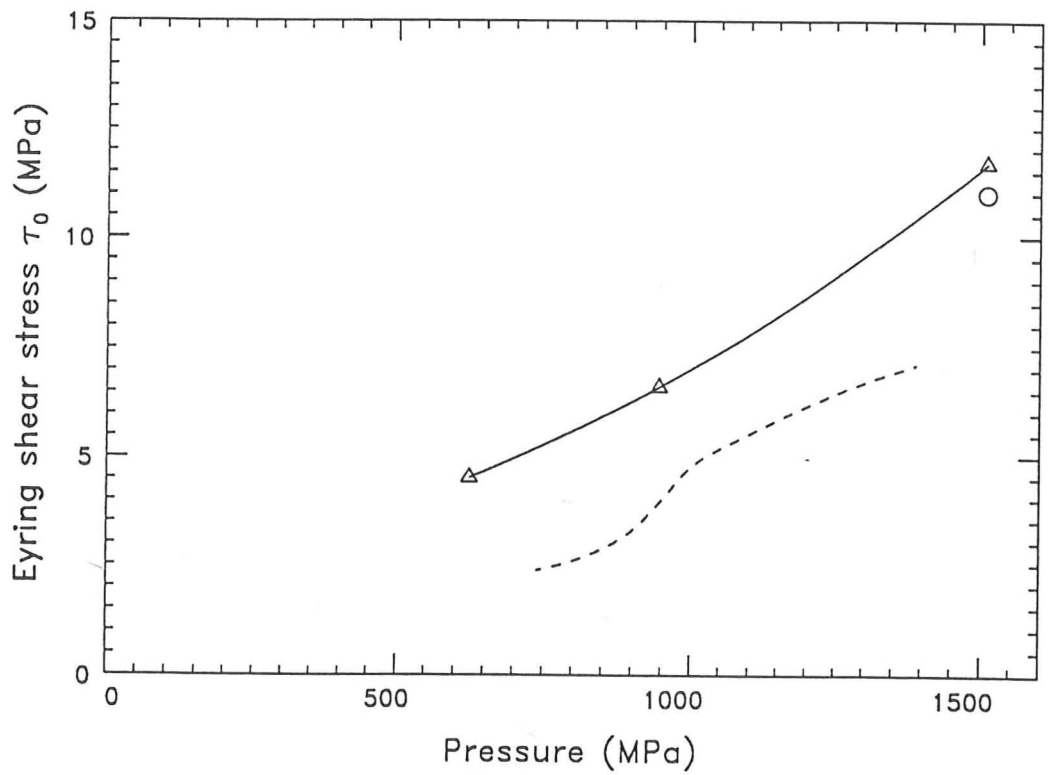
Eyring fit; $\tau_0=11.0$ MPa, $\eta=33$ Pas

Figure 2.5 Traction curve; $\bar{p} = 1510$ MPa at 80°C .



- KEY**
- Small strain viscosity at 40°C
 - ▽ Large strain viscosity at 40°C
 - Small strain viscosity at 80°C
 - △ Large strain viscosity at 80°C
 - ◇ Viscosity at 40°C
 - x Viscosity at 100°C
- } Disc experiments
- } Amsterdam viscometer
- Best fit at 40°C
 - - - Best fit at 80°C
 - ⋯ Roelands fit at 40°C
 - · - Barus equation at 40°C

Figure 2.6 Variation of viscosity with pressure for Somentor 31.



KEY

- △— Somentor 31 at 40°C
- Somentor 31 at 80°C
- - - HVI 650 at 60°C

Figure 2.7 Variation of Eyring shear stress with pressure for Somentor 31.

CHAPTER 3

SURFACE ASPERITY DEFORMATION IN METAL FORMING PROCESSES

3.1 Introduction

Bowden and Tabor [11] introduced the idea of asperity junctions as a mechanism for friction between poorly lubricated surfaces. To explain the high coefficients of friction found with clean metals McFarlane and Tabor [63] suggested that junctions grow under the combined action of normal pressure and tangential loading. Where surfaces are loaded together under dry conditions or with boundary lubrication most of the load is carried by the asperities in close contact. In these cases the friction between tool and workpiece will be controlled by the growth of the true areas of contact. Among many examples of metal working processes with boundary lubrication there has been recent interest in the surface modification during deep-drawing [102, 103].

Two factors complicate the picture of contact growth in metal forming processes. Firstly, at the high pressures involved there is interaction between contacting asperities and secondly, the deformation of the bulk material will affect the asperity deformation. Childs [16] and Wanheim and Bay [9, 104], among others, have investigated the first effect and find that, without any bulk deformation, the growth of contact area will be limited as the pressure increases.

The effect of bulk plasticity was highlighted by Greenwood and Rowe [38], who showed how asperities were flattened when deforming short cylinders with bulk deformation directly below the asperities. With taller cylinders which were free to barrel however, they found that asperities persisted. An early set of experiments by Fogg *et al.* [34, 85] showed how the area of contact ratio was increased in model asperities with bulk deformation of the substrate.

Recent work by Wilson and Sheu [86, 105, 111] has investigated the effect of bulk plasticity on asperity flattening when the lay of the roughness is parallel to the bulk straining direction ('longitudinal roughness'). They found that the rate of asperity

flattening with bulk straining was related to the spacing of the asperities and to the difference in pressure between 'loaded' and 'unloaded' parts.

Makinouchi *et al.* [62] have recently presented some elastic-plastic finite element solutions for the case of transverse roughness.

The present chapter presents a slip-line field analysis of flattening of transverse asperities and investigates further the flattening of longitudinal asperities.

3.2 Transverse roughness

3.2.1 Theory

As an idealised model of asperity deformation in a plastically deforming bulk, consider a rigid perfectly plastic block subjected, in plane strain, to multiple indentations on opposing surfaces and some load on its ends (figure 3.1). The indenters represent the discrete loading found when rough surfaces are in contact with a smooth die. In the first instance we shall consider the surface to be loaded normally, i.e. friction will be neglected. Figure 3.2a shows two typical indenters in contact with the surface of such a block, well away from the ends. An average pressure \bar{p} over the whole top surface is applied through indenters similar to those above ABC and $A'B'C'$. The slip-line field in figure 3.2a combines Hill's solution for the indentation of a strip of depth $2h$ [44] with the field for homogeneous loading and plastic deformation in the middle of the block. In regions 5 and 5' the slip-lines are orientated at 45° , so that below JKJ' the slip-line field is that for uniform biaxial loading; a criss-cross pattern of lines at 45° to the principal axes. For bulk yielding this region will be loaded so that the difference in stresses is $2k$, the plane strain yield stress. Region 3 is taken to be rigid.

In this case the rigidity of region 3 along the lines GK and $G'K$ constrains the deformation to consist of a series of rigid blocks similar to 5 and 5' separated by velocity discontinuities (e.g. GK , KL , LN etc.). Hence on vertical lines below B and B' , the centres of the indenters and below D , the midpoint between indenters, the sideways component of velocity is constant. Provided the distance to the centre of the block below JKJ' is an integral value of $2c$ (where $2c$ is the distance between indenters), the velocity fields from the top and bottom of the block will be compatible. Figure 3.2b shows the complete hodograph for such a block with the centre line located along

MNM' . This hodograph is simply obtained by taking the hodograph for Hill's forging solution (see for example [35], p.92) and adding the rigid block motion of the uniformly loaded region below GG' .

The fan angle ϕ is fixed by the condition that the hydrostatic pressure at G must be continuous between regions 4 and 5. In the field of figure 3.2, with a mean pressure \bar{p} on the whole top surface, the pressure under each indenter is $p_0 = \bar{p}(c/a)$, where $2a$ is the indenter width. Putting $A = a/c$, the hydrostatic pressure ρ_0 under the indenter is

$$\rho_0 = p_0 - k = \bar{p}/A - k \quad \{3.1\}$$

Using Hencky's equations the hydrostatic pressure ρ_1 at G in region 4 is given by

$$\rho_1 = \rho_0 - 4k\phi \quad \{3.2\}$$

Knowing that the material in the rigid regions 5 and 5' is under uniform biaxial loading and at yield with a tensile end stress σ_b and a compressive pressure \bar{p} , the Von Mises yield criterion gives

$$\bar{p}/2k + \sigma_b/2k = 1 \quad \{3.3\}$$

From the Mohr's circle, the hydrostatic pressure ρ_2 at G in region 5 is

$$\rho_2 = \bar{p} - k \quad \{3.4\}$$

But ρ_1 equals ρ_2 so that, combining equations 3.1, 3.2 and 3.4

$$\phi = \frac{\bar{p}}{4k} \frac{(1-A)}{A} \quad \{3.5\}$$

The stresses in Hill's solution for forging are a function of the fan angle ϕ and are only defined relative to an arbitrary hydrostatic pressure. Ewing [31] has computed the horizontal force across the slip-line CFG and hence the mean stress σ_e on BG for a hydrostatic pressure ρ_0 equal to zero. Adding the value of the hydrostatic pressure ρ_0 at B given by equation 3.1, the mean stress $\bar{\sigma}_a$ on BG becomes

$$\bar{\sigma}_a = \sigma_e - ((\bar{p}/A) - k) \quad \{3.6\}$$

With a uniformly loaded surface BB' the stresses would be homogeneous so that $\bar{\sigma}_a = \sigma_b = 2k - \bar{p}$. With the periodically loaded surface considered here the total

tensile force acting on the ends of the block in the x direction to produce bulk yielding is changed by a force F per unit width, given by

$$F = (\bar{\sigma}_a - \sigma_b)h \quad \{3.7\}$$

Using equations 3.3, 3.4 and 3.6, this simplifies to

$$F/2ka = (h/a) \left((\sigma_e/2k) - 2\phi - 1/2 \right) \quad \{3.8\}$$

h/a and $\sigma_e/2k$ are functions of ϕ only (obtained from the data computed by Ewing) so we can write

$$F/2ka = f(\phi) = f \left(\frac{\bar{p}}{4k} \frac{(1-A)}{A} \right) \quad \{3.9\}$$

The values for h/a , $\sigma_e/2k$ and $F/2ka$ at various fan angles ϕ are given in table 3.1. Since F is negative, the block yields at a lower total end load than for the uniform loading case with the same mean normal pressure \bar{p} .

While the 'slip-line field' proposed in figure 3.2 provides an upper bound on the loads in the co-indentation problem, to establish that the stress field is correct and unique it is necessary to show that yield is not exceeded in the undeforming region. As \bar{p} is increased the corner of the rigid region at C will become over-stressed when

$$\frac{\bar{p}}{A} > 2k \left(1 + \frac{\pi}{2} \right) \quad \{3.10\}$$

For small A deformation will now proceed with independent indenter fields with $\pi/2$ fan angles. For $A > 0.5$, Wanheim [104] provides the equivalent collapse mechanism, similar to backwards extrusion. For values of \bar{p}/A between $2k(1 + \pi/2)$ and the Wanheim collapse load, equation 3.8 now provides an upper bound on the loads rather than an exact solution. The exact solution will have a curved slip-line CE and a non-uniform distribution of pressure on the indenter face AC .

This restriction on the maximum allowable pressure for a given indenter spacing restricts the range of fan angles considered in the analysis. It has the effect of eliminating from consideration those solutions where, with fan angles greater than 45° , the fans from adjoining indenters overlap.

To complete the solution it would be necessary to ensure that yield is not exceeded throughout region 3. Although yield is not exceeded at the critical corners, an allowable stress field for this region has not been found.

To represent the way that the deformation is modified by loading the surface periodically, consider the velocity parameter W such that

$$W(\bar{p}, A) = \frac{v_a - v_v}{v_s} = \frac{v_f}{c\dot{\epsilon}_x} \quad \{3.11\}$$

v_a and v_v are the velocities of the loaded portions under the indenters and the unloaded surface respectively. $v_f = (v_a - v_v)$ is the relative velocity between the loaded and unloaded surfaces. v_s is the sideways velocity of the material in the mid-plane between the indenters below D and $\dot{\epsilon}_x$ is the mean longitudinal strain rate. As W increases the loaded parts of the indented surfaces move down more quickly than the unloaded parts. From the hodograph it can be seen that $W = h/a$.

i.e.
$$W = f(\phi) = f\left(\frac{\bar{p}(1-A)}{4kA}\right) \quad \{3.12\}$$

The relationship between W and \bar{p} is plotted in figure 3.3 with A as a parameter. Figure 3.3 has three regions separated by dashed lines. These are

- i) a region where the material is yielding in bulk and the corner C at the edge of the indenter is not over-stressed,
- ii) a region where, because the corner C is over-stressed, the solution merely provides an upper bound on load,
- iii) a region where no bulk deformation takes place but local deformation similar to reverse extrusion takes place, either with a Prandtl field for $A \leq 0.5$ or Wanheim's field for $A > 0.5$. The critical pressures at which this breakout occurs are indicated by arrows and the corresponding maximum fan angles ϕ_{\max} for each area of contact ratio A are also shown.

As the applied pressure tends to a uniform loading (either $\bar{p} \rightarrow 0$, or $A \rightarrow 1$), the fan angle ϕ tends to zero and W tends to 1. For uniform pressure on a rigid perfectly plastic material, rigid block deformation is admissible provided $-1 < W < 1$. As here, a slight compressive perturbation of the loading on the surface will stabilise the deformation with $W = 1$, while a tensile perturbation will give a block deformation with $W = -1$. When specimens are deformed in simple tension their free surfaces are roughened by this mechanism, since small differences in the yield stress can lead to significant differences in the deformation pattern. Strain hardening limits this effect for real materials.

Figure shows how this periodic loading of a rigid plastic block affects the velocities as compared with uniform loading.

- i) The process can be viewed as a perturbation of uniform deformation to a depth below the surface which is a function of the dimensionless group $(\bar{p}/4k)(1/A - 1)$
- ii) Due to the localisation of stress beneath the indenters the longitudinal tensile stress required to initiate bulk yielding is reduced. Relatively thin blocks will deform at significantly lower loads than for homogeneous loading. For thicker blocks this effect will become insignificant since the change in loading is confined to a surface perturbed layer.
- iii) Loaded portions of the indented surface move in more rapidly than unloaded parts.
- iv) As the mean pressure is increased the contact pressures on the indenters can reach those found when the bulk of the block is not deforming.

The theory is limited to a perfectly plastic solid, with the depth of the block some integral multiple (plus a constant) of the indenter spacing.

For a strain-hardening material the idealised velocity discontinuities found theoretically will not be present, but will become narrow zones of intense shear.

For non-integral depths of block the solution will become modified, rather in the way that Green [37] has modified the solution for frictionless compression between wide platens to accommodate non-integral width/depth ratios by using curved slip-lines and velocity discontinuities. For the periodic indentation considered here where the central bulk deforming region is not a multiple of $2c$, Green's field can be used in the central region to provide an upper bound on the load required for deformation. For a bulk deforming region greater than $2c$, the change in mean end stress due to the non-integral depth of the block is increased by at most 3.9%, indicating that the required modification to the slip-line field would be slight. Moreover, as the depth of the block increases, the change in loading due to a non-integral depth will decrease and the slip-line field will tend to that for integral depths near the surface.

It is interesting to note that the solution by Makinouchi *et al.* [62], using an elastic-plastic finite element method, also has the features found in the slip-line solution. In particular they found an elastic undeforming region under the surface between the indenters and a growth of contact area with bulk strain. Their solution also has diagonal

bands of high shear in the bulk of the material. They found that the influence of strain-hardening on the deformation process was slight.

The above theory may be extended in two ways

i) A block to which shear as well as normal tractions are applied to the indented surface. While no detailed calculations have been performed in the case of shear tractions as well as normal loading, a slip-line field very similar to that for the normal loading case will be appropriate. There will be a rigid region under each indenter with two fans of equal angle ϕ_2 centred on the edges of the indenter. The indenter fields can then be joined to the appropriate field of stress in the bulk of the block in a similar way to that for normal loading. For the case where the shear traction is applied in opposite directions on the top and bottom surfaces figure 3.4 shows a typical slip-line field and hodograph. For a block where the shear traction acts in the same direction on the top and bottom faces of the block, the fields shown in figure 3.4 will be a surface perturbation of Prandtl's solution with cycloidal slip-lines (see [44] p.232).

ii) A block with a serrated surface deformed by a flat platen. To illustrate how the basic theory may be applied to squashing a serrated surface, consider the geometry of figure 3.5 with a ridge slope θ of 20° . The serrated surfaces are now compressed by rigid flat dies with a mean normal pressure \bar{p} and a mean tensile stress $\bar{\sigma}$ is applied to the ends of the bar. Initially, without any longitudinal strain ϵ_x , the serrations are crushed in the manner described by Hill ([44] p.255). Neglecting the effect of displaced material on the surface's geometry, the contact pressure is approximately given by

$$p_0 = \bar{p}/A = 2k(1 + \pi/2 - \theta) \quad \{3.13\}$$

Bulk plastic flow will occur when $(\bar{p} + \bar{\sigma})$ satisfies

$$\frac{\bar{\sigma}}{2k} + \frac{\bar{p}}{2k} = 1 + \frac{F}{2ka} \frac{a}{H_0} \quad \{3.14\}$$

$2H_0$ is the depth of the undeformed block. The slip-line field of figure 3.2 then applies and the serrations will then be crushed further at a rate which is related to the longitudinal extension rate by the curves in figure 3.3.

Referring to figure 3.5, the rate of growth of the contact area $2a$ and the distance between indenters $2c$ is given by

$$\begin{aligned} \frac{da}{dt} &= \frac{v_a - v_v}{\tan \theta} \\ \frac{dc}{dt} &= v_s \\ \text{i.e.} \quad \frac{da}{dc} &= \frac{W}{\tan \theta} \end{aligned} \quad \{3.15\}$$

The relationship between the 'real area of contact ratio' A and the nominal longitudinal strain $\varepsilon_x = (c - c_0)/c_0$, is

$$\frac{dA}{d\varepsilon_x} = \frac{dA}{d\left(\frac{c-c_0}{c_0}\right)} = \frac{c_0}{c} \left(\frac{da}{dc} - A \right) = \frac{1}{(\varepsilon_x + 1)} \left(\frac{W}{\tan \theta} - A \right) \quad \{3.16\}$$

c_0 is half the distance between indenters before loading. By taking small increments of ε_x and using the value of W corresponding to the current value of A , with a constant mean pressure \bar{p} , the relationship between the real area of contact ratio and the nominal longitudinal strain can be plotted as a function of \bar{p} (figure 3.6). As $\bar{p} \rightarrow 0$, $W \rightarrow 1$ and equation 3.16 has the solution

$$\varepsilon_x = \frac{1}{1 - A \tan \theta} - 1 \quad \{3.17\}$$

For smaller slopes θ , the curves will be rather steeper varying roughly as $1/\tan \theta$.

The end stress will be determined by equations 3.9 and 3.14. For the initial geometry of figure 3.5 with $H_0/c_0 = 3.9$ and a mean pressure $\bar{p}/2k = 0.66$, the relation between real area of contact ratio A and the sum of the applied stresses $\bar{p}/2k + \bar{\sigma}/2k$ required for deformation is plotted in figure 3.7. Allowance has been made for the effect of longitudinal straining on this stress and for the effect of the reduction in depth of the specimen.

The influence of bulk plastic flow on the crushing of asperities can be appreciated from figure 3.6 (which has been computed for a regular array of 20° serrations). In the absence of bulk deformation a flat rigid die, loaded against the tips of the asperities with a mean pressure \bar{p} , will cause the serrations to crush in a well known manner by extruding the material displaced from the tips into the intervening gaps. The ratio of 'real' to 'apparent' contact areas A for different mean pressures appears on the vertical axis ($\varepsilon_x = 0$) in figure 3.6. If the block is now subjected to a mean bulk strain ε_x

parallel to the nominal surface, the serrations crush further without any increase in pressure, following one of the curves in figure 3.6 until they disappear entirely when $A = 1$. This process is achieved by the inhomogeneous deformation field, which permits the material below the true contacts to penetrate into the block at a greater rate than that which is located between the contacts.

Depending on the mean pressure \bar{p} and the depth of the block, the mean pressure \bar{p} and the mean end tension $\bar{\sigma}$ for bulk yield sum to somewhat less than $2k$ but, for blocks which are deep compared with the spacing of the serrations, this effect is small and $(\bar{p} + \bar{\sigma}) \approx 2k$.

3.2.2 Experiments – transverse roughness

To test the validity of the above theory nine ridges with spacing of 2.6 mm and an included angle of 140° were machined across opposite faces of a work-hardened commercially pure copper bar, with an original cross-section 20 mm wide and 10 mm deep in the ridged section. Specimens were loaded in a biaxial testing rig [69], compressed on the ridged surfaces by two flat, smooth anvils 28 mm long and gripped at the ends of the bars away from the ridged section to allow compressive or tensile loads in the bulk strain direction. Growth of the asperity contact areas with bulk deformation of the copper block was measured using a tool-makers microscope. Bulk strain was measured from a grid pattern on the unloaded faces of the specimens. After each loading increment the specimens were unloaded, the contact area measured, and they were relubricated with molybdenum disulphide grease. The average pressure on the ridged faces was held constant while the end load was increased. In the case where the normal pressure $\bar{p}/2k$ equalled 1.0 the end load was initially compressive to prevent bulk yielding. In all cases the out-of-plane spread was small compared with the in-plane strain.

The stresses were measured using strain gauge load cells on the rig. Small differences (up to 10%) in the shear yield stress k for each specimen were estimated from differences in Vickers hardness measurements between each specimen and that of the specimen used in a cube compression test. The Vickers hardness is expected to be approximately proportional to the flow stress of the material after a further strain of about 8% [93].

Figure 3.8 shows the results of a compression test to measure the stress-strain curve of the copper using a cylinder of initial height and diameter 15 mm machined from the copper bar. The cylinder faces were relubricated after each loading step and the effect of friction has been corrected for using Seibel's approximate formula ([44] p.277) with a coefficient of friction of 0.15. The shear yield stress was assumed to be $1/\sqrt{3}$ times the compressive flow stress (from the Von Mises yield criterion).

3.2.3 Results

Figure 3.9 shows the measured growth of asperity contact area A with bulk strain ϵ_x for five tests specimens loaded with nominal normal pressures on the ridged faces $\bar{p}/2k$ of 0.2, 0.4, 0.66, 0.8 and 1.0 and corresponding theoretical curves for $\bar{p}/2k = 0.4, 0.66$ and 1.0. Blue dye painted on the unloaded faces of the specimens was disrupted where shearing took place. The resulting pattern as bulk yielding took place is remarkably similar to the theoretical pattern of slip-lines. Figure 3.10 shows a photograph of a specimen loaded with a normal pressure $\bar{p}/2k$ of 0.66 just after the bulk material yielded. Undeformed areas at the unloaded parts of the surface can be clearly seen, as can the tendency of the bulk deformation to take the form of rigid blocks separated by bands of intense shear at 45° . The theoretical discontinuities become thin bands of intense shear due to the strain-hardening of the copper.

The measured sum of applied stresses on the specimen $\bar{p}/2k + \bar{\sigma}/2k$ is shown in figure 3.7 as a function of contact area A , for a normal pressure $p/2k$ of 0.66, with the corresponding theoretical line.

As deformation proceeds the actual shear yield stress of the material will increase due to strain hardening in the deforming regions. The effect on the sum of the applied stresses needed for deformation has been estimated by assuming that the strain in the regions of deformation (for example under the indenters and around the velocity 'discontinuities') is three times the nominal bulk strain of the specimen (c.f. the pattern of deformation seen in figure 3.10). The effective increase in shear yield stress can then be estimated from the stress-strain curve of figure 3.8. and the resulting correction to the sum of applied stresses is shown in figure 3.7.

An independent indication of the inhomogeneous deformation and hardening was provided by taking a specimen strained to a nominal bulk strain of 10% with a mean

normal pressure $\bar{p}/2k$ of 0.66. The area of contact ratio was then 0.7. The specimen was sectioned longitudinally and hardness measurements were made on the plane originally 5 mm below the unloaded surface of the specimen (i.e. exposing the material 5 mm below the surface seen in figure 3.10). The average Vickers hardness for undeformed regions outside the ridged section was 107 kg/mm^2 . The hardness directly under the unloaded sections of the ridged area was about 110 kg/mm^2 while under the indenters it was 123 kg/mm^2 . In the central bulk deforming region the average hardness was 114 kg/mm^2 . It was not possible to distinguish between areas of high and low shear in this region from the hardness measurements.

These percentage increases in hardness in the bulk deforming region of 7% and under the indenters of 15% agree reasonably with the observed deviation of the sum of applied loads from that for the theoretical rigid-plastic model (figure 3.7). The comparatively low hardness for the regions under the unloaded sections confirm that, even after quite high strains, these regions were deformed significantly less than the bulk material.

For the model asperities tested, the growth in contact area and corresponding forces required are in good agreement with theory, particularly at the higher normal pressures. At the lower normal pressures $p/2k$ of 0.2 and 0.4 after a small strain and for the higher normal pressures after considerable straining, asperities were flattened more slowly than predicted by the theory. While profilometer traces showed that the unloaded regions retained their original profile after small strains, indicating that they were rigid, at the largest strains the unloaded regions were clearly deforming. For a normal pressure $\bar{p}/2k$ of 1.0, this resulted in a slight decrease in area of contact ratio with bulk strain beyond a 12% strain. This effect is probably due to strain-hardening, which under these conditions means that the theoretical mode of deformation involving lines of intense shear through already strained material is less favourable than a more homogeneous pattern of strain. Because of the relatively large slopes of the model asperities, the strain needed to crush the asperities will be rather greater in these experiments than in normal engineering surfaces, where asperity slopes will typically be below 5°

3.2.4 Transverse random rough surfaces

The application of the theory to random rough surfaces is not simple. Any accurate model of the surface deformation process should take into account the statistical nature of the surface. Von Stebut [102] for example uses some statistical analysis with success to investigate the growth of contact of asperities where the substrate is elastic.

Figure 3.11a shows a rough surface created by unidirectionally roughening a copper specimen with 100 grit emery paper. After loading to just below bulk yielding, the asperities were only slightly flattened (figure 3.11b). while after a 12% bulk strain the surface has been considerably flattened (figure 3.11c). An estimate of the rate of flattening of asperities can be made by assuming that the rough surface behaves as a surface with regular ridges of constant slope, here taken as the mean slope of the surface measured by profilometer with a sampling interval of $4\ \mu\text{m}$. With the resulting slope of 19° , at a strain of 12%, the theoretical area of contact ratio would be 0.89. This is somewhat above the estimated experimental value of 0.71, but, given the approximate nature of the calculation, the difference is not too great.

It would be interesting to combine Von Stebut's statistical techniques to predicting surface deformation with the present analysis for asperity deformation with bulk plastic flow. Indeed, the effect of bulk plastic deformation on surface contact is likely to be marked in the case that Von Stebut is interested in, that of deep-drawing.

3.3 Longitudinal roughness

3.3.1 Theory

When the lay of the surface is in the same direction as the bulk plastic strain, crushing of the asperities involves deformation perpendicular to the bulk strain direction. The deformation field is then three-dimensional rather than one of plane strain, so that it cannot be analysed by the slip-line field technique. Wilson and Sheu [105] have analysed this problem using the kinematical bound theorem, in which an upper bound to the force to produce plastic flow is found from a calculation of the plastic work in an assumed mode of deformation. In this section Wilson and Sheu's results will be extended and an alternative deformation mode investigated.

The situation is idealised as shown in figure 3.12a. Periodic dies, of width $2a$ and spacing $2c$, indent the surface with a velocity v_a which exceeds the velocity v_v of the unloaded spaces between the dies. The indenter spacing does not change, that is the centrelines OP and SR remain straight and a fixed distance apart, while the half-space undergoes a uniform strain rate $\dot{\epsilon}_z$ in the longitudinal direction (i.e. perpendicular to the plane of the figure). Transverse plastic flow in the plane of the figure, due to the periodic loading, is confined to a surface layer of depth d . The ratio of the transverse flow to the bulk longitudinal flow is given by the parameter $W = v_f/c\dot{\epsilon}_z$, where $v_f = v_a - v_v$. This parameter governs the rate at which asperities crush with bulk longitudinal strain. It is the purpose of this calculation to obtain a best estimate of its value for any given mean load \bar{p} and contact ratio $A = a/c$.

In the case of homogeneous longitudinal deformation ($W = 0$) the uniform longitudinal tensile stress σ_b on the end faces is related to the mean pressure by

$$\sigma_b/2k + \bar{p}/2k = 1 \quad \{3.18\}$$

When indentation accompanies bulk plastic flow the force on the end face $OPRS$ changes by an amount F so that the net force is $\sigma_b cd + F$. Using the kinematical theorem, it is shown in appendix A that

$$\frac{F}{2kc^2} \leq \frac{\bar{p}}{2k} W(1 - A) + d/c - \frac{P_d}{2kc^2\dot{\epsilon}_z} \quad \{3.19\}$$

where P_d is the plastic deformation in the volume comprising the area $OPRS$ and of unit length. For any assumed mode of deformation the plastic deformation P_d is a

function of the assumed values of W and d . Thus, for any given value of $\bar{p}/2k$, the right-hand side of equation 3.19 should be minimised with respect to both W and d to obtain an optimum relationship between W and $\bar{p}/2k$. If different modes are compared, the one that minimises the right hand side of 3.19 is to be preferred. Although there is no guarantee that the velocity field with the best bound on the deformation load will produce the best approximation to the actual crushing rate, it is hoped that, where the assumed velocity fields include ones reasonably close to the actual field, this assumption will provide a good estimate of the crushing rate.

Sheu and Wilson [86] first explored a simple mode of deformation comprising two rectangular blocks of uniform strain with a velocity discontinuity along QT (shown dotted in figure 3.12a). They later [105] suggested an improved mode in which the deformation was diffuse without any velocity discontinuities. This mode implied that the velocity of the free surface was not uniform, varying from a maximum value of v_a at Q to a minimum value at R . v_f was then defined as $(v_a - \bar{v}_v)$ where \bar{v}_v is the mean velocity along QR .

A new mode of deformation is proposed in this chapter (see figure 3.12 and appendix A) comprising three regions A , B and C with velocity discontinuities along OQ and QS . The velocities in the transverse plane are shown in the hodograph of figure 3.12b, which scales linearly with depth from $y = 0$ to the surface. Expressions for the plastic dissipations associated with this field are derived in appendix A. The right hand side of 3.19 has been minimised with respect to depth d for various values of W for $A = 0.5$. The relationship between $F/2kc^2$ and W is then plotted in figure 3.13 for $\bar{p}/2k = 0.6$ and 1.0 and $A = 0.5$. The data of Wilson and Sheu have been used (see appendix B) to calculate corresponding curves for their mechanism with no velocity discontinuities for values of A between 0.1 and 0.9 , for mean normal pressures of between 0.2 and 1.0 . The results for $\bar{p}/2k = 0.6$ and 1.0 with $A = 0.5$ are included in figure 3.13. For each value of $\bar{p}/2k$ the 'best estimate' of W corresponds to the value for which $F/2kc^2$ is a minimum. In some of the cases using Wilson and Sheu's data, their results did not extend to sufficiently high or low values of W to be able to determine a minimum for $F/2kc^2$.

In their paper Wilson and Sheu obtained their estimate of the velocity ratio parameter W in a different way. Having minimised their dissipation with respect to depth,

they took the value of W to be that at which $F = 0$. It is clear from figure 3.13 that these values are appreciably different from those which minimise F .

For $\bar{p}/2k = 1$, the new mechanism gives a slightly lower upper bound to F at $W = 1.47$ compared with the value for Wilson and Sheu's field of 0.67. On the other hand, for $\bar{p}/2k = 0.6$, Wilson and Sheu's field gives the lowest bound at $W = 0.32$ compared with $W = 0.16$ for the new field.

We are now in a position to find the velocity ratio parameter W , as a function of \bar{p} and A , in a similar way to that found for transverse roughness in figure 3.3. This relationship is plotted in fig 3.14. Results for both the new field and for Wilson and Sheu's field are included for $A = 0.5$. Which of these values of W is better will depend on the value of $F/2kc^2$ for each mechanism.

With a given combination of load and area of contact ratio, the deformation may proceed either with only local deformation and crushing of the asperity tops, or with deformation throughout the bulk material. Equation 3.10 gives the condition for the deformation only to be local and this limit is indicated in figure 3.14 by arrows.

Strain hardening will not affect the upper bounds on F for first yield but, after some straining fields with velocity discontinuities will become less favourable with an increased value of the upper bound on F . Referring to figure 3.14, we can expect the velocity ratio parameter W , for a normal pressure of $\bar{p}/2k$ of 1, to tend to the minimum of the curve for Wilson and Sheu's field in these circumstances, since this field has a more homogeneous velocity distribution than the new mechanism with velocity discontinuities.

3.3.2 Experiments – longitudinal roughness

Specimens similar to those used to investigate transverse roughness were used to study the growth of contact areas for longitudinal roughness. Experiments were performed in two ways. For an average normal pressure $\bar{p}/2k$ of 0.6, ridges were machined along the specimen and the experiment performed in a similar way to those with transverse roughness. The normal load was kept constant and the end load increased until bulk yielding occurred. For higher normal loads ($\bar{p}/2k \approx 1.0$), in order to prevent out-of-plane spread dominating, the ridges were machined across the bar, and the end loads on the bar adjusted to prevent straining in that direction. The normal load was

then increased until bulk yielding occurred. In this case $\bar{\sigma} = 0$. The ridges had a slope θ of 20° . Bulk strain was measured using marks on the unloaded parts of the ridged surfaces. Over the measured central area the ridges remained parallel and there was little barrelling of the specimen, indicating that the test approximated adequately to conditions of plane strain with infinitely long ridges.

3.3.3 Results

Figure 3.16 shows the growth of contact area A with bulk strain for two specimens with average dimensionless normal pressures of 0.6 and 1.0. Wilson and Sheu's experimental results are also plotted. Figures 3.17a and b show a profile trace of the unloaded surface between two indenters initially and after a bulk strain of 19% ($\epsilon_z/\theta = 0.54$) for the experiment with $\bar{p}/2k \approx 1.0$. The tangents to the ridge flanks at the top and bottom of the groove have been drawn in for comparison. The included angle at the bottom of the groove is somewhat reduced while, near the contact areas, the ridge flanks have become less steep.

The results show that the true area of contact ratio increases with bulk strain at a constant load in a similar manner to transverse roughness (c.f. figure 3.9). By taking the tangents to the best fit curves in figure 3.16, experimental values of W can be deduced from equation 3.15 (c is constant in this case) for the two mean pressures. For the experiment with a nominal mean pressure $\bar{p}/2k$ of 1.0, the actual value of mean pressure will be somewhat lower than this value because of the inhomogeneous loading. The reduction in normal load has been estimated using the calculated value of $F/2kc^2$ from Wilson and Sheu's field for each area of contact ratio. These calculations are upper bounds, so the actual value of the mean normal pressure will be rather lower than these estimates, particularly at the lower area of contact ratios.

At the higher value of pressure of $\bar{p}/2k \approx 1.0$ with $A = 0.5$ the experimental crushing rate has an intermediate value between the estimates from the new velocity field and that of Wilson and Sheu. For $\bar{p}/2k = 0.6$, Wilson and Sheu's field gives a good estimate of the crushing rate while the new field gives a poor estimate. These results match the the 'goodness' of the bounds found theoretically. In fact, the closeness of the minimum values of $F/2kc^2$ found from the new field and Wilson and Sheu's field for $\bar{p}/2k \approx 1$ gives an indication that the true value of W is likely to lie between these

two extremes. The agreement between the theoretical estimate from Wilson and Sheu's field and the measurements is better at the higher values of A . Where A is small it is expected, by analogy with the transverse theory, that the field will have larger velocity discontinuities so that their field with no velocity discontinuities will not be as close to the actual velocity pattern.

These results confirm that estimated crushing rates from upper bound analyses of the load do, in this case, give reasonable approximations to the crushing rates where the class of velocity fields considered includes ones reasonably close to the actual velocity field.

To be able to use these results, it is helpful to have an empirical formula for the relationship between W , A and $\bar{p}/2k$. An approximation given by Wilson and Sheu [86] is plotted in figure 3.15 along with the simple formula

$$W = 3.81 \left(\frac{\bar{p}}{2k} \right)^2 - 4.38A \quad \{3.20\}$$

with the condition that $0.05 \leq W \leq 2.5$. This was chosen to be most appropriate around $A = 0.5$, with $\bar{p}/2k < 1.0$, since this was the requirement of the lubrication analysis of chapter 4.

The approximation used by Wilson and Sheu does not agree well with theory and experiment at small values of A . This is largely because they have tailored their approximation for W to tend to ∞ as the value of \bar{p} approaches the critical pressure at which only local deformation occurs. The deformation zone with local deformation is separated by velocity discontinuities from the rigid regions, while the deformation must extend throughout the workpiece with bulk deformation. As the pressure approaches the critical pressure in the bulk deformation regime, the velocity field does not tend to the velocity field for local deformation. Because of this the value of W will not approach the local deformation limit of ∞ at the boundary between local and bulk deformation as assumed by Wilson and Sheu. Similarly, with transverse roughness the crushing parameter does not tend to ∞ as the critical pressure is reached (figure 3.3).

Figure 3.17 shows that the unloaded portions of the surface do not remain with their initial profile but, while there is a velocity discontinuity at the edge of the indenter producing an increase in contact area, there is also a non-uniform distribution of normal velocity on the unloaded part of the surface. This may be expected, since the upper

bound analyses showed that a solution with a velocity discontinuity at the edge of the indenter gave a better bound for the initial stages of this experiment, while at smaller flattening velocities, Wilson and Sheu's solution with no velocity discontinuity would give a better bound. The experiments have an intermediate type of velocity distribution between these two extremes. This intermediate velocity field changes the shape of the unloaded part. Hence, after the asperities have been flattened somewhat, the velocity discontinuity travels out through a region with a smaller asperity slope θ than the initial one. The contact area then grows faster than would be predicted by a theory that did not take this into account.

3.3.4 Longitudinal random rough surfaces

A rough surface was prepared as for the transverse roughness experiments, but with the roughness lay parallel to the bulk straining direction. The average slope, with $4\ \mu\text{m}$ sampling, was 17° . The specimen was then strained with a normal pressure $\bar{p}/2k$ of 1.0. The surface initially and just before bulk yielding was similar to figures 3.11a and b. After a bulk strain of 12% the surface was considerably flattened (figure 3.11d). The area of contact ratio was estimated to be about 0.65. This compares with the experiments with regular triangular ridges of slope 20° where, with the same strain/slope ratio ϵ_z/θ of 0.40, the area of contact ratio was found to be 0.70 (from figure 3.16).

3.4 Conclusions

Two models of the process have been considered. These are idealised roughness which comprises uniform ridges either transverse to the direction of bulk strain or in the direction of bulk strain (longitudinal roughness). It has been shown by both theory and experiment that the ratio of real to apparent area of contact increases towards unity with constant nominal contact pressure, as a consequence of the bulk plastic strain of the material in both cases.

For transverse roughness a solution using slip-line fields has been found. The principal features of the solution are velocity discontinuities at the edges of the loaded regions, rigid regions under the unloaded surfaces and a pattern of velocity discontinu-

ities in the bulk of the material (see figure 3.2). These features have also been observed in a finite element solution recently published.

The theory has been applied to the crushing of asperities. The crushing rate is found to depend on the mean normal pressure on the rough surface and the real area of contact ratio. For high normal pressures good agreement between theory and experiments has been found although at the lower normal pressures, after some straining, strain hardening results in a somewhat lower crushing rate than predicted.

For longitudinal roughness, Wilson and Sheu's work has been extended and a new velocity solution considered. Theoretical results and further experiments give a clearer picture of the asperity crushing process. Inhomogeneous deformation fields allow more work to be done as the loaded surfaces move inwards more quickly than the average for the rough surface. The bulk can then yield at a lower average pressure than would be expected for homogeneous loading and the contact area can grow as a result of velocity discontinuities at the edge of the loaded regions. In addition the unloaded region of the surface will change in profile as the material closer to the contacting asperity tops is dragged down in relation to the material away from the contact areas.

A more accurate estimate of the initial crushing rate could be found by using a more complicated velocity field. To analyse the whole crushing process, it would be useful to estimate how the asperity profiles change during straining and to consider strain hardening. At present model experiments provide an indication of how these two factors affect the contact growth.

Experiments have been performed crushing asperities on random rough surfaces. The surfaces were found to crush roughly as expected, with a large increase in contact area with bulk strain, although the significant difference in flattening rate between transverse and longitudinal roughness predicted by theory was not found. A more sophisticated analysis, possibly using bearing area curves, should give more accuracy in applying the basic theories.

Equation 3.20 gives an empirical formula for the rate of crushing of longitudinal asperities when the substrate is deforming, which can be used in the lubrication analysis of chapter 4.

Table 3.1 Some dimensionless parameters associated with the slip-line field of figure 3.2 with fan angle ϕ .

ϕ ($^{\circ}$)	ϕ (rad)	h/a	$\sigma_e/2k$	$F/2ka$
0	0.0000	1.0000	0.5000	0.000
10	0.1745	1.3833	0.5499	-0.414
20	0.3491	1.8526	0.6715	-0.976
30	0.5236	2.4405	0.8420	-1.721
40	0.6981	3.1904	1.0505	-2.698
50	0.8727	4.1616	1.2904	-3.974
60	1.0472	5.4340	1.5568	-5.638
70	1.2217	7.1172	1.8454	-7.815

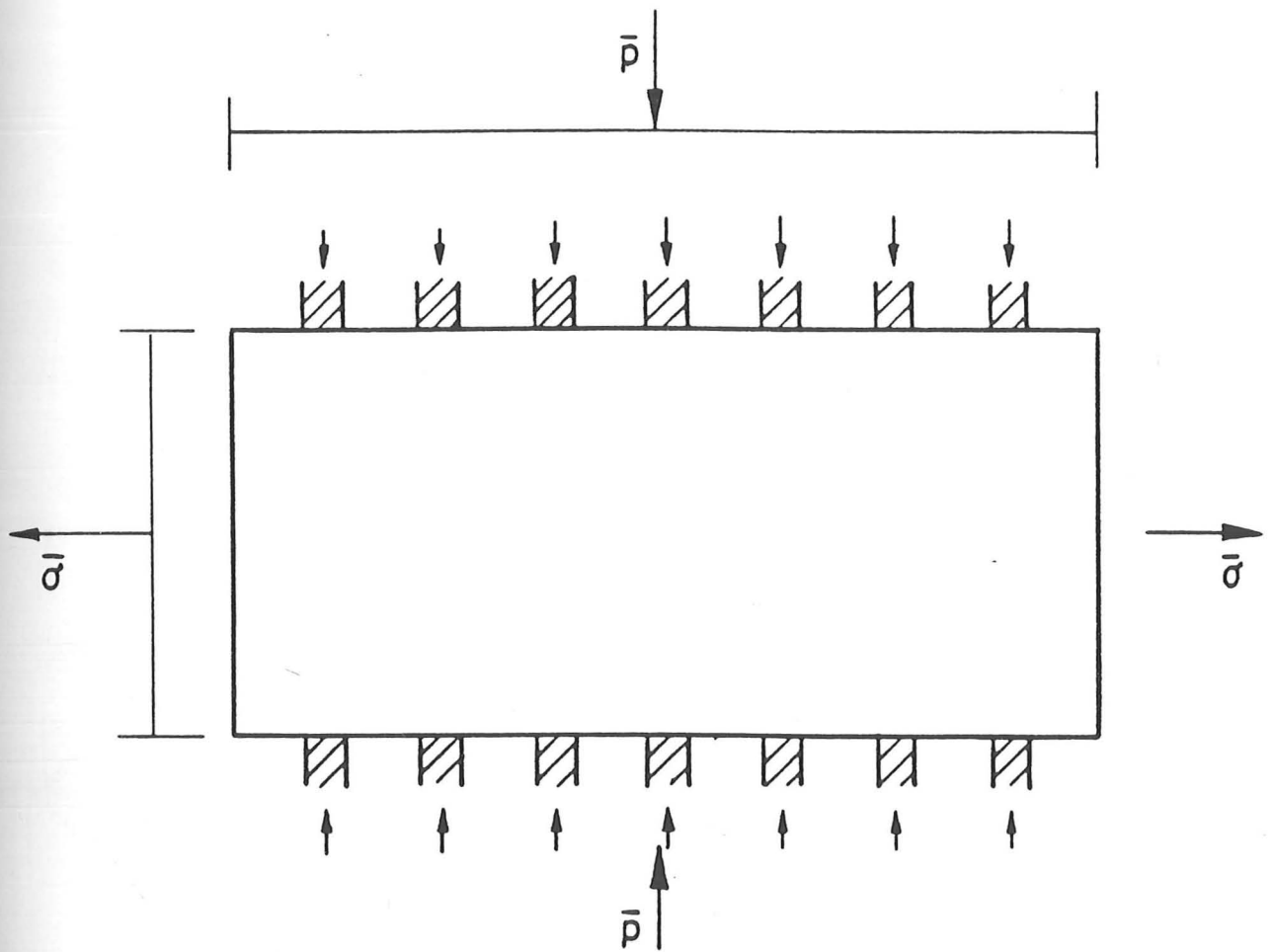


Figure 3.1 Idealisation of asperity and bulk plasticity interaction.

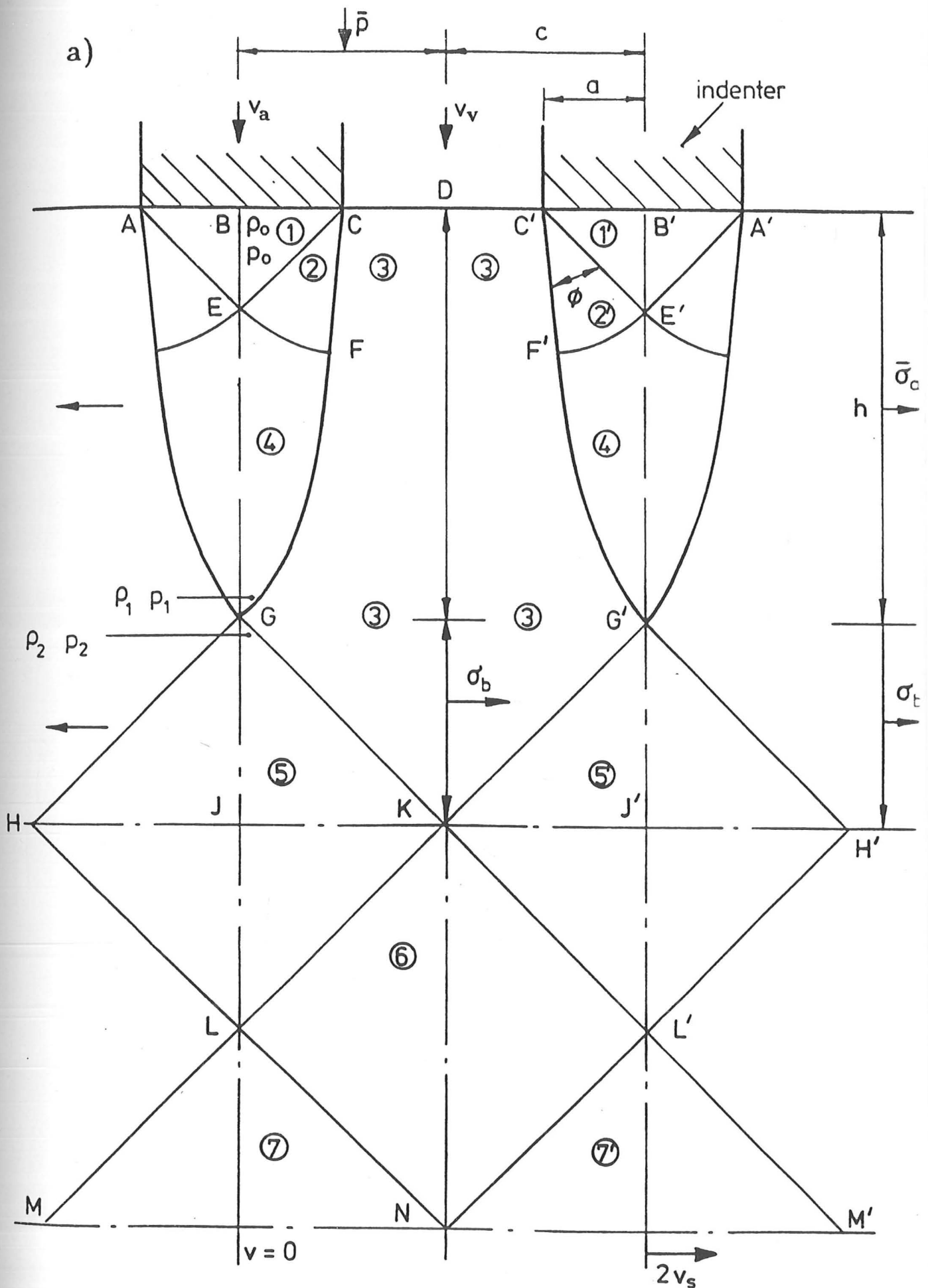


Figure 3.2 a) Section from indented block with the slip-line field

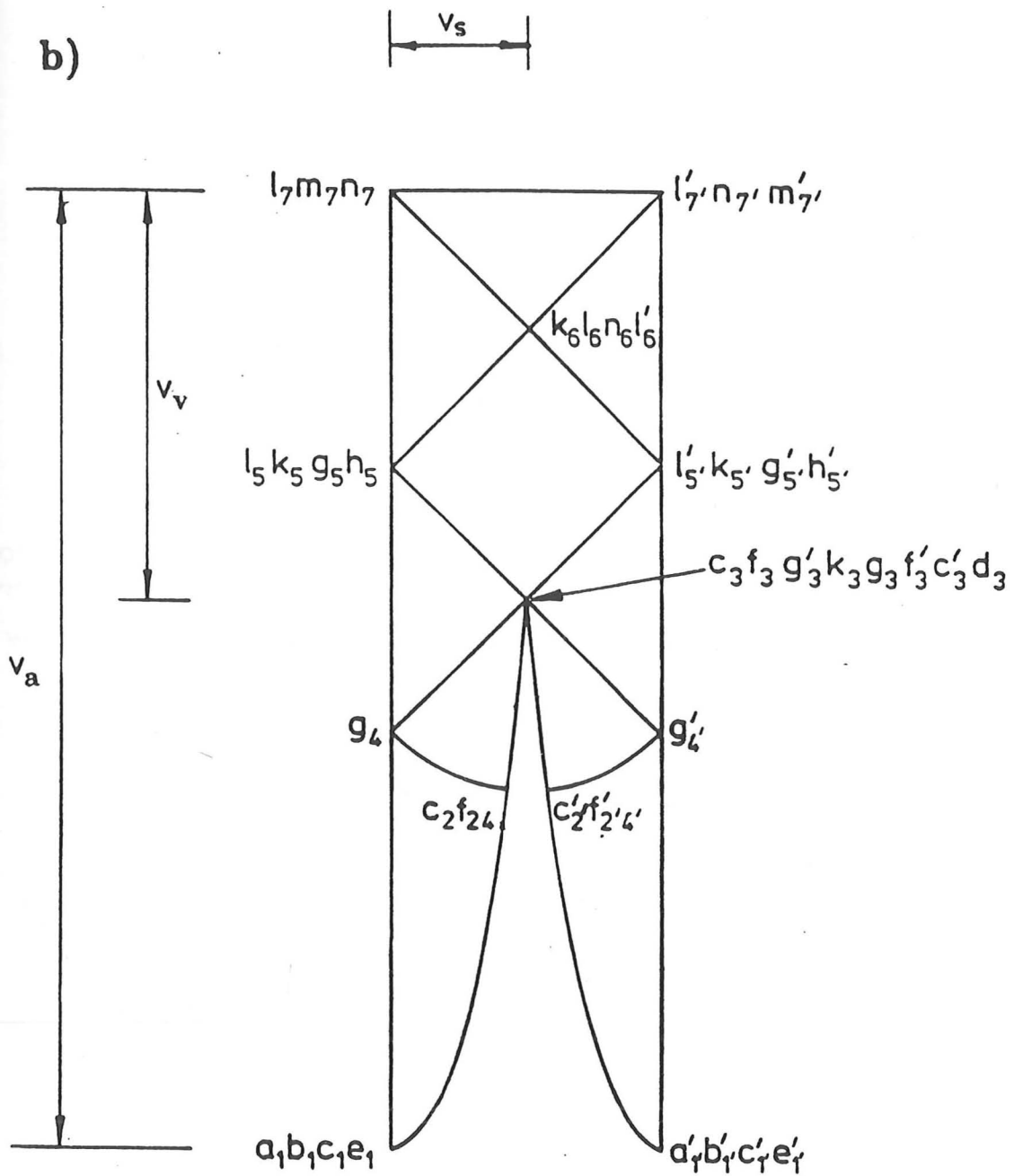


Figure 3.2 b) Hodograph for slip-line field.

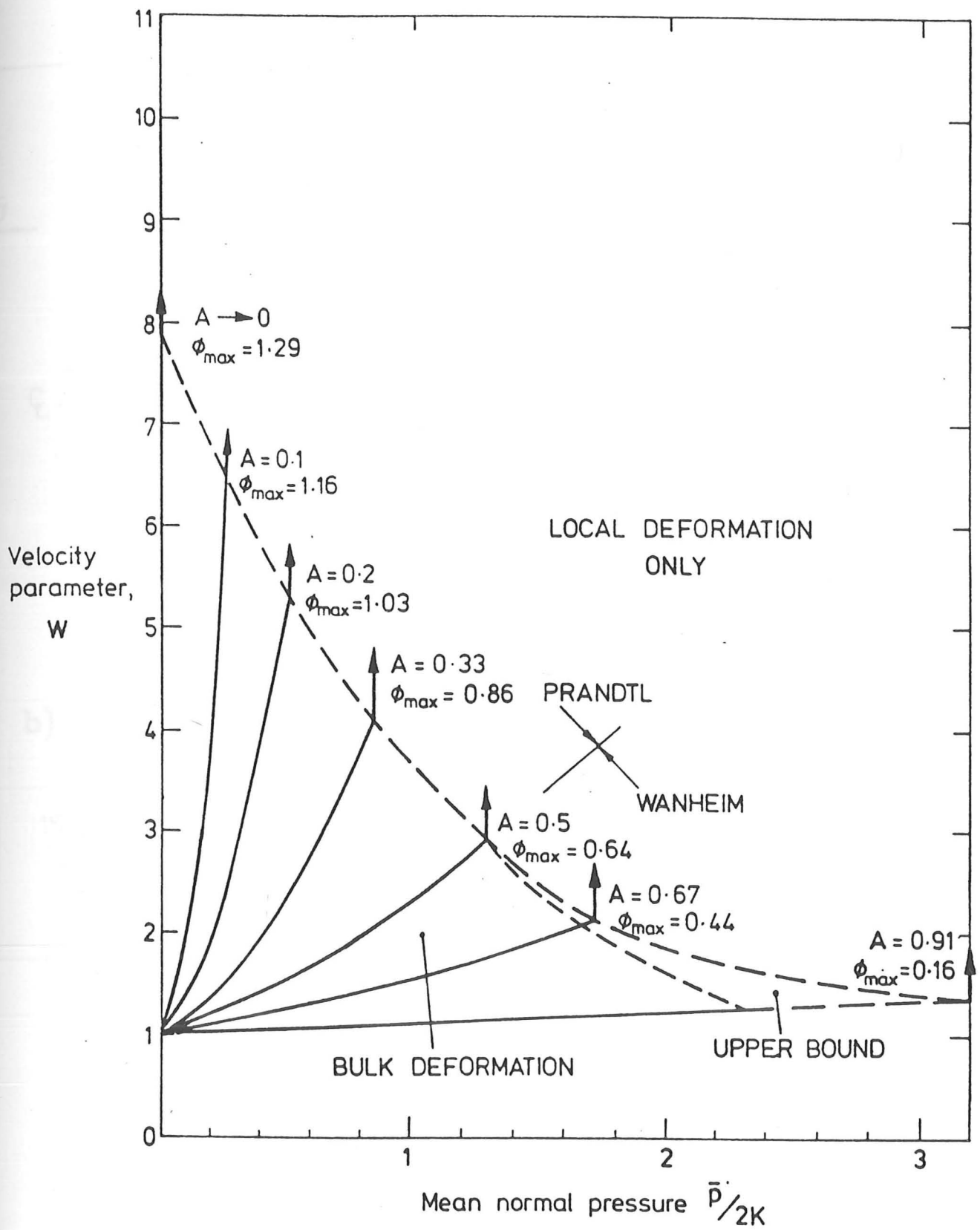


Figure 3.3 The effect of discrete loading on the surface velocity distribution — transverse roughness.

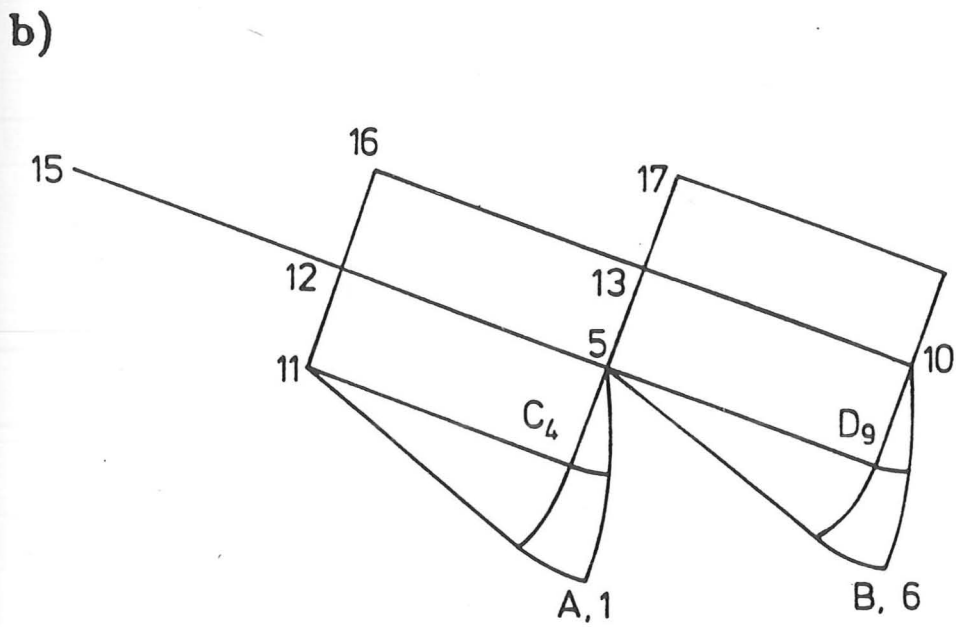
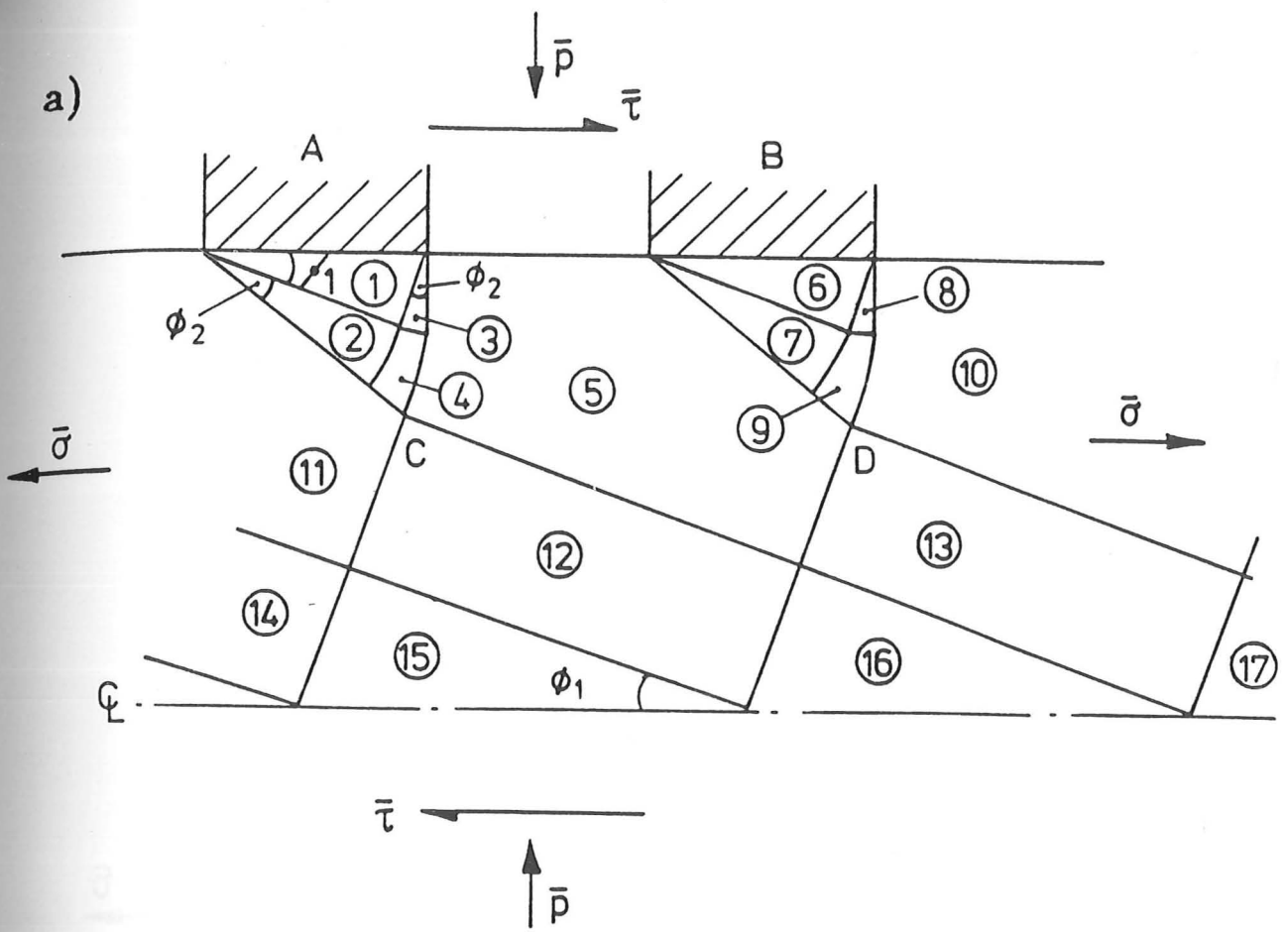


Figure 3.4 a) Slip-line field
b) Hodograph for applied shear and normal tractions.

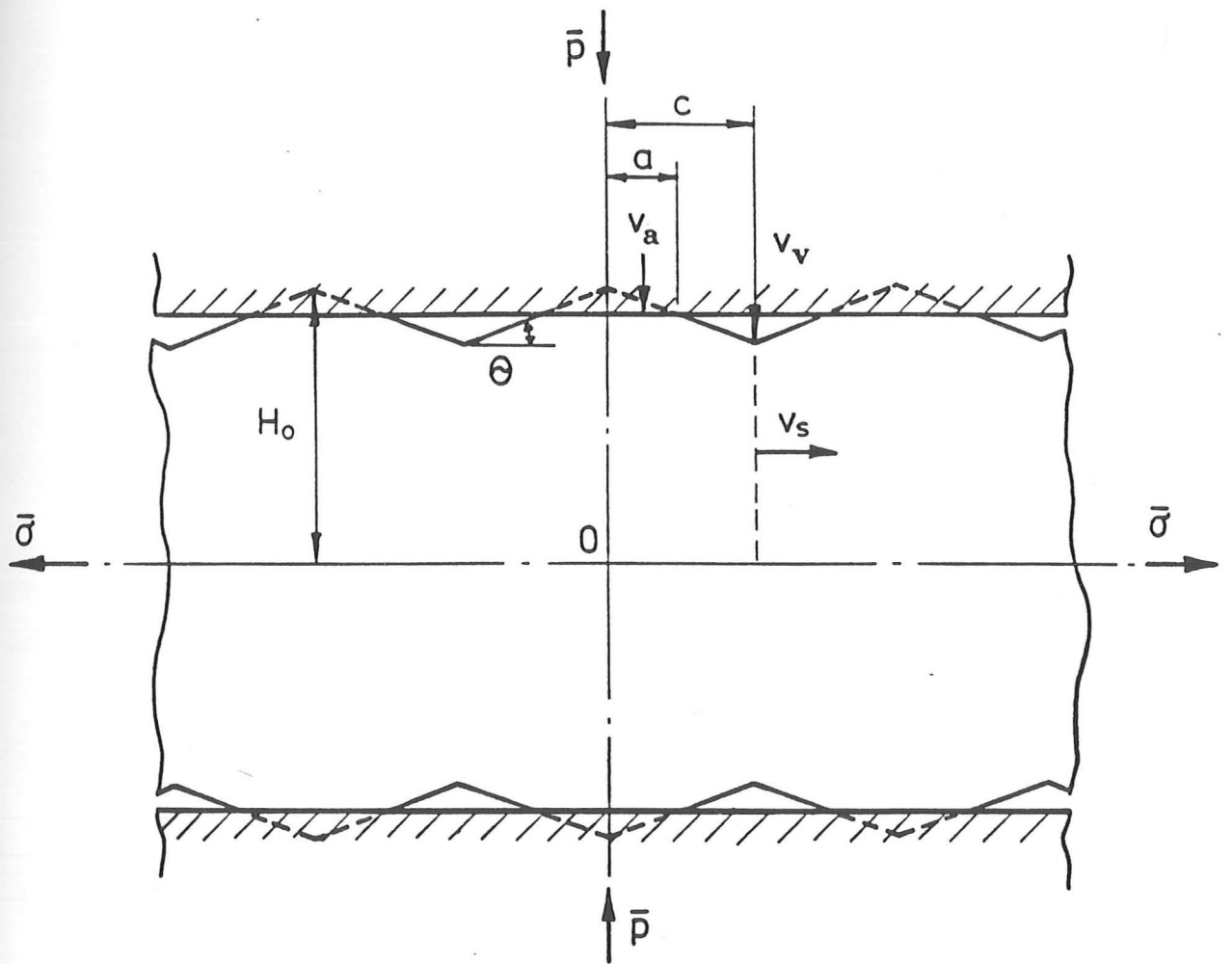


Figure 3.5 Crushing a serrated surface.

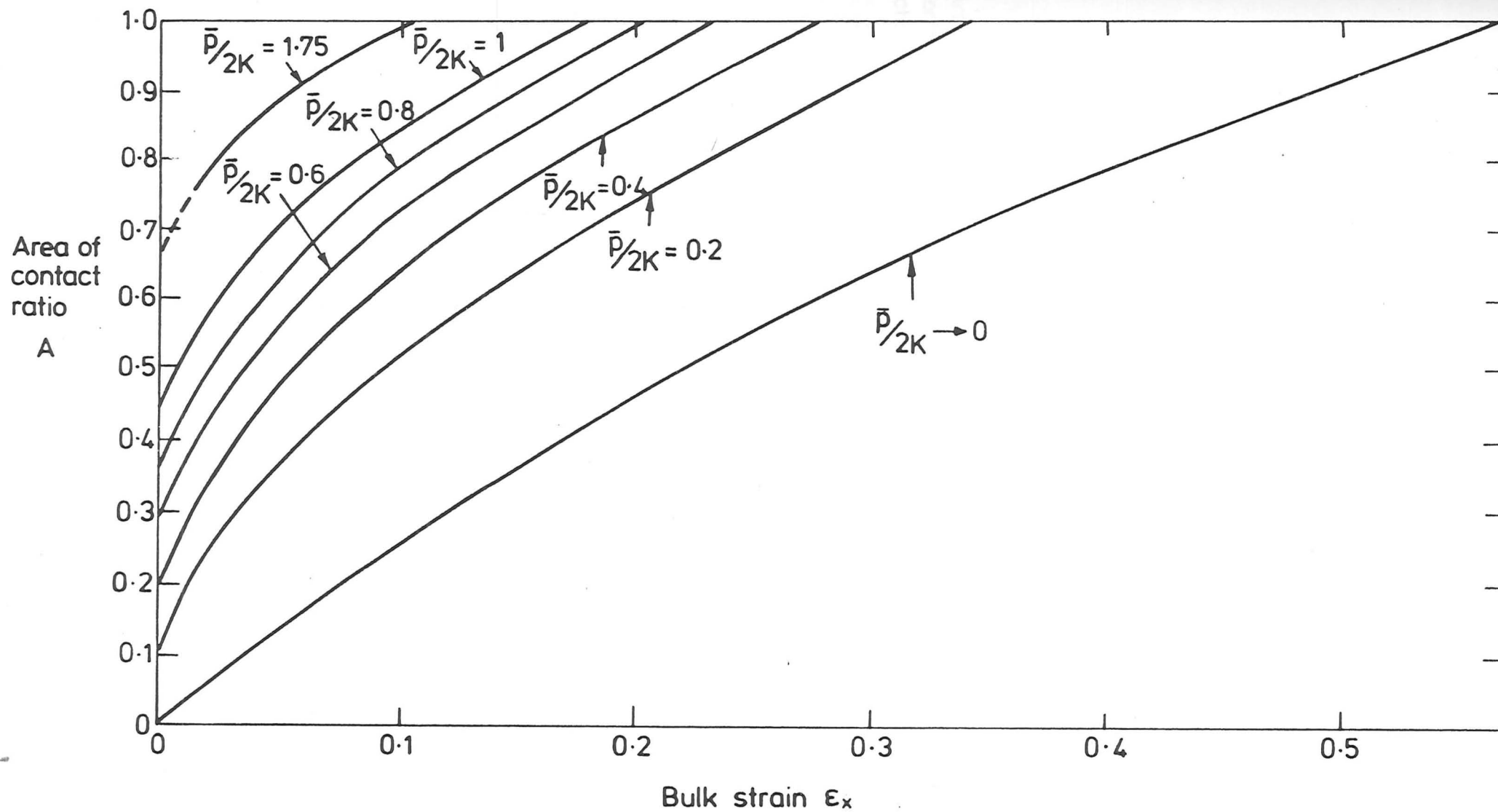


Figure 3.6 Theoretical growth of contact area with bulk strain — transverse roughness.

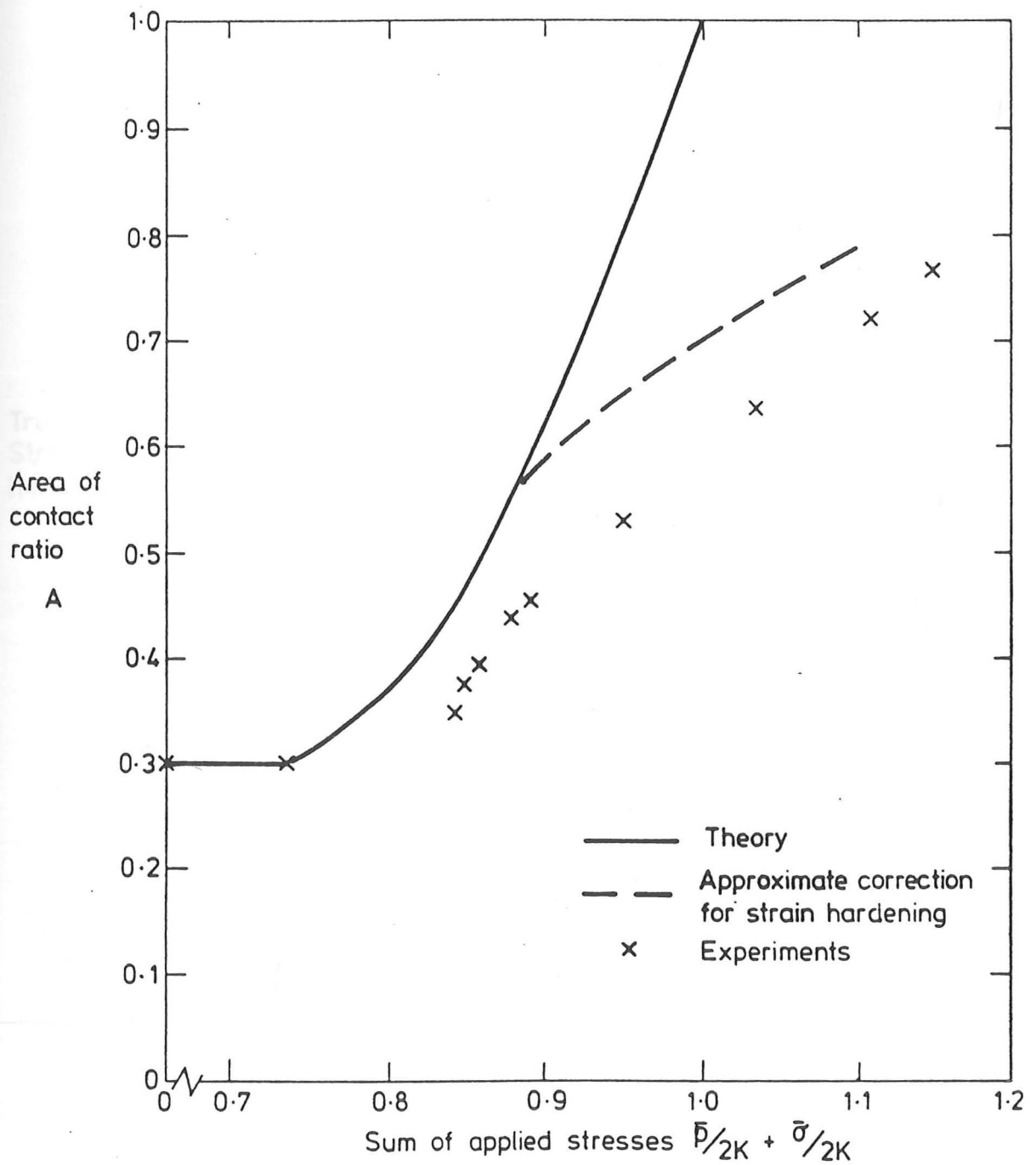


Figure 3.7 Stresses needed to crush transverse serrations on a bar. $H_0/c_0 = 3.9$, $\bar{p}/2k = 0.66$. Theory and experiment.

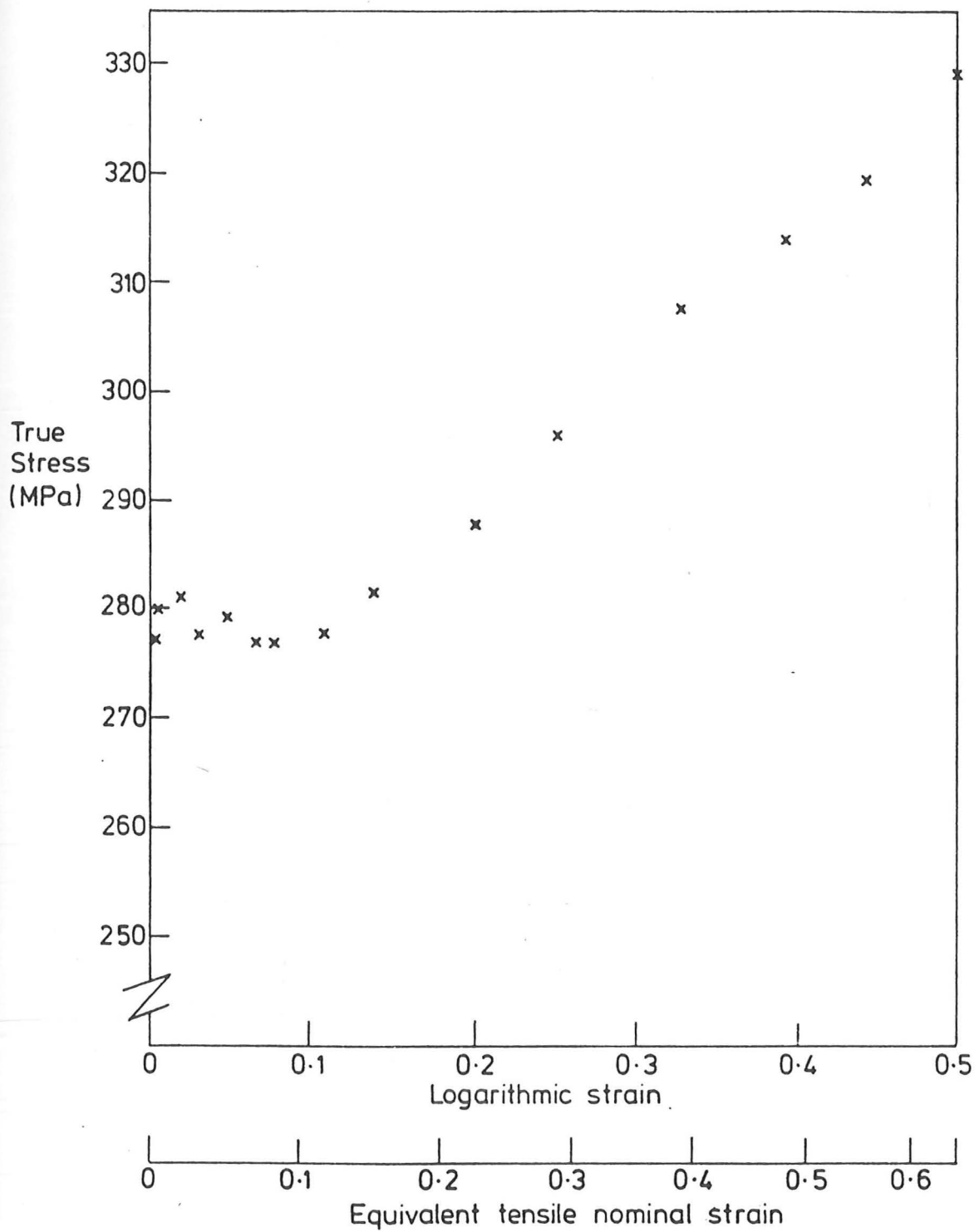
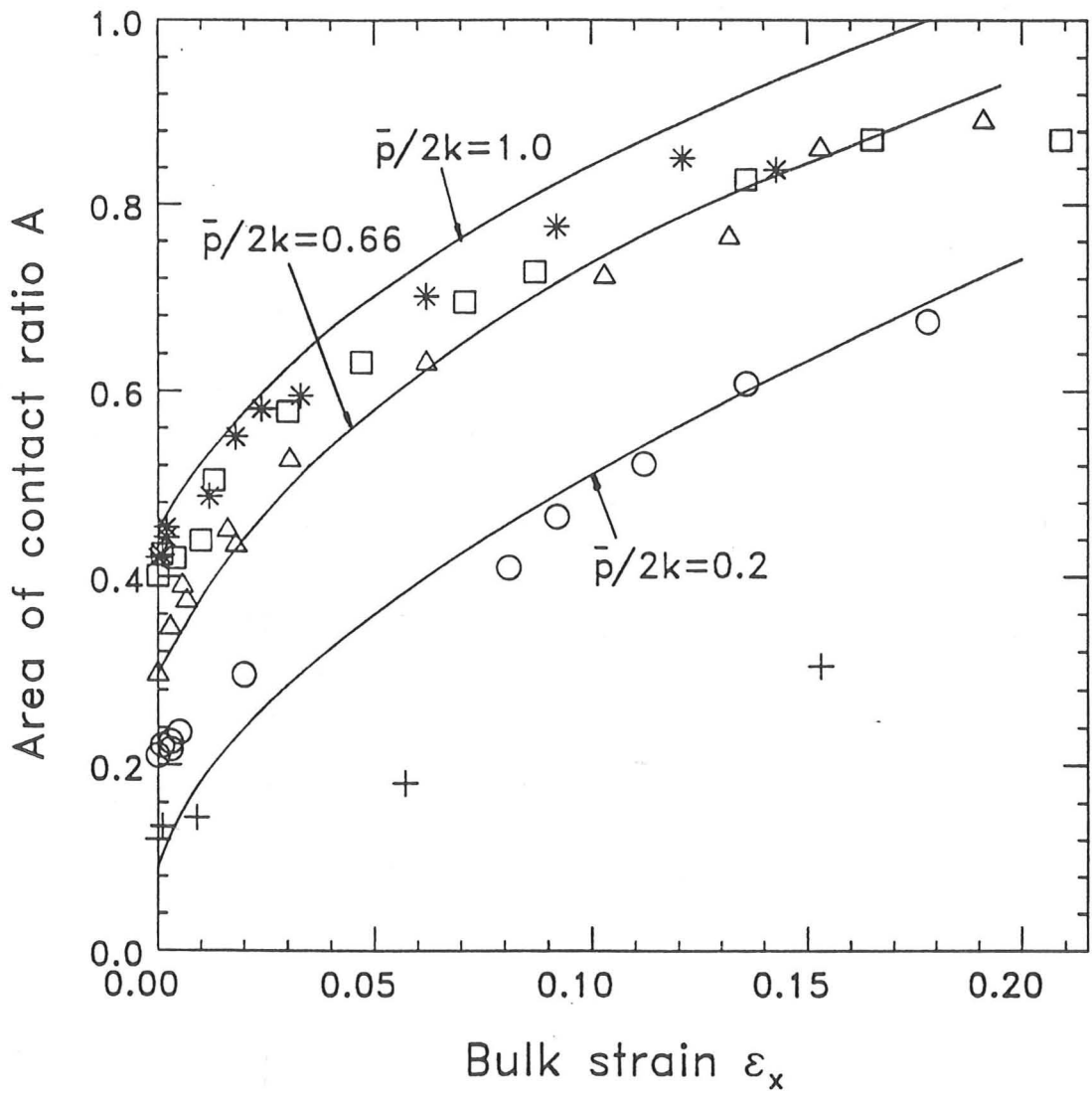


Figure 3.8 Stress-strain curve for the copper.



KEY

- Theory
- * Experiments $\bar{p}/2k=1.0$
- Experiments $\bar{p}/2k=0.8$
- △ Experiments $\bar{p}/2k=0.66$
- Experiments $\bar{p}/2k=0.4$
- + Experiments $\bar{p}/2k=0.2$

Figure 3.9 Measured growth of contact area with bulk strain for transverse ridges and comparison with theory.

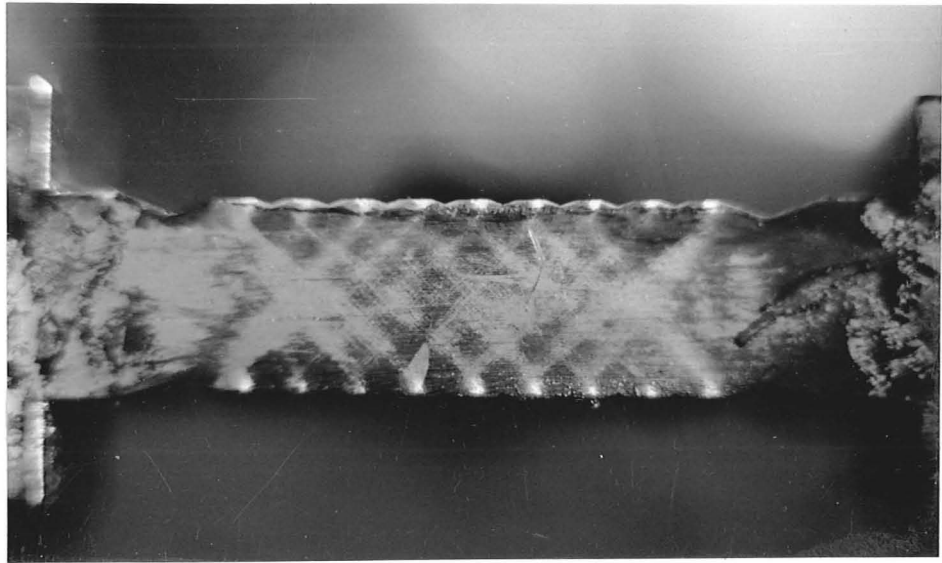


Figure 3.10 Experimental pattern of deformation for a specimen with transverse ridges ($\bar{p}/2k = 0.66$).

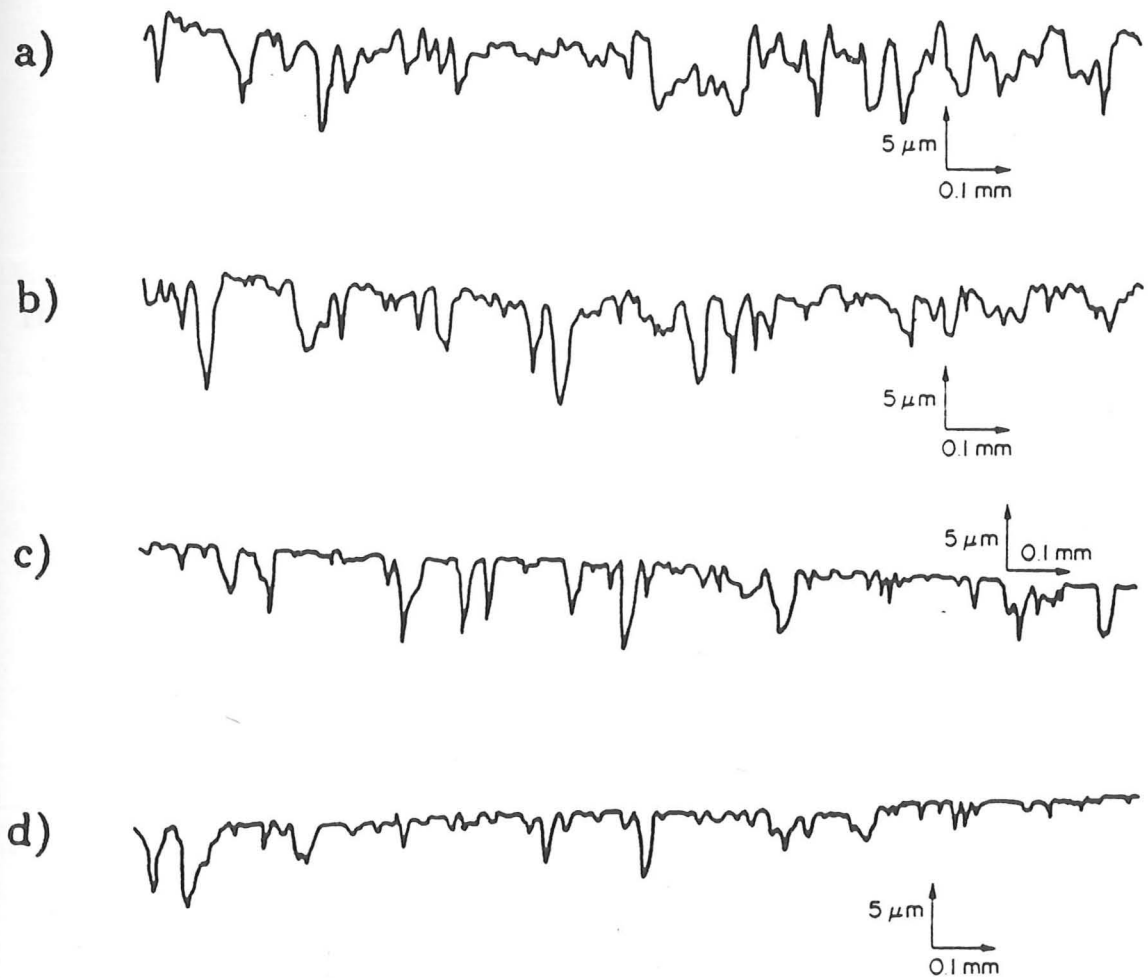


Figure 3.11 Crushing random rough surfaces

- a) Undeformed rough surface
- b) Surface just before bulk yielding
- c) Transverse roughness after a bulk strain of 12%
- d) Longitudinal roughness after a bulk strain of 12%.

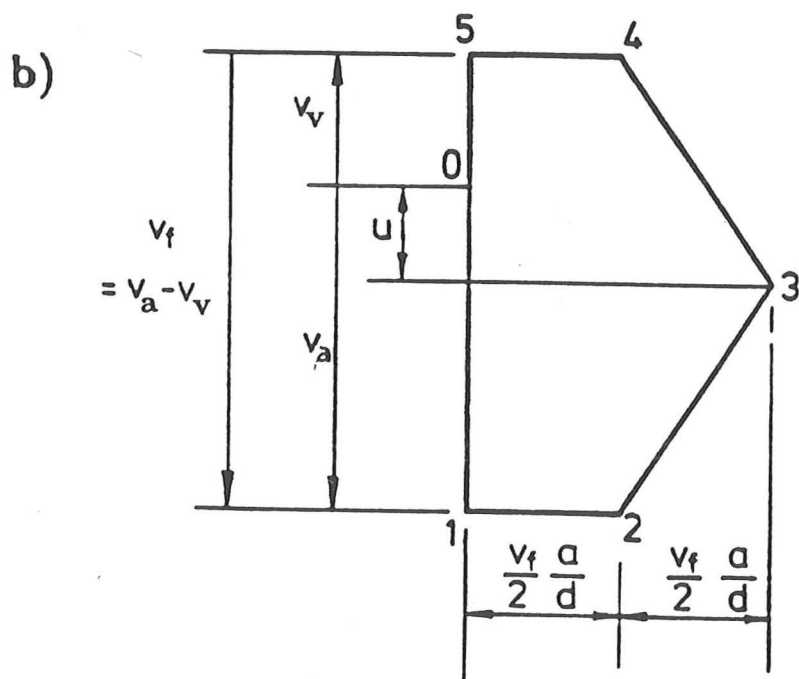
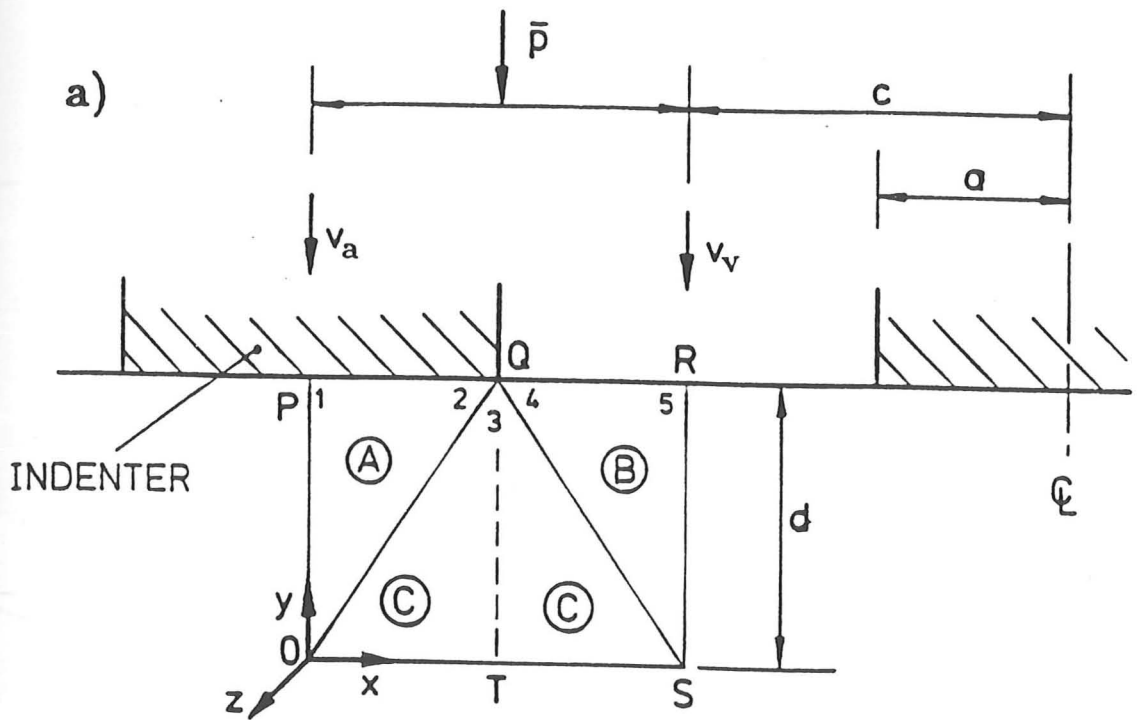


Figure 3.12 Idealisation of longitudinal roughness a) Velocity field b) Hodograph.

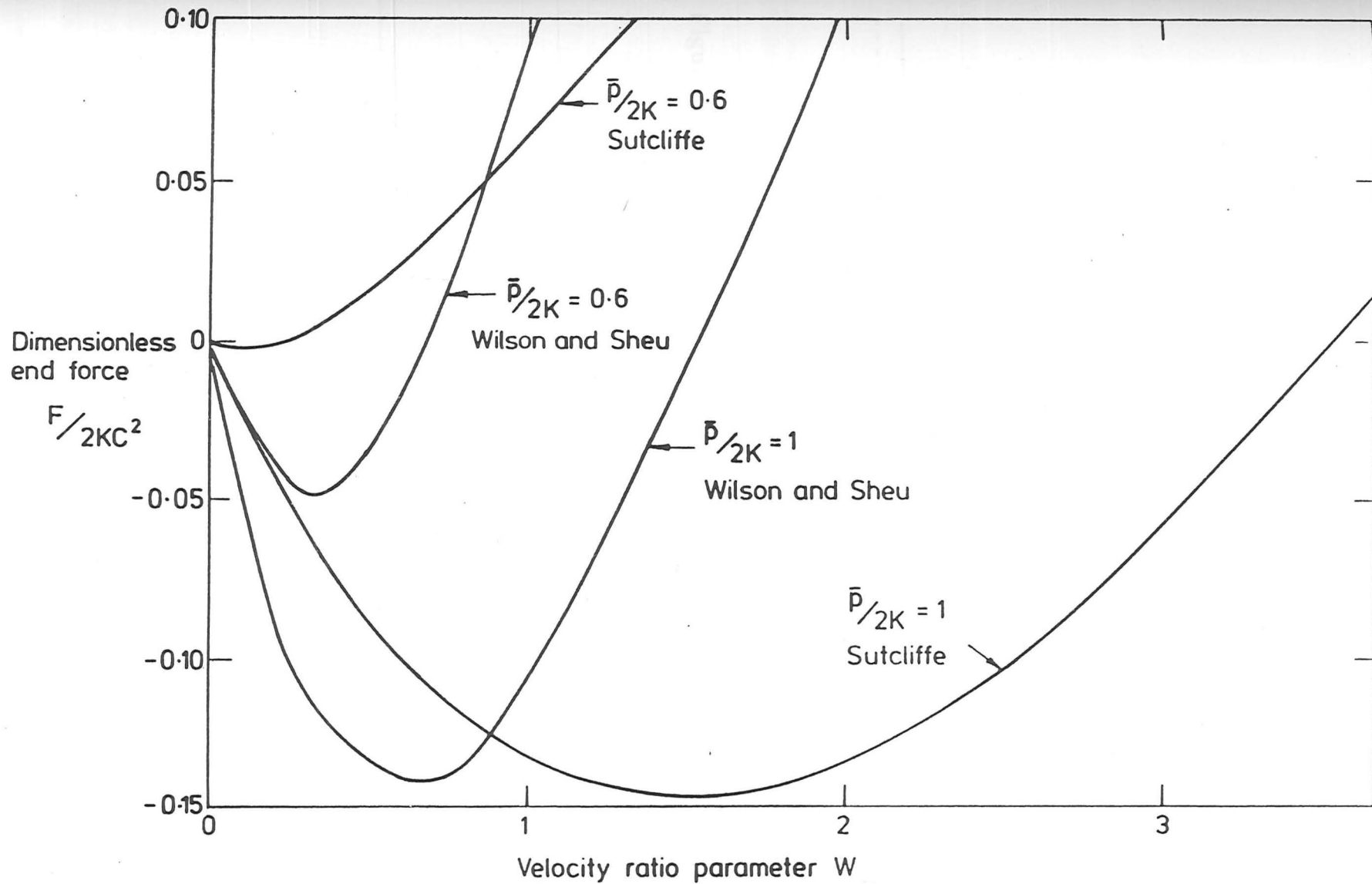
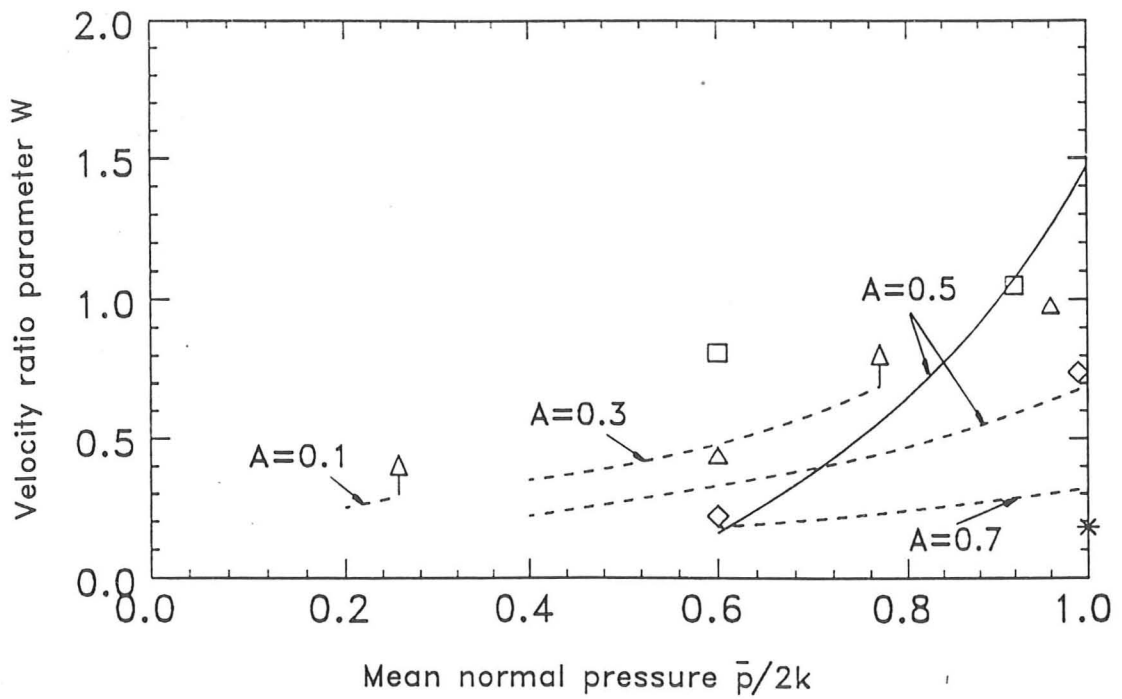


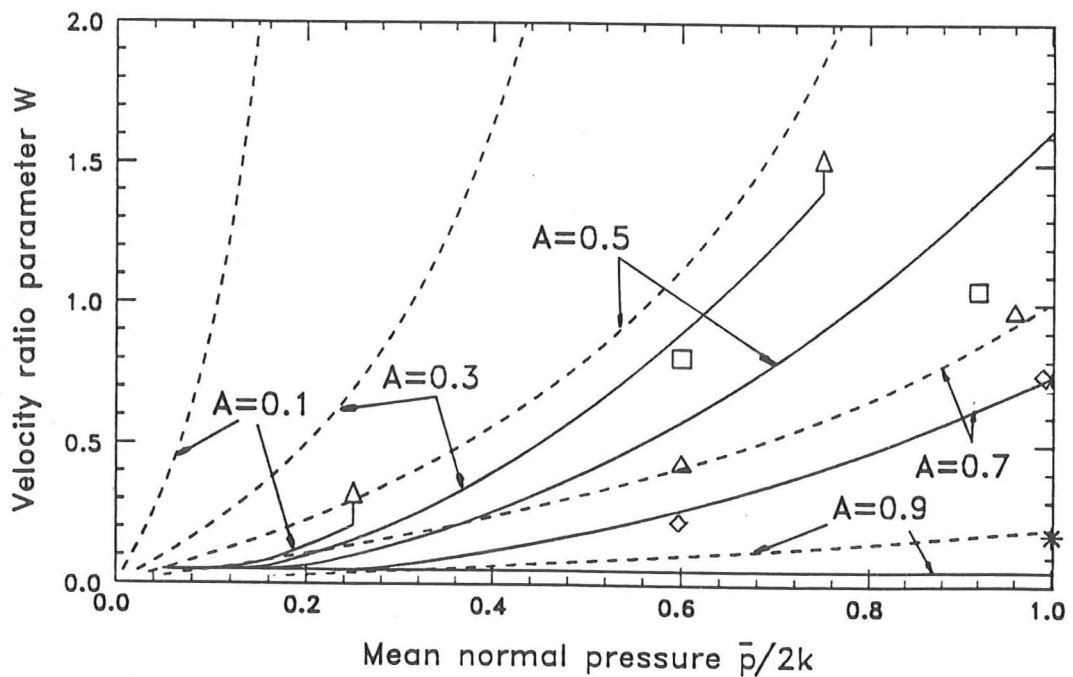
Figure 3.13 Upper-bounds on the change in end force for bulk yielding — longitudinal roughness, $A=0.5$.



KEY

- Theory - new velocity field
- - - Theory - Sheu's field
- Experiments A=0.35
- △ Experiments A=0.5
- ◇ Experiments A=0.7
- * Experiments A=0.9

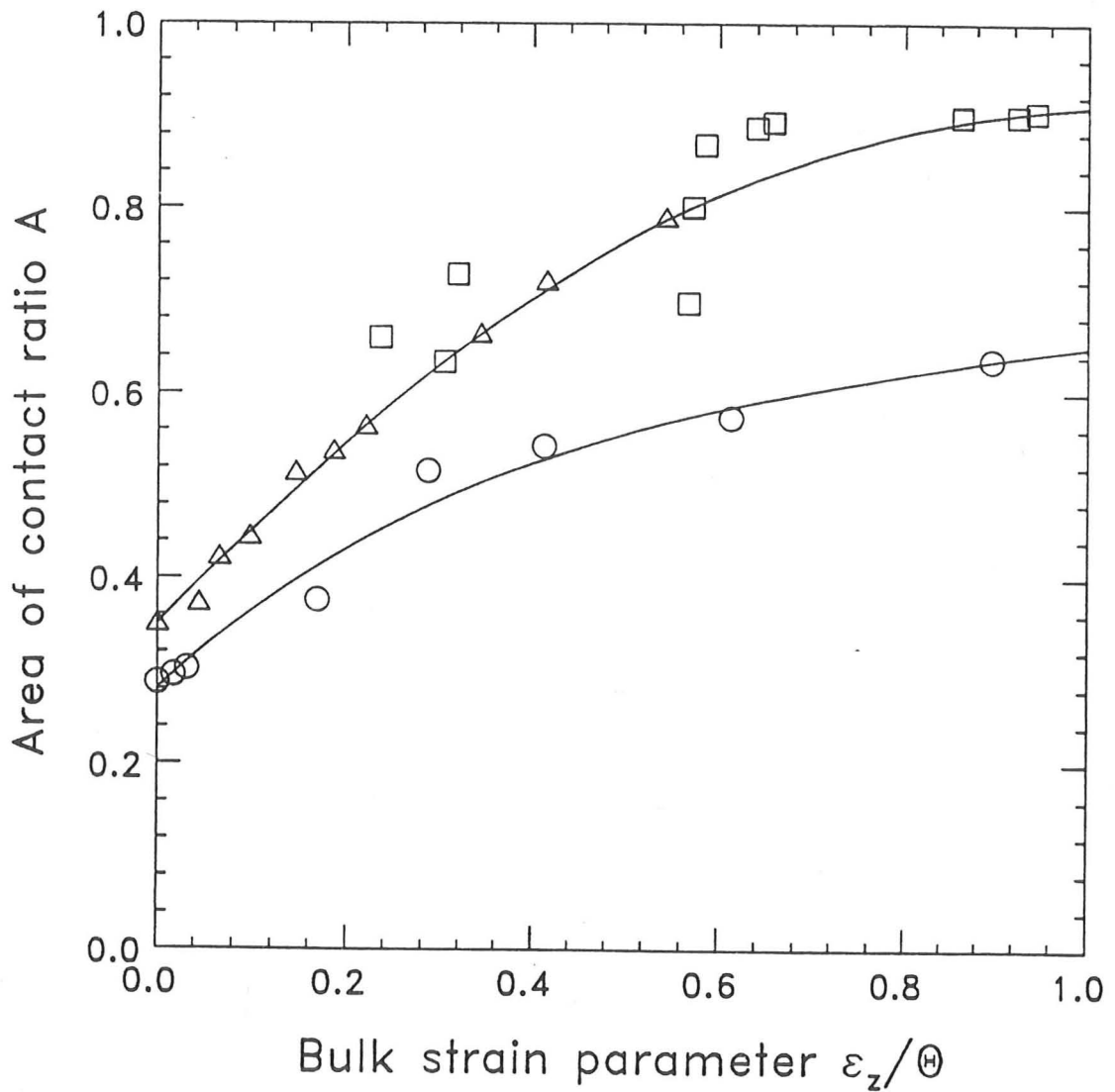
Figure 3.14 The effect of discrete loading on the surface velocity distribution - longitudinal roughness.



KEY

- MPFS approximation
- - - Sheu's approximation

Figure 3.15 Approximations to the velocity ratio parameter W .



KEY

- Best fit
- △ Experiments $\bar{p}/2k=1.0, \Theta=20^\circ$
- Experiments $\bar{p}/2k=0.6, \Theta=20^\circ$
- Sheu experiments $\bar{p}/2k=1.0, \Theta=10^\circ$

Figure 3.16 Measured growth of contact area with bulk strain for longitudinal ridges.

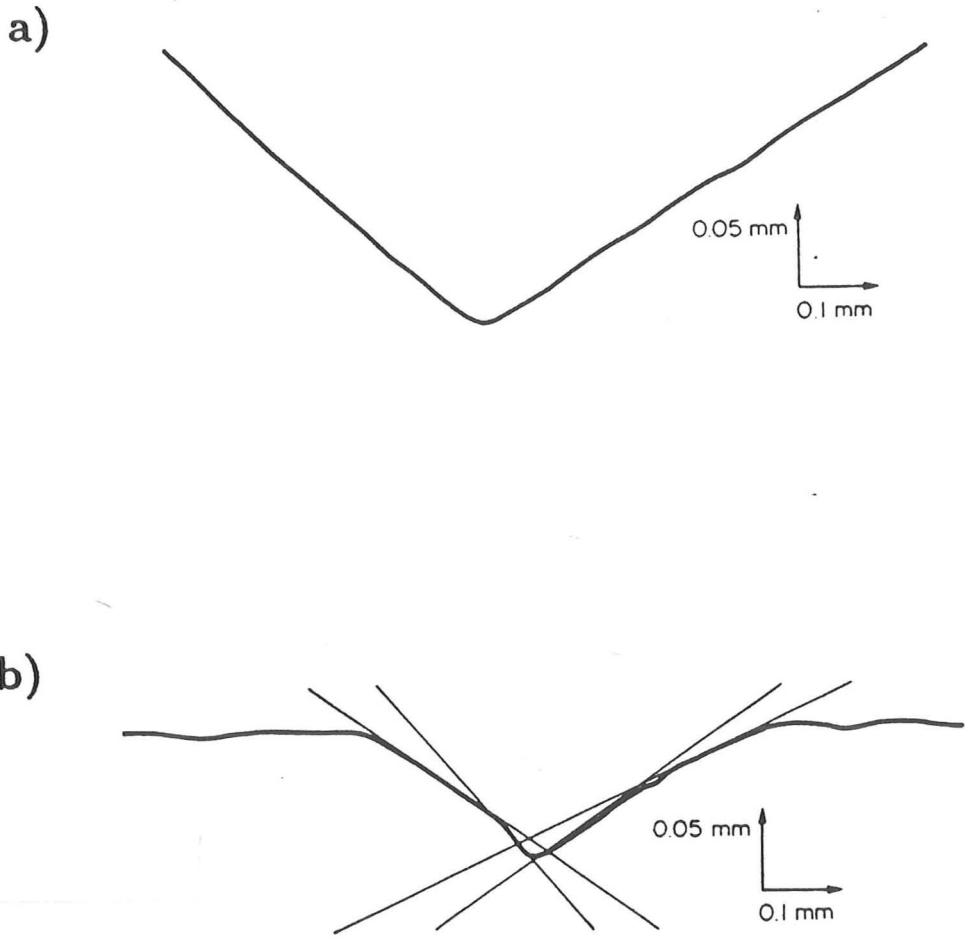


Figure 3.17 Longitudinal ridges a) Initial profile of unloaded surfaces b) Unloaded surfaces after a bulk strain of 19%.

CHAPTER 4

FILM THICKNESSES AND TRACTION IN ROLLING — THEORY

4.1 Introduction

Figure 4.1 shows a schematic of the rolling process in the mixed lubrication regime. The contact has been split into two zones — the regions where the bulk of the strip has not started to deform and the work zone where the strip is deforming in the bulk. The roughness is assumed to be circumferential, with the pseudo-Gaussian height distribution described in section 4.2.2, so that a cross section of the roll and strip profiles well away from the bite will resemble figure 4.1a, with no contact between the roll and strip. As the strip and roll approach, the softer workpiece asperities will be crushed by the hard roll. Figure 4.1b shows the geometry in this situation. Areas of 'contact' separate the valley regions which are filled with the lubricant. In the bulk deforming region the asperities continue to be crushed and the volume of oil in the valleys decreases further (figure 4.1c). Figure 4.2 shows the details of the asperity geometry in the area where the strip starts to deform in bulk. The roll is drawn as smooth in this diagram for clarity. The ratio of the areas of 'contact' to the width of the strip is A .

The friction force is made up of two components — that from the areas of close contact with a higher coefficient of friction and that from the valleys, which will have a lower coefficient of friction. To determine the friction components in each region we will need to calculate both the area of contact ratio A and the film thicknesses or friction conditions in each region.

To calculate this area of contact ratio A , it is necessary to investigate the hydrodynamic buildup of pressure in the oil in the valleys, since it is this pressurisation which keeps the roll and strip at least partially separated. Where the surface of the roll and strip are relatively well separated the lubricant filling the valleys will be pressurised due to the hydrodynamic action of the wedge shaped inlet region. It will be assumed that the film thicknesses under the asperity contacts are sufficiently small, compared

with the valley film thicknesses, that they can be neglected in this part of the analysis. The results of this part of the calculation then tell us both the area of contact ratio A and the film thickness in the valleys.

It is now necessary to determine friction conditions under the areas of contact. In previous analyses it has been considered that the distance between the roll and strip is so small under the contact areas that either the hydrodynamic film between workpiece and roll would break down and boundary additives determine friction [88] or that a limiting shear stress is reached in the oil [80]. This assumption is examined in section 4.6, in which an approximate hydrodynamic analysis is applied to the calculation of the film thicknesses under the asperities. In the cases considered where the areas of contact are significant, it is found that the valley films are rather greater than the films under the asperity contacts, but it is not always the case that the friction under the contacts will be solely due to boundary additives.

Where the friction under the contacts is due to boundary additives, the total friction can be found from the sum of the boundary friction coefficient under the contacts times the area of contact ratio and the hydrodynamic friction in the valleys.

The two parts of the calculation are combined in section 4.8 with the rheological measurements made in chapter 2 to calculate traction curves for a range of conditions typical of aluminium foil rolling.

Sheu [88] has analysed this lubrication problem to determine the film thicknesses under certain rolling conditions. The following calculation is similar to his in broad outline but the details of the calculations differ significantly. To simplify the calculation a number of assumptions have been made. These will be stated at the appropriate points in the calculation. The main assumption underlying the calculations however, is that the inlet region and the beginning of the work zone can be treated independently of the rest of the work zone and the exit region. The oil film is then considered to be determined in the inlet zone and at the beginning of the work zone. After this entry region, elongation of the strip through the bite will tend to thin the oil film. The amount of thinning can be estimated from the mass flow continuity of the oil by making some assumptions about the relative speeds of the strip and workpiece.

4.2 Film thicknesses in the valleys

4.2.1 Calculation of the oil pressures

The oil pressure buildup can be calculated by integrating a modified form of the Reynolds equation. The Reynolds equation for hydrodynamic buildup oil pressure, with smooth roll and strip, is given by

$$\frac{d}{dx} \left(h^3 \frac{dq}{dx} \right) + \frac{d}{dy} \left(h^3 \frac{dq}{dy} \right) = -12\eta_0 \bar{u} \frac{dh}{dx} \quad \{4.1\}$$

$\bar{u} = (u_R + u_S)/2$ is the mean of the roll and strip inlet speeds and h is the distance between the roll and the strip. This varies with both x and y , the rolling and transverse directions respectively. The oil viscosity η at a pressure p is related to the viscosity at ambient pressure η_0 by the Barus equation

$$\eta = \eta_0 e^{\alpha p} \quad \{4.2\}$$

where α is the pressure viscosity coefficient of the fluid. q is a reduced pressure given by

$$\alpha q = 1 - e^{-\alpha p} \quad \{4.3\}$$

The fluid has been taken as incompressible since compressibility in the inlet will have a negligible effect on the film thickness in metal working (see Appendix E for a discussion of compressibility effects in elasto-hydrodynamic lubrication). By assuming that the roughness is wholly longitudinal any variation in film thickness with time can be neglected. This assumption is justified where the slope of the asperities in the longitudinal direction is much less than the angle of the inlet between the roll and the strip, which is true for foil rolling and for the experiments presented in chapter 5. This assumption is supported by the observation that a typical length for the oil pressure to build up is rather less than the length of the asperities. If the roughness cannot be treated as wholly longitudinal, then Patir and Cheng [71] find that the hydrodynamic pressure buildup is enhanced and the resulting film thicknesses will be greater. The need for a good finish will limit the extent of hydrodynamic pits on the surface of the strip. Since the effects of pits on the pressure buildup is much less marked than that of peaks of the same amplitude, their influence on the hydrodynamic buildup will not be great unless they cover a substantial proportion of the surface.

As long as the film thicknesses separating the strip and roll are greater than a certain value, found by considering the two dimensional Reynolds equation, the pressure gradients in the transverse y direction can be neglected. The contact can then be split into two types — those regions of close 'contact' where the two dimensional Reynolds equation must be used and the intervening valleys where it is possible to neglect the transverse pressure gradients. In the regions where the film thicknesses are sufficiently small that pressure gradients in the transverse direction become significant, leakage of oil from these areas will have little effect on the oil pressure gradients in the valleys between them. The valleys, although in fact separated by the 'contacts', will be treated as though they were joined, each with the same reduced pressure q_v and corresponding pressure p_v given by equation 4.2, which does not vary with y . The Reynolds equation for the valley regions can be averaged over a length Δl greater than any roughness length scale in the transverse direction to give [5]

$$\frac{d}{dx} \left(\frac{dq_v}{dx} \frac{1}{\Delta l} \int_0^{\Delta l} h^3 dy \right) = -12\eta_0 \bar{u} \frac{1}{\Delta l} \int_0^{\Delta l} \frac{dh}{dx} dy \quad \{4.4\}$$

Integrating and simplifying we find

$$\frac{dq_v}{dx} = 12\eta_0 \bar{u} \frac{\bar{h}_v - \bar{h}_{v*} l_*/l}{\bar{h}_v^3 (1 + 3d_v^2/\bar{h}_v^2)} \quad \{4.5\}$$

where the total width of the valley regions in the width Δl is l . \bar{h}_v is the average film thickness of the valleys, omitting the regions of close 'contact' and d_v is the r.m.s. roughness of the valleys. Stars refer to conditions where the pressure gradient is zero. The change to the smooth Reynolds equation due to the roughness is given by the term $(1 + 3d_v^2/\bar{h}_v^2)$.

Wilson and Mahdavian [20, 109] give a correction to the Reynolds equation to take into account shear heating in the inlet region which reduces the viscosity of the oil. The correction factor C_m to be applied to the right hand side of equation 4.5 is

$$C_m = \left\{ 1 + 0.5 \left(L e^{-\alpha p} \left(1 - \frac{h_* l_*}{hl} \right)^2 e^{-\alpha p} \right)^{0.855} + 0.05 \left(4L e^{-\alpha p} \left(1 - \frac{u_R}{\bar{u}} \right)^2 \right)^{0.773} \right\}^{-1} \quad \{4.6\}$$

where $L = \eta_0 \beta \bar{u}^2 / k$. k is the thermal conductivity and β the temperature viscosity coefficient of the oil.

4.2.2 Roughness model

The mean depth of the valleys \bar{h}_v and the roughness of the valleys d_v can be found from the separation distance δ between the centre lines of the roll and the undeformed strip profile (figure 4.2). In calculating the film thickness and area of contact ratio the important feature of the roughness is the difference between the strip and roll profiles. It is unimportant whether the roll is smooth or rough, but in the latter case it should be remembered that crushing of the strip roughness will increase the conformity between the roll and strip and with complete crushing ($A = 1$) the strip will have the same roughness as the rolls. This difference in height between the roll and the strip can be viewed as a single composite roughness which will be modelled by Christensen's polynomial approximation to Gaussian roughness [18]. If h is the distance between the roll and strip then its probability density function $f(h/d_0)$ is

$$f(h/d_0) = \frac{35}{96} \left(1 - \left(\frac{h - \delta}{3d_0} \right)^2 \right)^3 \quad \left| \frac{h - \delta}{d_0} \right| \leq 3$$

$$= 0 \quad \left| \frac{h - \delta}{d_0} \right| > 3 \quad \{4.7\}$$

This polynomial expression is found to be a good approximation to the height distribution for the ground finish in foil rolling and in the experiments, as shown in figure 5.3. It will be assumed that the height distribution of the valleys is unaffected as the peaks are crushed so that the material from the peaks does not fill up the valleys. The residual r.m.s. roughness d_v and the mean height of the valleys \bar{h}_v can be calculated from the height distribution of the valleys. Where the film thickness in the valleys is much greater than the film thickness under the 'contacts', the mean film thickness over the whole contact including the regions of 'close' contact \bar{h} is related to the mean film thickness of the valleys \bar{h}_v by

$$\bar{h} = \bar{h}_v(1 - A) \quad \{4.8\}$$

The variation of the mean film thickness \bar{h} and the area of contact ratio A with the separation distance δ is shown in figure 4.3. The heights have been non-dimensionalised by the original r.m.s. roughness d_0 .

4.2.3 Roll shape

To calculate the oil pressure the separation distance between the roll and strip roughnesses must be found. When the substrate is not deforming this distance is determined by the shape of the roll. The bulk of the strip is assumed to be rigid and the oil film thickness is assumed to be much less than the change in the thickness of the workpiece. The length of the outlet region will then be insignificant compared with the length of the contact. For thicker strip the roll is assumed to remain circular with a slightly increased roll radius to take into account the elasticity of the roll. The roll flattening correction given by Hitchcock (see [79]) is used, where the ratio of the deformed to the original radius of the roll R/R_0 is

$$R/R_0 = 1 + \frac{2cF}{(t_1 - t_2)} \quad \{4.9\}$$

t_1 and t_2 are the strip inlet and outlet thicknesses, F is the load per unit length and c is an elastic constant equal to 2.2×10^{-11} m/N for steel rolls. F was taken as the contact length times the yield stress of the strip. The maximum value of the correction ratio R/R_0 was 1.24 for the hard 0.115mm strip calculations, so that errors in using Hitchcock's formula will be small.

In the case of thin foils the elasticity of the rolls dominates and it is no longer adequate to assume that the rolls are circular. Although there is no general solution for the roll shape, Fleck and Johnson [33] have addressed the problem in an approximate way, modelling the elastic deflections of the roll using a 'mattress' model. Their analysis provides a means of assessing whether the Hitchcock flattening assumption will be reasonable, or whether the roll profile will differ significantly from the circular shape. Mear and Zhang [64] have produced one solution using a more complete analysis. They solve the elasticity and plasticity equations for the foil and roll numerically to find the roll shape and pressure distribution in the contact zone, assuming a constant coefficient of friction of 0.03, but do not give the shape in the inlet region. This may be found by integrating the effect of this pressure distribution. The elastic deflections $v(x)$ relative to the deflection at x_0 are given [51] by the convolution

$$v(x) - v(x_0) = \frac{2}{\pi E'_R} \int_{-\infty}^{+\infty} p(s) \ln \left(\frac{x-s}{x_0-s} \right) ds \quad \{4.10\}$$

The pressure p is only non-zero on the contact arc, so that choosing x_0 just outside the contact avoids any singularity in the integration, which has been performed here

numerically using Zhang's pressure distribution under the contact. The actual shape of the roll is given by the sum of the original shape and the elastic deflections. The new calculated shape outside the contact, together with the roll shape and the contact pressure under the contact given by Zhang are illustrated in figures 4.4a and b. The additional loading from the oil and asperity pressures in the inlet non-deforming region will alter the inlet shape further. However, this effect will probably change the final smooth film shape only slightly. Uncertainties in the inlet shape arising from the way the friction is modelled are likely to have a rather stronger influence on the entraining angle at the inlet and hence the film thickness.

The actual curved shape of the roll was used in the calculations in the rigid and bulk deforming regions for thick strip, while the bulk deforming region was approximated as straight for the calculation with the thin foil. However, if the length of the inlet region of interest is sufficiently small it would be possible to approximate the shape of the roll by a straight section of the correct slope, as shown for example in figure 4.2.

4.2.4 Without bulk deformation

The oil pressure in the region before the material begins to deform in bulk is found from integrating equation 4.5. The separation distance δ between the strip and roll roughnesses is determined by the shape of the roll in the inlet.

Under the regions of close contact the contact pressure will rise, either from the hydrodynamic wedge action, or from the pressure transmitted through an additive film, until the peaks are crushed down. Whether the contact on the asperity tops is plastic or elastic is governed by the plasticity index $\psi = E'(d_0\kappa)^{1/2}/(2H)$, where $E' = \frac{1}{2}(1/E'_s + 1/E'_r)^{-1}$ is the equivalent elastic modulus for the strip and roll; E'_R and E'_S are the plane strain moduli of the roll and the strip. H is the hardness of the strip which will be assumed to equal $2.57\sigma_y$, where σ_y is the plane strain yield stress of the workpiece. $d_0 = (d_S^2 + d_R^2)^{1/2}$ is the initial combined r.m.s roughness of the strip and roll and κ is the curvature of the asperity tips. For area of contact ratios above 0.05 Halling *et al.* [40] show that the elastic part of the contact will be insignificant if ψ is greater than 2. This is the case for the experiments described in chapter 5 and for aluminium foil rolling conditions, so the assumption of plastic contact is justified. The difference in the pressure on the peaks p_a and in the valleys p_v when the substrate is

elastic must then equal the hardness of the asperities

$$\text{i.e.} \quad p_a - p_v = 2.57\sigma_y \quad \{4.11\}$$

When rolling hard materials with very smooth rolls the asperity contacts may not be wholly plastic.

As the separation distance between the roll and the strip decreases, the area of contact ratio increases and the pressure in the valleys builds up due to the hydrodynamic action. Eventually the sum of the loads on the peaks and in the valleys will be sufficient to make the bulk of the material deform. The analysis of chapter 3 shows that this will happen at a slightly lower load than would be the case with uniform loading. However friction in the inlet will increase the longitudinal stress in the strip, requiring a slightly increased normal load for yield. These two effects will both be small and will tend to cancel each other, so will be neglected. The yield condition then becomes

$$p_a A + p_v(1 - A) = \sigma_y \quad \{4.12\}$$

Working hardening of the strip will occur in the bite and increase the yield stress. However, the effect of this on the film thickness can be neglected if the region determining the film thickness is close to the inlet.

4.2.5 Bulk deformation

The separation distance δ depends only on the roll geometry when the bulk of the strip is not deforming, but when the substrate starts to deform the separation can no longer be determined simply from the rigid geometry. The analysis of chapter 3 must be applied to the problem to consider the further deformation of the asperities when the material is deforming in bulk. The results of this chapter can be used to find the non-dimensional crushing rate W of the asperities. The relationship between W , A and the effective mean crushing pressure \bar{p} is taken from equation 3.20. The effective mean pressure \bar{p} is the actual mean pressure minus the hydrodynamic pressure in the valleys ($\sigma_y - p_v$).

This information about the crushing of the asperities allows us to determine the change in separation distance δ between the roll and strip roughnesses in the bulk deforming region. Referring to figure 4.2, let ϕ be the angle that the valleys make with

the strip centre line and let θ be the angle that the asperity tops make with the centre line. θ is equal to the slope of the roll and ϕ is given by

$$\phi = (v_a - v_v)u_s \quad \{4.13\}$$

where v_a and v_v are the crushing velocities normal to the strip surface of the asperity tops and valleys respectively. The change in separation distance δ is

$$\frac{d\delta}{dx} = \phi - \theta \quad \{4.14\}$$

The straining rate $\dot{\epsilon}$ in the rolling direction is related to these slopes and the strip thickness using mass flow continuity.

$$\frac{t\dot{\epsilon}_x}{2} = \theta u_s A + \phi u_s (1 - A) \quad \{4.15\}$$

It has been assumed that the strip thickness t is adequately approximated by the entry strip thickness t_1 in the region of interest. Using the definition of the bulk deformation crushing parameter W and equations 4.14 and 4.15, ϕ can be related to the angle at which the roll approaches the strip centre line, θ by the expression

$$\frac{\phi}{\theta} = 1 - \left(\frac{t_1}{2W\lambda} + 1 - A \right)^{-1} \quad \{4.16\}$$

where λ is the wavelength of the asperities. Sheu gives a similar expression in his thesis for the change in separation distance in the bulk deforming region. For the thick strip, θ is given by the curved shape of the rolls, while for the thin foil calculations θ was assumed to be constant and equal to the average slope of the front 7% of the plastic region, which was 0.00409.

It is not obvious what value to take for the relevant length λ . Smaller asperities will deform with more difficulty and larger wavelengths (perhaps better viewed as shape errors) will be accommodated in the bite by differences in the longitudinal position at which the strip yields without affecting the asperities themselves. The length chosen to typify crushing over all the wavelengths in the roughness was the distance where the auto-correlation function has fallen to 0.1. This measure of the length scale emphasises the importance of the larger wavelengths in the crushing process since these lengths are crushed more easily.

4.2.6 Calculation method

In the non-deforming region equation 4.5 must be integrated using the shape of the rolls to find the variation of mean film thickness \bar{h} with x . In the bulk deforming region equation 4.5 relating the oil pressure to the film shape and equation 4.16 relating the film shape to the pressure then form coupled differential equations which must be integrated to find the buildup of oil pressure in this region. The mean rolling speed \bar{u} will be taken as the mean rolling speed at the inlet, consistent with the assumption that the region of interest is close to the inlet where the strip has nearly its entry thickness. Thermal effects will not be included in this region.

In the rigid region, the pressure in the valleys rises and the area of contact ratio increases going into the bite. The end point of this region is determined from the yield condition, equation 4.12.

In this analysis where the strip speed and thickness in the critical area is assumed constant, the end point of the asperity crushing process in the bulk deformation region is reached when the pressure in the valleys rises to the yield stress of the strip. There will then be no driving force to crush the asperities further. This end point is theoretically approached asymptotically. The crushing rate will tend to zero as the pressures equalise at which point the tendency of the pressures to equalise will also tend to zero. However this asymptotic behaviour is artificially prevented in the integration by taking a minimum crushing rate W of 0.05. The final film thickness and the area of contact ratio were not found to be significantly changed by taking smaller values of this minimum crushing rate.

The equations to calculate the oil pressure in the bite were integrated numerically using a NAG routine (D02CBF), with guessed values of the two unknowns, the separation distances at the end of the rigid and bulk deformation regions. These were adjusted until two conditions were satisfied, that the mean pressure at the end of the rigid region satisfied the yield criterion and that the hydrodynamic pressure at the end of the bulk deforming region reached the yield stress. The pressure gradient was assumed to be zero at the end of the bulk deformation region to give the constant of integration in the Reynolds equation 4.5.

The calculations show how the area of contact ratio and the pressure in the oil

vary going into the nip. Figure 4.7a shows a typical variation of oil pressure p/σ_y and area of contact ratio A in the different regimes of the calculation. The distance x is non-dimensionalised with respect to the contact length b . For $x < 0$, the bulk of the strip is rigid and the separation distance is determined by the rigid roll. The area of contact ratio and the reduced pressure rises until the sum of the pressures under the contacts and in the valleys reaches the yield stress at $x = 0$. For $x > 0$, the bulk material deforms and the asperities are crushed further with the mechanism described in chapter 3. Eventually the pressure in the valleys reaches the yield stress of the material at $x \approx 0.1$.

The most important parameter in determining the friction is the area of contact ratio A . However, where the asperity film thickness is negligible, this is directly related to the mean film thickness \bar{h} (see figure 4.3) which is used instead in presenting the results in order to make a comparison with smooth conditions. Where the film thickness under the asperities is not negligible, the contribution from the asperities must be added to \bar{h} to give a true mean film thickness.

The effects of tension on the strip at inlet and exit have not been considered. For smooth strip the effect of inlet tension is to give the same film thickness as for a strip with the yield stress reduced by the magnitude of the inlet stress. By considering those parts of the calculation which involve the yield stress, it can be seen that a similar result will also apply for the rough contacts. The hardness of the asperities in the region that is not deforming in bulk will be wrong, so that the films found will not be quite correct by making this substitution, but the difference will probably be small. Because the outlet region does not affect the calculation, outlet tension will not affect the film thickness, except via its influence on the roll geometry.

4.3 Dimensional analysis

The independent variables in the calculations are

$$(u_R, \eta_0, \alpha, k, \beta, R_0, \sigma_y, E'_R, t_1, t_2, \lambda, d_0, \mu)$$

μ represents the friction characteristics in the nip and affects the dependence of the strip speed on the roll speed.

Nine independent dimensionless groups are required to describe the process. These will be formed from the combinations of the above variables and from related groups.

Although these calculations are aimed at determining the coefficient of friction, some assumptions have been made about the friction conditions. For the foil rolling calculation, the shape of the roll is determined by a calculation based on a constant coefficient of friction of 0.03. Changing the rolling conditions will change this, but since only one calculation is available it is not possible to take this into account. This further complication would also mask the effect of the other variables on the film thickness generated. For thick strip, the equivalent assumption that has been made is that the neutral point is close to the exit plane so that the strip speed at exit is the same as the roll speed. The inlet speed is related to the exit speed of the strip by mass flow continuity. For normal rolling operations in the mixed lubrication regime, the strip will be prevented from skidding because of the friction in the bite, so that this assumption will be good. The influence of friction will be included in the ratio of the mean entraining speed \bar{u} to the roll speed u_R .

The contact length b and the slope of the roll θ_0 just before the strip deforms plastically will be included as variables. These variables will be determined in different ways in the thick strip and thin foil regimes, but by including them explicitly, these differences can be eliminated for the groupings used to describe the process. From the geometry of the contact for thick strip, b and θ_0 are given by

$$b = \sqrt{(t_1 - t_2)R} \quad \{4.17\}$$

$$\theta_0 = b/R \quad \{4.18\}$$

For the thin foil the numerical values of b/R and θ_0 are 0.0241 and 0.0036.

The dependent variables that are of interest are \bar{h} and A . In order to investigate the effect of roughness it is helpful to introduce $\Lambda_s = h_s/d_0$ and $\Lambda_r = \bar{h}/d_0$, the ratio of the mean film thickness to the initial roughness for smooth and rough conditions.

The dimensionless dependence can then be expressed as

$$(\Lambda_r, A) = f \left(\frac{h_w}{d_0} (\Lambda_s), \frac{t_1}{\lambda}, \alpha\sigma_y, \frac{h_w}{\theta_0 b}, \theta_0, \frac{d_0}{b}, \frac{\bar{u}}{u_R}, \frac{E'_R}{\sigma_y}, L \right) \quad \{4.19\}$$

where

$$h_w = \frac{6\alpha\eta_0\bar{u}}{\theta_0(1 - \exp(-\alpha\sigma_y))} \quad \{4.20\}$$

It is now possible interpret the groups physically.

$h_w/d_0 (\Lambda_s)$. If the film thickness is determined in a sufficiently short distance in the entraining direction the shape of the roll in the inlet may be taken as straight. For isothermal conditions the Reynolds equation can be integrated straightforwardly to give Wilson and Walowit's film thickness h_w given in equation 4.20 [107]. h_w/d_0 is then the Λ ratio for a film thickness based on smooth conditions. In the presentation of results, a smooth film thickness h_s and corresponding Λ_s calculated from the program using the full integration taking into account the effect of roll curvature and thermal shear heating on the film thickness will be used. The difference between h_w and h_s will be negligible if thermal effects and the curvature of the roll in the inlet region are small. For the case where thermal effects are small the correction to be made to the Wilson and Walowit formula to take into account roll curvature is examined in chapter 5 and plotted in figure 5.5.

Where Λ_s is large, the effect of roughness on the film thickness will be small. Where $\Lambda_s < 3$, for the roughness distribution assumed, there will be some contact between the roll and the strip and the roughness will affect the Reynolds equation in the inlet. When Λ_s is less than about 1, the area of contact becomes significant, so that the strip yields before the pressure in the valleys reaches the yield stress. The oil pressure buildup in the deforming zone must then be taken into account to give accurate film thicknesses.

$h_w/(\theta_0 b)$. If a straight inlet is assumed with isothermal conditions and smooth rolls, the distance at which the reduced pressure rises to 20% of its final value is given by $8.5h_w/\theta_0$ and the point of inflection in the reduced pressure curve is given by $0.5h_w/\theta_0$. Hence this parameter determines the length in which the pressure builds up

in the inlet region compared with the length of the contact. Where this group is not small the curvature of the rolls will affect the pressure buildup significantly. This effect is considered by Walowit and the correction to take into account roll curvature is given in figure 5.5. In the cases considered where roughness was important this group was small, so that the inlet region will nearly be straight. Using equations 4.17 and 4.18, this group can be written $2h_w/(t_1 - t_2)$, showing that it is also the ratio of a smooth film thickness to the reduction on strip thickness.

In most rolling processes the height of the roughness d_0 will be rather less than the reduction in strip thickness $(t_1 - t_2)$ taken during the process. In the mixed lubrication regime which is being considered here, the smooth film thickness h_w will be about equal to or less than the strip roughness. Combining these two observations, we can infer that the parameter $h_w/(t_1 - t_2)$ or $h_w/(\theta_0 b)$ will generally be small in mixed lubrication rolling processes, so that the inlet region can be taken as straight.

L and \bar{u}/u_R . These parameters only influence the effect of shear heating on the Reynolds equation. Wilson and Murch [108] find a thermal correction factor using Wilson and Mahdavian's thermal Reynolds equation [109], based on a straight line inlet, to correct this film thickness for shear heating in the inlet region. The correction factor C_L is

$$C_L = \left\{ 1 + 0.28(\alpha\sigma_y)^{0.38} L^{0.8} \left(1 + \left(1 - \frac{\bar{u}}{u_r} \right)^2 \right) \right\}^{-1} \quad \{4.21\}$$

In fact, when roll curvature is significant, the thermal correction C_L over corrects for thermal effects. Although thermal effects were significant in some of the calculations with large Λ ratios, they were small where roughness was important.

θ_0 . When $h_w/(\theta_0 b)$ is small, then, as long as the other groups are the same, the inlet and bulk deforming regions are geometrically similar, with just an alteration in the length scale. This is relatively clear for the rigid region but for the bulk deforming region this is not so obvious. However equation 4.16 shows that the shape of the oil film in the deforming region is proportional to the slope of the roll at that point, so that geometrical similarity is preserved there too. Because of this, changes in θ_0 can be expected to have no influence on the entrained film thickness.

d_0/b . A similar argument applies to this dimensionless group. Although the length of the inlet and deforming region are changed with different values of d_0/b , the roughness height itself is not important.

E'_R/σ_y . This factor influences the amount by which the rolls are deformed elastically. When the Hitchcock flattening formula is appropriate, the rolls remain circular, so that the only effect of this parameter is on θ_0 and b . However these have no influence on the crushing process when the inlet region can be considered as straight, so that E'_R/σ_y will not have any effect either.

t_1/λ . The crushing of asperities in the bulk deforming zone is affected by this parameter (see equation 4.16). Larger values of roughness length λ or smaller strip thicknesses will increase the ease with which the asperities crush, giving smaller films. From equation 4.16 it can be seen that changing this parameter will also show how sensitive the calculations are to the accuracy of the bulk plastic asperity crushing analysis from chapter 3 and to the choice of length scale λ for the roughness.

$\alpha\sigma_y$. The hydrodynamic equation involves the reduced pressure q , while the crushing of the asperities, both in the elastic and bulk deformation regions, is dependent on the actual pressure p . The difference in these two pressures is determined by $\alpha\sigma_y$. The reduced pressure at which the material first yields and the crushing process is affected by changing this parameter. For small values of $\alpha\sigma_y$, changes in $\alpha\sigma_y$ will have little effect since the reduced pressure tends to the actual pressure. As $\alpha\sigma_y$ approaches 1, the difference between the reduced and actual pressures will become important. In all the calculations done here the crushing of asperities is more rapid in the rigid than in the deforming region, although this need not always be true. If a greater part of the pressure buildup is in the bulk deforming region where the angle between the asperity tops and the valleys is reduced, then the final film thickness will be increased, in the same way that a smaller inlet angle results in a larger film thickness for smooth rolls and strip (c.f. equation 4.20). For smaller values of $\alpha\sigma_y$, the value of αq for first yield of the bulk will be smaller, with more of the pressure buildup in the bulk deforming region resulting in larger films.

The thermal correction also depends on $\alpha\sigma_y$, with larger values having larger hydrodynamic pressures and viscosities, so giving rise to a greater shear heating effect.

Where the inlet geometry can be taken as straight and where shear heating is small, there are only three dimensionless groups that influence the oil film and area of contact, Λ_s , $\alpha\sigma_y$ and t_1/λ .

The effect of these parameters has been considered qualitatively. More detailed quantitative results will now be presented.

4.4 Results of valley film thickness calculations

The results will be presented in two ways. Firstly, the final film thicknesses calculated for a range of conditions will be presented, assuming that the asperity film thicknesses are negligible. From these results the area of contact ratios can be found from figure 4.3. Then the actual variation in pressure and film thickness through the contact for a selection of these calculations will be shown.

In the calculations, conditions appropriate to two sets of conditions have been used; those corresponding to some experimental measurements on a rolling mill and those which could be found rolling aluminium foil industrially. Calculations have been performed in a similar way to experimental technique by changing a physical parameter. The corresponding change in the relevant dimensionless groups will be detailed so that the effect of these groups can be seen. The basic set of conditions used are given in table 4.1. Figures in brackets indicate the conditions used unless stated otherwise. The physical variables which have been changed in the calculations are the rolling speed, the roll radius, the strip reduction, the yield stress of the strip, the wavelength of the asperities, the combined roughness of the strip and roll and the inlet strip thickness.

Rolling speed, u_R . The most important effect of changing the rolling speed is in changing Λ_s . Since Λ_s is the most influential group in the analysis, this has been varied by changing the rolling speed for each set of results, to show the differences in the relationship between Λ_s and Λ_r when the other variables are altered.

The effect of speed on the results is shown in figure 4.5. As the speed is reduced, Λ_s becomes smaller and the effects of roughness become important, as demonstrated by the difference between the values of Λ_r and Λ_s given by the different curves (which correspond to different values of yield stress). In addition L and $h_w/(\theta_0 b)$ will change with varying speed, but these changes are shown below to be negligible.

Thermal heating parameter L , roll radius R_0 , roughness d_0 and reduction $(t_1 - t_2)/t_1$. The effect of L on the relationship between Λ_s and Λ_r was investigated by eliminating thermal heating from the calculation. Changing the roughness d_0 only

changes the groups d_0/b , $h_w/(\theta_0 b)$ and L for the same values of Λ_s , while changes in the roll radius also affects θ_0 . A change in the reduction affects \bar{u}/u_R in addition to the above groups. Since, for thicker strip, changing σ_y/E'_R only alters the roll curvature through the Hitchcock flattening, the influence of this parameter will be the same as the effect of changing R_0 . With thin foil, changing R_0 or σ_y/E'_R may have more profound consequences.

The changes that were made to the base-line case given in brackets in table 4.1 to investigate these effects were

- (i) no thermal heating,
- (ii) a roll radius of 785mm,
- (iii) a combined roughness of $0.1\mu\text{m}$
- (iv) a reduction of 0.39.

As indicated by the dimensionless analysis, none of these changes should have any influence on the film thickness where the inlet can be considered straight and thermal effects are small. This is confirmed by the calculations, in which none of the variables changed had a significant effect on the results and would be indistinguishable if plotted on figure 4.5. Where any changes are observed in the relationship between Λ_r and Λ_s , it is possible to infer that the changes are due not to changes in the groups L , d_0/b , $h_w/(\theta_0 b)$, θ_0 , \bar{u}/u_r or σ_y/E'_R , but to changes in the remaining three groups Λ_s , $\alpha\sigma_y$ and t_1/λ .

Yield stress σ_y . Changing the yield stress will alter the groups $\alpha\sigma_y$ and σ_y/E'_R significantly. In addition the changes in h_w will alter the groups $h_w/\theta_0 b$ and L slightly, for the same value of Λ_s . Since the effect of all these groups apart from $\alpha\sigma_y$ have been shown to be insignificant, changes in the yield stress will identify the effect of $\alpha\sigma_y$ on the relationship between the rough and smooth Λ ratios. This effect is shown on figure 4.5, where four different yield stresses have been included. The lower yield stresses give higher film thicknesses for Λ_s less than 1, because, as explained in the dimensional analysis, the pressure buildup is then weighted towards the rigid region.

Roughness length λ and inlet thickness t_1 . The roughness length λ only affects the group t_1/λ , while changes in t_1 also affect θ_0 , d_0/b , $h_w/(\theta_0 b)$ and L . Since the effect of all these groups except t_1/λ has been shown to be negligible in the thick

strip regime, changes in either of these parameters will pinpoint the effect of t_1/λ on the process. Figure 4.6 shows the effect of changing each of these variables. Firstly the length λ is changed with a inlet strip thickness of 0.7 mm. Secondly the inlet strip thickness is altered while the value of λ is held constant at $30\mu\text{m}$. The values of the reductions for these calculations with different inlet thicknesses were slightly different, to match the experiments in chapter 5, taking values of 0.14, 0.20 and 0.10 for the 2.82mm, 0.7mm and 0.115mm strips respectively. For the calculation with 0.02mm foil, the roll elasticity is important and the calculated roll shape of figure 4.4 was used with a reduction of 0.25. The value of λ chosen for this calculation was 15μ , to match the type of roughness typical in industry. The actual values of the group t_1/λ are labelled and have been chosen so that the calculations can be directly compared. It can be seen that the effect of both changes are the same. The difference with $t_1/\lambda = 3.83$ at the smallest values of Λ_s arises because the integration with the 0.115mm foil and $\lambda = 30\mu\text{m}$ extends almost to the end of the plastic zone so that the roll cannot be considered as straight in the region of interest. The difference in mean valley film thickness \bar{h}_v in the two cases is not great but, with small values of Λ and large values of A , the mean film thickness \bar{h} is sensitive to small changes in the mean valley film thickness \bar{h}_v . The area of contact ratio A is not sensitive and this is not very different in the two calculations.

With smaller values of t_1/λ , the roughness crushes more easily in the plastic region and the resulting film thicknesses are smaller.

It is interesting to note that results with the thin foil and $\lambda = 15$ and for 0.7 mm strip and $\lambda = 525\mu\text{m}$, which both have values of t_1/λ of 1.33, are very similar. This may be rather unexpected, since different models of the roll shape were used in each case. This emphasises the way that the film thickness is not dependent on the geometry of the inlet as long as it can be considered straight in the region of interest. In the foil rolling case, there is a slight discontinuity in slope at the point where the foil deforms, which does not occur for the thick strip, but it appears that this discontinuity does not significantly alter the calculation.

It has been argued that changing θ_0 , d/b , $h_w/(\theta_0 b)$, σ_y/E'_R and \bar{u}/u_r will have no effect on Λ_r for thick strip, but for thin foil the ratio of the slope of the roll in the rigid and plastic zones will change as these parameters are varied. Although the effect of

Λ_s , t_1/λ and $\alpha\sigma_y$ will be similar for thick strip and foil, it is not possible for the thin foil to be sure that the effects of the other parameters will be negligible.

In the calculation available the slopes in these regions are similar, but it is not clear whether this will always be the case. If it is, then it is reasonable to suppose that the above groups will still have no influence and the groups that remain, Λ_s , t_1/λ and $\alpha\sigma_y$ will be the only important dimensionless variables. However it is conceivable that, moving further away from the thick strip regime, the difference between these slopes will become greater and we can then expect some small influence from the other groups that affect the inlet shape.

In order to appreciate how the film thickness is controlled, it is useful to show the buildup of pressure and the mean film thickness and corresponding area of contact ratio change in the nip for the different conditions. Figure 4.7a-e show different conditions corresponding to changes in Λ_s , $\alpha\sigma_y$ and t_1/λ . The x axis is non-dimensionalised with respect to the contact length b ; note that the film thickness is determined for x/b small, as assumed in the theory. For each set of conditions the ratio of the separation distance to the roughness δ/d_0 , the area of contact ratio A , the reduced pressure αq and the actual pressure p/σ_y are plotted. These graphs illustrate the way that the balance of the pressure buildup changes as Λ_s , $\alpha\sigma_y$ and t_1/λ change. Figure 4.7a is the base line case. Other plots should be compared with this to identify the effects of the various parameters. Figures 4.7b and c show the effect of changing Λ_s . Figure 4.7d shows the effect of a smaller value of $\alpha\sigma_y$ and figure 4.7e shows the effect of changing the strip thickness. In figure 4.7e a thin foil result has been shown. In each case the buildup of pressure in the inlet region is essentially determined by Λ_s . The plastic region affects the rigid inlet region slightly as the backflow, given by $\bar{h}_{v*}l_*$, alters the Reynolds equation 4.5 in the inlet. The pressure buildup in the plastic region is then governed by the ease with which the asperities crush.

4.5 Comparison with Sheu's theory

The relationship between the smooth and rough Λ ratios may be compared with the calculations of Sheu. He uses the flow factor method of Patir and Cheng to find the effect of roughness on the entraining pressure buildup. He is then able to find the effect of different amounts of directionality in the lay of the roughness on the crushing process. The roughness orientation is given by γ , the ratio of the auto-correlation lengths in the longitudinal and transverse direction. The new analysis is appropriate for $\gamma = \infty$. It should be noted that the flow factor method is derived for elastic contacts with small areas of contact. Its extension to smaller values of Λ , certainly below 0.5 and probably below 1, will not be entirely accurate. This difficulty of calculating hydrodynamic pressure gradients in the areas where Λ is small is also encountered in the new analysis and is overcome in the new theory by making the simplifying assumption that the valley pressures are all the same in the region of contact, with a roughness determined by plastic contact conditions. Moreover the asperity crushing model used by Sheu which is appropriate for longitudinal roughness will be inaccurate if $\gamma < 1$ (transverse roughness) and in that case the analysis presented in chapter 3 should be used. For transverse roughness chapter 3 shows that the asperities are more easily crushed, which will tend to counteract the effect of the increased pressure buildup for transverse roughness given by the flow factor method. Because of these differences, the increased films found by Sheu for smaller values of γ with Λ less than 1 may not be found in practice. For $\Lambda > 1$, the film thickness is determined by the region where contact between the roll and strip is small and the increase in pressure gradient and film thickness for transverse roughness given by the flow factor approach will be reasonable.

The values of crushing parameter W used by Sheu are shown in figure 3.15. The effect of using these values of W which are rather larger, particularly at small area of contact ratios, than can actually be expected will be the same as the effect of having smaller values of t_1/λ .

A value of crushing parameter W tending to ∞ corresponding to no valley pressure appears to have been assumed at the entry to the deforming region rather than the smaller value corresponding to the difference in valley and asperity pressures at that point, which is determined by the yield condition. The calculation has then been expressed by the differential equations relating dW/dx , $d\bar{h}/dx$ and dq_v/dx . This as-

sumption will presumably result in smaller film thicknesses than would be the case if the initial condition were chosen correctly.

Sheu includes the thinning of the oil film due to elongation of the strip in the work zone. The end point of his bulk deformation calculation is then not approached asymptotically, since the thinning of the oil film in the work zone requires some crushing of asperities and a difference in asperity and valley pressures through the work zone. Where the bulk deforming zone in which the pressure is determined is much less than the contact length, the value of this residual crushing will be small and the assumption of the new theory that it tends to zero will not affect the film thickness. The relationship that Sheu finds between Λ_s and Λ_r is given with the results of his experimental measurements in the next chapter in figure 5.12 for $\alpha\sigma_y = 3$. This may be compared with the results of the above calculation with a similar value of $\alpha\sigma_y = 4.18$. Sheu's value of t_1/λ is not stated. A figure for t_1/λ of 17 has been used for the new calculations, corresponding to an inlet strip thickness of 1.02mm and a roughness length λ of $60\mu\text{m}$. These figures have been tentatively chosen in an attempt to match Sheu's experimental measurements. The agreement between the new calculation and the calculation of Sheu for $\gamma = 3$ is reasonable. This may be a coincidence if the effects of the different crushing models used in the two cases and a possibly incorrect estimate of t_1/λ cancel out.

4.6 Film thicknesses in the regions of close contact

When the film thickness between the roll and strip becomes sufficiently small, it is no longer possible to neglect variations in pressure in the transverse direction and the full two dimensional Reynolds equation must be used. The contact then consists of these regions where the pressure may vary in the transverse direction and the valleys which are assumed to have a uniform pressure. Since the film thickness under the contacts will be assumed to be much less than the valley film thicknesses, the length scale for pressure buildup under the 'contacts' will be much less than that for the valleys and the pressure under these contacts can be considered as an addition to a constant pressure in the surrounding valley regions. A hydrodynamic analysis of the pressure buildup under the contacts will first be considered. The resulting film thickness must then be compared with the thickness when the oil is no longer believed to behave as a

bulk fluid, or with the length of additive molecules in the oil which will interfere with the hydrodynamic buildup of pressure, to see if the use of the hydrodynamic equations is justified in this region.

First contact will be made by the very tops of the asperities with a very small contact width, because of the irregular nature of the roughness. In order to extract a meaningful film thickness for the contact areas, these initial contacts will be disregarded and the calculations will be based on slightly wider contacts of width λ_a . For the purpose of calculations this is taken as one third of the correlation distance λ of the roughness. The geometry of the contact is shown in figure 4.8. It has been modelled as flats of width λ_a on the top of the strip roughness intersecting with the roll to form a wedge shaped inlet with valleys on either side. The angle of this inlet wedge is taken as θ , the slope of the roll at a position, arbitrarily chosen, where the area of contact ratio A is 0.1. By modelling the problem in this way the larger contact areas are emphasised, since the friction will depend on the mean film thickness separating these larger areas. However the initial asperity contacts of smaller width will be less well lubricated and will have smaller film thicknesses separating them from the roll. Even where the larger contact areas are separated from the roll by a thick oil film, additives may still play an important rôle in protecting these smaller initial contacts from scuffing. In extreme cases, even the additives may be inadequate and then some metallic contact will occur.

With this inlet shape, the two-dimensional Reynolds equation may be solved using a modification of a program initially written by Tønder [91] which inverts the matrix given by the finite difference formulation of the Reynolds equation to find the pressure in the inlet. The boundary conditions chosen for this calculation were zero pressure at the sides of the contact wedge and at a distance m from the end of the inlet wedge and a zero pressure gradient at the end of the inlet. The reduced pressure in the valleys at the sides of the contact may be added directly to the additional reduced pressure in this wedge region found from the finite difference program. With such a simple geometry, there are only two dimensionless groups which determine a corresponding dimensionless pressure, the ratio ν of the width of the contact, in this case λ_a , to the length of the inlet region m and the ratio of the height at the beginning of the wedge h_i to the height at the exit h_a . Where ν is large the side leakage of oil may be neglected,

and the reduced pressure q_{ns} is given by

$$q_{ns} = 12\eta_0\bar{u} \int_{h_i}^{h_a} \frac{h - h_a}{h^3} dx \quad \{4.22\}$$

For an infinite inlet height the reduced pressure q_∞ is

$$q_\infty = \frac{6\eta_0\bar{u}}{\theta h_a} \quad \{4.23\}$$

and the ratio of the reduced pressure buildup with a finite inlet height h_i to that with an infinite inlet length is

$$\frac{q_{ns}}{q_\infty} = \left(1 - \frac{h_a}{h_i}\right)^2 \quad \{4.24\}$$

To study side leakage a height ratio was chosen so that this ratio q_{ns}/q_∞ of reduced pressures was 0.8. The effect on the maximum reduced pressure q of varying ν was found and expressed as a ratio of the actual reduced pressure to that which would occur with no side leakage q/q_{ns} . It was found necessary to use a large number of nodes to give accurate agreement with the analytical solution for the case where side leakage was not considered. To order to accommodate the inaccuracies in the side leakage case, a calibration curve was used to correct for the error in pressure buildup as a function of the number of nodes in the pressure curve. Store and CPU time limited the ability to refine the mesh indefinitely. The results of this set of computations is shown in figure 4.9. For $\nu > 2.5$, side leakage has no effect on the pressure buildup, but as ν becomes less than one, there is a very marked decrease in the buildup of pressure as values of q/q_{ns} fall below one.

It is useful to define an effective entraining length m_e , as an inlet length which would give the same pressure rise if there were no side leakage present. Figure 4.9 shows how the ratio of this effective length to the width of the inlet varies with ν . It can be seen that the effect of side leakage is to reduce the effective length of the inlet region, for $\nu \leq 1$, to 0.6 times the width of the contact. Figure 4.10, which is the reduced pressure plot for $\nu = 0.3$, shows why this occurs. The buildup of pressure only happens close to the end of the contact. Away from the end oil leaks away to the sides and the length of this region does not affect the pressure buildup.

This result may be included in the program calculating the film thickness in the valleys. When the area of contact ratio reaches 0.1, the slope θ is calculated and hence the reduced pressure rise corresponding to an infinite inlet height from equation 4.23.

This expression includes the unknown film thickness h_a . The effective length for buildup of pressure is $0.6\lambda_a$ giving an inlet to exit height height ratio h_i/h_a

$$\frac{h_i}{h_a} = 1 + \frac{0.6\theta\lambda_a}{h_a} \quad \{4.25\}$$

The ratio of the pressure q_∞ to the actual reduced pressure q is then given by equation 4.24, again as a function of the unknown film thickness at the end of the wedge h_a . If the asperity peaks are to be crushed, the difference between the pressures p_v in the valleys and that under the asperities must equal $2.57\sigma_y$. The reduced pressure under the asperity q_a is then related to the reduced pressure in the valleys q_v by

$$\alpha q_a - \alpha q_v = (1 - \alpha q_v)(1 - e^{-2.57\alpha\sigma_y}) \quad \{4.26\}$$

These equations can be reduced to a cubic equation

$$\Delta Q \frac{h_a}{h_w} \left(\frac{h_a}{h_w} \frac{h_w}{0.6\theta\lambda_a} + 1 \right)^2 = 1 \quad \{4.27\}$$

where

$$\Delta Q = (1 - \alpha q_v) \frac{1 - e^{-2.57\alpha\sigma_y}}{1 - e^{-\alpha\sigma_y}} \quad \{4.28\}$$

h_w is taken from equation 4.20 with the inlet angle θ . $0.6\theta\lambda_a/h_w$ is an effective aspect ratio of the width of the contact to a typical hydrodynamic length for pressure buildup.

The ratio of the asperity film thickness to a smooth film thickness h_a/h_w is a function of ΔQ and $0.6\theta\lambda_a/h_w$. Figure 4.11 shows this relationship for four values of ΔQ . For small values of $\Delta Q h_a/h_w$, equation 4.27 has the solution

$$\frac{h_a}{h_w} = \left(\left(\frac{0.6\theta\lambda_a}{h_w} \right)^2 \frac{1}{\Delta Q} \right)^{1/3} \quad \{4.29\}$$

The value of ΔQ is a function of the valley pressure and $\alpha\sigma_y$, but for small values of Λ_s the reduced pressure in the valleys will be small and ΔQ is a function just of $\alpha\sigma_y$. The corresponding values of $\alpha\sigma_y$ are marked on figure 4.11.

Where the valley pressure is not small the values of ΔQ from equation 4.28 must be used. For those cases where q_v is not known but $\Lambda_s < 0.5$ an estimate may be made assuming that the reduced pressure $\alpha q_v = 0$. For $\Lambda_s > 2$ the valley pressure will be close to the yield stress of the strip.

Figure 4.11 shows that the films under the contacts depend on the effective aspect ratio of the inlet region under the asperities and on the pressure of the surrounding valleys. The film thickness under the asperities decreases with the wavelength λ_a of the asperity tops considered. Where $0.6\theta_o\lambda_a/h_w$ is small the asperity films will be much less ^{than} the smooth film thickness. The assumption that the calculations of the pressure buildup in the valleys and under the asperity contacts can be treated independently will be reasonable. For the thick strip calculations, the maximum value of this effective aspect ratio is about 0.3 and the assumption will be good. In the foil calculations the aspect ratio is less than 0.2 for speeds greater than 3 m/s, but at the slowest speed of 1 m/s, the analysis predicts an asperity film thickness half the smooth film thickness. This suggests that the calculations of the oil pressure in the valleys and under the asperities should be considered together to give a more accurate estimate of the film thickness and area of contact ratio in this case.

The simplified analysis given in this section may give a reasonable indication of the film thickness expected under the contacts, if hydrodynamic theory still holds there. However, the calculations may be affected by a number of factors. Sheu and Wilson [87] show that, where the oil exhibits a critical shear stress and behaves as a plastic solid, the reduction in the shear stress that the fluid can support in the inlet wedge may severely reduce the load carrying capacity or film of film thickness of the asperities. However, where the fluid shows an Eyring viscous behaviour, Higginson [43] shows that the reduction in asperity film thickness is much less than that calculated by Sheu and Wilson.

Once the asperity tops become flattened, further side leakage of oil from under the asperities may occur in the short section in the inlet and at the beginning of the bulk deforming region where there is a pressure difference between the asperity tops and the valleys. This side leakage may be enhanced by the non-Newtonian behaviour of the oil, as suggested by Johnson and Higginson [50] for a limiting shear stress and as suggested by the results of chapter 6 and Appendix D where the oil behaves as a Eyring viscous fluid.

4.7 Results of the film thickness calculations for foil rolling

The relationship between Λ_r and Λ_s for thin foil rolling is given by figures 4.5 and 4.6. However it is not easy to calculate the smooth film thickness and hence Λ_s in foil rolling without knowing the inlet roll shape. One possible method is to use the results of Dowson and Higginson [23] for elastohydrodynamic contacts. The formula of Dowson and Toyoda (equation 2.6) summarises their calculations and later findings. Some modification to this should be used to make it more relevant to foil rolling. The contact length for foil rolling is close to that of a Hertz contact with an effective radius half the radius of each roll. The inlet shape between the roll and the foil is then given by half the Hertz separation of the two rolls in contact under the same load. However these conditions are identical to those of a roll loaded against a flat under half the load. The Dowson and Toyoda formula should thus be used with the roll radius, but half the actual load. An alternative strategy, where the inlet shape is known, is to use the straight line integration of the Reynolds equation in the inlet given by Wilson and Walowit's formula equation 4.20. The film thicknesses using the formulae of Dowson and Toyoda or Wilson and Walowit are compared in table 4.2 with the full integration of the smooth film thickness from the program using the actual inlet shape of figure 4.4. The value of θ used in Wilson and Walowit's formula was taken as 0.0058, the average for x/b between -0.05 and 1 . The variables used in the calculations are given in table 4.1; the rolling speed was varied to give the change in Λ_s and Λ_r , plotted on figure 4.6. These film thicknesses would be the same if for example, η , were different, as long as the dimensionless group $\alpha\eta u/R$ is the same. If $\alpha\sigma_y$ is greater than say 2 , the reduced pressure at the end of the inlet will still be close to $1/\alpha$ and the smooth film thickness will not be significantly affected. The film thickness would change, however, if the groups affecting the roll shape in the inlet were different.

At the higher speeds with larger $h_w/(\theta b)$, the straight line approximation is no longer adequate and the actual film thickness is rather less than from Wilson and Walowit's formula. Dowson and Toyoda's formula is poor at low speeds but becomes better at large speeds. The roll shape for two elastic rolls is not similar to the actual shape in the foil rolling case close to the deforming region but is a better approximation away from the contact.

Table 4.2 shows that Wilson and Walowit's formula, applied to a suitable straight

line approximation to the inlet region, can give reasonably accurate estimates of the smooth film thickness, without performing the full integration. When further foil inlet shapes become available, this result can be used to deduce smooth film thicknesses. The area of contact ratios, asperity and valley film thicknesses can then be deduced using figures 4.3, 4.5, 4.6 and 4.11.

Table 4.2 also shows the mean valley film thickness \bar{h}_v and the area of contact ratio under the nip A from the valley film calculations. The mean film thickness \bar{h} neglecting the asperity films, which is plotted in figure 4.7, is given from the mean valley films by equation 4.8. A more accurate estimate of the mean film thickness \bar{h}_t may be made by including the asperity film thickness h_a

i.e.
$$\bar{h}_t = \bar{h}_v(1 - A) + h_a A \quad \{4.30\}$$

Table 4.2 also includes the valley pressure αq_v when A reaches 0.1, which is used in the calculation of the asperity film thickness.

The variation of the valley and asperity film thicknesses and the area of contact ratio with the rolling speed are given graphically in figure 4.12.

When the asperity films are added to the mean films from the valley calculations to give the total mean film thickness \bar{h}_t , the difference between the smooth film thickness and this more accurate mean film thickness is rather small. For these conditions, the reduction in film thickness under the asperities is offset by the increased film thickness in the valleys. If different asperity wavelengths or strip thicknesses were chosen, the smooth and rough mean film thicknesses would not necessarily be as close.

An indication of whether the traction under the asperities is likely to be hydrodynamic or due to boundary action may be obtained by comparing the calculated hydrodynamic films with the lubricant or boundary additive length. The length of both typical foil rolling lubricants and the additives is of the order of 3nm (the length that Schey gives for calcium stearate [82]). It is not clear how thick the actual additive layers will be, but they will presumably be several molecules thick. At the same time, the shearing at the interface will prevent them building up indefinitely. It seems plausible that, with the asperity film thicknesses calculated for speeds of 5 and 10 m/s of 31 and 18nm, the surfaces may be kept apart sufficiently for friction to be determined by the bulk fluid properties. The shear stresses in the oil, even under the asperities,

are rather smaller than the Eyring stress or limiting stress of the oil, because of the low viscosity of the foil rolling oil in the entry region. Hence the reduction in asperity film thickness for non-Newtonian fluids due to the mechanisms of Sheu and Wilson or Higginson and Johnson will not be significant.

4.8 Traction curves for foil rolling conditions

Table 4.2 provides the information necessary to deduce traction curves for the foil rolling conditions of table 4.1. The change in friction coefficient μ can be found as the relative sliding speed Δu between the roll and strip increases. Under the regions of close contact it will be assumed that the traction is determined by the bulk fluid properties with a film thicknesses h_a and a strain rate $\Delta u/h_a$. To calculate the friction contribution from the valleys a strain rate $\Delta u/\bar{h}_v$ will be assumed using the average valley film thickness. The shear stress in the oil is given from these strain rates by the Eyring law

$$\tau = \tau_0 \sinh^{-1} \left(\frac{\eta \Delta u}{\tau_0 h} \right)$$

with the oil properties τ_0 and η measured in chapter 2 for Somentor 31. The results of these measurements were interpolated to find the viscosity η and Eyring shear stress τ_0 at a temperature of 60°C.

The friction coefficient is made up of two parts — from the asperity tops

$$\mu_a = \frac{\tau_0 A}{p} \sinh^{-1} \left(\frac{\eta \Delta u}{\tau_0 h_a} \right) \quad \{4.31\}$$

and from the valleys

$$\mu_v = \frac{\tau_0(1-A)}{p} \sinh^{-1} \left(\frac{\eta \Delta u}{\tau_0 \bar{h}_v} \right) \quad \{4.32\}$$

The total friction coefficient is the sum of these two components. The solid lines in figure 4.13 show the calculated friction curves for $u_r = 5$ m/s with a pressure p of 625MPa, where the value of the Eyring stress τ_0 is 4.5MPa. The separate contributions from the valleys and from the asperity tops and the total friction coefficient are shown. Figure 4.13 shows that the friction contributions from the valleys and from the contact regions in this case are similar, if the asperity friction is indeed governed by the bulk properties of the lubricant as has been assumed. The curvature of the asperity friction contribution reflects the non-linear behaviour of the oil at the higher strain rates.

To illustrate the effect of oil side leakage on the asperity films and on the friction, the same case was considered, but the asperity film thickness was taken as one third of that given in table 4.2. The new contribution to the total friction from the asperities in this case is shown dotted in figure 4.13. The valley friction component will be the same. Because of the non-linear behaviour of the oil at the higher slip ratios, the increase in friction is not large except at the smallest sliding speeds.

The oil properties and the film thicknesses will depend on the rolling speed and the pressure. Figure 4.14, which is the traction curve for $u_r = 10\text{m/s}$ and a pressure of 625MPa, should be compared with figure 4.13 to show the effect of an increased rolling speed on the traction curves calculated. At a rolling speed of 10 m/s the contribution from the valley friction becomes more important than the friction component from the asperity contacts, reflecting the decrease in the contact area ratio. While the balance between the asperity contact and valley friction components changes with the increased speed, the total friction remains similar for a given slip rate.

Pressure affects the traction curves only through the change in viscosity and Eyring stress. Figures 4.15 and 4.16 show the traction curves for $u_r = 5\text{m/s}$ and pressures of 230 and 1510MPa respectively. The coefficient of friction is larger at the higher pressures because there is an exponential increase in viscosity with pressure. At the lower pressure the asperity friction dominates, but at the higher pressure, due to the non-Newtonian viscosity, the contributions from the valleys and the asperities are again similar.

The oil has been assumed to behave as an Eyring viscous fluid under the asperities, but it is possible to consider two further mechanisms of friction. The first mechanism occurs if the strain rate in the oil is sufficiently high, when the oil may begin to behave as a plastic solid. However it was found in chapter 2 that Somentor 31 did not behave as a plastic solid at least up to friction coefficients of 0.045, so that this behaviour would not be expected for the conditions of figures 4.13 to 4.16.

Alternatively, it is possible that the friction under the contacts is due to the shearing of boundary additives. Briscoe *et al.* [12] have measured the strength of calcium stearate, a boundary soap that can be expected to have very similar properties to the aluminium soaps found in foil rolling. They found that the shear strengths were not affected significantly by the thickness of the boundary layer, or by the sliding speed,

but increased with pressure and decreased with temperature. Although they only give the variation of shear strength with pressure at 20°C, it is possible to extrapolate the results to the temperature of 60°C assumed in the foil calculations, using the variation with temperature at a single pressure that they find. At pressures of 230, 625 and 1510MPa, the shear strength of the calcium stearate is 3.2, 8.3 and 55MPa respectively. The contribution to the total friction from the asperities would then be 0.007 for the pressures of 230 and 625MPa and 0.019 at a pressure of 1510MPa. These estimates of boundary friction will be independent of sliding speed and should be added to the contributions from the valleys to give the total friction.

The values of friction coefficient derived are significantly lower than the generally quoted values [32, 65, 81, 97, 99]. There appears to be two reasons for this. With hydrodynamic lubrication, the low viscosity of the foil rolling oil, and its non-Newtonian behaviour at high shear rates leads to rather lower shear stresses, except at the highest pressures, than those deduced from Newtonian behaviour of the generally thicker oils considered elsewhere. Where friction is due to the boundary lubrication mechanism, the boundary shear strengths typically assumed tend to be much greater than those measured by Briscoe *et al.* at metal working pressures [97, 98].¹

¹ An important conclusion from the theory is that the pressure under the asperities is no greater than the mean pressure, in contrast to elastic rough contacts where the pressure under the asperities is greater than the mean pressure. If this were not appreciated, this could explain the high values of boundary shear strengths sometimes used.

4.9 Conclusions

The effect of the parameters controlling film thicknesses in the rolling process has been examined theoretically. Results are summarised by figures 4.5 and 4.6. The films generated are most strongly dependent on Λ_s , the ratio of the film thickness for smooth surfaces to the combined r.m.s. roughness of the strip and foil. For thick strip Λ_s may easily be estimated from Wilson and Walowit's formula (equation 4.20). Equation 4.21 gives an approximate correction factor for the effect of shear heating in the inlet and figure 5.5 gives the factor to take into account the roll curvature on the smooth film thickness. For thin foil the effect of speed on Λ_s is calculated for the roll shape known.

The rough mean film thickness from the valley calculations can be found using figures 4.5 and 4.6, as a function of the parameters $\alpha\sigma_y$ and t_1/λ . The area of contact ratio A may be deduced from the rough mean film thickness from figure 4.4. These results assume that the film thicknesses under the contacts are small compared with the valley films. Where this is not the case the calculation of the area of contact ratio outlined above will still be correct but, if a more accurate estimate of the mean film thickness is required, the asperity film thickness given by the calculation of section 4.6, multiplied by the area of contact ratio A , should be added to the mean film thickness from the valley film calculations.

Table 4.2 summarises the results of these calculations for the foil rolling case considered, giving the variation of the area of contact ratio and the film thicknesses with speed.

The traction can be estimated from the area of contact ratio and the mean film thicknesses under the valleys and under the contact regions knowing the oil's rheology by using equations 4.31 and 4.32. Traction curves have been calculated for aluminium foil rolling conditions using the measured oil properties of chapter 2, assuming that the friction under the contacts is still determined by the bulk properties of the lubricant. The effect of the non-Newtonian properties of the oil on the traction behaviour are included. Friction coefficients of between 0.002 and 0.05 were found for slip ratios of 0.3 with a rolling speed of 5m/s, depending on the pressure.

Where the friction on the contact areas is determined by boundary additive properties, the calculated area of contact ratios can be used to determine the contribution

from these regions given the shear properties of the additives. The contributions to friction from the asperity contacts was then found to vary between 0.007 for a pressure of 230MPa to 0.019 for a pressure of 1510MPa.

Table 4.1 Conditions of calculations and experiments.

The oil viscosity has been approximated by

$$\eta = \eta_0 \exp(\alpha p - \beta(T - T_0))$$

where T is the temperature, with a pressure viscosity coefficient by

$$\alpha = \alpha_0 + c_\alpha(T - T_0)$$

The oil density ρ given in the following table is assumed to be constant with temperature.

	Strip calculations	Thin foil calculations	Sheu's experiments	Experiments of chapter 5
η_0 (Ns/m ²)	1.915	1.0×10^{-3}	6.76	1.915
β (°C ⁻¹)	0.079	0.0139	0.106	0.079
α_0 (m ² /N)	3.29×10^{-8}	1.0×10^{-8}	3.48×10^{-8}	3.29×10^{-8}
c_α (m ² /N°C)	-	-	-0.033×10^{-8}	-0.027×10^{-8}
k (W/m °C)	0.125	0.125(assumed)	0.129	0.125
ρ (kg m ⁻³)	-	-	900	915
T_0 (°C)	20	60	25	20
T (°C)	20	60	22.6-24.4 (25)	18.6-21.8
R_0 (mm)	78.8-788 (78.8)	88.9	50.8	78.8
E'_R (GPa)	220	230	220	220
u_R (m/s)	0.003-1.0	1.0-30	0.05-0.5	0.014-0.92
t_1 (mm)	2.82-0.115 (0.70)	0.020	1.020	2.82-0.115
$(t_1 - t_2)/t_1$	0.0013-0.30 (0.17)	0.25	0.20-0.49 (0.20)	0.0013-0.30
d_0 (μm)	0-1.0 (1.0)	0.1	2.4-3.1 (3.0)	0.11-1.0
λ (μm)	7.5-525 (30)	15	60	30
σ_y (MPa)	10.6-200 (85)	230	119	10.6-200

Table 4.2 Film thicknesses and area of contact in foil rolling, $d_0 = 0.1\mu\text{m}$.

u_r m/s	Smooth contact			Rough contact				
	h_s μm	h_w μm	h_d μm	\bar{h}_v μm	h_a μm	\bar{h}_t μm	A	αq_v
30	0.237	0.323	0.294	0.217	—	—	0.01	—
10	0.097	0.108	0.136	0.110	0.031	0.088	0.28	0.64
5	0.055	0.054	0.084	0.079	0.018	0.047	0.53	0.38
3	0.036	0.032	0.059	0.062	0.013	0.028	0.69	0.24
1	0.014	0.011	0.027	0.042	0.006	0.010	0.88	0.08

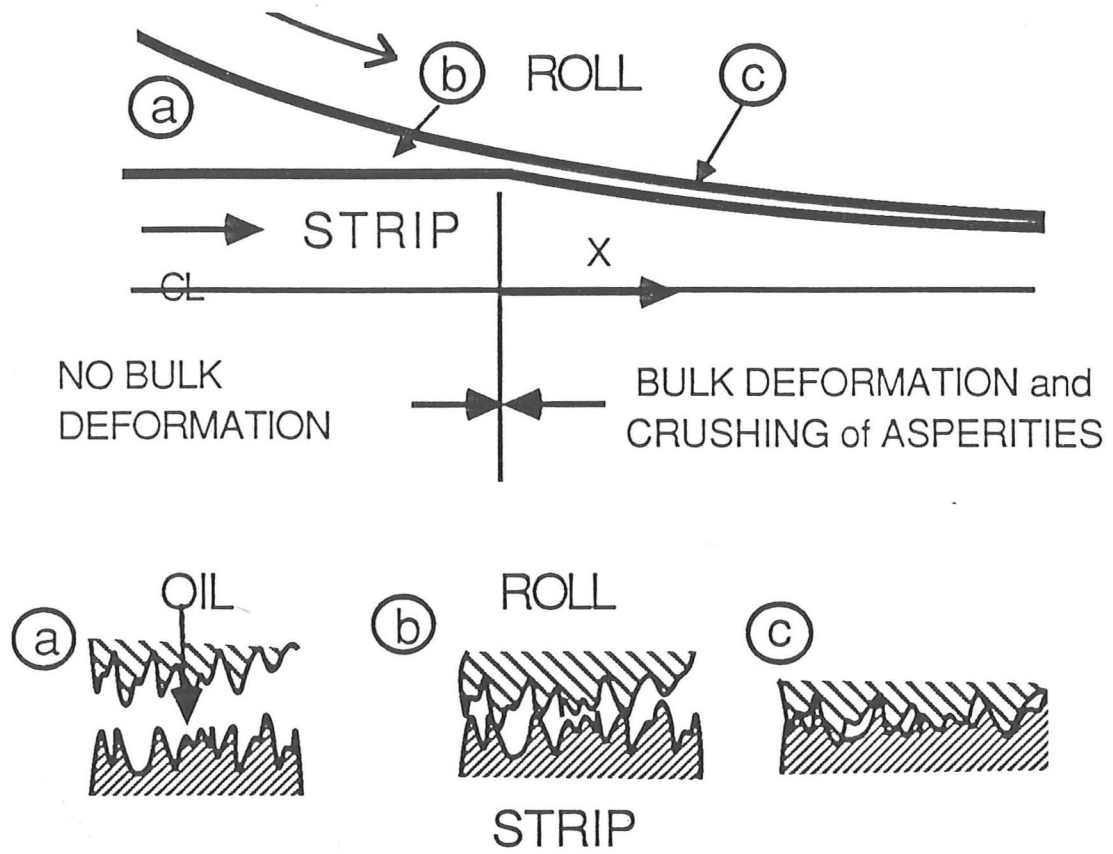


Figure 4.1 Schematic of rolling process
 a) Transverse section away from bite
 b) Near bulk deforming region
 c) In bulk deforming region.

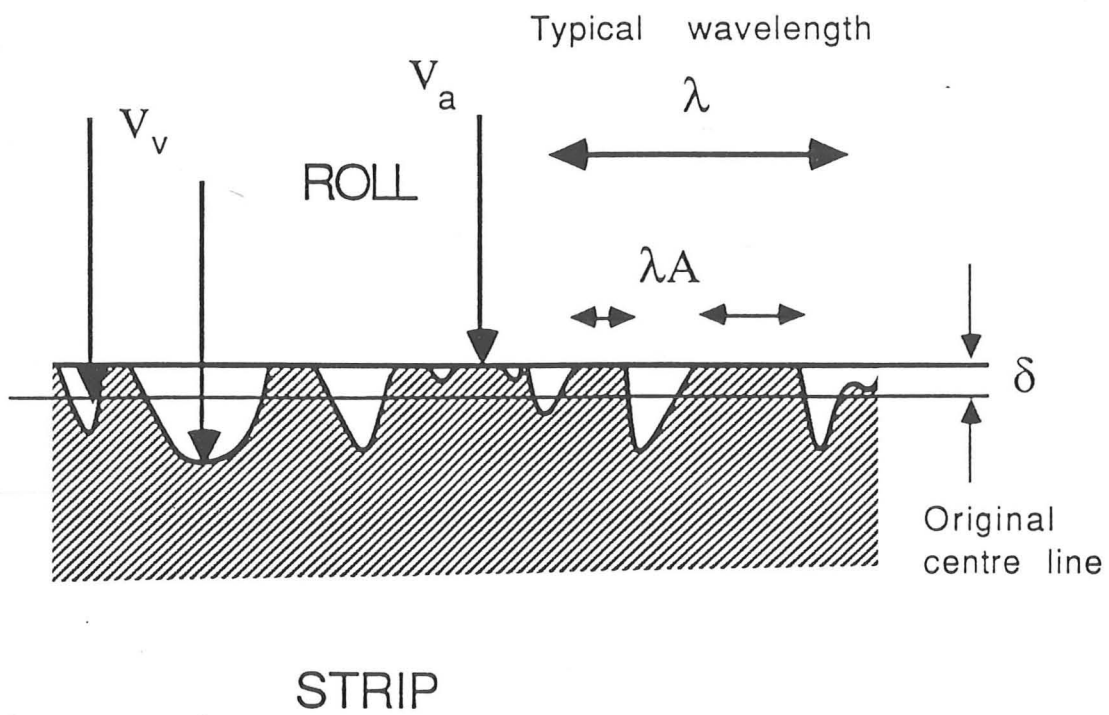
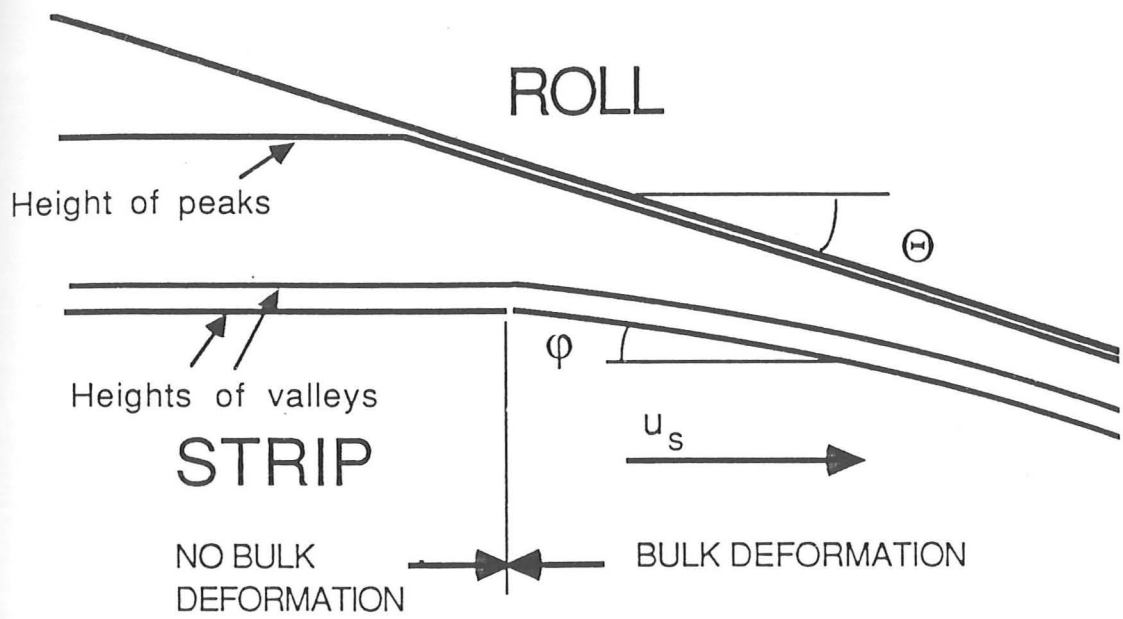


Figure 4.2 Details of the asperity geometry.

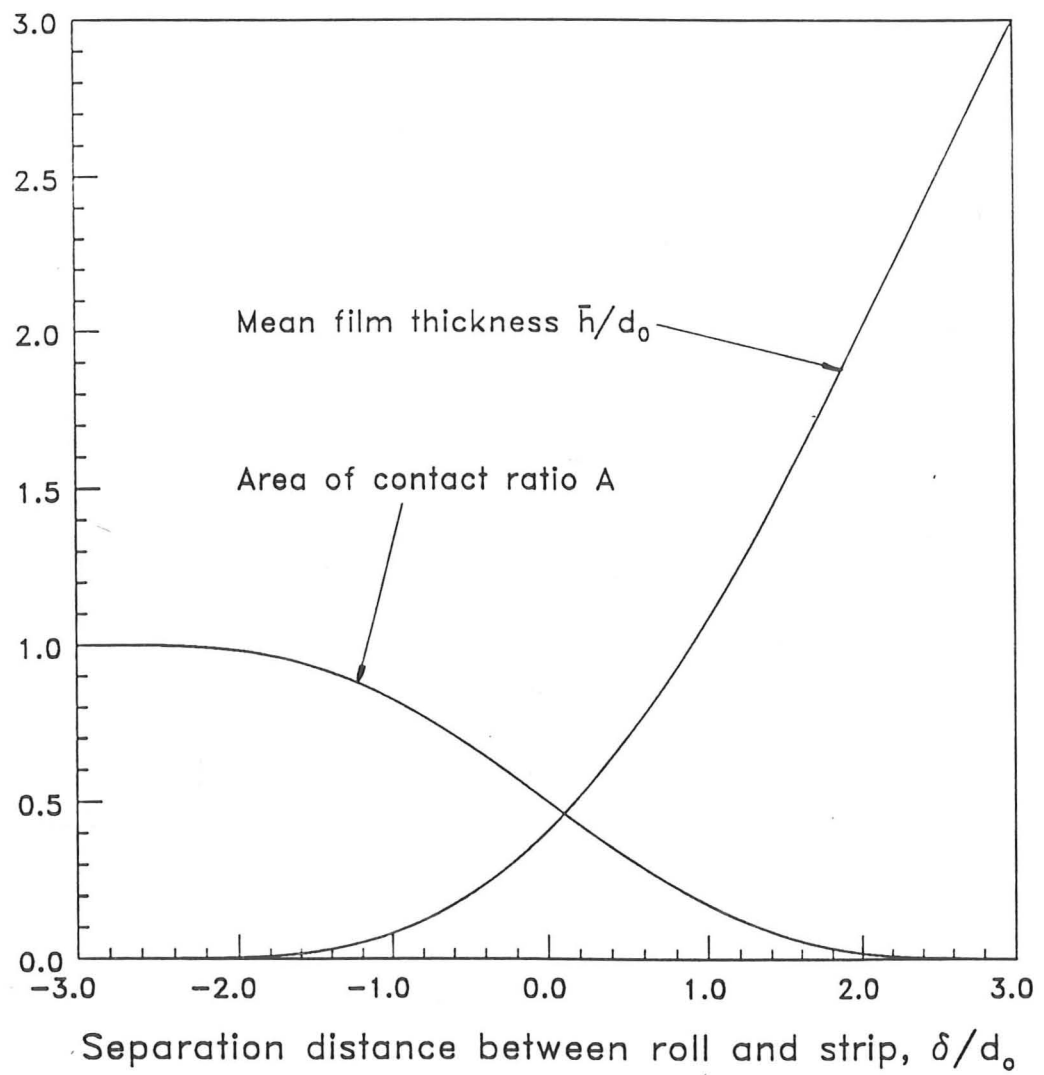
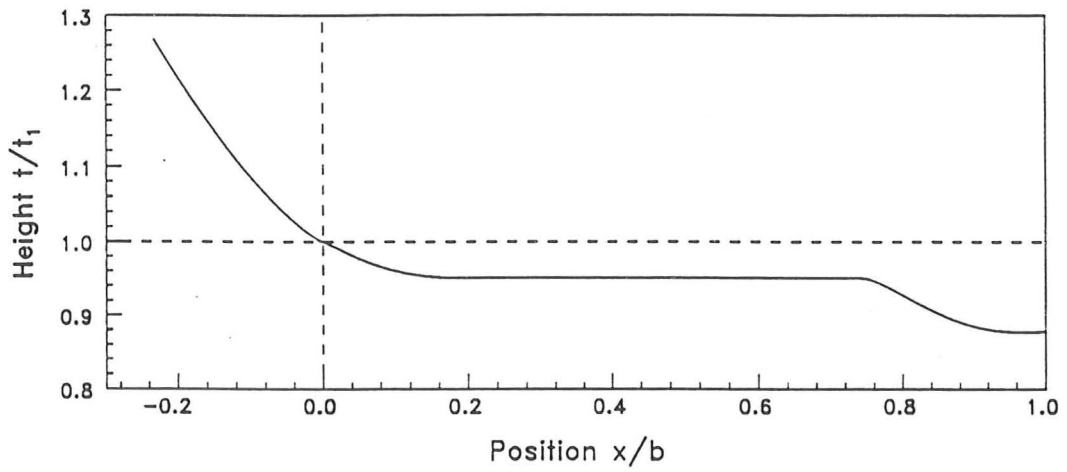


Figure 4.3 Area of contact ratio and mean film thickness for the polynomial roughness model.

a)



b)

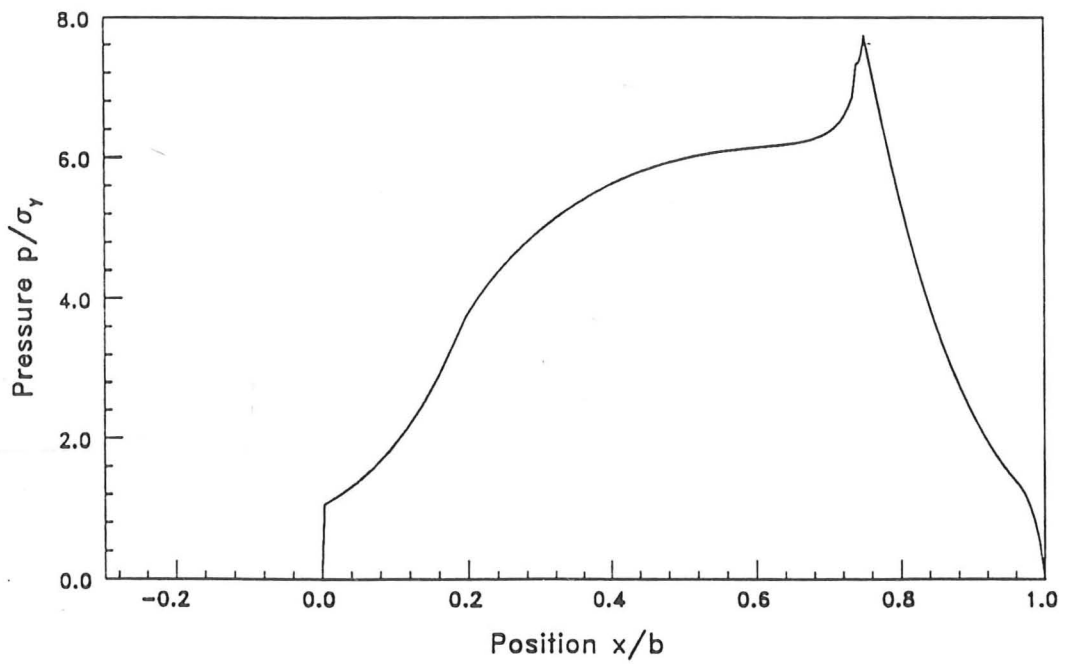


Figure 4.4 a) Roll shape
b) Pressure distribution for thin foil.

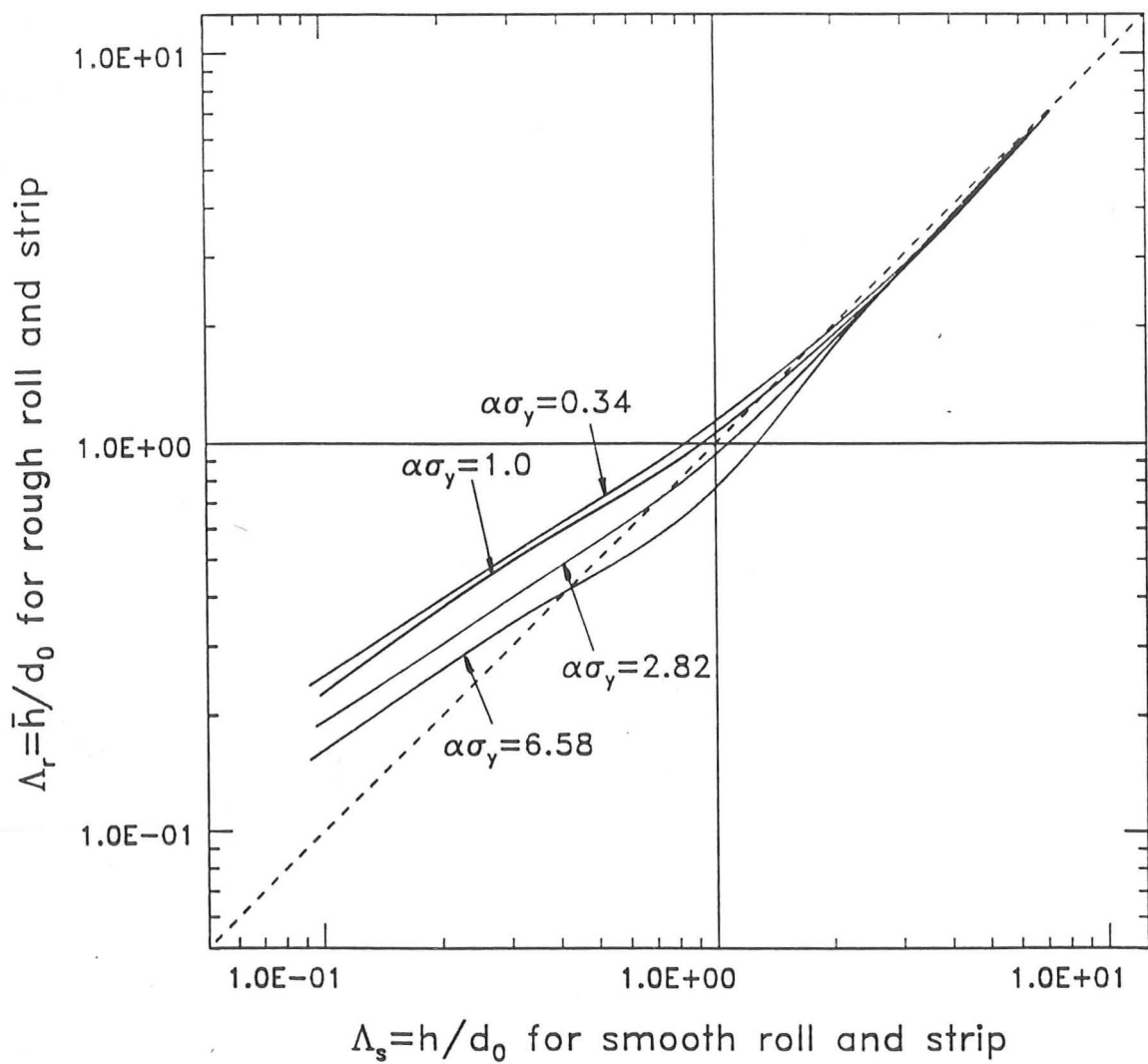
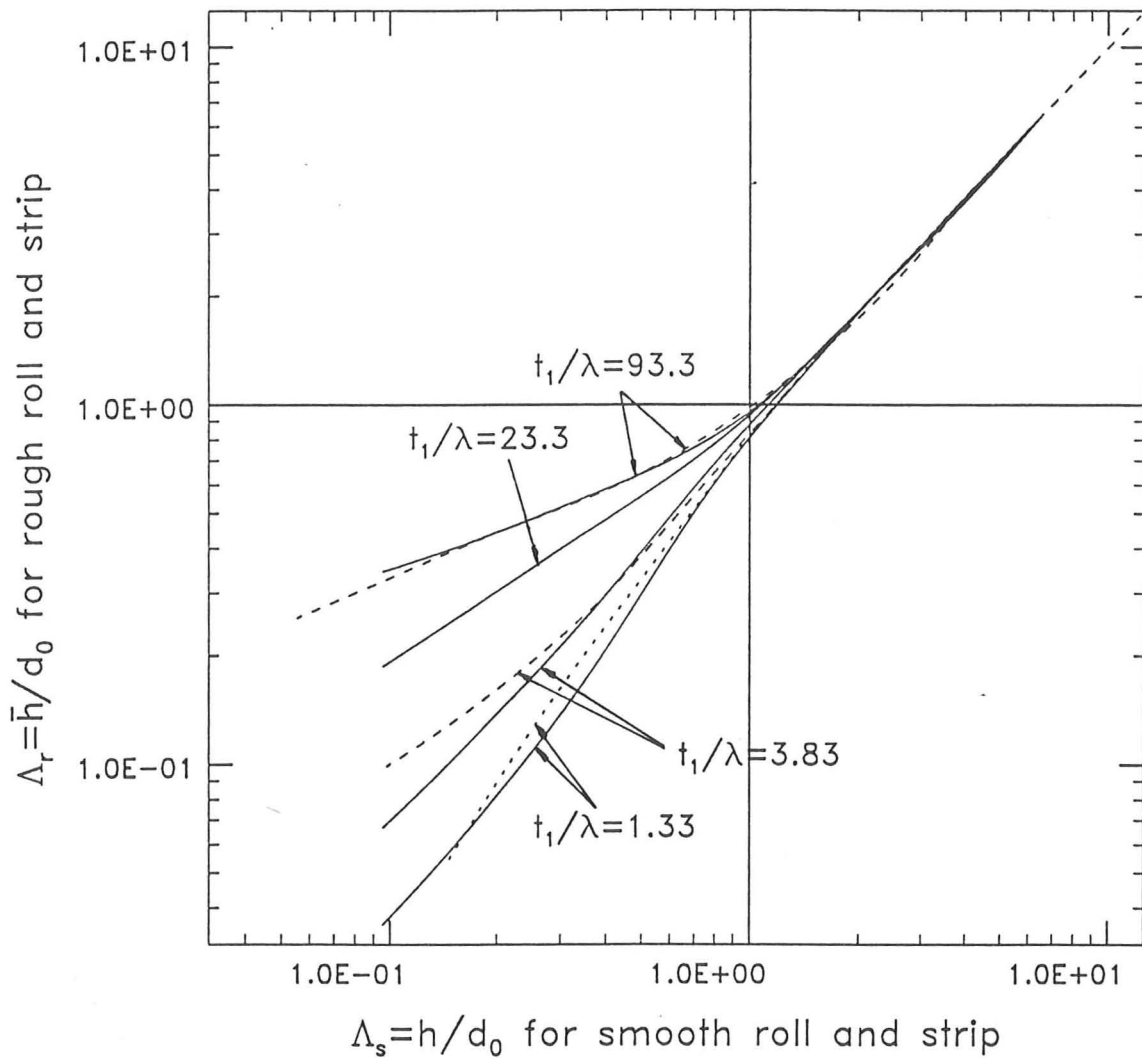


Figure 4.5 The effect of Δ_s and $\alpha\sigma_y$ on the rough film thickness ratio Δ_r .
 — $t_1/\lambda = 23.3$.



- KEY
- Fixed $\lambda = 30\mu\text{m}$ - varying t_1
 - Fixed $t_1 = 0.7\text{mm}$ - varying λ
 - Thin foil $t_1 = 0.02\text{mm}$, $\lambda = 15\mu\text{m}$

Figure 4.6 The effect of Δ_s and t_1/λ on the film thickness ratio Δ_r
 — $\alpha\sigma_y = 2.82$ (2.3 for thin foil).

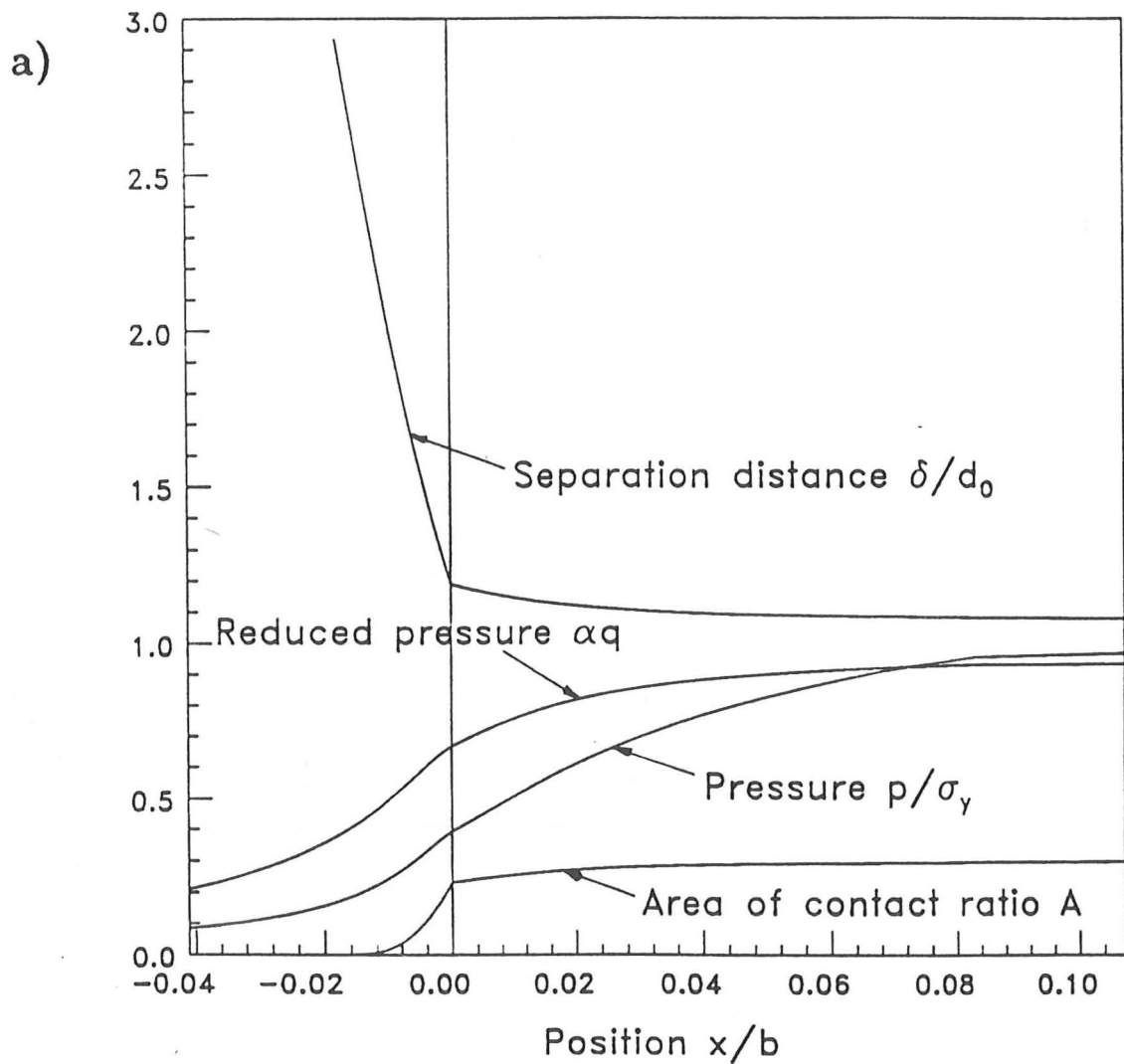
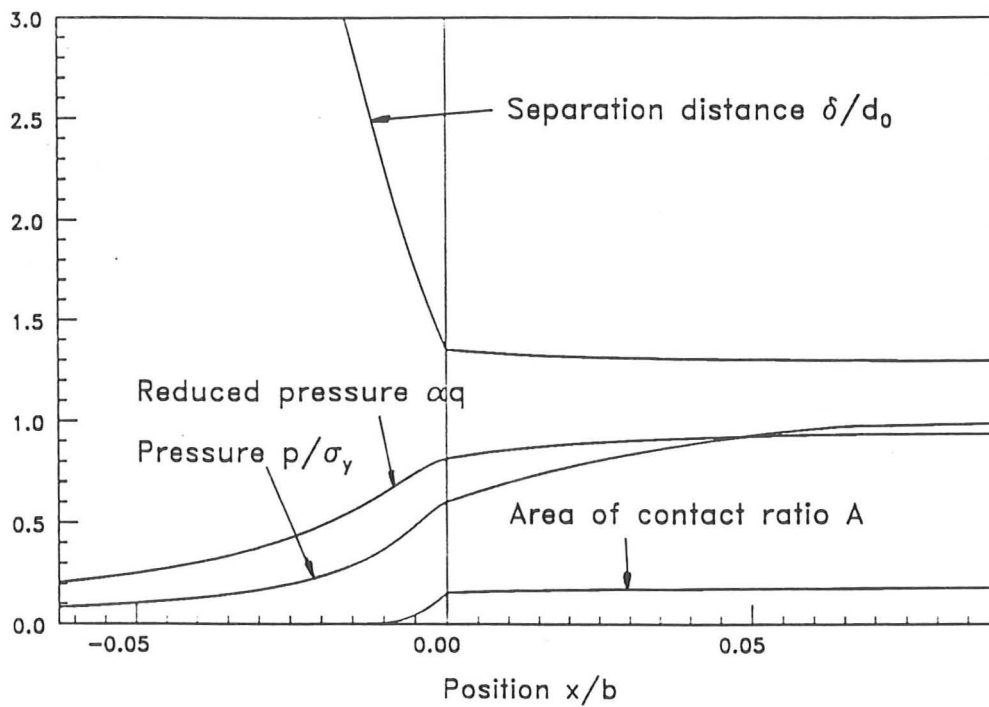


Figure 4.7 The variation of pressure, film thickness and area of contact ratio

a) $\Lambda = 0.8$, $\alpha\sigma_y = 2.82$, $t_1/\lambda = 23.3$

b)



c)

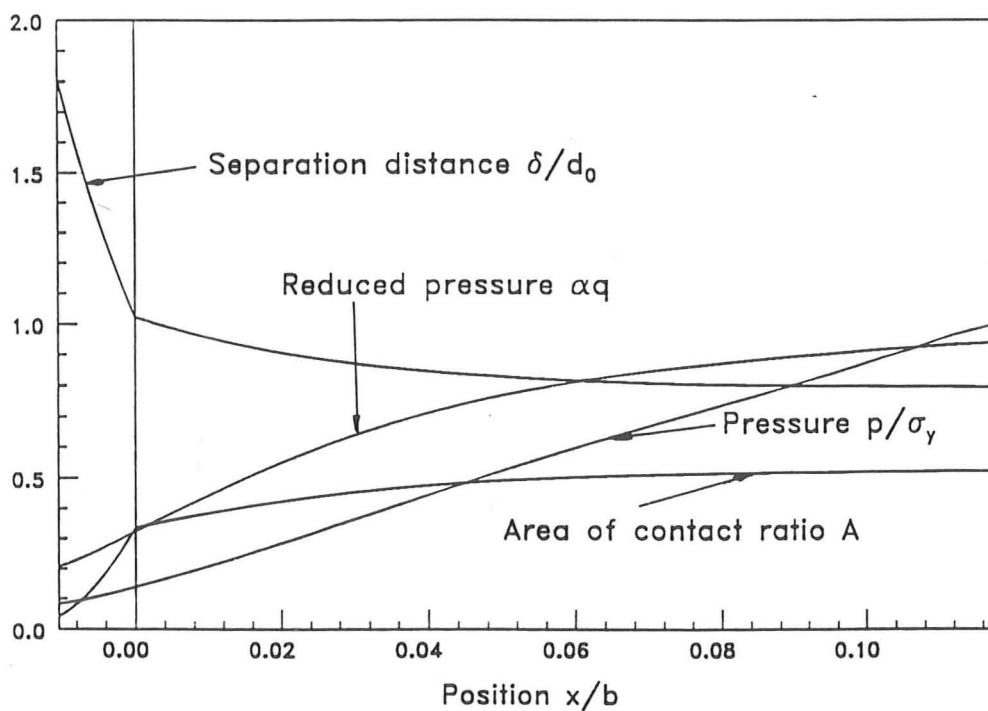
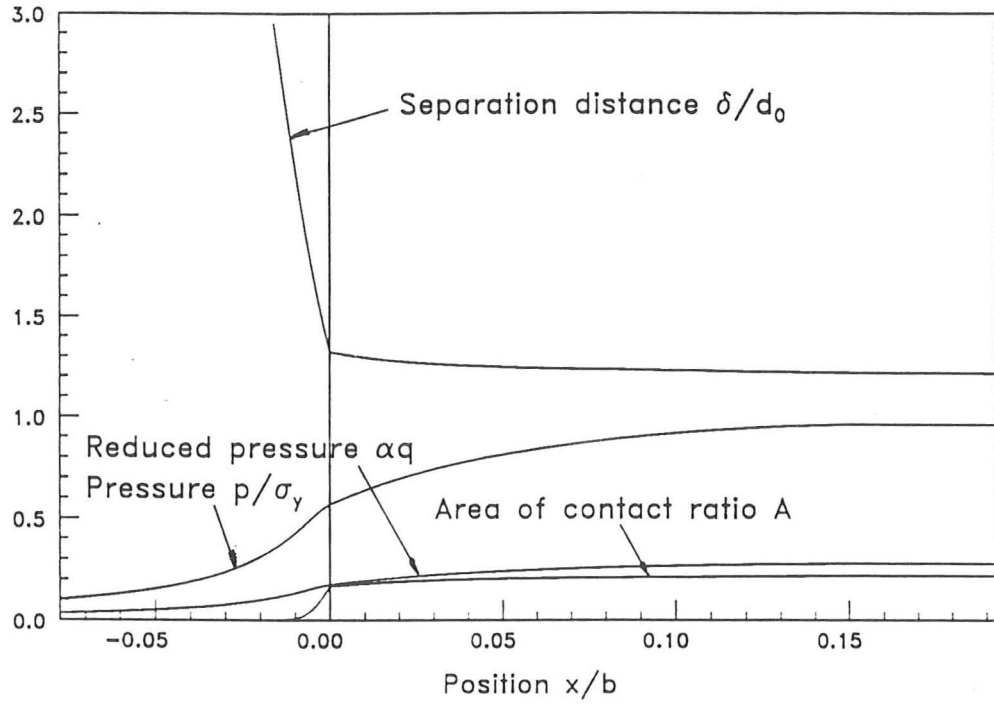


Figure 4.7 The variation of pressure, film thickness and area of contact ratio

b) $\Lambda = 1.2$, $\alpha\sigma_y = 2.82$, $t_1/\lambda = 23.3$

c) $\Lambda = 0.3$, $\alpha\sigma_y = 2.82$, $t_1/\lambda = 23.3$

d)



e)

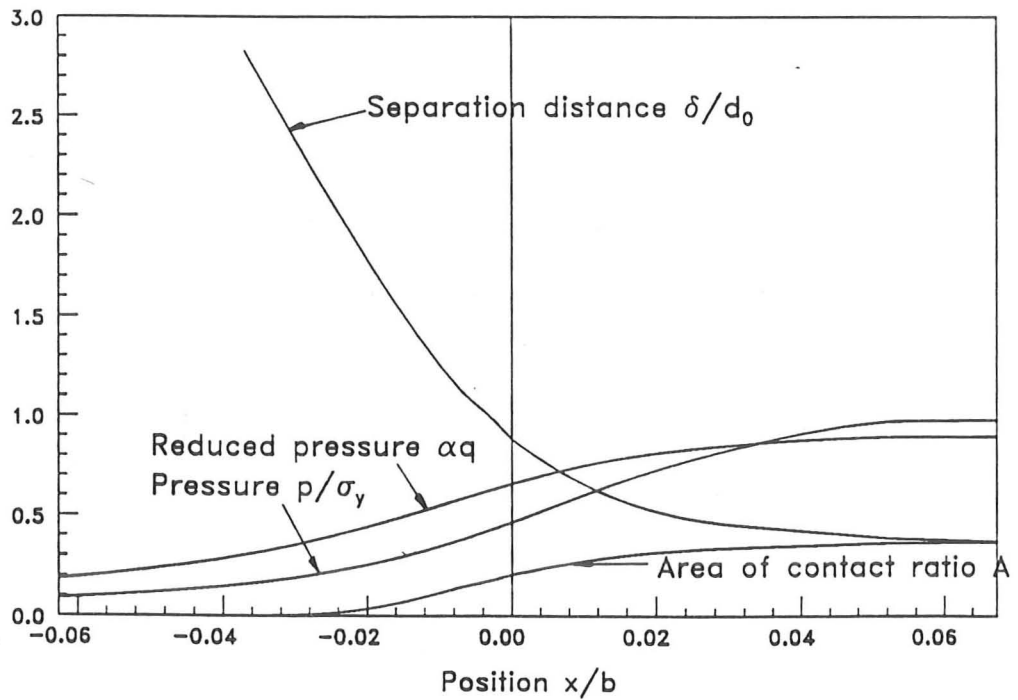


Figure 4.7 The variation of pressure, film thickness and area of contact ratio

d) $\Lambda = 0.8$, $\alpha\sigma_y = 0.34$, $t_1/\lambda = 23.3$

e) $\Lambda = 0.8$, $\alpha\sigma_y = 2.30$, $t_1/\lambda = 1.33$.

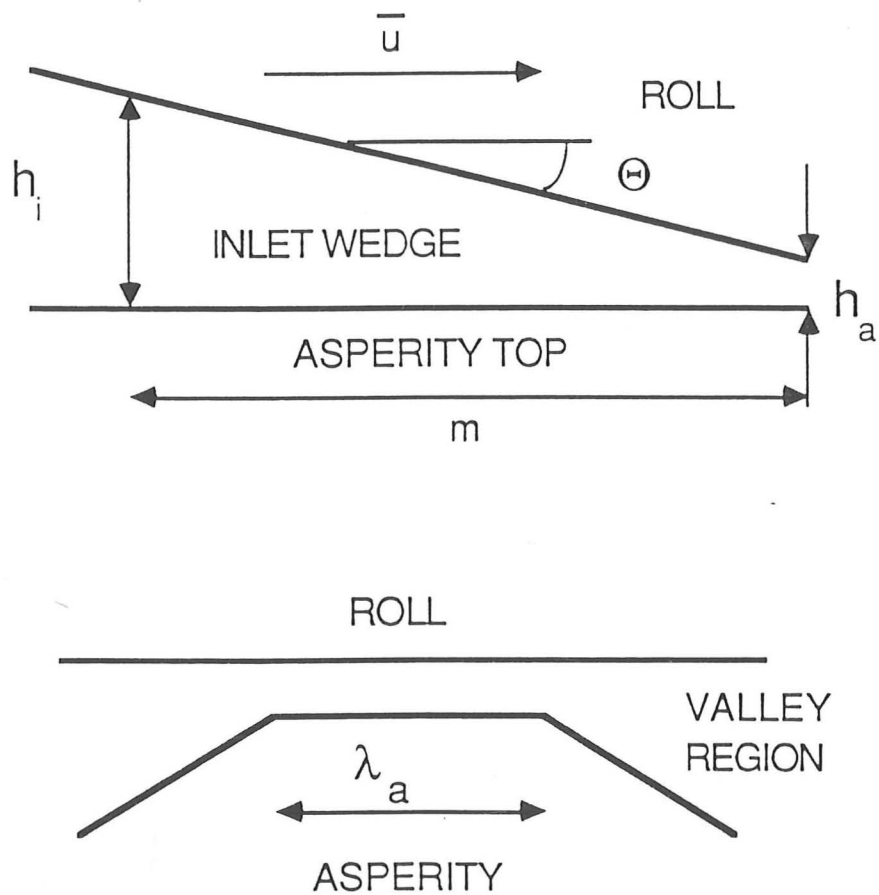
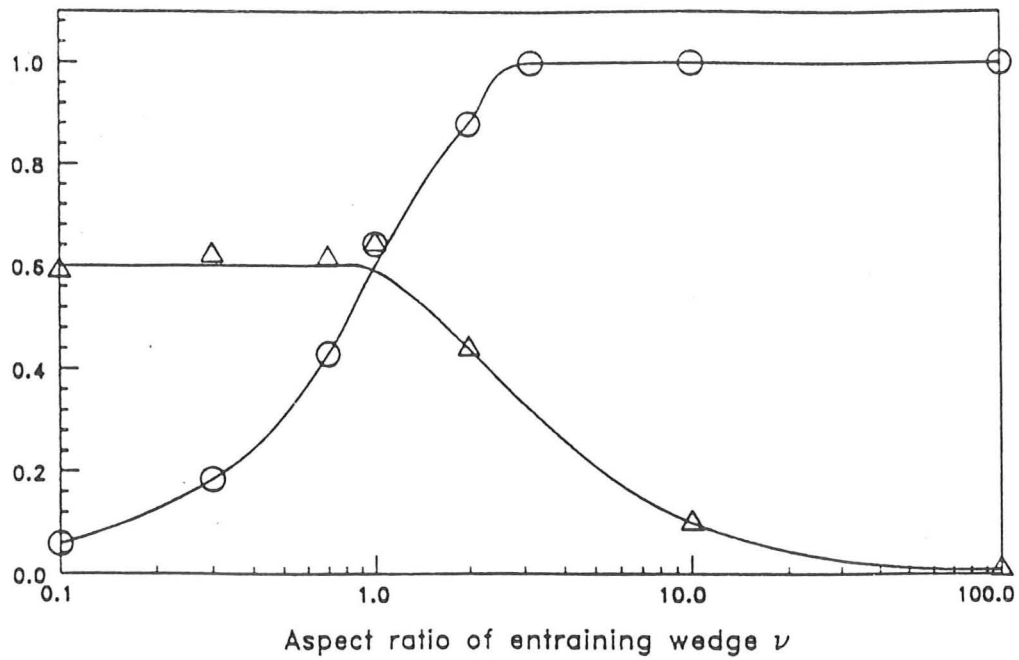


Figure 4.8 Geometry of asperities in the region of close contact.



- KEY**
- Ratio of reduced pressures with and without side leakage q/q_{ns}
 - △ Effective build up length m_e/λ_a

Figure 4.9 The effect of side leakage on the pressure build up.

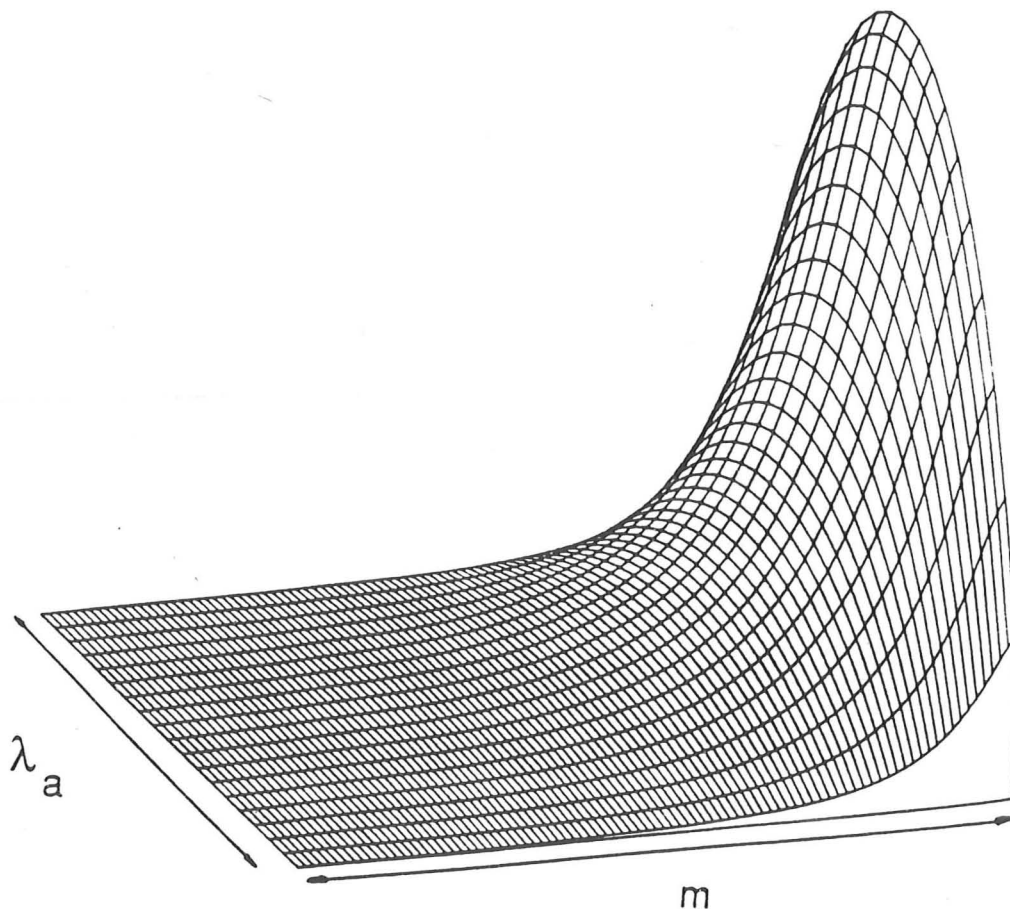


Figure 4.10 Reduced pressure distribution in entraining wedge with side leakage, $\nu = \lambda_a/m = 0.3$.

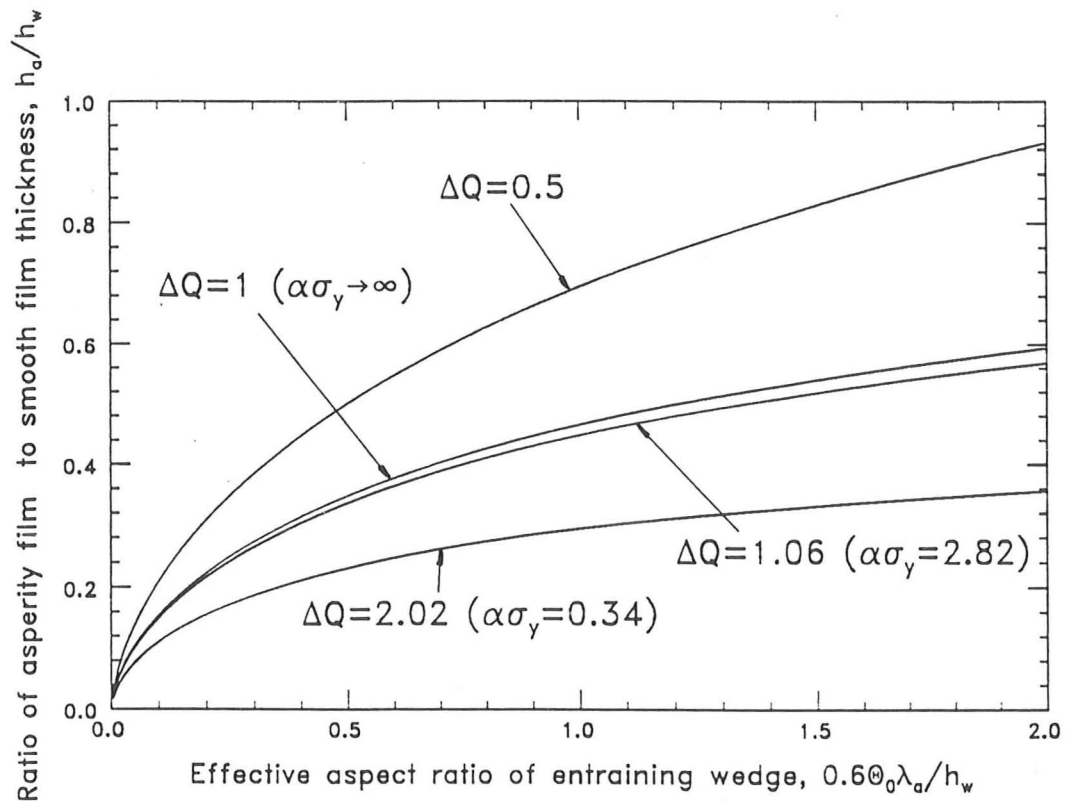


Figure 4.11 Film thicknesses under the asperity contacts.

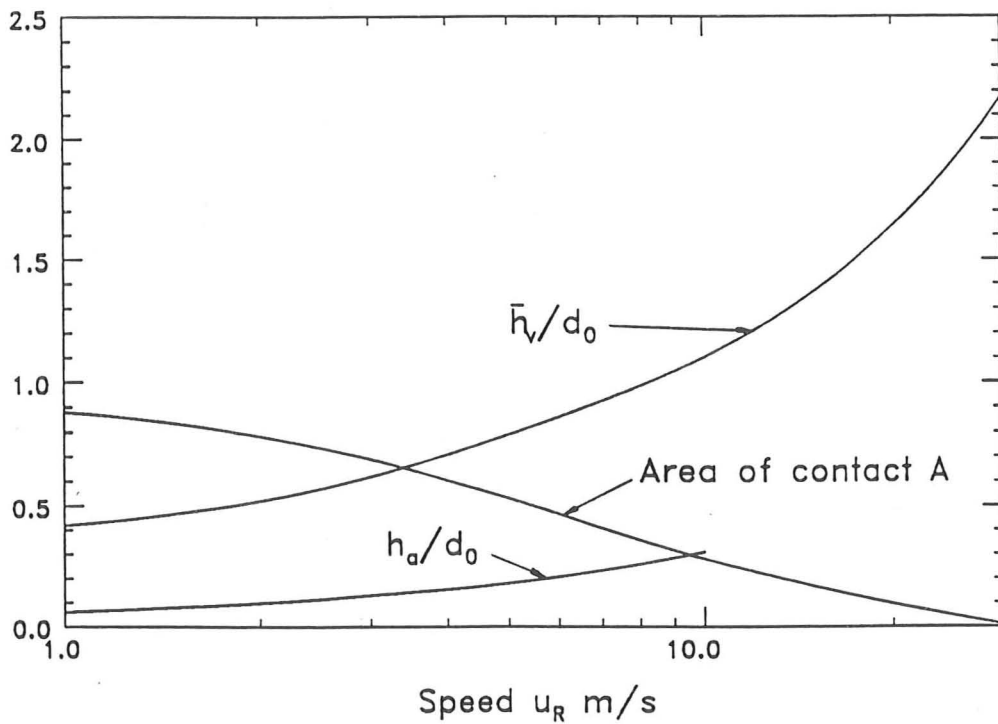
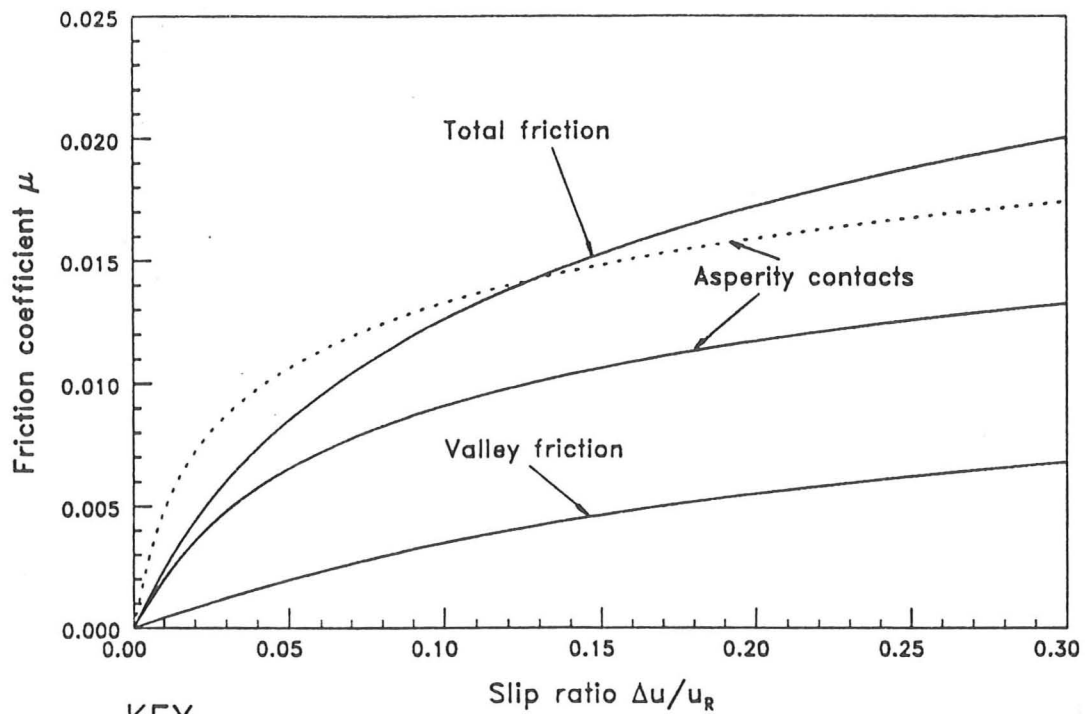


Figure 4.12 Film thicknesses and area of contact in foil rolling.



KEY

..... Effect of reducing h_a by $1/3$

Figure 4.13 Traction curve for foil rolling, $u_r = 5$ m/s, $p = 625$ MPa ($\eta = 0.87$ Pas, $\tau_0 = 4.5$ MPa).

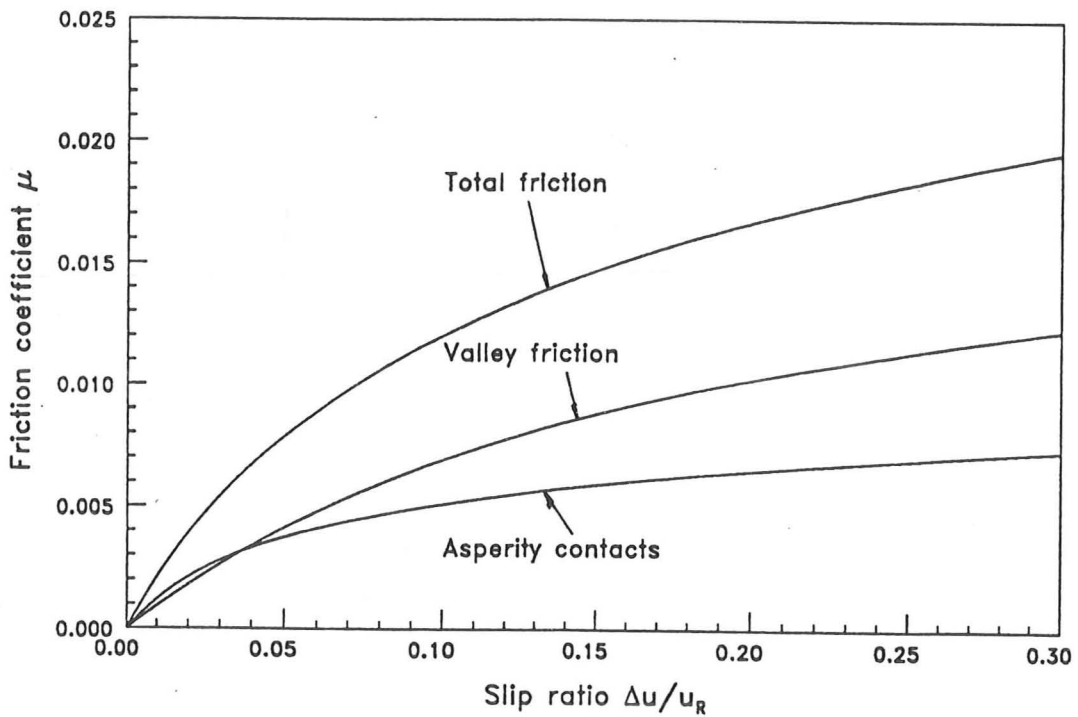


Figure 4.14 Traction curve for foil rolling, $u_r = 10$ m/s, $p = 625$ MPa ($\eta = 0.87$ Pas, $\tau_0 = 4.5$ MPa).

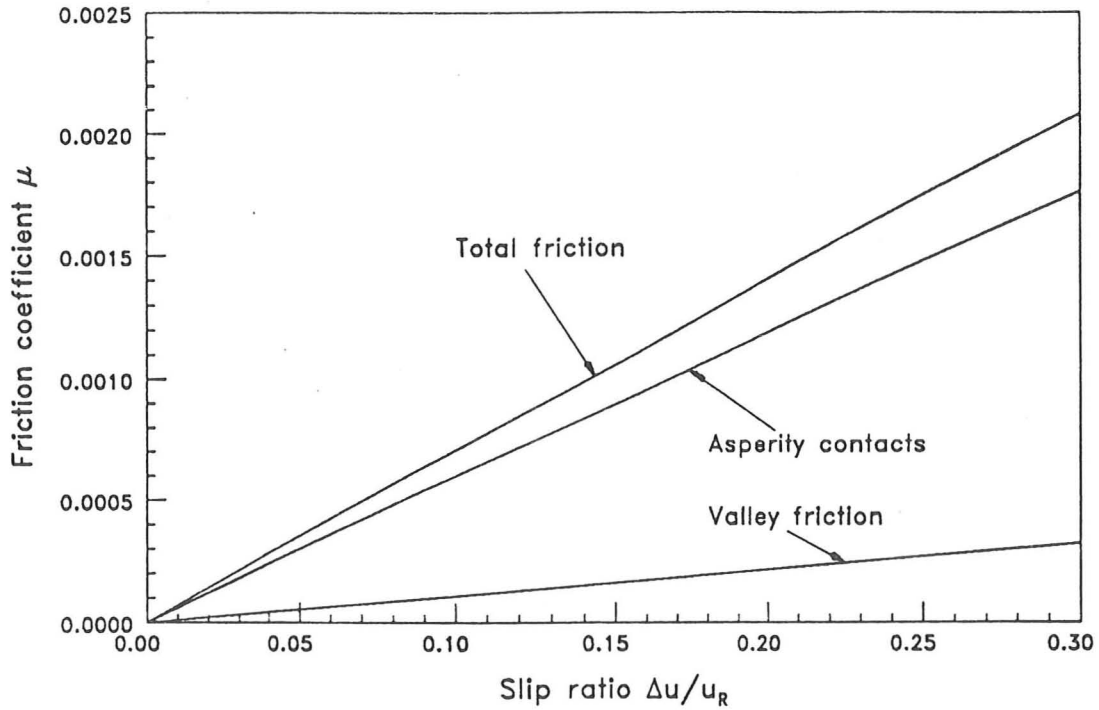


Figure 4.15 Traction curve for foil rolling, $u_r = 5$ m/s, $p = 230$ MPa ($\eta = 0.0094$ Pas, $\tau_0 = 2.0$ MPa).

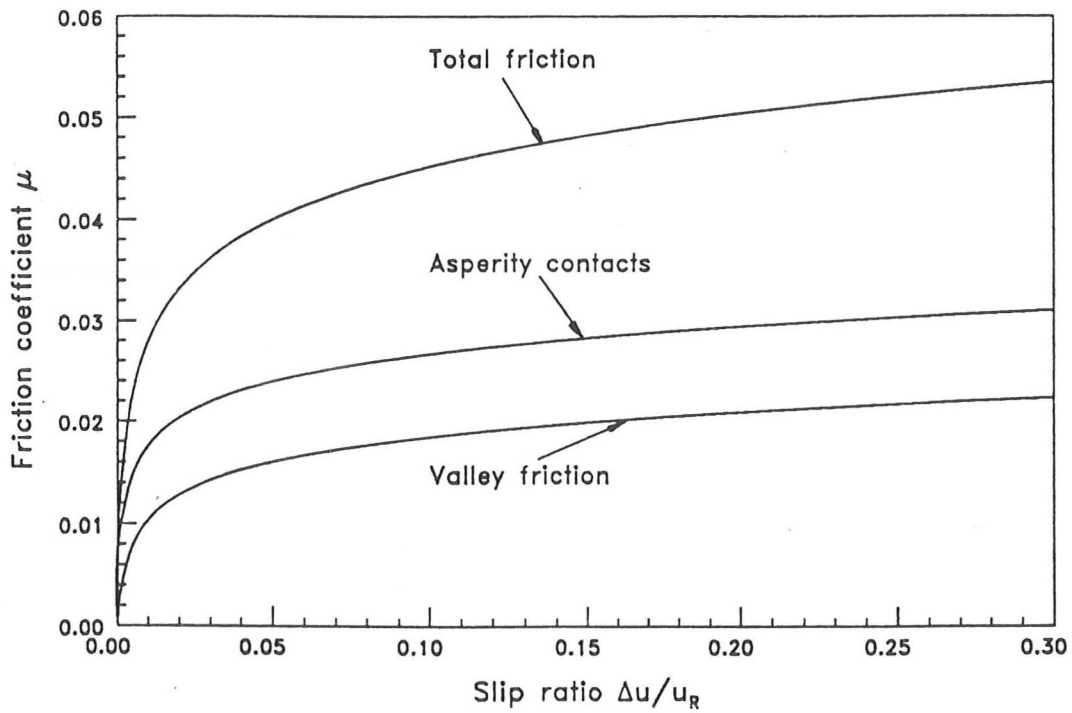


Figure 4.16 Traction curve for foil rolling, $u_r = 5$ m/s, $p = 1510$ MPa ($\eta = 167$ Pas, $\tau_0 = 11.35$ MPa).

EXPERIMENTAL MEASUREMENTS OF FILM THICKNESS IN ROLLING

Theoretical calculations of film thicknesses in rolling strip and foil have been described in chapter 4. This chapter describes a series of experiments to investigate the film thickness and area of contact on a laboratory rolling mill. The range of variables altered in the experiments has been chosen to cover a wide range of values of the groups found to be relevant from the theory.

5.1 Experimental setup

5.1.1 Rolling mill

The mill used was a two-high experimental mill driven by a variable speed motor. The roll diameter was 157.5mm and the roll width 178mm. The reductions in strip thickness taken were adjusted by varying the screw down on the roll support bearings. Rolls used in production processes are prepared by grinding, so the rolls used in the experiments were also ground to produce a similar circumferential finish. Two finishes were produced, a rough finish with a r.m.s. roughness of $0.70\mu\text{m}$ for a 'cut off' wavelength of 0.3mm and a smooth finish with a roughness of $0.08\mu\text{m}$.

5.1.2 Materials

To cover a wide range of conditions three materials were used; work-hardened 1200 alloy aluminium, 1200 alloy aluminium which was annealed and then rolled with a 5% reduction and lead. The stress-strain curves for the aluminium specimens, as measured in a plane stress tensile test, are given in figures 5.1a and b. The plane strain yield stresses, which was taken as 1.15 times the 0.2% proof stress in plane stress, were 85MPa and 200MPa for the soft and hard aluminium respectively. The plane strain yield stress of the lead was estimated from a tensile test as 10.3MPa. Creep of the lead can be neglected at the strain rates found in the rolling experiments.

By first rolling the specimens dry with a 5% reduction, the roughness of the rolls

was transferred to the strips. The resulting roughness of the strips before making film thickness measurements had either the smooth or the rough $0.7\mu\text{m}$ finish of each of the two roll finishes. This method of generating a roughness on the strip produced a very consistent finish, exhibiting the longitudinal ground finish found in production rolling and a consistent height distribution close to the assumed model of the roughness. Figure 5.3 shows the initial roughness profile and its corresponding height distribution. The auto-correlation length λ for the roughness transferred onto the strip was measured as $30\mu\text{m}$. Figure 5.14a is a micrograph of a rough specimen produced by this process. The small reduction had the additional advantage of producing a sharper yield point for the annealed aluminium. The initial thickness of the strips was between 2.8mm and 0.115mm.

The accuracy of the measurements is likely to be better with larger specimens, so most strips were fairly large, about 300mm long in the rolling direction and 60mm wide. However, with the thinner foils the differential conditions across the width of the contact, due to only part of the strip being lubricated in the experiments, made the rolling process very unstable so that the foil buckled grossly during rolling. In order to make any measurements with the foils, rather small pieces of foil were used (about $85 \times 20\text{mm}$). Although this increases errors in the measurements, by carefully considering all the causes of error, the effect of the strip size can be shown to have little effect on the oil films produced. A correction factor has been used for the effects considered.

5.1.3 Oil

The oil used in the experiments was HVI 650, a base mineral oil. Properties at higher pressures have been measured by Evans [30]. Additional measurements were made in a disc machine at a lower pressure of 127 MPa to determine the non-Newtonian behaviour of the oil here. A summary of its properties is given in table 4.1.

5.1.4 Experimental method

Two methods were used to measure the mean oil film thickness in rolling strip and thick foil. The first method is that described by Azushima[4]. Specimens were carefully cleaned with acetone and a small weighed drop of oil placed on the front of the strip. The accuracy required in weighing the oil drop (to within 0.05mg) made it necessary to use a balance with an enclosure to avoid draughts. The larger strips would not fit inside the enclosure, so the oil weight was deduced from the reduction in weight of the syringe from which the oil was dripped. For those foil specimens small enough to fit inside the balance, the oil weight (in these cases on the limit of accuracy of the balance) was checked from the increase in weight of the strip.

The rolls were cleaned carefully with acetone and the speed of the mill measured by counting the passage of reflective strips on the end of the roll shaft with an electronic counter. Roll speed could be adjusted with an electronic controller. It was assumed that, with the relatively small strips and the reductions taken and with the large inertia of the rolls, the speed of the rolls was constant as the strip was rolled. A contact thermocouple was used to measure the temperature of the rolls. The strip was then rolled and the area over which the oil spread out measured from a tracing of the patch with a planimeter. The area which the oil covers is clearly visible because the lubricated region has a different surface finish from the areas which were unlubricated. Figure 5.2 shows a typical oil patch (note the scale, marked in centimetres). The rolling direction is along the length of the strip.

An alternative estimate of the film thickness was obtained for those strips where the roughness of the strip was flattened by the smooth rolls. An analogue signal of the roughness was obtained from a profilometer and converted to a digital record using a data logger. The digital signal could then be processed with a computer. In order to eliminate the 'd.c.' signal from the trace the roughness was averaged using a moving average of 0.3 mm. Because the flattened distribution was skewed, this method of averaging did not produce the uniform flat top evident in the original signal. To recover this feature of the trace the signal was further averaged twice, including only the highest 20% of the roughness, since it is these features which define a true mean height. Figure 5.3 shows that this averaging process does not introduce any bias into the original symmetrical distribution of unflattened roughness.

The film thickness under the flattened tops of the asperities is assumed to be small and the position of the roll was taken as the height which had 99% of the roughness below it. The remaining 1% of the roughness above this point is due to the roughness of the roll. By summing the valley areas below the roll height the mean film thickness was determined. Figures 5.3 and 5.4 show an initial roughness trace and corresponding probability height distribution and the trace and height distribution for a flattened roughness. The position taken as the roll height for the flattened profile is marked in figure 5.4a. It can be seen that the valley height distributions are unchanged by the crushing, as assumed in the crushing theory, while the flattened areas produce a peak in the height distribution. The area of contact ratio may be estimated by the area of the probability height distribution above the height where the distribution has been affected by the crushing. This height is marked by a vertical line in figure 5.4b. For the profile of figure 5.4 the calculated mean film thickness is $0.46\mu\text{m}$ and the area of contact ratio is 0.23. This method of measurement was used both for some experiments where an excess of oil was smeared on the strip and for specimens used in the oil drop experiments. In the latter case traces from positions on the oil patch close to the front of the patch and near the end showed no significant difference in film thickness.

The reduction in strip thickness was either measured directly with a micrometer for the thicker strips, or found by measuring the change in length of the thinner strips. Spread of the strip will be negligible.

The mean oil film thickness on the strip including the areas of contact at the exit from the bite \bar{h}_e can be deduced knowing the oil drop weight and density and the area that it covered. To correct for the thinning of the oil film through the bite, it was assumed that the outlet strip speed was the same as that of the rolls. The inlet strip speed u_S is then found from the reduction in strip thickness.

$$u_S = u_R \frac{t_2}{t_1} \quad \{5.1\}$$

using the notation of chapter 4. This is likely to be near the actual case. The assumed position of the neutral point will not affect the comparison between theory and the experiments since this assumption is used in both the inferred experimental and theoretical films.

Considering continuity of the oil mass flow rate, the inlet mean film thickness \bar{h}

corresponding to the calculations in chapter 4 is

$$\bar{h}_e u_R = \bar{h}(u_S + u_R)/2 \quad \{5.2\}$$

and

$$\bar{h}_e/\bar{h} = \frac{1}{2} \left(1 + \frac{t_2}{t_1} \right) \quad \{5.3\}$$

5.1.5 Operating conditions

The general operating conditions in the experiments are given in table 4.1 and details of each of the measurements taken are given in tables 5.1a, b and c. Values of Λ_r given in these tables are based on the mean film thickness at the entry to the bite \bar{h} , which is related to the exit film thickness by equation 5.3. The experiments to investigate the effects of roughness were performed either with rough strip and rolls giving a combined roughness d_0 of $1.0\mu\text{m}$, or with smooth rolls and rough strip with a combined roughness of $0.7\mu\text{m}$. The reduction was generally between 8% and 15%, although some measurements had very small and large reductions. To investigate the way that the surface finish of the rolls was transferred to the strip, a series of experiments was done with smooth rolls and rough strip ($d_0 = 0.7\mu\text{m}$). The roll speed was changed so that Λ_s , the ratio of the smooth film thickness to the surface roughness, was varied from 0.22 to 23. Finally, because of differences between the expected film thicknesses at large Λ ratios and those found experimentally, some measurements were made with smooth strip and rolls ($d_0 = 0.11\mu\text{m}$), so that the effects of roughness could be neglected over the whole range of speeds used in the rough tests.

5.2 Experimental corrections to the film thickness

5.2.1 Effect of starvation on film thickness

In the theory of chapter 4 and in industrial rolling practice there is an excess of oil in the inlet but in the measurements using an oil drop, starvation of the inlet will occur because of the limited size of the oil drop. The film thickness in the experiments will be reduced since the pressure buildup starts closer to the bite than assumed. As the oil 'reservoir' in the inlet wedge is depleted during rolling this effect becomes more pronounced. Tsao and Wilson [100] investigate this effect for a straight inlet. However, in the experiments where starvation was significant, the effect of the roll curvature on

the inlet buildup was also significant. Walowit (see [100]) has calculated the effect of roll curvature on the oil buildup when fully lubricated. The following analysis combines these two effects and is similar in essence to these existing analyses.

The geometry of the inlet is assumed to be that of figure 4.1 where x is measured in the rolling direction from where the strip starts to deform in bulk. The front of the oil drop is at x_i . The smooth isothermal film thickness h_* is determined by the condition that the pressure at the end of the inlet is equal to the yield stress found by integrating the Reynolds equation

$$1 - e^{-\alpha\sigma_y} = 12\eta_0\bar{u}\alpha \int_{x_i}^0 \frac{h - h_*}{h^3} dx \quad \{5.4\}$$

$$h = h_* + \frac{(b - x)^2 - b^2}{2R} \quad \{5.5\}$$

When $x_i = -\infty$ this integral defines the ratio of the smooth film thickness $h_{*\infty}$ to that for a straight inlet h_w as a function of the group $h_w/(\theta_0 b)$. For isothermal rolling, this gives the effect of roll curvature on the difference between the smooth film thickness and Wilson and Walowit's film thickness h_w given in equation 4.20. This relationship is plotted in figure 5.5, which is essentially Walowit's result. With starvation the film thickness is also a function of x_i . If the volume of oil remaining at that stage is v , and the oil is spread out over a width w of the strip, v and x_i are related by

$$\frac{v}{w} = \int_{x_i}^0 h dx \quad \{5.6\}$$

If the initial drop size is v_0 , then the starved mean film thickness $\bar{h}_{st} = v_0/S$ of the resulting drop can be found by integrating the area S that the oil covers as the oil drop depletes.

$$\frac{v_0}{\bar{h}_{st}} = \int_{v_0}^0 \frac{1}{h_*} dv \quad \{5.7\}$$

The effect of oil starvation can be found by comparing this film thickness \bar{h}_{st} with the film thickness $h_{*\infty}$ found by taking the integration from $x = -\infty$. Assuming a constant width w , this ratio $\bar{h}_{st}/h_{*\infty}$ is a function of only two variables, namely the dimensionless roll curvature $h_w/(\theta_0 b)$ and the dimensionless oil drop volume $(v_0\theta_0/(h_{*\infty}^2 w))$ and is calculated here by a combination of exact and numerical integrations. This relationship is plotted in figure 5.6. The results correspond to those found by Tsao and Wilson when $h_w/(\theta_0 b)$ equals 0, but differ significantly from that curve for even quite small roll curvatures.

This calculation is for the isothermal Reynolds equation, but the results were used to apply a correction to the theoretical film thickness from the integration of the thermal Reynolds equation. The correction was applied to the theoretical smooth film thicknesses, so that the actual Λ and hence the effect of roughness on the film thicknesses would be the same in the experiments and the theory. In applying the correction the width of the oil drop w was taken as the maximum width of the oil patch. This overestimates the effect of starvation, since the width of the oil patch rapidly reduces at the end of the test, giving a longer pressure buildup than assumed in the end region where starvation is most important. The maximum starvation correction factor used for some of the lead foil experiments with large Λ ratios was 0.85, but generally this factor was greater than 0.95.

The values of Λ_s and h_s quoted in table 5.1 include this correction.

5.2.2 Effect of limited oil drop size on side leakage

The theoretical estimate of the film thickness assumes that there is no transverse pressure gradient across the contact. In fact, because of the limited width of the oil drop in the experiments, there will be some side leakage of oil. This will have the effect of reducing the oil pressure gradient in the entraining direction and hence the film thickness in the bite. Variation in film thickness across the bite will be determined by the shape of the oil drop meniscus in the inlet and by the side leakage of oil. As the oil is depleted the meniscus shape will change, producing the 'cigar-shaped' oil patch on the strip. Initially the width of the oil drop increases due to side flow of oil in the inlet, then, as the inlet reservoir of oil is depleted, the flow of oil out from the centre of the drop decreases and the oil at the edge of the drop is used up. This process and the ellipticity of the oil drop patch were found to depend on the rolling conditions.

The effect of the side leakage on the pressure rise is found from the two-dimensional Reynolds equation. This problem has already been investigated in chapter 4. Figure 4.8 shows how the pressure buildup is reduced with side leakage of the oil, as a function of ν , the ratio of effective length of the contact to the width. Here the length of the pressure buildup was taken as the distance for a straight inlet where the reduced pressure would have risen 15% of the final unstarved reduced pressure and the width was taken as $w/2$, half the maximum width of the contact patch. This will overestimate the effect of side

leakage. Points with values of ν less than 2.5 were rejected.

5.2.3 Effect of thick films on the contact arc length

Theoretical estimates of film thickness in chapter 4 assume that the film thickness is much less than the reduction in strip thickness to determine the shape of the inlet and the length of the contact arc. For smooth isothermal conditions the ratio of the film thickness to the reduction in strip thickness is $2h_{*\infty}/(t_1 - t_2)$. This is approximately double the parameter $h_w/(\theta_0 b)$. Where these groups are not small the hydrodynamic conditions in the outlet must also be considered. In order for the pressure to drop to ambient at the end of the contact, the strip finishes deforming before the line joining the centres of the rolls. The position where the strip starts to deform will also be further away from the centre of the rolls than the assumed contact length b from equation 4.17. For isothermal conditions, it is possible to combine an outlet analysis for rigid rolls originally given by Martin (see [51]) with the inlet analysis for curved rolls and smooth strip described in subsection 5.2.1.

The boundary condition that $dp/dx = p = 0$ at the exit point has been used, the oil pressure through the intermediate deforming region has been taken as equal to the yield stress of the strip and the strip speed has been taken as constant through the bite. The position at which the strip finishes deforming was altered until the boundary conditions in the inlet and outlet regions are both satisfied for a given value of $h_{*\infty}/(t_1 - t_2)$. Changes in the film thickness and the position where the strip first yields can then be assessed when $h_{*\infty}/(t_1 - t_2)$ can no longer be considered small. For $h_{*\infty}/(t_1 - t_2) = 0.1$, the solution is little changed, with a reduction in film thickness of less than 1%. The point at which the strip starts to deform is about 8% further from the centre lines of the rolls than the contact length b given by equation 4.17. When $h_{*\infty}/(t_1 - t_2) = 1.6$ the corresponding changes in film thickness and position at which the strip yields are 4% and 25%. As the values of $h_{*\infty}/(t_1 - t_2)$ are always below 0.65 and less than 0.2 for all but the foil specimens with large values of Λ , this effect can be neglected.

5.3 Film thickness measurements at large Λ ratios

Before presenting results for strips where Λ_s is small and roughness affects the film thicknesses, results where Λ_s is large will be considered. Even when the roughness was insignificant with $\Lambda_s > 5$, the smooth theory and experimental measurements were not in good agreement. The experimental film thicknesses from the smooth strip measurements and from the experiments with rough strip where $\Lambda_s > 5$, corrected for thinning in the bite, are given in figure 5.7 (the grouping of the smooth points in this plot is the same as the grouping in table 5.1c). The combined roughness of roll and strip was $0.11\mu\text{m}$ for the smooth experiments.

A number of hypotheses were considered to determine why this discrepancy between theory and experiments arises for thick films, since without this explanation it will be difficult to interpret the results for smaller Λ ratios. It is observed that the thick strip results are close to the theory, but the foil and lead results are well below the theoretical film thicknesses. In order to give the same inlet geometry as in the foil tests, some thick strip was used with a very small reduction ratio, but films were still close to the smooth theory. An indication of the repeatability of the measurements is given by the cluster of points with 0.435mm smooth strip and experimental film thicknesses around $4\mu\text{m}$, which all had very similar operating conditions. The main cause of errors were felt to be in weighing the smallest drops of oil and in measuring the strip and foil thicknesses or lengths.

To assess whether the effects of side leakage or starvation might have been underestimated, a number of repeat tests were performed with the same rolling conditions, but different oil drop sizes. Two oil drops, one large and one small enough to give large starvation corrections of up to 0.7 were applied on the front of the same strip, so that conditions were identical. These points are paired together in table 5.1c. There was found to be no significant difference between the measured film thicknesses with large oil drops and those with very small drops. Different values of h_s given for each pair in table 5.1c appear because different values of the starvation correction were applied to each point. Applying the correction tends to separate the two sets of the results with small and large drops, indicating that these large corrections overestimated the effect of starvation. The value of $h_{*\infty}/(t_1 - t_2)$ was greatest for these experiments, but there does not appear to be any correlation between the difference between theory and

experiment and the value of $h_{*\infty}/(t_1 - t_2)$. For example the 2.8mm strip with small reductions had values of $h_{*\infty}/(t_1 - t_2)$ up to 0.25 with no effect on the film thickness, while many of the results with large discrepancies had smaller values of $h_{*\infty}/(t_1 - t_2)$.

Turning to the experiments where the strip roughness was crushed by the smooth rolls, electron micrographs and profilometer traces of the roughness were taken at the sides and end of the oil patch. These showed that the regions with greater crushing and hence smaller film thicknesses where starvation or side leakage had affected the film thicknesses were small compared with the overall dimensions of the oil patch as shown in the micrograph of figure 5.14c.

Errors in estimating the inlet shape due to elasticity of the rolls or rounding of the strip at the inlet would be expected to increase the film thicknesses. Tsao and Wilson [100] find no evidence of rounding of the inlet in rolling experiments. Elastic deflections of the rolls would be insignificant for the lead specimens which still exhibit this discrepancy. The effects of shear heating in the inlet can be estimated using the thermal correction factor C_L equation 4.21. This factor was as small as 0.65 for some of the experiments — though both the 2.8mm strip with small reduction and the foil experiments have similar corrections. However, the correction for lead was negligible, so errors in estimating shear heating cannot account for the discrepancy either. The effect of the non-Newtonian properties of the oil in reducing the inlet pressure gradient was included in some theoretical calculations, but this also was not found to give any significant reductions in theoretical film thicknesses. The effect of any residual films left on the rolls would be greatest with smaller film thickness and become insignificant with the thickest experimental films.

An alternative suggestion for this reduction in experimental film thickness was investigated — that the different friction conditions on the top and bottom of the strip, because one side is lubricated with an oil drop and the other side is unlubricated, affect the inlet geometry. If the strip is deflected down in the inlet the effective angle between the strip and the roll will be increased, giving a smaller film thickness. In the limit the strip or foil will be forced to 'wrap round' onto the bottom roll. The inlet angle will then be doubled. Where curvature of the rolls is small this will give half the theoretical film thickness; where curvature is important the reduction in film thickness will be slightly less. The magnitude of the discrepancy measured is in good agreement

with this hypothesis. Moreover there is a good correlation between the flexibility of the strip and the difference between smooth theory and experiments. With the thick strip the measurements were in good agreement with theory, but for the foil and for the lead the differences were greatest, tending to the factor of half expected from the hypothesis but never greatly exceeding this error.

In order to test this hypothesis experimentally a further set of tests were performed with smooth strip at speeds which had given film thicknesses significantly below the theoretical values. Slow motion video recordings of the strip shape as it entered the bite showed that the assumption that it went in level was far from true. However it was not possible to see clearly the region of interest just a millimetre or so from the entry to the bite. The region further from the bite deflected both up and down with no correlation between the direction in which it deflected and whether the oil drop was on the top or bottom of the strip. It is interesting to note that the strip always curved at the exit towards the region with better lubrication.

Experiments were performed in which oil drops of roughly equal weight were put on both sides of the strip in an attempt to give a more symmetrical lubrication. The strip then went through the mill in a very unstable manner, flapping up and down rapidly as it went through the mill. The oil patch generated was irregular, with wide regions on one side mirrored by narrow regions on the other side. Additional experiments were done with an excess of oil on the surface which did not have the measured oil drop on it, in an attempt to give more even lubrication conditions in the area of the oil drop, but the rolling process was still unstable. Experimental film measurements in which both sides are lubricated were significantly higher than the corresponding tests with oil on just one surface, although the results showed quite a lot of scatter. The ellipticity of the oil patch depended on whether the resulting oil drop was thick or relatively thin, suggesting that the scatter in films measured was due to differences in the way that the strip went through the mill, rather than in errors in measurement. Although the theoretical film thickness was only occasionally attained in these experiments with lubrication on both sides, it is unsurprising that the smooth steady Reynolds equation does not agree well with the average films found from a very unsteady process with quite extreme side leakages. However, the experiments demonstrate the effect that a change in the lubrication conditions can have on the way that the strip enters the bite. The increase in experimental films found lends support to the suggestion that it is the

difference in friction between the top and bottom of the strip which is reducing the experimental films below those calculated by integrating the Reynolds equation.

5.4 Film thicknesses with rough contacts

To check the oil drop and the valley integration methods of determining film thicknesses with rough contacts, both methods were used on a number of strips. When the film thickness is much more than the roughness the asperities will not be crushed and the valley film measurement will give a film thickness equal to $2.15d_0$ for the roughness height distribution assumed, although the actual film thickness may be greater than this. The results of these measurements are shown in figure 5.8. There is good agreement between the two methods of measuring film thicknesses when the roughness is significantly crushed for $\Lambda_s < 1.5$. This confirms that the film thickness under the asperity tops is not affecting the oil drop measurements, since if it were significant, the valley integration method would underestimate the films and would give smaller films than the oil drop measurements. The theoretical asperity films from the analysis of section 4.6 would be expected to increase the average film thickness by up to 20% for the smallest Λ ratios for the strips with the smallest inlet angle θ_0 , but would generally not be expected to make a significant contribution to the mean film thickness.

Those traces with significant crushing were included in the film thickness results if an oil drop measurement was not taken. These results would not be affected by starvation or side leakage of oil, since an excess of oil was applied.

Results have been split into nine distinct groups, to differentiate the two influences, yield stress and strip thickness, which are found theoretically to influence the crushing process. The strip thicknesses will be classed according to their inlet thicknesses as thick (2.8 mm), medium (0.9 – 0.64mm) and foil (180 – 115 μ m). The three materials used were hard and soft aluminium and lead. Results are presented in figures 5.9, 5.10 and 5.11 to cover the three strip thicknesses and are subdivided in the plots by yield strength. The smooth film thickness in Λ_s has been calculated using the method of chapter 4. The rough film thickness in Λ_r is the mean film thickness including the 'contact' areas, corrected for thinning in the bite using equation 5.3. Theoretical relationships between the smooth and rough Λ ratios for soft aluminium are included on the plots for inlet thicknesses of 2.82, 0.70 and 0.115mm. The effect of the different

yield stresses on the theoretical film thickness relationship can be judged from figure 4.5, which was calculated for the medium strip thickness. The values of $\alpha\sigma_y$ of 0.34, 2.82 and 6.58 correspond to lead, soft and hard aluminium respectively.

In order to show how the 'wrap round' hypothesis, in which the strip is supposed to be forced onto the unlubricated roll, would change the theoretical films, this assumption was included in a set of calculations for the soft aluminium. The influence of the wrap round is shown on figure 5.10. The films are reduced by a factor of about 2 at high Λ ratios, but are unchanged for small Λ where the film thickness is largely determined in the bulk deforming region.

Further experimental results have been deduced from the raw data given by Sheu in his thesis, in which he measured experimental films using the oil drop technique in a regime where roughness was important. The conditions of his experiments are given in table 4.1. The initial thickness of Sheu's specimens, which were of work hardened aluminium, was 1.02mm and the final strip thicknesses were between 0.816mm and 0.525mm. It appears that the roughness was somewhat longitudinal in structure, but Sheu does not give details of the length scale of the roughness. The roughness was prepared by 'hand lapping' and a value of $60\mu\text{m}$ was chosen for the theory to represent a possible length scale. There is also some indication in his computer listing that this was the value that he used. The smooth and experimental Λ ratios has been calculated here in an identical way to that used in the experiments described on this chapter. The results of these calculations are given in figure 5.12¹. The scatter in the experimental measurements at the largest Λ ratios makes it difficult to draw conclusions for thick films. Thermal effects are quite large here — the straight inlet thermal correction C_L is 0.56 for the two points with highest Λ ratios. However the reduction in films for $1 < \Lambda < 2$ is significant and could be explained by the deflection of the 1.02mm strip in the inlet due to the uneven lubrication. This explanation has been proposed to account for similar reductions in film thickness at large Λ ratios with a strip thickness of 0.7mm. The theoretical film thickness found from chapter 4 appropriate to Sheu's conditions is included in figure 5.12, along with Sheu's theoretical calculations.

¹ This plot differs from that given in Sheu's thesis both because of the slightly different methods used for calculating the smooth film thickness (up to a 10% difference) and because Sheu uses inaccurate values of the pressure and temperature viscosity coefficients for the oil in his thesis.

yield stresses on the theoretical film thickness relationship can be judged from figure 4.5, which was calculated for the medium strip thickness. The values of $\alpha\sigma_y$ of 0.34, 2.82 and 6.58 correspond to lead, soft and hard aluminium respectively.

In order to show how the 'wrap round' hypothesis, in which the strip is supposed to be forced onto the unlubricated roll, would change the theoretical films, this assumption was included in a set of calculations for the soft aluminium. The influence of the wrap round is shown on figure 5.10. The films are reduced by a factor of about 2 at high Λ ratios, but are unchanged for small Λ where the film thickness is largely determined in the bulk deforming region.

Further experimental results have been deduced from the raw data given by Sheu in his thesis, in which he measured experimental films using the oil drop technique in a regime where roughness was important. The conditions of his experiments are given in table 4.1. The initial thickness of Sheu's specimens, which were of work hardened aluminium, was 1.02mm and the final strip thicknesses were between 0.816mm and 0.525mm. It appears that the roughness was somewhat longitudinal in structure, but Sheu does not give details of the length scale of the roughness. The roughness was prepared by 'hand lapping' and a value of $60\mu\text{m}$ was chosen for the theory to represent a possible length scale. There is also some indication in his computer listing that this was the value that he used. The smooth and experimental Λ ratios has been calculated here in an identical way to that used in the experiments described on this chapter. The results of these calculations are given in figure 5.12¹. The scatter in the experimental measurements at the largest Λ ratios makes it difficult to draw conclusions for thick films. Thermal effects are quite large here — the straight inlet thermal correction C_L is 0.56 for the two points with highest Λ ratios. However the reduction in films for $1 < \Lambda < 2$ is significant and could be explained by the deflection of the 1.02mm strip in the inlet due to the uneven lubrication. This explanation has been proposed to account for similar reductions in film thickness at large Λ ratios with a strip thickness of 0.7mm. The theoretical film thickness found from chapter 4 appropriate to Sheu's conditions is included in figure 5.12, along with Sheu's theoretical calculations.

1 This plot differs from that given in Sheu's thesis both because of the slightly different methods used for calculating the smooth film thickness (up to a 10% difference) and because Sheu uses inaccurate values of the pressure and temperature viscosity coefficients for the oil in his thesis.

5.5 Results

The theory of chapter 4 shows that, of the variables that have been altered in the experiments, changes in the relationship between the rough and smooth Λ ratios can be expected with differences in strip thickness or yield stress, but the results should not be altered by the actual reduction or roughness amplitude. No difference in film thicknesses with the 0.7 and 1.0 μm roughnesses was observed, and these measurements have been grouped together in the results. This is also true for the small differences in reduction taken for the different tests in each group of results. Although a few measurements were done with reductions rather different from the normal 8–15% these were mostly in the thick film regime where the effect of the crushing process on the film thickness is not important. The experiments of Sheu with different reductions do not, however, show significant differences in film thicknesses even at small values of Λ .

Despite the scatter in the results, the experiments give reasonable agreement with the theory. At large Λ ratios, the difference between smooth theory and experiments has been attributed to the wrap round of the strip around the unlubricated roll. If this wrap round hypothesis is correct, then the results for $\Lambda < 1$ should be uninfluenced by this effect and a direct comparison can be made between the different strip thicknesses and the theory. As shown from the theory, the relationships between Λ_s and Λ_r then begin to diverge, depending on the parameters t_1/λ and $\alpha\sigma_y$. The effect of t_1/λ in changing the film thickness is as expected from the theory, with smaller films for the foils than for the medium thickness strips at the same Λ ratio. The correspondingly thicker films expected for large strip thicknesses are not apparent from the one experimental point in this regime. More points would be needed to draw any conclusions from the thick strip measurements at the smallest values of Λ . The theoretical influence of $\alpha\sigma_y$ is not very great. Experiments with the medium strip thickness (figure 5.10) do show a difference between the results for soft and hard aluminium at lower values of Λ_s , but this difference may easily be due to experimental scatter.

Results have been presented in terms of film thicknesses so far, but the friction characteristics in the bite will depend on the area of contact ratio. For those experiments in which the roughness was crushed by the smooth rolls, the area of contact ratio was estimated directly from the profiles. By using the theoretical relationship between mean film thickness and area of contact ratio for the assumed roughness distribution

given by figure 4.3 a theoretical area of contact ratio corresponding to the measured film thickness could also be derived. The results of these two area of contact ratio estimates are plotted in figure 5.13. Agreement between these two estimates of area of contact ratio is satisfactory.

Electron micrographs of the flattened surfaces showed the smooth areas flattened by the roll and the intervening valleys. With the aluminium specimens, the valley roughness became pitted as the differences in the grains allowed inhomogeneous deformation. The areas of contact are restrained by the roll, so that roughening is inhibited there. With the lead specimens, the appearance of the roughness was rather different. Large scale features dominated the surface appearance and it was not easy to make out the flattened and valley areas from the micrographs. The roughness traces demonstrated that the length scale of the valley roughness had increased, but also showed that there was a flattened area on the tops of the asperities. Figures 5.14a, b and c are three micrographs of the initial roughness, a flattened aluminium strip roughness and a flattened lead strip roughness. The edge of the oil patch, where the smooth roll roughness has been transferred to the strip, can be seen in figure 5.14b showing the extent of the region near the edge where the crushing has been affected by the edge conditions.

5.6 Conclusions

It was found that the experiments did not give good agreement with an existing theory when the effects of roughness were not important. After careful consideration of the various factors which could cause this discrepancy, it was concluded that the differential friction conditions on the two sides of the strip were causing the strip to enter the bite unlevel. This discrepancy was most marked for the foil and flexible lead strip and was not observed for the thick rigid strip. Experiments in which the friction conditions on both surfaces were altered supported this hypotheses, although the results of these measurements had a good deal of scatter because the entry of the strip into the bite was then very unstable.

This uneven lubrication is, of course, an artifact of the experiment and would not occur normally in industry. However it is interesting to speculate on whether the foil rolling process, in which the strip is very flexible, may be stabilised by the application

of tension to the foil to avoid this problem. A 'herringbone' pattern on the surface of the foil, similar to that found in industrial aluminium foil rolling [21], was observed in the experiments with the foil and the thinnest oil films. This pattern was found to be made up of bright areas where the foil had thinner films and less shiny areas where the film thickness was greater and the roughness less flattened. These areas corresponded, presumably, to points where the foil was deflected upwards or downwards in the inlet. It seems likely that the corresponding industrial problem is caused by a similar instability in the way that the foil enters the mill.

The effect of the three variables Λ_s , $\alpha\sigma_y$ and t_1/λ has been observed experimentally. The large effect of Λ on the film thickness expected theoretically was found in the experiments. Under the conditions of these experiments the effects of $\alpha\sigma_y$ and t_1/λ were secondary and, although there is some evidence from the experiments of the effect of these variables, the scatter in results is generally greater than the differences between the theoretical predictions. Theoretically deduced area of contact ratios from these experimental measurements of film thickness are found to be in reasonable agreement with experimental measurements of the area of contact ratio from profilometer traces.

Table 5.1a Details of experimental points;
 - rough roll and strip ($d_0 = 1.0\mu\text{m}$).

				oil drop					
t_1	t_2	u_R	T	weight	area	\bar{h}_e	w	Λ_s	Λ_r
mm	mm	m/s	°C	mg	sq. in.	μm	mm		
hard aluminium, $\sigma_y=200$ MPa									
0.630	0.561	0.063	18.6	1.99	4.64	0.74	25	0.84	0.78
0.630	0.559	0.923	18.6	19.17	7.54	4.38	35	6.76	4.64
0.630	0.556	0.020	18.6	0.88	8.23	0.18	25	0.27	0.20
0.630	0.556	0.186	18.6	3.41	3.33	1.76	25	2.19	1.87
0.630	0.563	0.111	18.6	3.07	6.10	0.87	28	1.41	0.92
0.630	0.551	0.305	18.6	12.87	13.55	1.64	40	3.20	1.75
0.630	0.561	0.043	18.6	2.44	9.51	0.44	30	0.60	0.59
soft aluminium, $\sigma_y=85$ MPa									
0.700	0.624	0.477	20.3	9.24	5.25	3.03	37	4.13	3.20
0.700	0.624	0.028	20.3	2.02	8.75	0.40	30	0.30	0.42
0.700	0.624	0.837	20.3	26.55	12.45	3.67	46	6.00	3.87
0.700	0.621	0.477	20.3	13.29	8.55	2.68	35	4.13	2.84
0.700	0.625	0.837	20.3	1.41	0.64	3.79	12	5.67	4.01
0.700	0.624	0.055	20.3	1.17	4.20	0.48	26	0.62	0.51
0.700	0.631	0.014	20.3	0.60	3.25	0.32	20	0.18	0.34
0.700	0.681	0.188	22.5	5.60	5.98	1.61	32	2.74	1.63
0.700	0.58	0.188	22.5	4.08	7.68	0.91	32	1.32	1.00
0.700	0.424	0.188	22.5	3.95	15.02	0.45	33	0.81	0.57
0.700	0.417	0.066	22.5	1.64	13.67	0.21	28	0.29	0.26
0.700	0.681	0.065	22.5	4.08	8.48	0.83	33	1.14	0.86
0.700	0.586	0.065	22.5	3.03	11.06	0.47	33	0.51	0.51
0.700	0.681	0.919	22.5	18.72	8.48	3.80	35	8.27	3.85
0.700	0.586	0.919	22.5	16.88	9.56	3.04	40	4.86	3.31
0.700	0.429	0.919	22.5	9.15	11.61	1.36	35	3.04	1.69
2.82	2.45	0.441	20.4	20.96	20.30	1.78	50	2.06	1.90
2.82	2.45	0.113	20.4	3.19	9.50	0.58	30	0.59	0.62
2.82	2.45	0.126	20.4	5.45	12.40	0.76	35	0.66	0.81
2.82	2.45	0.923	20.4	20.74	11.20	3.19	28	3.45	3.41
2.82	2.45	0.042	20.4	1.25	8.10	0.27	23	0.22	0.28
lead, $\sigma_y=10.3$ MPa									
0.720	0.664	0.046	22.5	1.62	2.07	1.35	20	1.47	1.40
0.720	0.663	0.268	22.5	6.59	3.54	3.21	25	7.30	3.34
0.720	0.657	0.925	22.5	15.31	3.59	7.34	30	16.60	7.68
0.720	0.669	0.092	22.5	2.44	2.46	1.71	21	2.90	1.77
0.980	0.728	0.268	22.5	12.49	12.07	1.78	40	3.48	2.04
0.720	0.691	0.169	22.5	4.89	3.21	2.62	25	5.32	2.69

Table 5.1b Details of experimental points;
 — smooth roll and rough strip ($d_0 = 0.7\mu\text{m}$)

				oil drop method			asperity crushing				
t_1	t_2	u_R	T	weight	area	\bar{h}_e	\bar{h}_e	A	w	Λ_s	Λ_r
mm	mm	m/s	°C	mg	sq. in.	μm	μm		mm		
hard aluminium, $\sigma_y=200$ MPa											
0.115	0.101	0.103	20.1	1.03	1.86	0.95			16	2.96	1.44
0.115	0.101	0.674	20.1	3.44	1.76	3.37	1.92		17	10.29	5.14
0.115	0.101	0.283	20.1	1.67	1.33	2.16	1.22		16	6.14	3.29
0.115	0.954	0.019	20.1	0.23	1.45	0.27	0.26	0.66	12	0.57	0.42
0.115	0.103	0.626	20.1	0.51	1.38	0.64	0.58	0.23	15	1.99	0.94
0.115	0.100	0.042	20.1	0.38	1.61	0.41			15	1.30	0.63
0.638	0.575	0.071	21.7	4.21	11.00	0.66			33	1.11	1.00
0.640	0.570	0.146	21.8				0.79	0.13		2.04	1.20
0.640	0.568	0.157	21.8				0.87	0.12		2.16	1.31
0.640	0.577	0.082	21.8				0.47	0.37		1.26	0.71
0.640	0.582	0.082	21.8				0.59	0.29		1.31	0.90
0.640	0.577	0.055	21.8				0.42	0.40		0.86	0.64
soft aluminium, $\sigma_y=85$ MPa											
0.115	0.103	0.131	18.6				1.20			4.13	1.80
0.115	0.102	0.105	18.6	1.43	2.13	1.16	1.19		14	3.44	1.76
0.115	0.100	0.014	18.6	0.32	2.38	0.23			13	0.63	0.36
0.115	0.101	0.241	18.6	1.28	1.23	1.79	1.54		13	5.99	2.71
0.115	0.102	0.022	18.6	0.18	1.04	0.30	0.37	0.30	10	0.87	0.45
0.690	0.620	0.071	21.7	3.48	8.64	0.69			33	1.08	1.04
0.700	0.555	0.071	21.7				0.59	0.23		0.73	0.73
0.700	0.568	0.030	21.7				0.27	0.47		0.33	0.43
0.700	0.570	0.051	21.7				0.36	0.40		0.56	0.57
0.695	0.558	0.146	21.7				0.77	0.13		1.50	1.21
lead, $\sigma_y=10.3$ MPa											
0.180	0.148	0.048	21.0	0.27	0.60	0.77	0.67	0.10	10	2.86	1.23
0.180	0.137	0.067	21.0	0.75	1.59	0.81	0.98	0.17	16	3.31	1.31
0.180	0.170	0.235	21.0	3.21	1.69	3.27	1.84		18	11.00	4.80*
0.180	0.159	0.110	21.0	1.94	1.87	1.79	1.68		19	6.71	2.71
0.180	0.155	0.013	21.0	0.86	2.70	0.55	0.62	0.30	18	1.10	0.84
0.180	0.164	0.627	21.0	5.63	1.81	5.30	1.94		20	17.57	8.01*
0.700	0.642	0.024	21.0	0.52	1.18	0.76	0.69	0.20	14	1.29	1.13
0.700	0.650	0.068	21.0	1.05	1.10	1.64	1.02	0.17	14	3.34	2.43
0.700	0.618	0.041	21.0	0.75	1.48	0.87	0.61	0.33	12	1.80	1.31
0.710	0.640	0.678	21.7	18.09	6.66	4.68			30	19.00	8.27
0.710	0.650	0.373	21.7	10.66	4.42	4.15			29	13.00	6.19
0.710	0.640	0.918	21.7	30.84	8.25	6.44			38	23.29	9.67
0.710	0.640	0.102	21.7	9.77	7.37	2.28			37	4.31	3.43
0.710	0.650	0.062	21.7	6.97	7.24	1.66			36	2.97	2.47
0.710	0.670	0.055	20.7				1.61				
0.710	0.660	0.093	20.7				2.29				
0.710	0.660	0.039	20.7				1.55				
0.710	0.500	0.039	20.7				0.95	0.07		1.13	1.71

* Points rejected because $\nu < 2.5$.

Table 5.1c Details of experimental points;
 — smooth roll and strip ($d_0 = 0.11\mu\text{m}$).

				oil drop				
t_1	t_2	u_R	T	weight	area	w	h_s	\bar{h}
mm	mm	m/s	°C	mg	sq. in.	mm	μm	μm
soft aluminium, $\sigma_y=85\text{ MPa}$								
2.38	2.08	0.300	21.8	7.52	8.20	30	1.47	1.69
2.38	2.10	0.920	21.8	16.64	8.35	36	3.56	3.65
2.40	2.09	0.540	21.8	12.58	8.38	35	2.37	2.77
2.38	2.10	0.070	21.8	1.74	6.59	25	0.38	0.48
0.447	0.429	0.241	19.2	5.24	3.47	26	4.67	2.63
0.443	0.423	0.924	19.2	3.17	1.24	18	9.22	4.45
0.429	0.385	0.529	17.8	12.39	5.35	33	6.10	4.15
0.432	0.392	0.123	17.8	3.11	4.32	26	2.08	1.28
0.428	0.390	0.095	17.8	2.98	5.12	26	1.57	1.04
0.432	0.370	0.071	17.8	0.85	1.45	16	1.3	1.04
0.438	0.385	0.280	17.8	4.16	3.50	25	4.19	2.13
2.39	2.36	0.503	17.6	17.45	5.40	34	6.52	5.62
2.38	2.35	0.252	17.6	10.75	5.27	32	4.06	3.54
2.39	2.35	0.923	17.6	29.23	6.22	38	9.22	8.15
2.40	2.36	0.104	17.6	4.07	3.54	26	1.89	2.00
2.38	2.34	0.060	17.6	1.96	2.28	22	1.09	1.49
0.435	0.360	0.629	19.0	26.06	15.95	46	5.47	3.07
0.428	0.355	0.425	19.0	16.78	13.12	42	4.14	2.40
0.430	0.365	0.079	19.0	1.66	5.07	25	1.01	0.61
0.432	0.375	0.112	19.0	4.23	9.47	33	1.49	0.82
0.428	0.375	0.223	19.0	10.45	14.25	41	2.81	1.34
0.445	0.390	0.920	17.8	22.87	8.31	40	9.02	4.94
0.445	0.390	0.920	17.8	0.94	0.30	10	7.38	5.62*
0.428	0.350	0.920	19.0	17.82	8.71	39	6.75	3.87
0.428	0.350	0.920	19.0	0.57	0.24	15	6.39	4.03
0.428	0.368	0.920	19.0	2.00	0.94	18	7.00	3.98
0.428	0.368	0.920	19.0	21.18	9.17	26	7.30	4.01
0.428	0.370	0.920	19.0	3.07	1.43	40	7.96	4.00
0.428	0.370	0.920	19.0	0.64	0.28	8	6.10	4.34*
0.432	0.385	0.920	19.0	8.27	3.82	40	8.22	4.88
0.432	0.385	0.920	19.0	5.35	2.73	8	6.30	4.15*
0.432	0.375	0.920	19.0	21.05	9.59	23	7.28	3.62
0.432	0.375	0.920	19.0	1.54	0.73	13	6.80	3.89*

* Points rejected because $\nu < 2.5$.

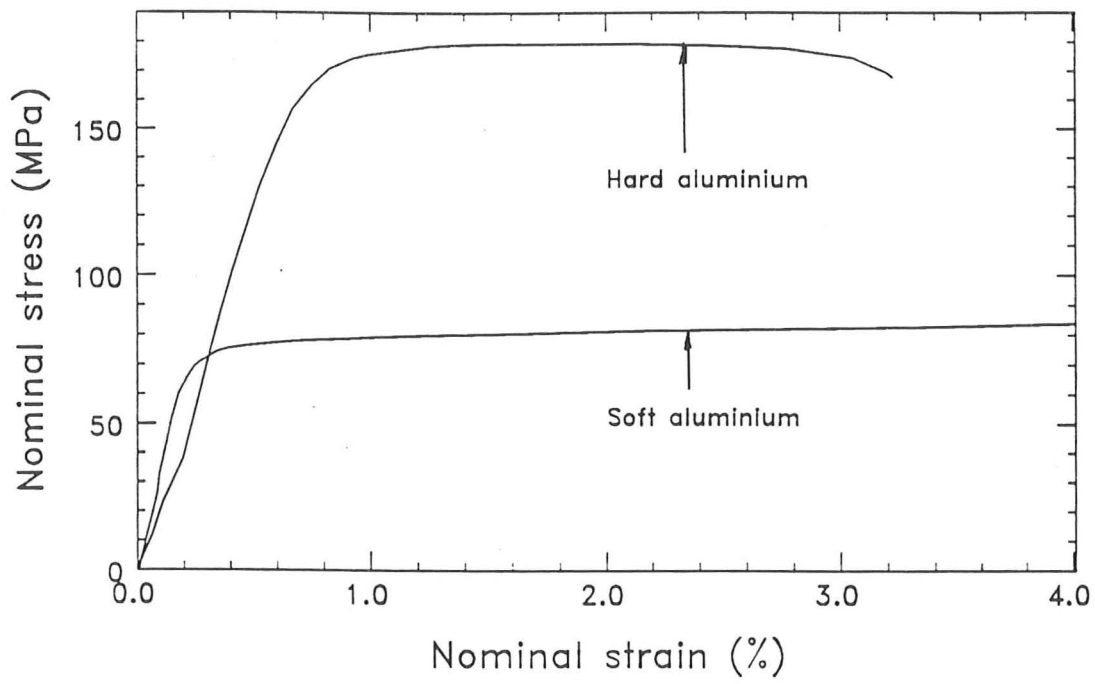


Figure 5.1 Plane stress tensile tests

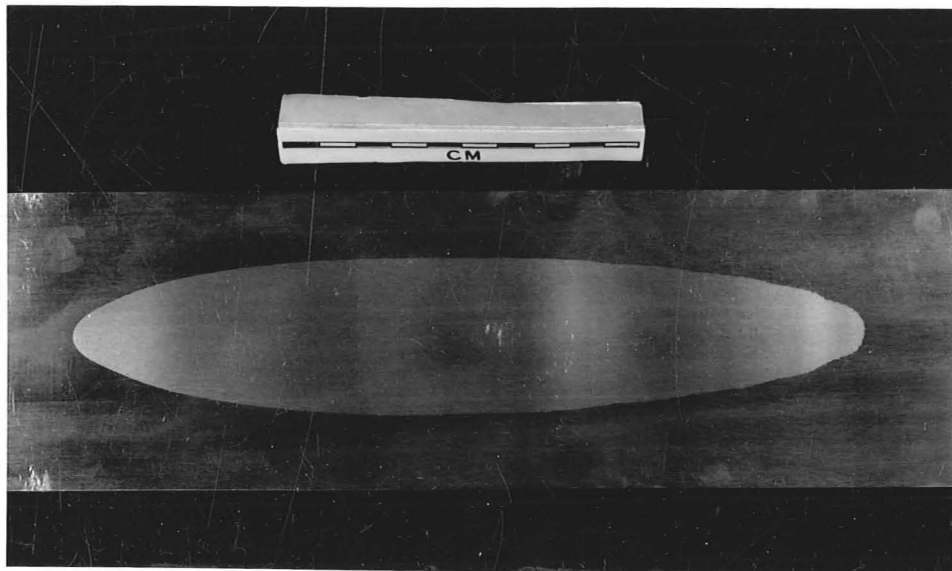
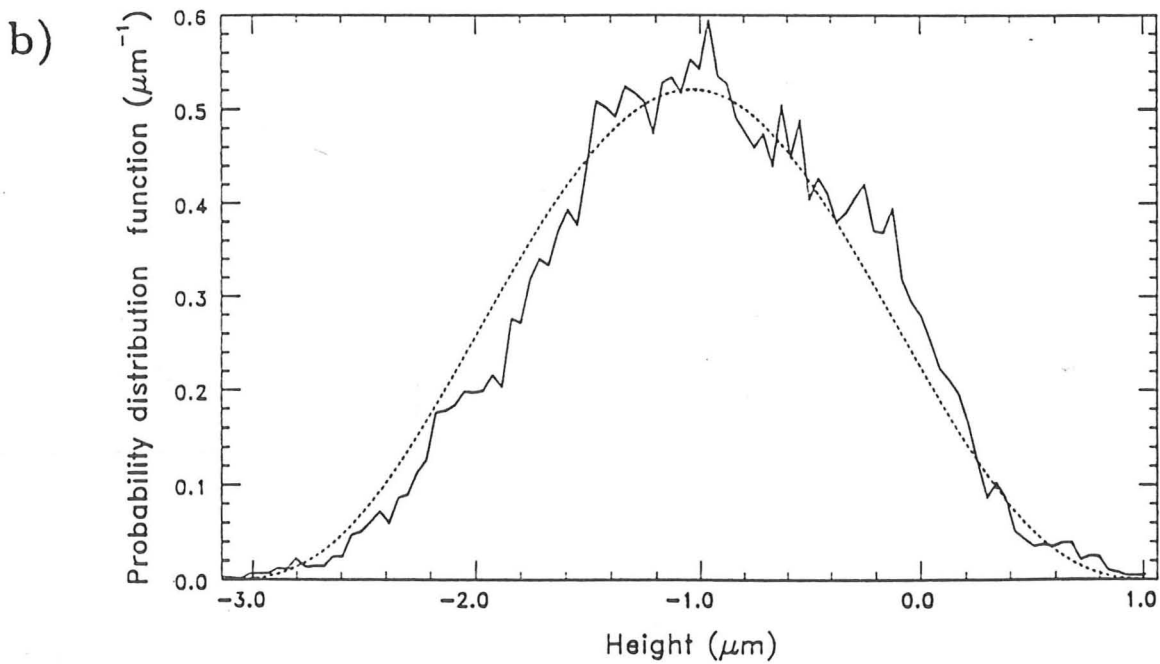
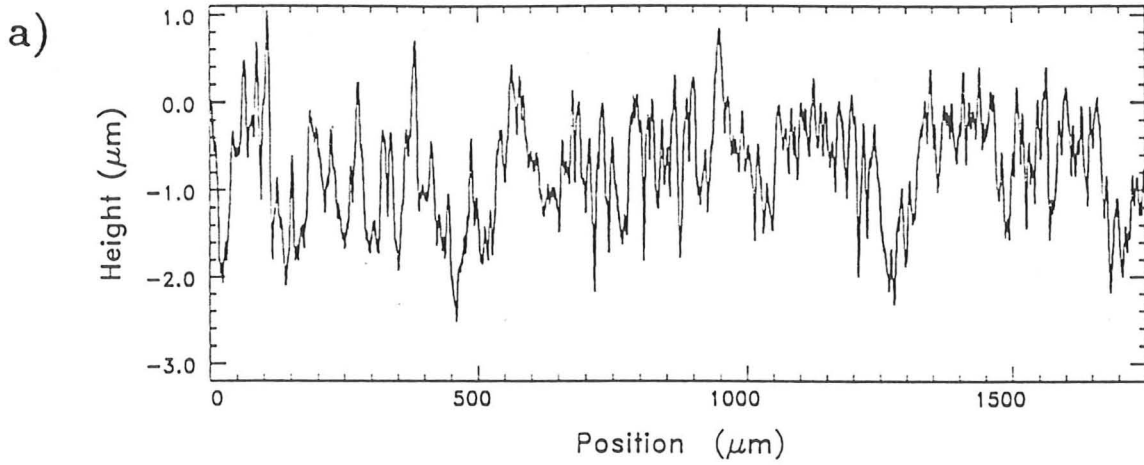


Figure 5.2 Typical strip finish after an oil drop experiment.



KEY

- Measured probability distribution function
- Polynomial approximation to roughness, $d_0 = 0.7\mu\text{m}$

Figure 5.3 Unflattened strip roughness a) Profile, b) Height distribution.

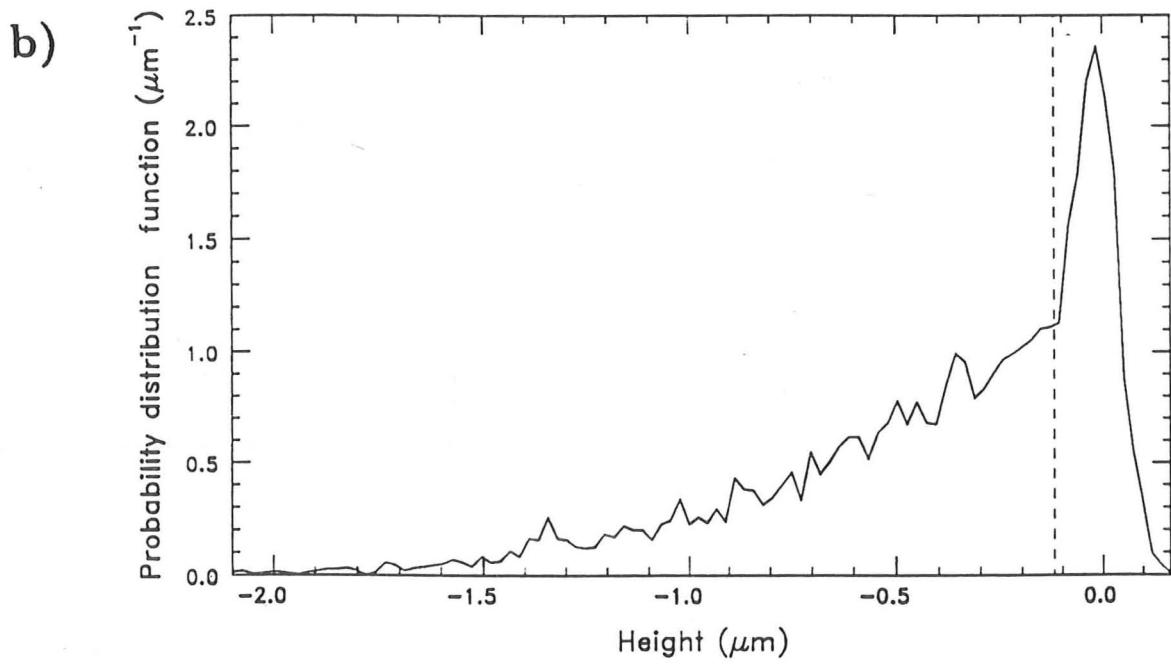
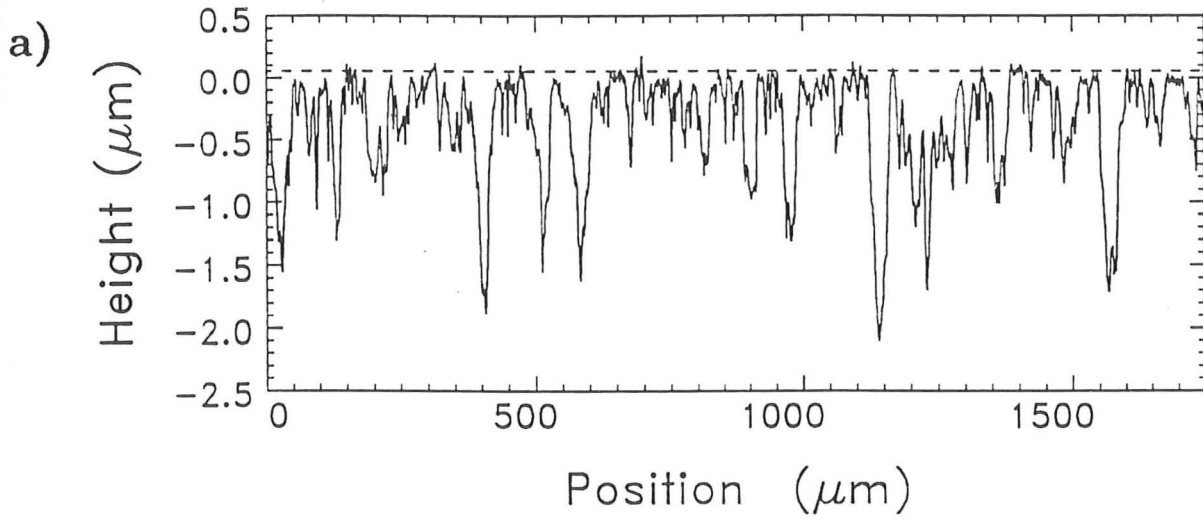


Figure 5.4 Flattened strip roughness a) Profile, b) Height distribution.

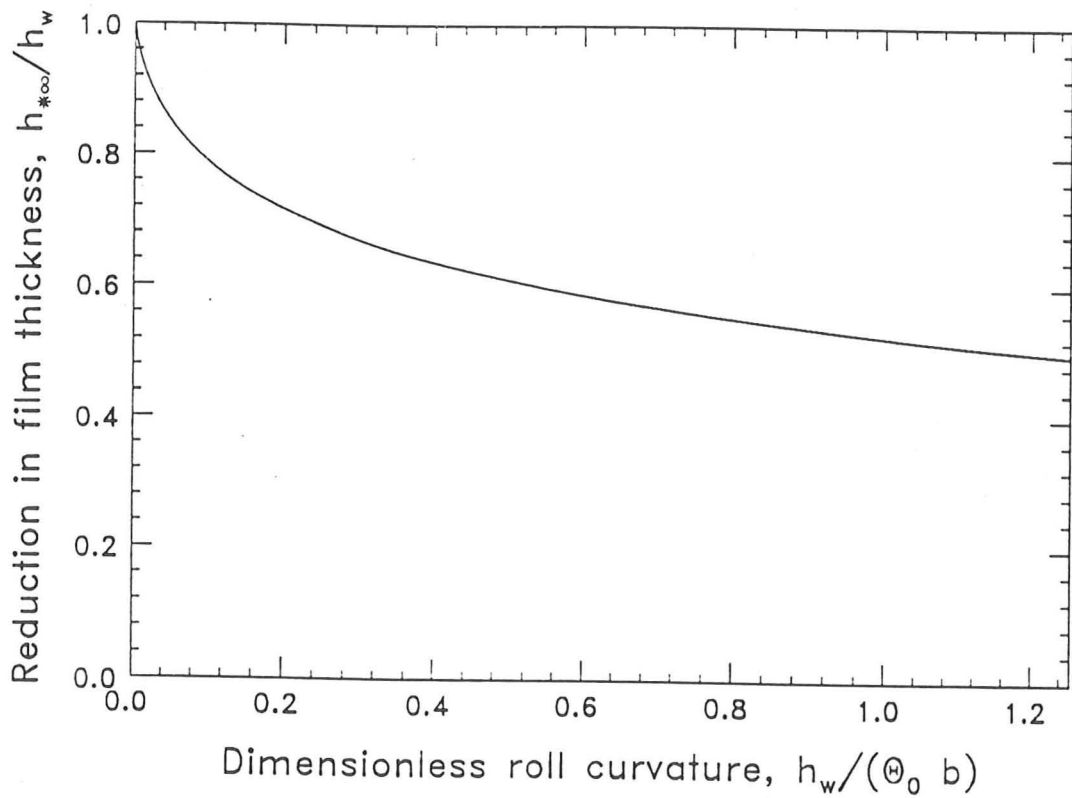


Figure 5.5 The effect of curvature on the smooth isothermal film thickness.

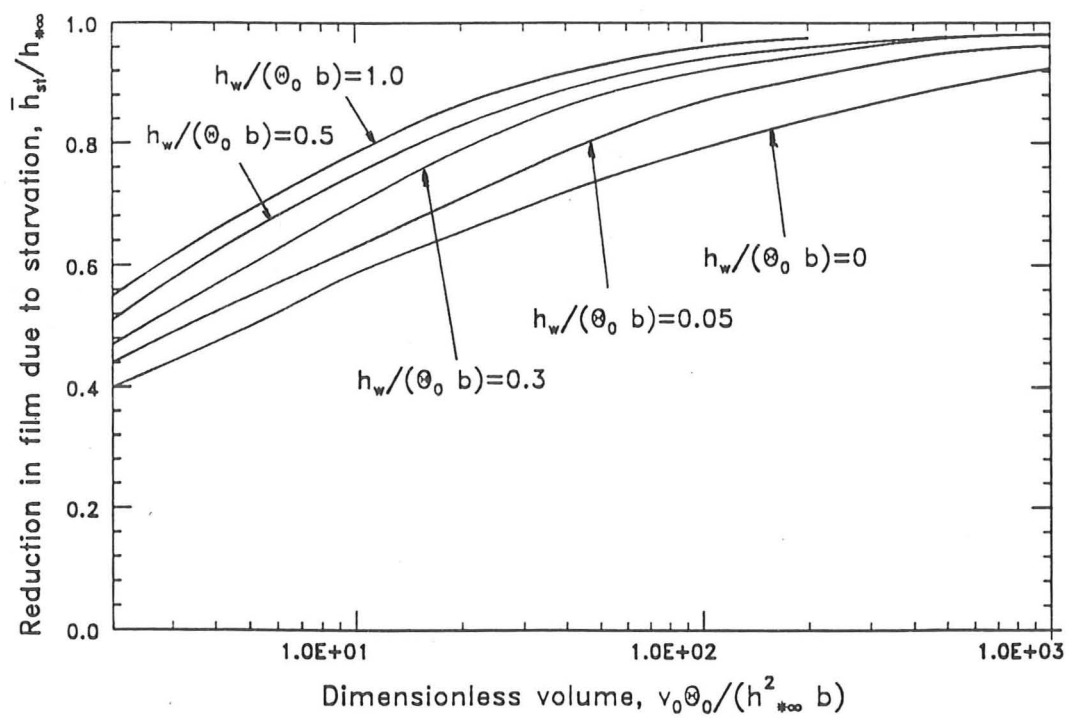
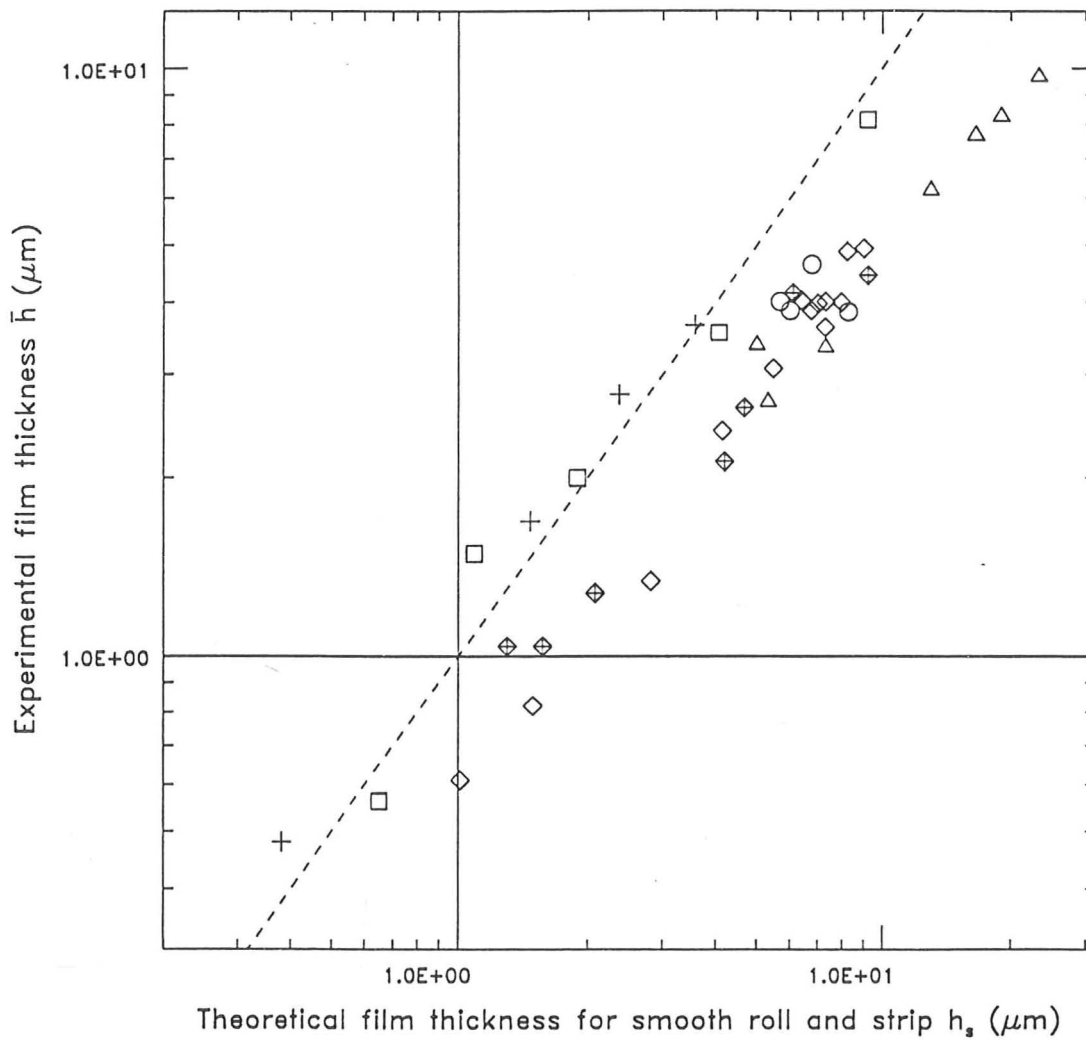


Figure 5.6 The effect of starvation for curved inlets.



KEY

- + 2.38→2.08mm smooth soft aluminium
- ◆ 0.447→0.429mm smooth soft aluminium
- 2.39→2.36mm smooth soft aluminium
- ◇ 0.435→0.360mm smooth soft aluminium
- 0.7mm aluminium
- △ Aluminium foil and 0.7mm lead

Figure 5.7 Film thicknesses for $\Lambda_s > 5$.

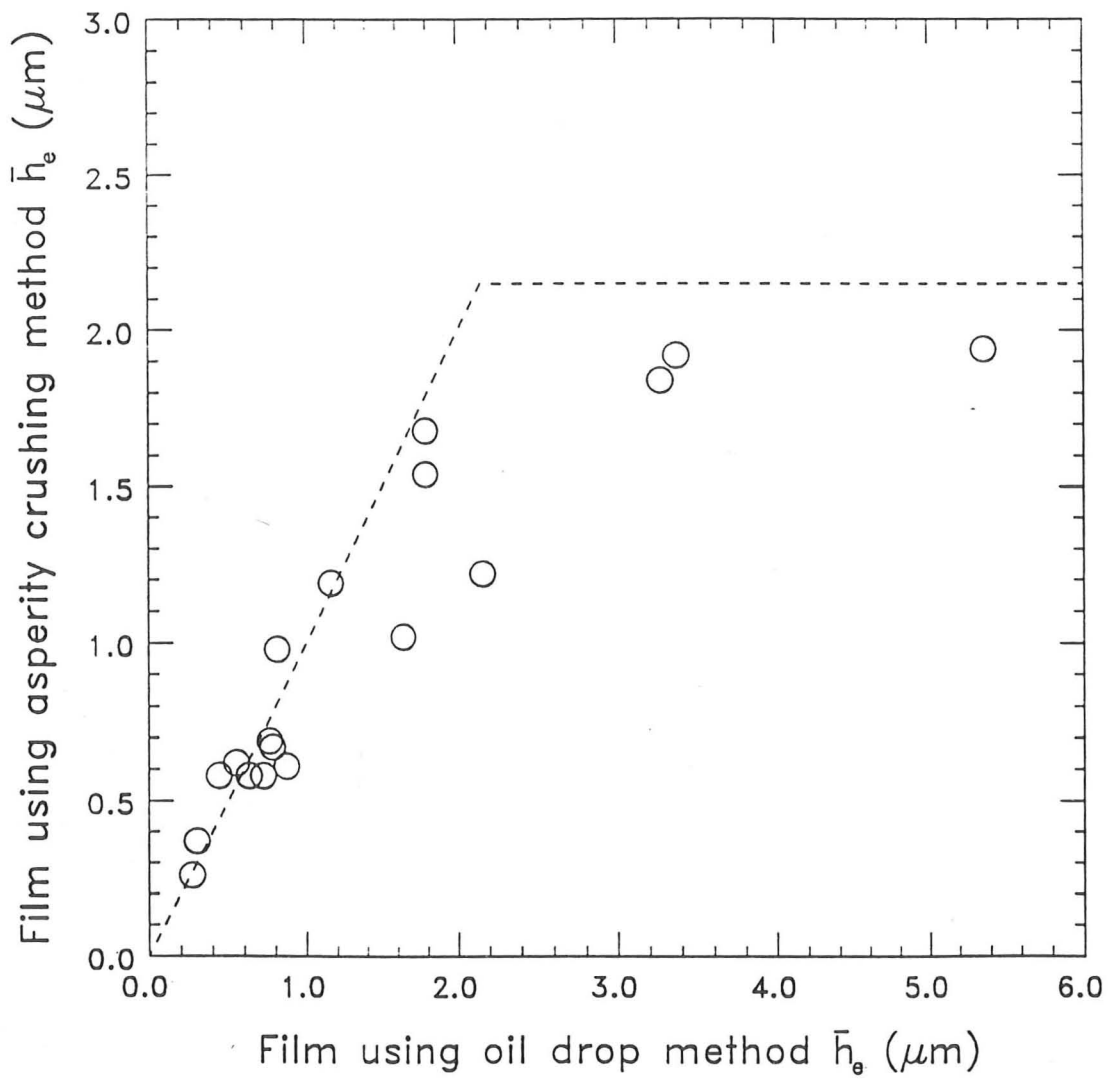
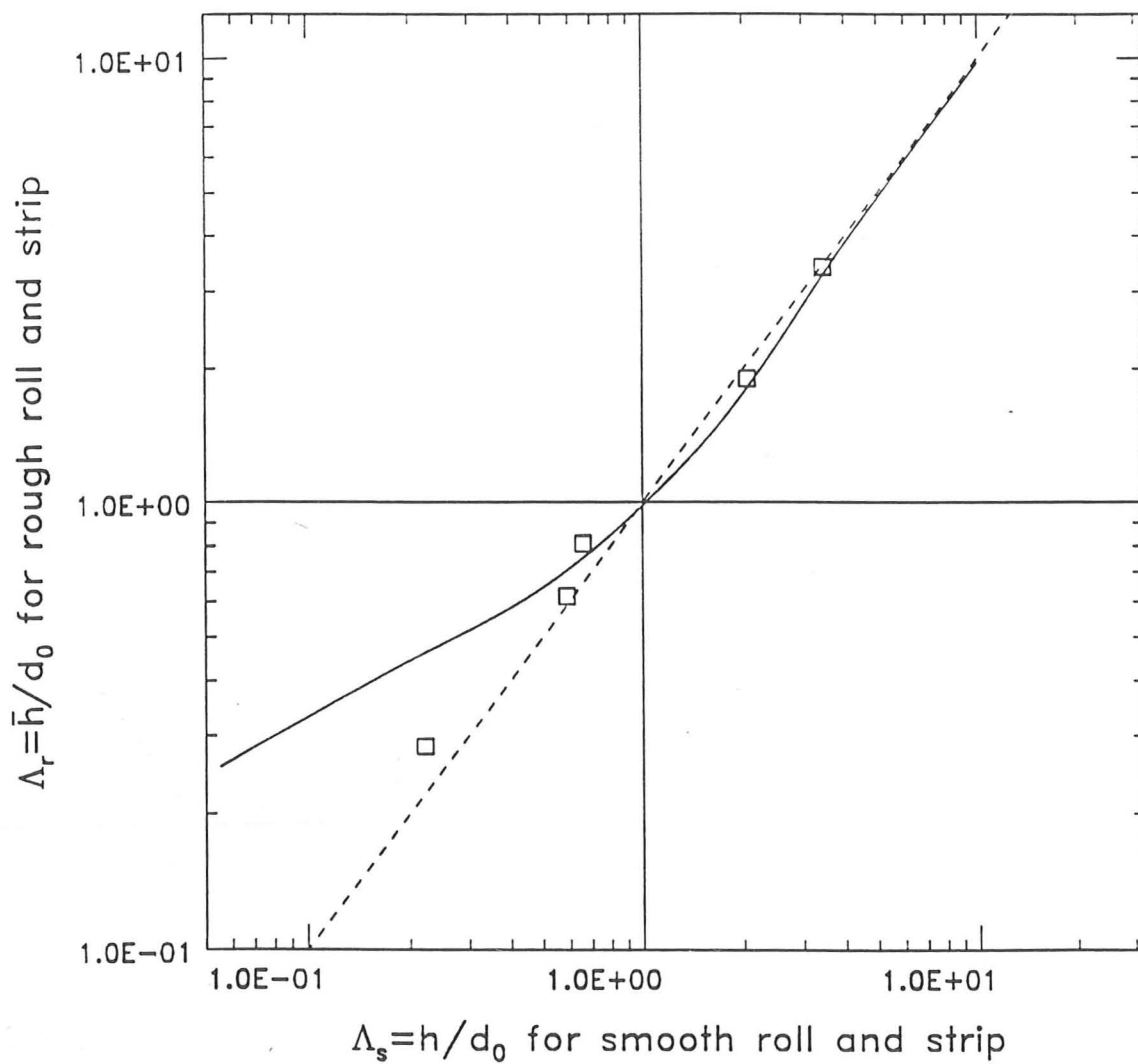


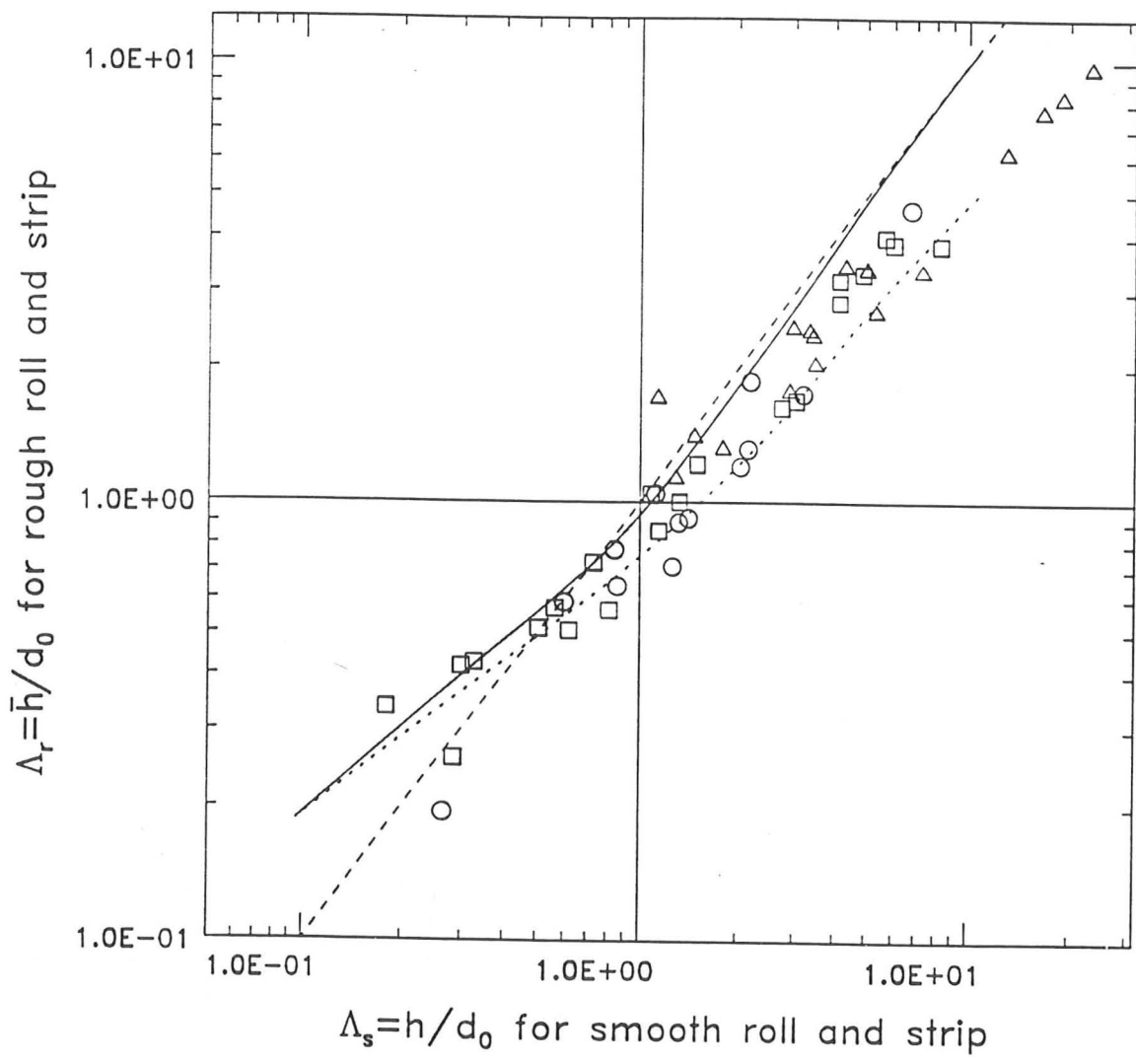
Figure 5.8 Comparison between oil drop and asperity crushing film measurements.



KEY

- Theory — soft aluminium
- Soft aluminium

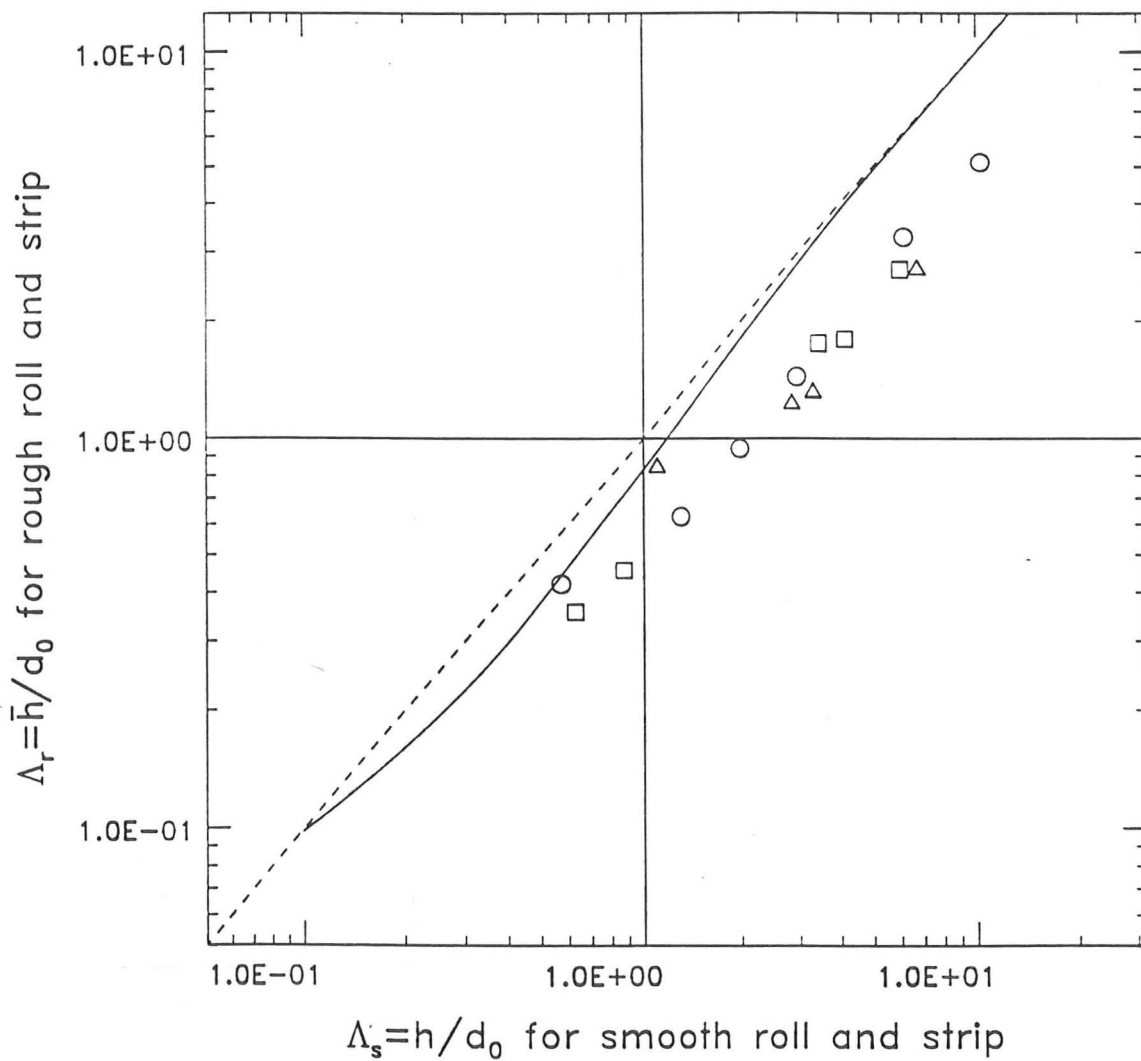
Figure 5.9 Experimental film thicknesses — 2.8 mm strip.



KEY

- Theory — soft aluminium.
- - - Soft aluminium with wrap round
- Hard aluminium
- Soft aluminium
- △ Lead

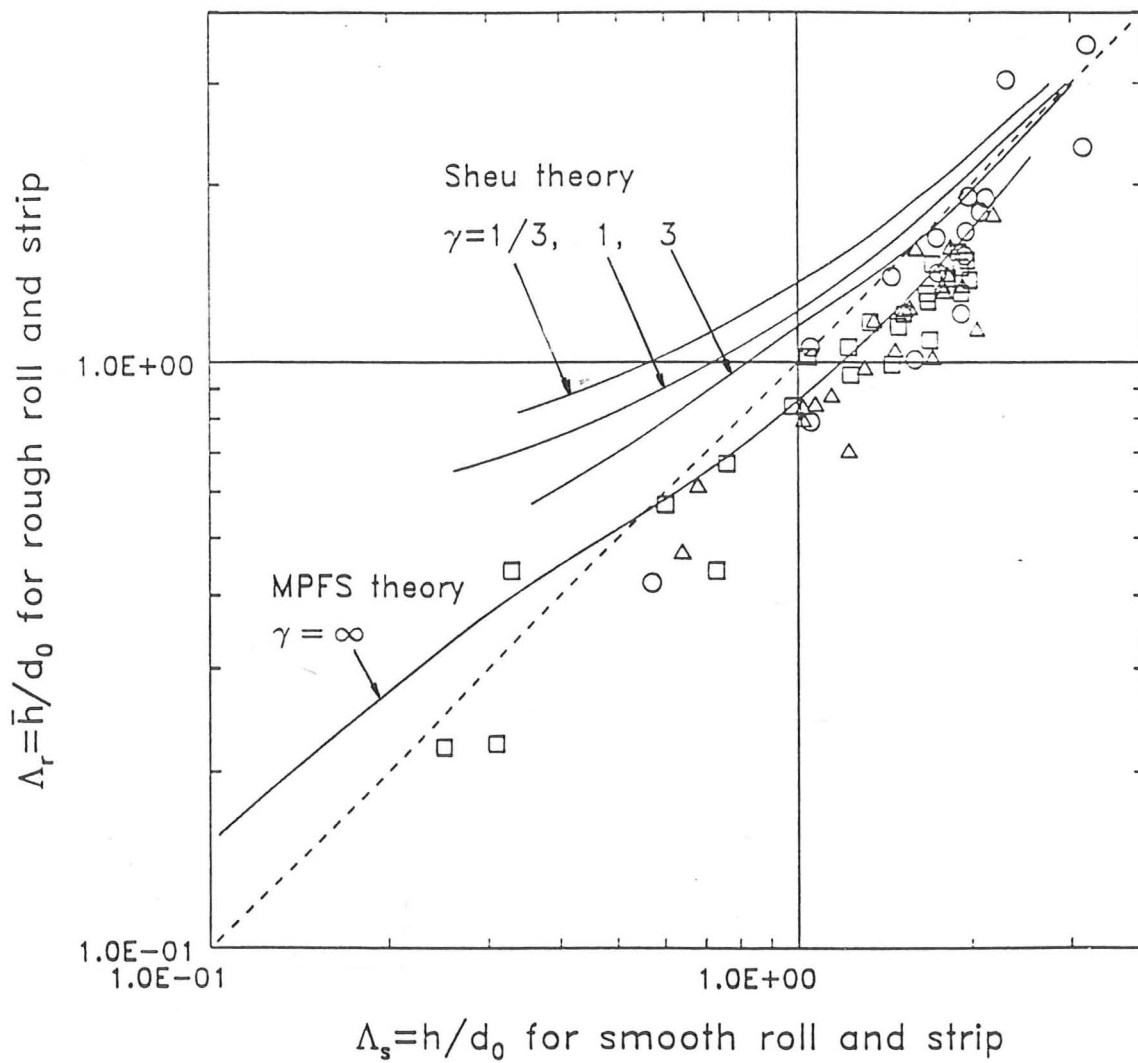
Figure 5.10 Experimental film thicknesses — 0.9–0.64 mm strip.



KEY

- Theory — soft aluminium
- Hard aluminium
- Soft aluminium
- △ Lead

Figure 5.11 Experimental film thicknesses — 0.180–0.115 mm strip.



KEY

- $t_1 = 1.02\text{mm}, t_2 = 0.816\text{mm}$
- $t_1 = 1.020\text{mm}, t_2 = 0.685-0.732\text{mm}$
- △ $t_1 = 1.02\text{mm}, t_2 = 0.65-0.525\text{mm}$

Figure 5.12 Sheu's experimental and theoretical film thicknesses.

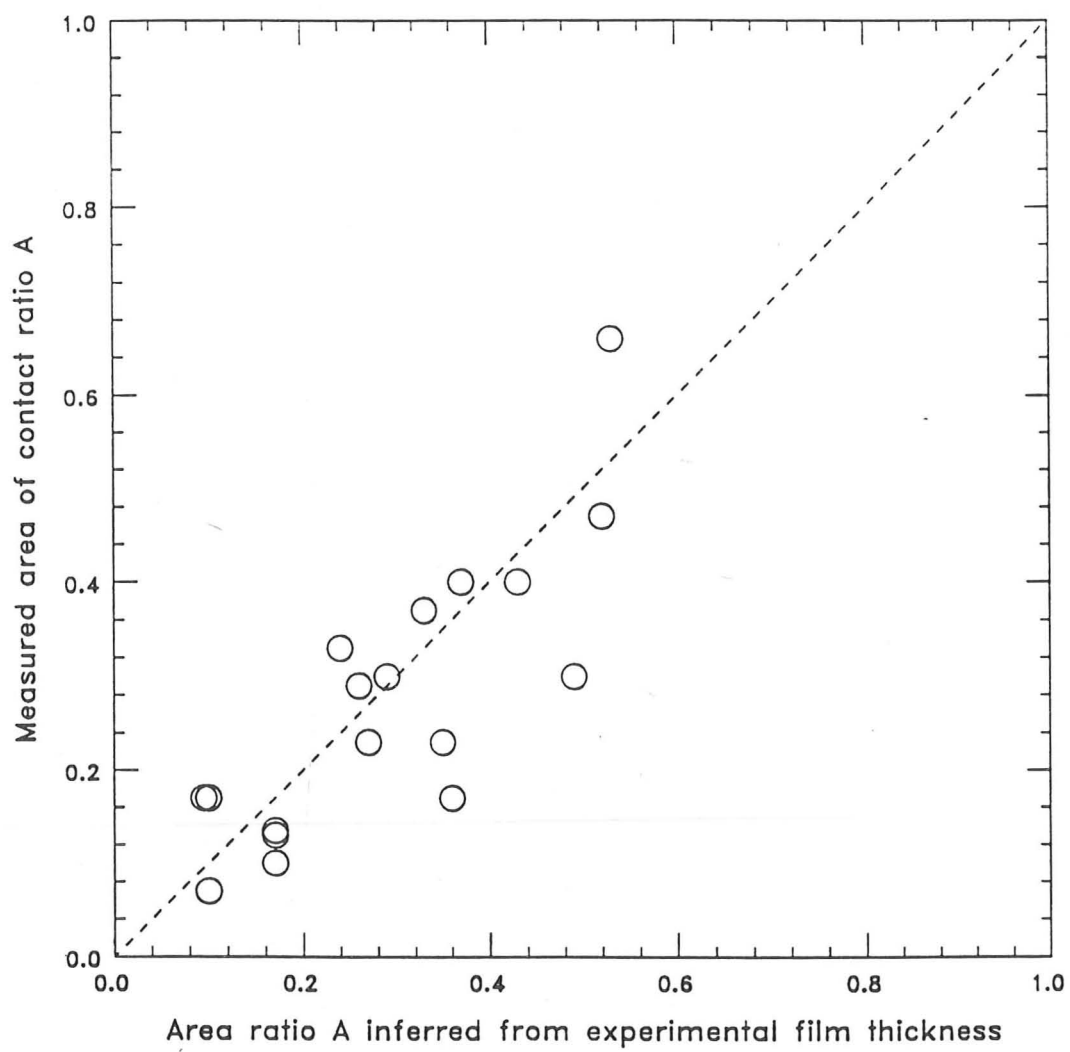
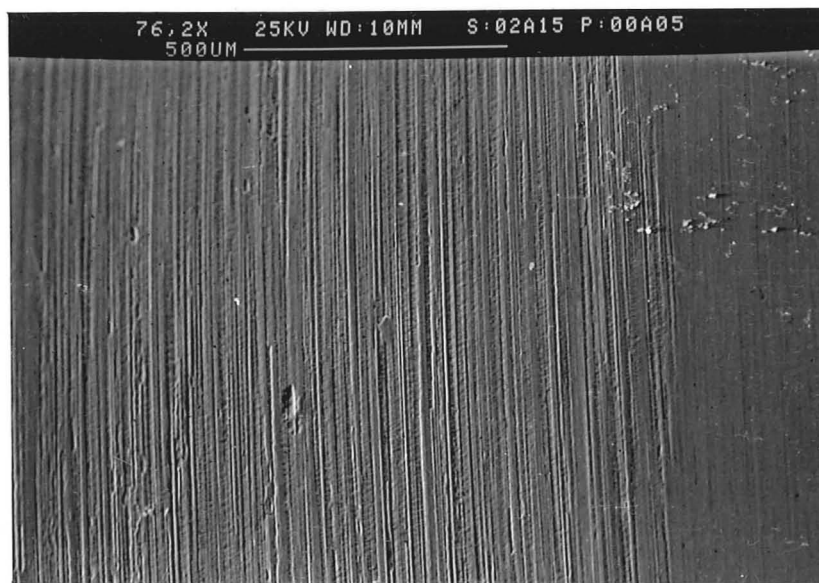


Figure 5.13 Experimental area of contact measurements.

a)



b)



c)

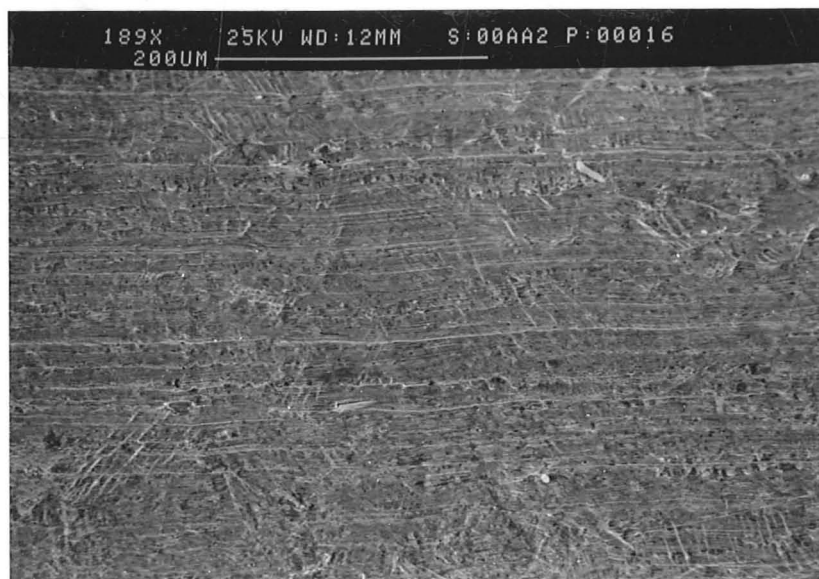


Figure 5.14 Micrographs of strip surfaces
a) Undeformed strip
b) Aluminium foil $\Lambda = 0.59$
c) Lead foil $\Lambda = 1.14$.

CHAPTER 6

MEASUREMENT OF TRACTION IN A MIXED LUBRICATION EXPERIMENT

6.1 Introduction

The results of theory and experiments have shown how the separation of strip and roll by an oil film and the real area of contact may be estimated in a rolling operation. Friction may then be split up into two components. Where the surfaces are well separated friction will be due to the shearing of the oil and can be simply calculated if the oil rheology and the straining rate of the oil are known. The friction coefficient will then be that typical of hydrodynamic friction, typically in the range 0.005–0.05.

Where the asperities have been crushed down any oil film separating the surfaces of the roll and the workpiece will be rather small (perhaps 10's of nanometres). In these regions friction may be due to one of the several mechanisms described in the introductory chapter.

The aim of this experiment is to measure friction coefficients for a mixed contact in a disc machine, where the traction forces and the film thickness separating the two surfaces can be estimated more confidently than in a rolling mill experiment. Although the film thicknesses in these experiments cannot be measured, it is possible, by making appropriate assumptions about the conditions under the contact, to infer film thicknesses from the known rheological properties of the oil and the traction measurements. It will be assumed that the only contribution to friction is due to the shearing of the oil behaving as expected from measurements of its bulk properties. Experimental film thicknesses can then be inferred from traction measurements and compared with theoretical estimates of the film thickness.

Many metal working processes and most foil rolling operations are in the mixed lubrication regime, which the experiments are designed to span. The details of the change in traction behaviour will be slightly different in these elastic contact experi-

ments as compared with metal rolling contacts. In the elastic case the area of close contact stays essentially constant as Λ becomes smaller, while the load shifts from a uniform distribution to being concentrated on the contacts. The increase in pressure under the close contacts results in an increased viscosity and this, together with the increased shear rate because of the smaller films there, causes the increase in traction with increased roughness. In metal rolling, it is shown that the asperities crush rapidly at the beginning of work zone until the pressure in the valleys equals the pressure under the asperities. However, the contact ratio increases with smaller Λ and it is this, combined with the reduction in film thickness under the asperities that causes the increase in traction with smaller Λ . Nevertheless it is hoped to show that, at least in this simple case, hydrodynamic theory can be used to derive film thicknesses under the asperities and the traction behaviour can then be explained in terms of the bulk fluid rheology.

6.2 Experimental setup

The disc machine used in these experiments is described in chapter 2 and in reference [30]. The lubricant used was Shell Vitrea 68, a base mineral oil with a viscosity at ambient pressure and 25°C of 0.135Pas.

6.2.1 Discs

In this series of experiments two 76 mm diameter discs were used. One was a smooth hardened steel disc with a roughness of 0.015 μm r.m.s. The other disc was aluminium and was prepared in three ways. For a series of experiments in which the effect of roughness on traction could be neglected, the aluminium disc was ground and polished. Its initial roughness was 0.01 μm r.m.s and its roughness after the experiments was 0.04 μm r.m.s. To investigate the effect of roughness, the aluminium disc was turned on a lathe with different feed rates and depths of cut to generate two finishes with a regular array of circumferential ridges (actually spirals). The resulting profiles after turning are given in figure 6.1a with half the peak-to-peak amplitude d of 0.7 μm and figure 6.2a with half the peak-to-peak amplitude of 4.75 μm . For the experiments these ridges were flattened in two ways. After rolling at slow speed (0.47m/s) with a mean nominal pressure of 205 MPa the 0.7 μm disc had a finish shown in figure 6.1b. To flatten the discs still further, the discs were run together at a higher load ($\bar{p} = 412\text{MPa}$) and

run at slow speed with maximum traction. This produced the profiles shown in figures 6.1c and 6.2b. The traces were digitised and the r.m.s roughness of the discs and their flattened areas estimated.

The pressure needed to squash the ridges would have been approximately constant across the ridge and about equal to the Vickers hardness of the disc (measured as 106.5kg/mm^2). On unloading, the resulting profile of the discs was slightly curved. It was found necessary to estimate this transverse curvature over the central four-fifths of the contact. Johnson [51] gives the elastic deflections for the indentation of a semi-infinite elastic half-space by a uniform pressure. For the $4.75\mu\text{m}$ disc indented by a pressure equal to the Vickers hardness, the theoretical curvature over the central four-fifths of the flattened region is 1100 m^{-1} . This agrees exactly with an experimental measurement taken from a magnification of this profile. The excellent agreement is no doubt fortuitous. For the flattened $0.7\mu\text{m}$ disc profiles, the less regular profiles made any measurement of curvature difficult and the curvature was taken as the same as for the $4.75\mu\text{m}$ disc.

6.2.2 Operating Conditions

Most of the experiments were performed at 25°C , with a nominal pressure based on line contact conditions of 205 MPa. In addition some tests were performed at 30°C at the highest speed of 3.63 m/s, where it was found difficult to prevent the disc temperature rising due to frictional heating. To measure the rheology of the oil at a higher pressure, a traction curve was also measured at a mean pressure of 412 MPa with the smooth discs. The correction for thermal heating in the nip described in chapter 2 was applied to give isothermal traction curves. This had a maximum value of 2°C at the highest rolling and sliding speeds but was generally negligible.

Conditions were varied by changing the rolling speed so that a range of Λ ratios were covered. The flattened $0.7\mu\text{m}$ disc had Λ ratios in the range 0.88–3.58, while the $4.75\mu\text{m}$ disc experiments were in the range 0.09–0.55, where Λ is defined as the ratio of the theoretical film thickness for smooth discs h_d (from equation 2.6), to half the peak-to-peak roughness height d . This is a slightly different measure of roughness height than normally used. With this definition significant asperity 'contact' can be expected for Λ ratios of below 1. In fact, for the geometries considered, the difference

between this measure of roughness and the more usual r.m.s. roughness is not very great. The range of Λ covered for each disc was limited by the combination of speeds and torques that the disc machine could supply. Smooth disc experiments had Λ ratios greater than 14, so that the effect of roughness will be negligible. For convenience the value of d will be used in identifying each disc roughness.

Johnson and Evans [27, 28] find that mineral oils start to behave as elastic solids for Deborah numbers above about 1. In these experiments Deborah numbers are less than 0.01, so that the oil will behave as a viscous fluid.

6.3 Results

6.3.1 Smooth discs

The shear stress and strain rates in the nip can be derived from the traction measurements with smooth discs using the method described in chapter 2. That chapter gives expressions for the mean normal pressure \bar{p} and the smooth film thickness h_d (equations 2.4 and 2.6). The measured relationship between shear stress and strain rate at the two mean pressures are shown in figure 6.3a, together with curve fits using the Eyring rheological model. For the measurements at a mean pressure of 205 MPa the shear stress is not sufficiently above the Eyring stress without excessive sliding to determine τ_0 directly. Here the Eyring stress and large strain viscosity have been found by fitting a relationship of the form of equation 2.2 to the stress-strain results. The Newtonian viscosity for Vitrea 68 is plotted in figure 6.4 along with the viscosity of Turbo 33 [95], a very similar oil that Vitrea 68 has replaced. The extrapolation of the results to higher pressures was guided by the results for the Turbo 33. Similarly, the effect of pressure on the Eyring stress found for HVI 650 by Evans [30] was used to extrapolate the Eyring stress measurements given in figure 6.5 to the higher pressures. The pressure viscosity index for Turbo 33 ($2.2 \times 10^{-8} \text{m}^2/\text{N}$), measured in an Amsterdam high pressure viscometer [30], was used in calculating the film thicknesses. Deduced high pressure viscosities for Vitrea 68 confirm this value within the limits of experimental error.

6.3.2 Rough discs

In order to make a direct comparison between the rough and the smooth experiments, traction curves have been converted to nominal stress–nominal strain curves using the same method as for the smooth disc experiments.

$$\text{i.e.} \quad \tau_n = \mu \bar{p} \quad \{6.1\}$$

where \bar{p} is the Hertz mean pressure for line contact. The nominal strain rate based on a smooth film thickness is given by

$$\dot{\gamma}_s = \frac{\Delta u}{h_d} \quad \{6.2\}$$

where h_d is the Dowson and Toyoda mean film thickness for line contact give by equation 2.6. Any effects of roughness on the traction curves will then be seen by a change away from the nominal stress–nominal strain rate curves for smooth discs at the same nominal mean pressure. Although the true stresses and strains in the oil films will be different from the nominal ones, these differences cannot be estimated *a priori* without making some assumptions about the rough contact conditions, and in some cases these differences cannot be estimated reliably at all. Results are shown for the four geometries of figures 6.1a, b and c and for figure 6.2b in figures 6.3a–d respectively. The traction results become inaccurate at the lowest nominal strain rates due to the difficulty in measuring both the sliding speed and the traction force with any accuracy at the lowest sliding speeds.

For the $0.7\mu\text{m}$ disc, a rough disc traction curve was also measured at 30°C . The corresponding smooth traction curve has been inferred from the curve at 25°C , knowing the variation in low pressure viscosity with temperature (a reduction of 30%), with a slight allowance for the change in pressure viscosity index with temperature. For this test with $\Lambda = 3.58$, there is no significant change from the behaviour with smooth discs, confirming the results of Evans and Johnson with rough discs [29].

At lower speeds the film thickness is reduced giving smaller Λ ratios. The effect of roughness then becomes significant, as can be seen by comparing the measured curves with those found with smooth discs at the same nominal pressures. For Λ ratios between about 2.7 and 1 the effect of the roughness is to raise the nominal shear stress curves above those found for the smooth discs. However the traction curves still show a speed

dependence characteristic of Eyring fluids, with an exponential increase in traction coefficient with the sliding speed, or nominal strain rate at higher shear stresses.

As the Λ ratio is decreased further below about 1, for example with the smallest Λ ratio with the $0.5\mu\text{m}$ disc and for all the results with the $3.0\mu\text{m}$ disc, the traction curves tend to lie close together with no further increase in the nominal stresses at a given nominal strain rate.

The plots show how at high and low Λ ratios ($\Lambda > 3$ or $\Lambda < 1.0$) the traction behaviour in these experiments is relatively independent of the Λ ratio. Between these extremes there is a transition in traction behaviour, reflecting the transition between a fairly uniform loading and shear rate across the width of the contact, to a situation in which there is a concentration of load under the asperity peaks. In order to describe this transition it is useful, at least for the well defined geometries used in the experiment, to show how the film thickness under the asperity peaks varies as the Λ ratio changes. There will be a corresponding change in the distribution of load between the valleys and the regions under the asperity peaks. If both the film thickness and the pressure across the contact can be estimated for any Λ ratio then, knowing the oil rheology, it would be possible to calculate the traction curves.

6.4 Deduction of experimental film thicknesses

To interpret the traction results, it is useful to consider two extreme conditions of roughness. Where $\Lambda > 2$ there will be little pressure variation across the width of the contact. At the other extreme, where $\Lambda \leq 0.88$ there will be negligible pressure in the valleys and the traction is determined by the viscosity and shear rates under the asperity peaks.

6.4.1 With uniform pressure ($\Lambda > 2$)

Where the oil pressure across the width of the contact is uniform the traction will be given by the sum of the shear stresses across the width of the contact, with a constant viscosity but with varying shear rates due to the variation in film thickness. The thinner films under the asperity peaks will have higher strain rates than in the equivalent line contact. These higher strain rates will give rise to higher shear stresses

in these regions. Conversely there will be lower strain rates and shear stresses in the valleys than in the equivalent smooth line contact. In these experiments the net effect is an increase in mean shear stress as the traction on the asperity peaks dominates the overall traction coefficients. In order to simplify the calculation, while retaining the essential features of the real geometry of the contact, the profiles have been idealised by two flat regions as shown schematically in figure 6.6, with an area of contact ratio A_0 and a film thickness under the asperity peaks of h_a . The depth of the valleys is d_1 ; for the calculations this was taken as 1.4 times the half amplitude d to reflect the actual distribution of asperity heights found for the flattened $0.7\mu\text{m}$ discs for which this calculation was used. The values of the relevant dimensions are given in table 6.1. The contact length will be assumed to be the same as for smooth contacts, given by equation 2.3. The mean shear stress has contributions from the regions with small and large film thicknesses. Using the constitutive relationship for the oil, the shear stresses and strain rates are related by,

$$\tau_n = A_0 \tau_0 \sinh^{-1} \left(\frac{\Delta u \eta}{h_a \tau_0} \right) + (1 - A_0) \tau_0 \sinh^{-1} \left(\frac{\Delta u \eta}{(h_a + d_1) \tau_0} \right) \quad \{6.3\}$$

The ratio of the nominal strain rate $\dot{\gamma}_e$ for a rough experiment to the strain rate $\dot{\gamma}_s$ for a smooth experiment at the same nominal pressure and shear stress can be determined from one of the graphs. It is merely the horizontal offset between the two curves at a given nominal shear stress τ_n . The sliding speed in the rough experiment is given by

$$\Delta u = \dot{\gamma}_e h_d \quad \{6.4\}$$

Then, using the constitutive relationship (equation 2.2, neglecting the elastic term $\dot{\tau}/G$) and equation 6.2 and substituting into equation 6.3 we derive a relationship between the strain rate ratio $\dot{\gamma}_e/\dot{\gamma}_s$ and the film thickness ratio h_a/h_d ,

$$\frac{\tau_n}{\tau_0} = A_0 \sinh^{-1} \left(\frac{\dot{\gamma}_e h_d}{\dot{\gamma}_s h_a} \sinh \left(\frac{\tau_n}{\tau_0} \right) \right) + (1 - A_0) \sinh^{-1} \left(\frac{\dot{\gamma}_e h_d}{\dot{\gamma}_s (h_a + d_1)} \sinh \left(\frac{\tau_n}{\tau_0} \right) \right) \quad \{6.5\}$$

This implicit equation can be used to find the film thickness ratio h_a/h_d for the assumed geometry for any value of τ_n/τ_0 and $\dot{\gamma}_e/\dot{\gamma}_s$. At sufficiently small Λ ratios, deduced values for h_a will no longer be compatible with the assumption that there is no increase of pressure under the asperity peaks. This assumption has been tested by examining the theoretical buildup of pressure under the asperity peaks under these conditions using a program described in section 6.5.1.

6.4.2 With no pressure in the valleys ($\Lambda \leq 0.88$)

For cases where $\Lambda \leq 0.88$, integration of the hydrodynamic equations shows that the oil pressure in the valleys is negligible. All the load is then taken on the peaks, with a consequent increase in pressure and hence viscosity there. The viscosity in the valleys is small by comparison and hence the contribution to traction from these regions can be neglected. If A_1 , the ratio of the area of contact in which the pressures are significant in the rough experiments to this area for smooth line contacts, can be estimated the mean pressure under these regions will be \bar{p}/A_1 and the mean shear stress under these regions will be τ_n/A_1 . If we take as a reference case a film thickness equal to the smooth contact film thickness h_d , the nominal shear stress-strain rate relationship that would be found can be deduced from the oil rheology. The ratio of the nominal strain rate found in the experiments to the strain rate found for the reference film thickness at a given nominal shear stress $\dot{\gamma}_e/\dot{\gamma}_s$, then equals the ratio of the mean film thickness under the loaded contacts to the line contact film thickness h_a/h_d . The actual shear stresses under the contacts are of course higher than the nominal shear stresses, being τ_n/A_1 .

Estimating the true area of contact ratio area, was not straightforward. Because the flattened profiles were formed by loading the disc asperities until they yielded, there will be some elastic recovery on unloading from the flattened state. The resulting unloaded profile then has a slightly concave profile. Any subsequent loading at a lower pressure will not completely squash out this elastic recovery. Instead only a fraction of the flattened top will actually be in contact.

Appendix C derives three different estimates of the area of contact ratio A_1 . The best estimate is taken as that due to Greenwood's numerical calculation [39] where $A_1 = 0.363$. The effect that the different estimates of contact area would have on estimated experimental film thicknesses can be seen from figure 3b, where the resulting graphs for smooth contact appropriate for individual Hertz contacts ($A_1 = 0.394$) and using Greenwood's width calculation, with his approximation to the contact length ($A_1 = 0.313$) are shown. The difference in the inferred film thicknesses at a given nominal stress τ_n is then the horizontal offset between the smooth lines at this stress.

This method for estimating film thicknesses is only appropriate when all the load is taken on the asperities. If the deduced film thickness is greater than the smooth

film thickness h_d , then there will certainly be a significant pressure buildup in the valleys and a correspondingly lower mean pressure and hence viscosity under the peaks. Estimates assuming that all the load is taken on the peaks will then overestimate the true minimum film thickness.

In addition to calculating the size of the contact Greenwood also calculates the maximum difference in elastic deflection across the contact. For these experiments this is found to be about $0.125\mu\text{m}$. This suggests that the effect of elastic deflections on the pressures in the valleys will be small in most cases. When the pressure is concentrated on the peaks the valleys will be rather reduced in depth, but in these cases the size of the valleys is unimportant since there is no pressure buildup there anyway, as long as the valleys are not squashed completely flat. Since the depth of the valleys is greater than the maximum elastic deflection this will not be the case. In less extreme cases where the pressure distribution is more constant across the width, the elastic deflections will be negligible. However, it is possible that there will be some effect in the transition regime. It is found that the exact distribution of the pressure between the peaks and valleys is rather sensitive to the geometry. Any elastic flattening could, in these cases, have a significant effect on the pressures generated and hence on the traction.

6.4.3 Results of film thickness deductions

By assuming either that the pressure across the contact is uniform, or that all the load is taken on the peaks, film thicknesses have been deduced from the rough traction curves. These film thicknesses have been deduced for nominal shear stresses of 2 and 4MPa where the pressure is assumed uniform, and at 4 and 7.5MPa where all the load is assumed to be on the asperity peaks. Results are given in table 6.2. Results in brackets in table 6.2 correspond to calculations where the assumptions used in deducing the film thickness (either that the pressure is all concentrated on the peaks or is uniform across the width) are not found to hold. In general this was found to be the case for Λ between 0.88 and 2. In these cases the film thickness will then be of an intermediate type between these two extremes. It is likely that, where the film thickness ratio deduced by assuming no pressure rippling falls below 0.1, the film thickness is underestimated as the areas of higher pressure contribute to the traction measured. Similarly, the deduced film thicknesses assuming that all the load was carried

on the asperity tops will overestimate the film thicknesses if some of the load is in fact carried by the pressure in the valleys. In effect in the transition region between the two calculations for Λ between 0.88 and 2 the deduced film thicknesses are likely to be inaccurate. Results for a nominal shear stress of 4MPa are plotted in figure 6.7 for those film thicknesses with Λ less than 0.88 or greater than 2.

By comparing the results at the two different nominal stresses in table 6.2, it can be seen that the deduced film thickness is independent of the nominal shear stress for those cases where the pressure is assumed uniform. Where there is no valley pressure however, the deduced film thicknesses are significantly less at the higher nominal shear stresses.

The thinning of the films at the higher shear stresses can also be deduced from figures 6.3a-d. Noting that the ratio of the deduced film thickness to the smooth contact film thickness is merely the horizontal offset between rough traction curves and the appropriate reference traction curve, the fact that the rough curves are steeper than the corresponding reference curves implies that the film thicknesses are thinning at the higher strain rates.

This is to be expected, since it can be shown that, in the Eyring viscous regime, side leakage of oil is enhanced by sliding in the direction of rolling. (Details are given in appendix D.) This will reduce the film thickness under the contact. Under the contact, the reduction in effective viscosity in the side leakage direction due to non-Newtonian flow is the same as the reduction in effective viscosity in the rolling direction. For experiments with $\Lambda < 0.88$, the effective viscosity is reduced by a factor of 4.3 at a nominal shear stress of 4 MPa and by 50 at 7.5 MPa, indicating that side leakage enhancement may well be significant at the higher shear stress. The actual effect of enhanced side leakage on the central film thickness generated is hard to gauge and it may change significantly with the operating conditions.

If the film thickness were assumed not to change with sliding speed then the slope of the rough curves implies a Eyring shear stress of 5.2 MPa. For similar mineral oils (see figure 6.5), these Eyring shear stresses are not found until pressures well above those under the asperity peaks, suggesting that the need to extrapolate measurements with smooth discs to slightly higher pressures cannot be the cause of the apparent thinning of the oil films with sliding.

Since the rolling speeds are small with the lower Λ ratios, the oil temperature rise in the bite is also small. In any case a rise in temperature would give a *decrease* in traction with sliding speed, when compared with the isothermal case, rather than the increase found.

6.5 Theoretical film thicknesses

To compare the deduced experimental minimum film thicknesses with elasto-hydrodynamic theory two methods are used to analyse the problem, appropriate to each of the two extremes where the oil pressure is constant across the contact and where the load is only carried on the asperity peaks.

6.5.1 With uniform pressure ($\Lambda > 2$)

Where the oil pressure is uniform, the numerical integration procedure described in chapter 4 has been modified to calculate the oil pressure buildup. The measured r.m.s. of the profile is used to modify the smooth Reynolds equation according to equation 4.5. The inlet shape in the circumferential direction is taken as that of a Hertz line contact. The mean film thickness is then adjusted until the reduced pressure at the beginning of the Hertz flat equals $1/\alpha$. The difference between the mean film thickness and the minimum film thickness under the asperity peaks is dependent on the geometry of the roughness profile. This is also the distance between the top of the asperities and the mean height of the roughness which was measured from the particular geometry of figure 6.1c using a simple program and the digitised profile. (This distance was found to be $0.46\mu\text{m}$ for the geometry of figure 6.1c.) Results are only calculated using the profile of figure 6.1c, since this is the profile corresponding to most of the experimental measurements in this regime. Similar results would apply to profiles having a similar shape although the exact position of the theoretical curve will also depend on the inlet shape and the height of the asperities.

To determine where the assumption of a constant pressure distribution across the valleys becomes invalid the two dimensional Reynolds equation is also considered in the inlet. For this calculation a slightly different geometry is assumed, taking truncated triangular ridges with a flattened area equal to half the width of the asperity spacing.

(In this calculation the actual shape of the asperities is relatively unimportant.) The circumferential shape is taken to be Hertzian. A modification of Tønder's program [91] described in chapter 4 is used which solves the finite difference formulation of the hydrodynamic equations. The boundary conditions applied are zero transverse pressure gradient at the midpoint between contacts and zero pressure gradient at entry to the Hertz flattened section. Small differences in pressure across the entry to the contact will quickly be reduced due to slight elastic deflections and due to side leakage away from the pressure peaks. However as the pressure differences going into the flattened region become larger, the effects of elasticity will become more important. In the extreme the contact then behaves as an elastohydrodynamic point contact and side lobe constrictions are formed which restrict the side leakage of oil and allow a greater rise in pressure gradient across the contact. In this case the oil film thickness must be rather less than the elastic deflections. Assuming that the elastic deflections are still rather less than the amplitude of the roughness, the oil pressure in the valleys will be much less than the pressures under the flattened areas and can be neglected.

6.5.2 With no pressure in the valleys ($\Lambda \leq 0.88$)

Where there is negligible oil pressure in the valleys the contact resembles a row of individual point contacts. It will be assumed that results for individual point contacts can be applied to this row of contacts. The presence of neighbouring asperities will affect the width of each individual contact appreciably (as found for example in appendix C) but it is likely that the critical inlet area will be sufficiently similar in shape in the two cases to have little effect on the central film thickness.

Appendix E addresses the estimation of central film thicknesses in isolated elliptical contacts. It is found that the film thickness can be estimated applying a correction for the effect of side leakage of oil in the inlet region to a theoretical calculation of the film thickness by Hooke [46] which neglects side leakage. The effect of side leakage is determined by a parameter n/b , the ratio of a typical hydrodynamic length to the Hertz semi-width for the contact. Figure E.2 shows how the film thickness is reduced from Hooke's film thickness as n/b increases. The reduction in film thickness is influenced by a parameter c expressing how far into the piezo-viscous region the contact is and by the ellipticity ratio ψ of the Hertzian contact, where $\psi = b/a$, the ratio of the

semi-minor and major axes of the contact ellipse. In these experiments c is 10 and the ellipticity ratio is about 0.13. For this case the 'MPFS' curve in figure E.2 is shown to be appropriate. Appendix E shows in more detail how the theoretical film thickness can be calculated.

6.5.3 Results of theoretical film thickness calculations

Theoretical film thicknesses have been plotted on figure 6.7 along with the inferred experimental thicknesses. For $\Lambda < 1$ the modification to Hooke's calculation has been used to deduce theoretical film thicknesses. For Λ greater than say, 0.88, pressure will buildup in the valleys and an analysis ignoring this will not be accurate. For Λ greater than 2, the curve calculated by integrating the averaged Reynolds equation assuming no pressure gradients is to be preferred. Between $\Lambda = 0.88$ and 2, neither method is to be believed. Where no pressure in the valleys is assumed, the predicted film thickness would have some pressures there; where the pressure is assumed uniform, there will certainly be some higher pressures on the peaks, causing elastic deflections and preventing the predicted close approach of the surfaces.

In the region in which neither calculation is appropriate, it has not been found possible to estimate either theoretical or experimental film thicknesses with confidence. However qualitative arguments lead to an approximate way of estimating the theoretical film thickness under the contact. As the Λ ratio increases the hydrodynamic pressure in the valleys will increase and the load on the asperity peaks will decrease. Although the film thickness under isolated contacts is strongly influenced by the speed and material parameters, it is only weakly affected by the load on the asperity tops. For example the maximum change in load on the asperity tops is given by $1/A_1$ which would give a change in central film thickness of 9% according to Hooke's analysis. The major influences as the Λ ratio increases are the reduction in the side leakage of oil in the inlet as the hydrodynamic pressure in the valleys increases and the change in elastic deflections of the asperities as the pressure in the valleys increases. As long as the hydrodynamic pressures in the valleys are not too large, the isolated point contact film thickness may still give a good approximation to the film thickness under the asperity tops.

Karami *et al.* [55] consider just this type of transition from the situation with no

pressure in the valleys, to one with a more even distribution of pressure across the contact. They considered an array of asperities with an ellipticity ratio of 0.57 and varied the load by a factor of 8, solving the hydrodynamic and elastic equations numerically. Although Λ changed little with increasing load from 2.3 to 1.8, the elasticity of the asperity tops caused a significant increase in the valley pressures as the gap in the valleys closed. The ratio of the pressure on the contact centre line under the asperity peaks to the pressure midway between asperities then decreased from 5 to 1.8 so that the oil pressure distributions from adjacent asperities begin to interact quite strongly. In figure E.2 the ratio of the central film thickness to Hooke's film thickness for these results has been plotted for these points which are not isolated.. These points agree quite well with similar results for isolated contacts; the presence of the adjacent contacts and the significant valley pressures only cause a slight increase in asperity film thickness due to the reduced side leakage and reduced load under the asperities. The results at the higher loads correspond to the points with the smaller values of n/b ,

This approach suggests a way of deriving 'theoretical' traction curves for the intermediate cases. Taking the geometry of the $0.5\mu\text{m}$ disc, the film thickness in the transition region will be taken from Hooke's modified analysis (shown in figure 6.7). As a simple approximation to what might be the actual situation, the pressure in the valleys has been assumed to vary linearly with the Λ ratio from zero at $\Lambda = 0.88$ to the mean nominal pressure at $\Lambda = 2.04$. The mean pressure under the peaks can be found by considering the distribution of the load between the peaks and the valleys. The rheology of the oil there and the assumed film thickness can then be used to derive traction curves at each Λ ratio. These are shown along with the measured traction curves in figure 6.3c. Agreement is good, suggesting that this view of the contact may be close to the actual pressure and film thickness distribution.

6.6 Conclusions

Experiments have been performed to show how the traction behaviour in mixed lubrication changes from full film lubrication to a type of micro-elastohydrodynamic lubrication. At these two extremes, film thicknesses inferred from the experiments are found to be in reasonable agreement with the new theoretical estimates. The converse is also true that, if we had used the theoretical film thicknesses to derive traction curves, these curves would have given good agreement with the experiments.

Where the load was taken on the peaks, with peak shear stresses well above the Eyring shear stress, it was found that the deduced oil films were significantly smaller at higher sliding speeds. This does not appear to be due to errors in deducing these films, but is more likely to be due to the effect of non-Newtonian flow on side leakage producing a thinning of the film.

In the intermediate regime for $0.88 < \Lambda < 2$, where there is significant pressure in the valleys but also significantly higher pressures under the peaks, the traction behaviour is well described by assuming that the film thickness under the asperity peaks is unaffected by the valley pressures and is given by the analysis suggested in appendix E. In this approximation the valley pressures are relatively unaffected by the film thickness under the peaks and are assumed to have a simple variation with speed. The traction behaviour is then governed by the rheology of the oil under the peaks, while the pressure under the peaks and the viscosity of the oil there is determined by the total load minus the load taken by the hydrodynamic pressure in the valleys. However the exact nature of the transition may be strongly influenced by the elasticity of the asperities. In these experiments the maximum elastic squashing of the asperities was not sufficient to influence the buildup of pressure in the valleys strongly. Where the asperities are relatively 'soft' as for example in the work of Karami *et al.* and recent work by Seabra and Berthe [84], the valley depth and the buildup of pressure there is significantly changed as the Λ ratio changes and the asperity tops become more loaded. In extreme cases the asperities can be squashed almost flat by small pressure ripples and the sharp change in the traction behaviour as Λ falls below 2 will not be observed.

In these experiments, the traction behaviour even at small Λ ratios is well described by considering only the bulk properties of the oil, in contrast to the results of Bair and Winer, who found a breakdown in bulk lubrication for $\Lambda < 1$, or Evans and Johnson,

who find that this occurs for $\Lambda < 0.5$. Because of the relatively wide 'asperities' used, the film did not appear to breakdown for $\Lambda = 0.09$ with films as small as 8nm. This is the same film thickness as that deduced from the traction experiments of Mizuno and Okamoto [66], in what was inferred to be a micro-plasto-hydrodynamic regime when sliding began to influence friction. With less advantageous lubrication conditions, for example with narrower asperities or a distribution of asperity wavelengths, the films under the asperity peaks may become too small to allow full film lubrication and in these cases a higher traction coefficient can be expected if the surfaces are not separated by an adequate chemical layer of boundary lubricants.

Table 6.1 Asperity geometry

	d (μm)	r.m.s roughness (μm)	A_0	wavelength λ (μm)
Figure 6.1a	0.7	0.47	0.3	90
Figure 6.1b	0.55	0.40	0.35	90
Figure 6.1c	0.50	0.40	0.44	90
Figure 6.2a	4.75	3.37	–	140
Figure 6.2b	3.0	2.26	0.44	140

Table 6.2 Experimentally deduced film thicknesses

a) Assuming no pressure ripple.

Disc roughness d	Λ	Film thickness ratio h_a/h_d	
		$\tau_n = 2\text{MPa}$	$\tau_n = 4\text{MPa}$
0.7 μm	3.58	1.00	–
	1.93	(0.072)	(0.094)
0.55 μm	2.16	0.29	0.33
	1.85	(0.038)	(0.032)
	1.58	(0.005)	(0.003)
0.50 μm	2.70	0.51	0.50
	2.04	0.19	0.14
	1.42	(0.01)	(0.01)

b) Assuming all load carried on peaks.

Disc roughness d	Λ	Film thickness ratio h_a/h_d	
		$\tau_n = 4\text{MPa}$	$\tau_n = 7.5\text{MPa}$
0.55 μm	1.85	(11.7)	–
	1.58	(2.14)	–
	1.44	(1.51)	–
	1.29	(0.28)	–
0.50 μm	2.04	(18.2)	–
	1.42	(3.47)	–
	1.26	(1.17)	–
	1.06	(0.42)	(0.32)
	0.88	0.23	0.10
3.0 μm	0.55	0.23	0.12
	0.34	0.26	0.13
	0.21	0.33	0.13
	0.15	0.25	0.09
	0.09	0.22	0.09

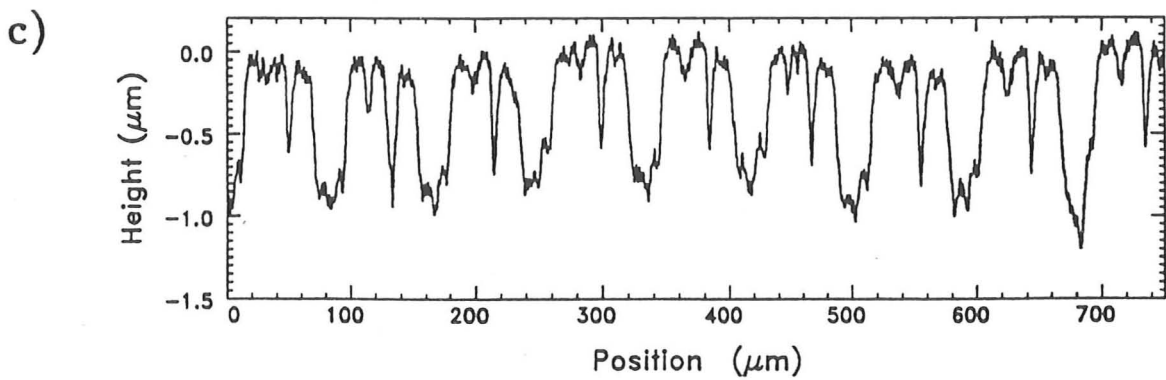
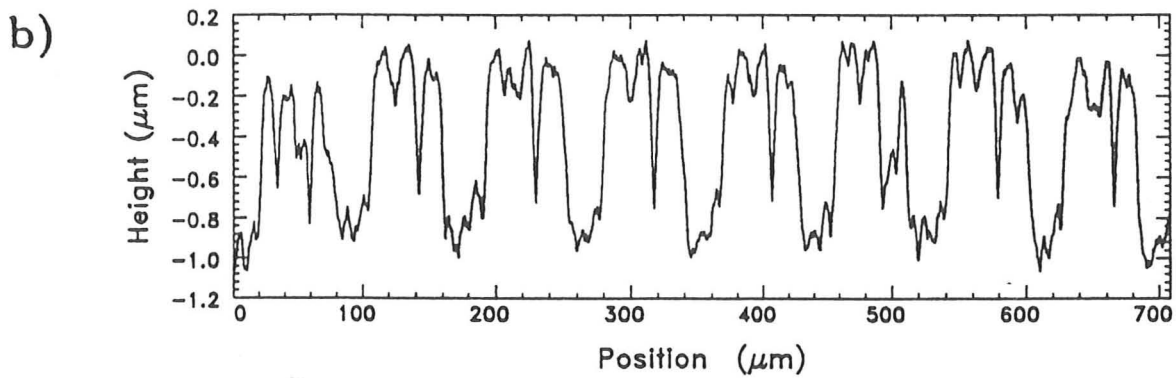
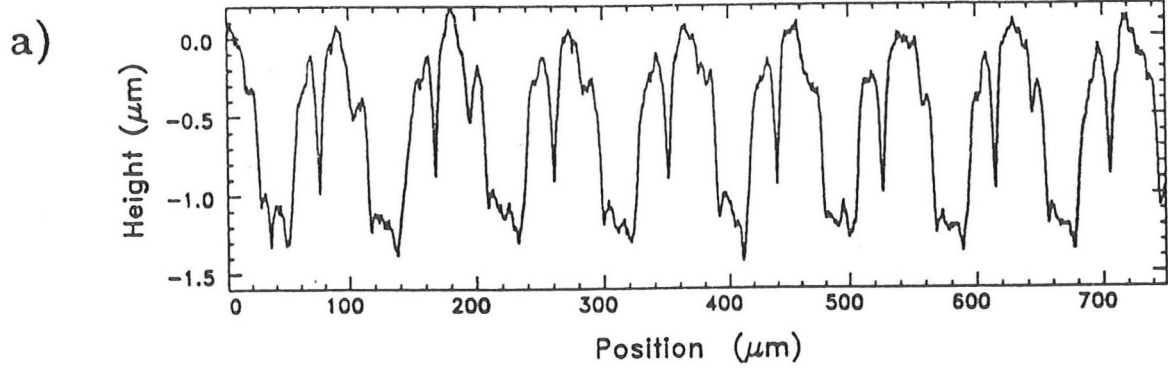
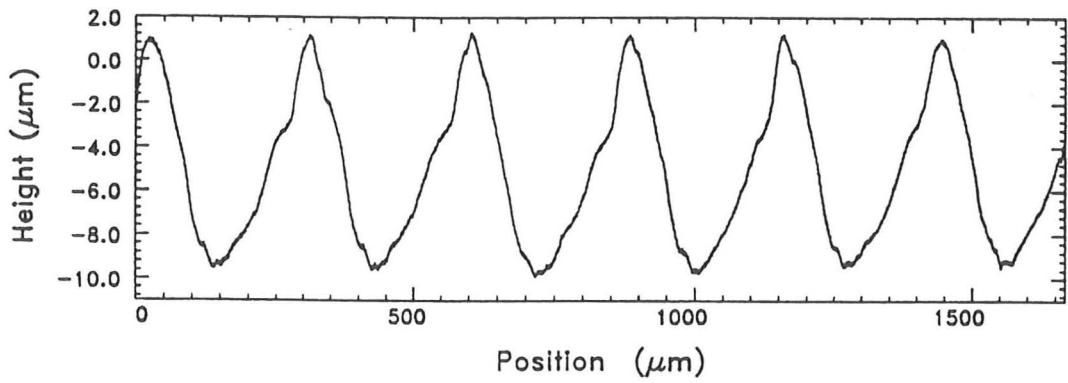


Figure 6.1 Disc roughness profiles a) $d = 0.7\mu\text{m}$,
b) $d = 0.55\mu\text{m}$,
c) $d = 0.50\mu\text{m}$.

a)



b)

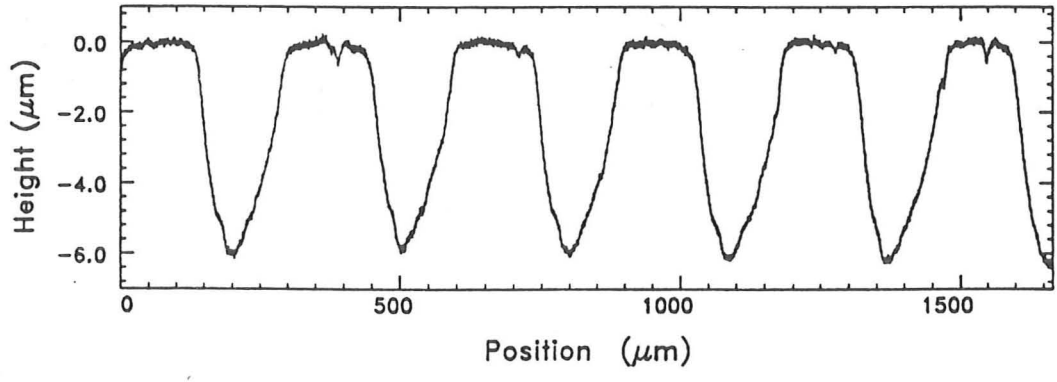
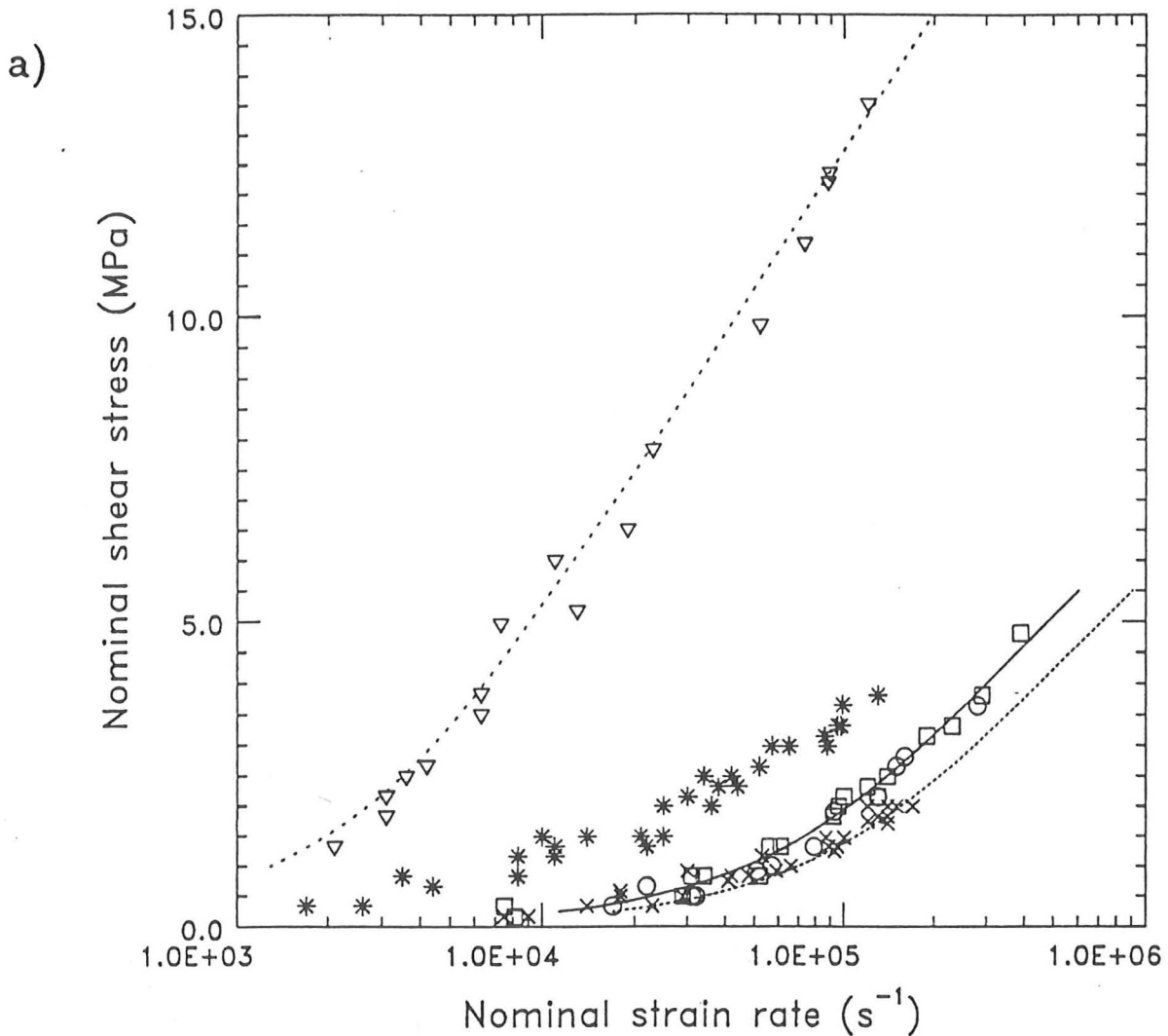


Figure 6.2 Disc roughness profiles a) $d = 4.75 \mu\text{m}$,
b) $d = 3.0 \mu\text{m}$.

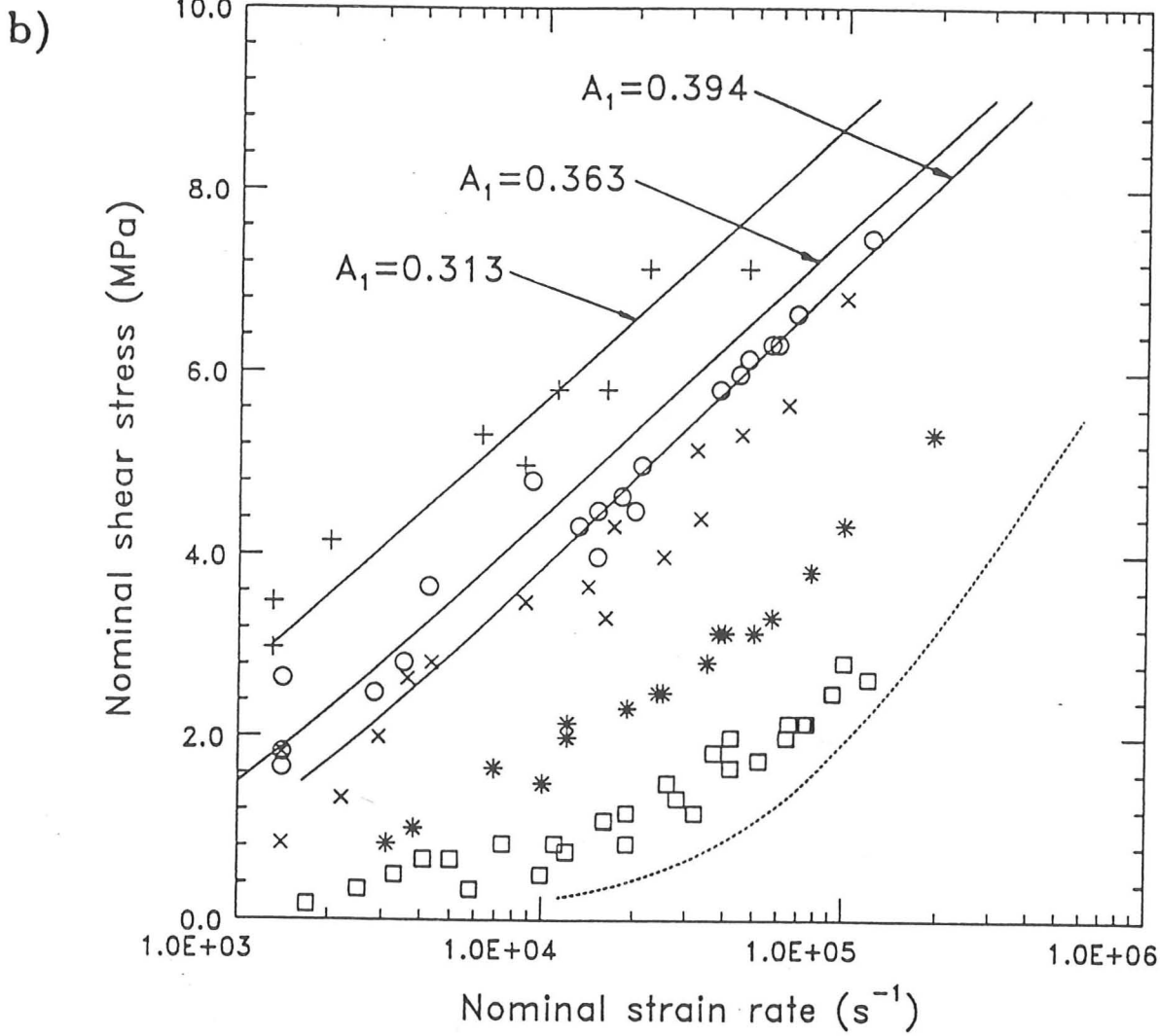


KEY

- $\Lambda=32, u=1.18\text{m/s}, \bar{p}=205 \text{ MPa at } 25^\circ\text{C}$
 - $\Lambda=15, u=0.39\text{m/s}, \bar{p}=205 \text{ MPa at } 25^\circ\text{C}$
 - ▽ $\Lambda=27, u=1.18\text{m/s}, \bar{p}=412 \text{ MPa at } 25^\circ\text{C}$
- } smooth disc

- Fitted curve to smooth discs results, $\bar{p}=205 \text{ MPa at } 25^\circ\text{C}$
 - Estimated curve for smooth discs, $\bar{p}=205 \text{ MPa at } 30^\circ\text{C}$
 - Fitted curve to smooth discs results, $\bar{p}=412 \text{ MPa at } 25^\circ\text{C}$
 - * $\Lambda=1.93, u=1.18\text{m/s}, \bar{p}=205 \text{ MPa at } 25^\circ\text{C}$
 - x $\Lambda=3.58, u=3.93\text{m/s}, \bar{p}=205 \text{ MPa at } 30^\circ\text{C}$
- } $d=0.7\mu\text{m}$

Figure 6.3 Traction measurements
a) Smooth discs and for $d = 0.7\mu\text{m}$,



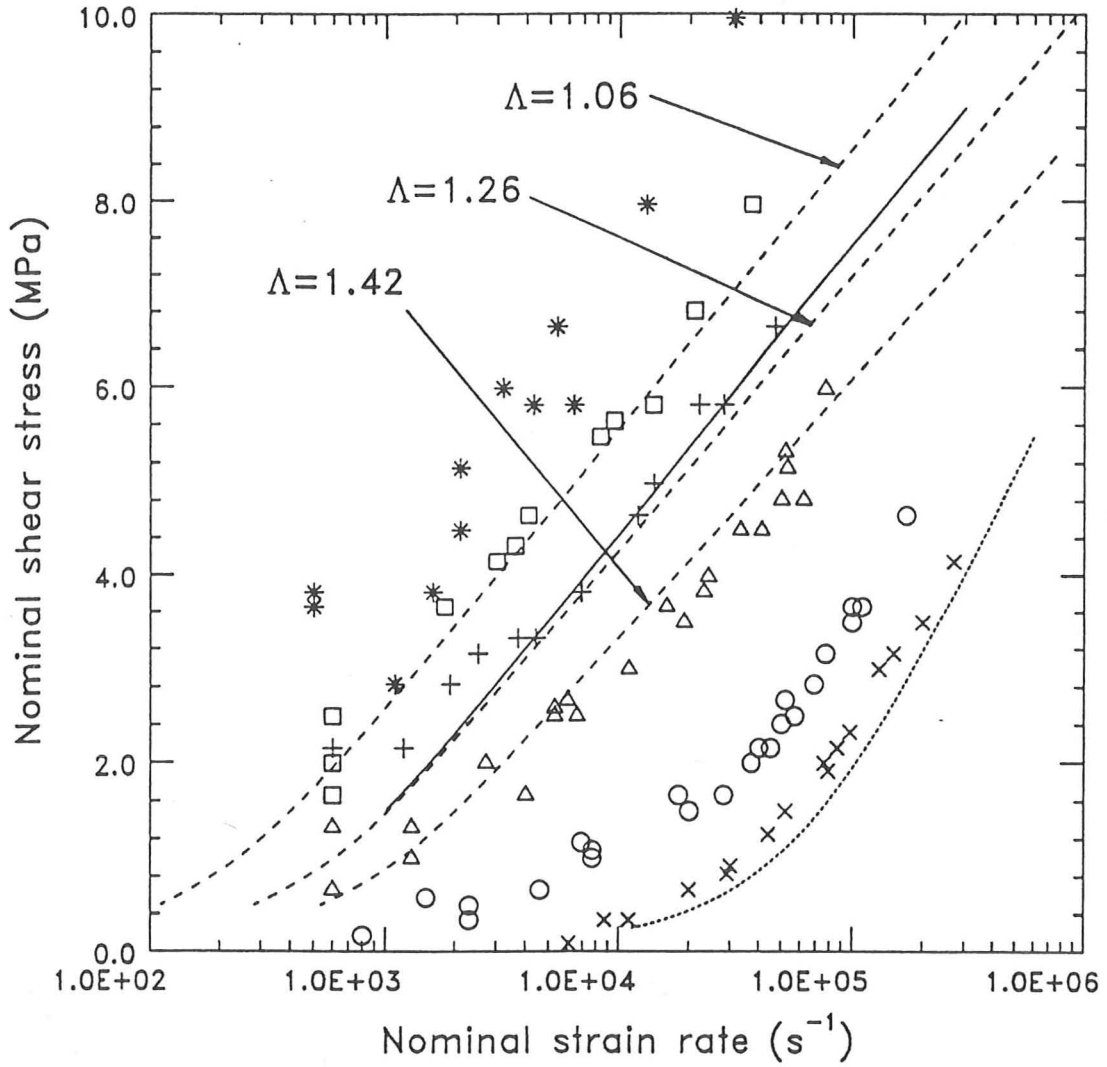
KEY

- $\Lambda=2.16, u=0.982m/s$
- * $\Lambda=1.85, u=0.785m/s$
- × $\Lambda=1.58, u=0.628m/s$
- $\Lambda=1.44, u=0.550m/s$
- + $\Lambda=1.29, u=0.471m/s$

..... Traction curve for smooth discs
 — Reference curves

Figure 6.3 Traction measurements
 b) $d = 0.55\mu m$,

c)



KEY

- × $\Lambda=2.70$, $u=1.178\text{m/s}$
- $\Lambda=2.04$, $u=0.785\text{m/s}$
- △ $\Lambda=1.42$, $u=0.471\text{m/s}$
- + $\Lambda=1.26$, $u=0.393\text{m/s}$
- $\Lambda=1.06$, $u=0.314\text{m/s}$
- * $\Lambda=0.88$, $u=0.236\text{m/s}$

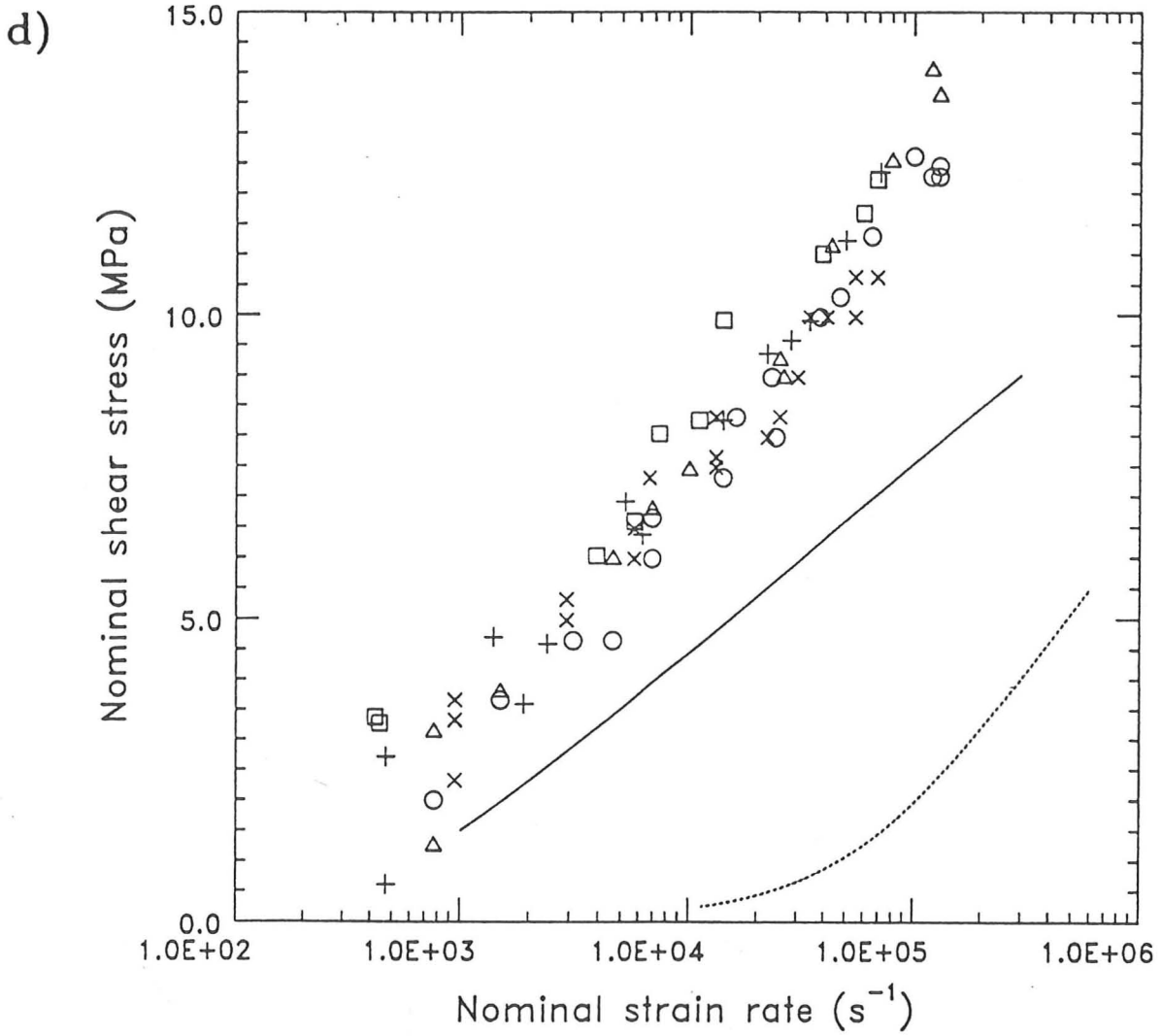
..... Traction curve for smooth discs

———— Reference curve, $A_1=0.363$

- - - - - Estimated traction curves for intermediate Λ

Figure 6.3 Traction measurements

c) $d = 0.50\mu\text{m}$,

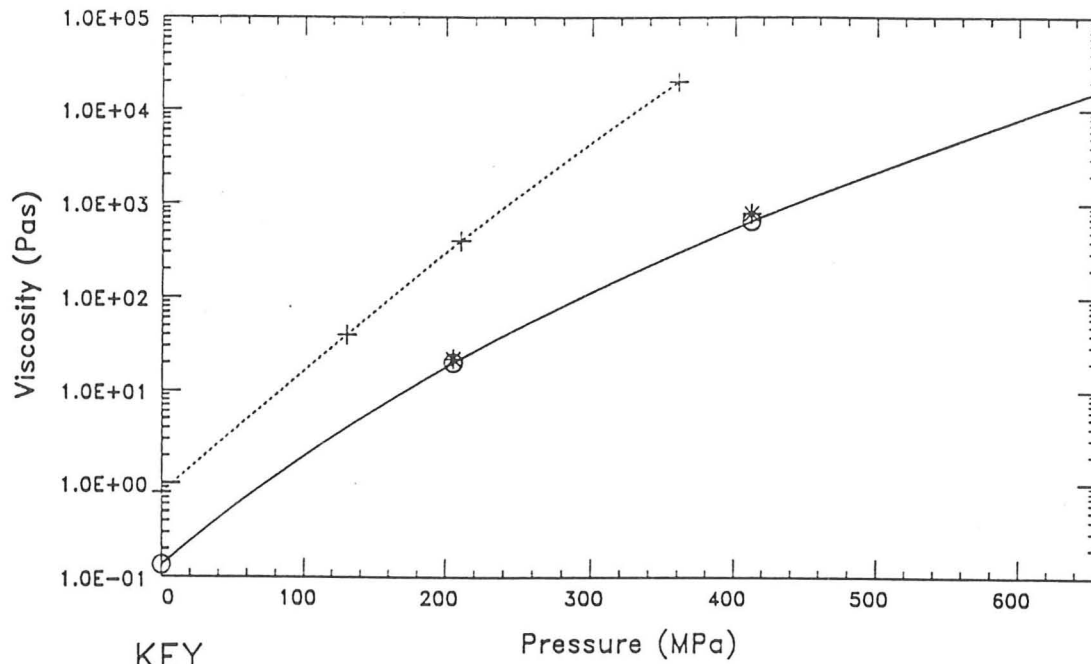


KEY

- × $\Lambda=0.55$, $u=1.57\text{m/s}$
- $\Lambda=0.34$, $u=0.785\text{m/s}$
- △ $\Lambda=0.21$, $u=0.393\text{m/s}$
- + $\Lambda=0.15$, $u=0.236\text{m/s}$
- $\Lambda=0.09$, $u=0.118\text{m/s}$

----- Traction curve for smooth discs
 ————— Reference curve, $A_1=0.363$

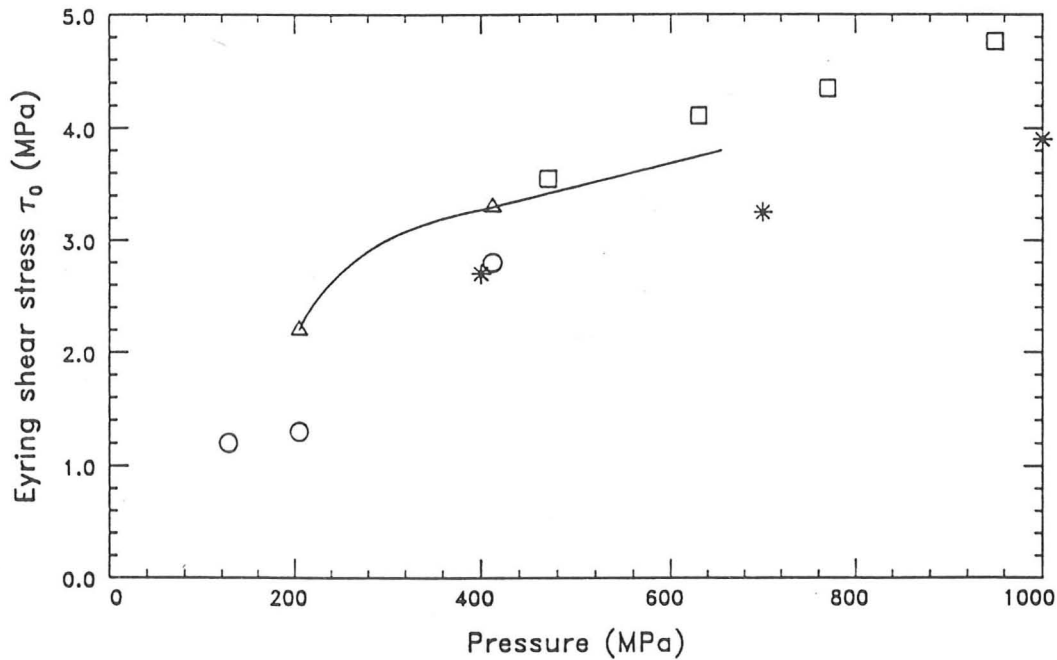
Figure 6.3 Traction measurements
 d) $d = 3.0\mu\text{m}$.



KEY

- Vitrea 68 small strain viscosity at 25°C
- * Vitrea 68 large strain viscosity at 25°C
- Extrapolation used for Vitrea 68
-+..... Turbo 33 at 30°C (Tevaarwerk)

Figure 6.4 Viscosity of Vitrea 68 and Turbo 33 mineral oils.



KEY

- ▲ Vitrea 68 at 25°C
- * Turbo 33 at 30°C (Tevaarwerk)
- HVI 650 at 30°C (MPFS)
- HVI 650 at 40°C (Evans)
- Best approximation to data for Vitrea 68 at 25°C

Figure 6.5 Eyring stress τ_0 for Vitrea 68 and similar mineral oils.

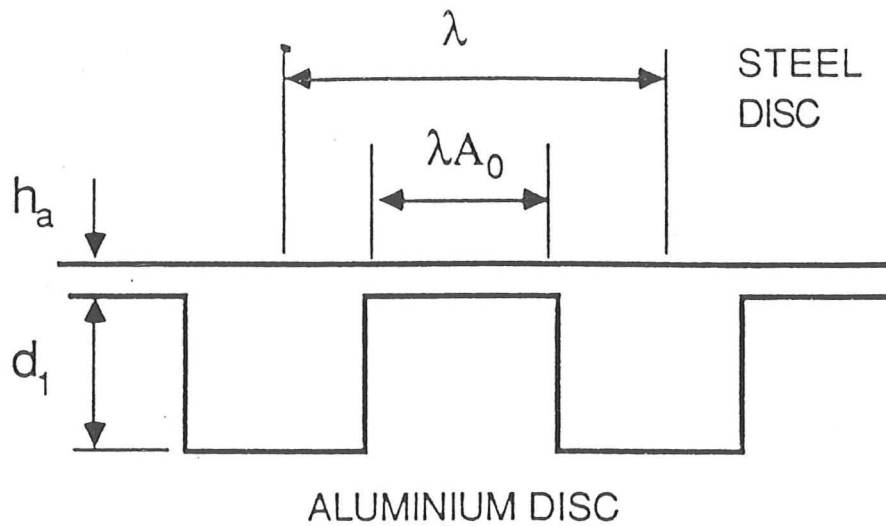
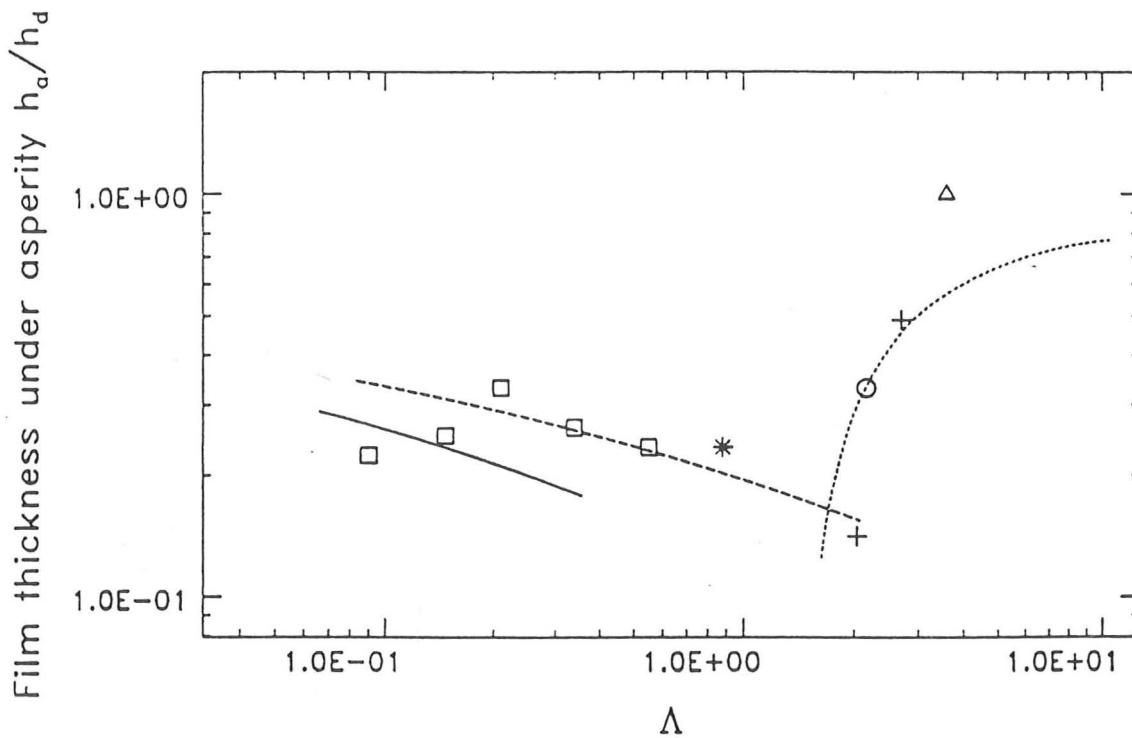


Figure 6.6 Idealisation of the asperity geometry used to deduce film thicknesses where $\Lambda > 2$.



KEY

- Δ Experiments, $d=0.7\mu\text{m}$
 - \circ Experiments, $d=0.55\mu\text{m}$
 - $+$ Experiments, $d=0.5\mu\text{m}$
 - \square Experiments, $d=3.0\mu\text{m}$
 - $*$ Experiments, $d=0.5\mu\text{m}$
- } Assuming a uniform pressure
- } Assuming all load on peaks

- Modified Hooke theory for $d=3.0\mu\text{m}$
- - - - - Modified Hooke theory for $d=0.5\mu\text{m}$
- MPFS theory assuming a uniform oil pressure for $d=0.5\mu\text{m}$

Figure 6.7 Experimental and theoretical film thicknesses.

CHAPTER 7

CONCLUSIONS

The physical processes determining friction and lubrication in metal rolling have been examined in this dissertation. Conditions appropriate both to strip and thin foil rolling in the mixed lubrication regime have been considered.

To calculate film thicknesses and friction in metal rolling, two effects had first to be considered.

- i) Lubricant properties. Although the shear behaviour of the lubricants used in rolling are adequately modelled by a Newtonian viscosity in the inlet, the behaviour in the bite at higher pressures may be non-Newtonian. Measurements of the rheological properties of Somentor 31, a rolling oil used industrially in aluminium foil rolling, have been made at the high pressures and shear rates found in practice using the disc machine technique described in [28]. It was found that the shear behaviour of this oil was well described by the Eyring rheological model.
- ii) Crushing of asperities in metal working. The generation of the oil film partially separating the strip and roll is determined by the combination of hydrodynamic action of the oil in the entraining wedge and the mechanics of the deformation of the asperities on the strip as they come into contact with the hard roll. Crushing of asperities where the substrate is not deforming is reasonably well understood but, where the bulk material is deforming, the crushing process has received less attention. Earlier workers have shown that the crushing of asperities can be much enhanced under these circumstances. Chapter 3 addresses this aspect of the problem. In that chapter conditions where the lay of the roughness is either perpendicular ('transverse roughness') or parallel ('longitudinal roughness') to the straining direction are considered. In the first case a slip-line field has been found. For the longitudinal roughness an upper bound approach used by Wilson and Sheu has been extended. In both cases experiments have been performed using work hardened copper blocks to measure the crushing process and the growth of the contact area as the bulk material strains. For transverse roughness, this growth in contact area is found to agree well with the theory at high mean pressures, but

is less good where the mean normal pressure is smaller, or where the asperities undergo large strains. The results of the theoretical and experimental results for longitudinal results have been approximated by a simple empirical formula relating the crushing rate to the mean pressure, suitable for use in the lubrication analysis.

In the analysis of the generation of films in rolling, this crushing mechanism has been combined with a suitably modified Reynolds equation to calculate the hydrodynamic buildup of pressure in the inlet. The calculation of the film thicknesses under the asperity 'contacts' and in the intervening valleys have been considered separately. The roughness of the roll and strip has been modelled as wholly longitudinal, although it is appreciated that there will be some transverse hydrodynamic pits on the strip. It is argued that these will not affect the pressure buildup significantly where the lubrication is in the mixed regime. For most conditions of mixed lubrication rolling only three dimensionless groups influence the film thickness generation in the valleys and under the areas of close contact, Λ_s , the ratio of the smooth film thickness to the roughness height, t_1/λ , the ratio of the strip inlet thickness to the 'wavelength' of the roughness and $\alpha\sigma_y$, the product of the pressure viscosity of the lubricant and the yield stress of the strip. The effect of these parameters on the valley film thickness is found for strip and foil rolling conditions. The area of contact ratio can be deduced from these film thickness calculations. In many cases, the mean film thickness does not change greatly whether or not roughness is significant, but the underlying mechanisms are very different in the two cases.

In the region of close contact under the asperities a novel approach to the calculation of film thicknesses is introduced, based on an effective entraining length in the inlet region. Although this calculation neglects side leakage of oil in the bite, it provides at least a first approximation to the film thickness under the contacts.

The calculations of the film thicknesses under the contacts and in the valleys have been used, with the results of measurements of the shear behaviour of an aluminium foil rolling lubricant, to deduce traction curves for foil rolling. The total friction is made up of contributions from the asperity contacts and from the valleys. Because there is uncertainty about the mechanism of friction under the contacts, friction calculations for both 'micro-plasto-hydrodynamic' and boundary lubrication have been derived. Results for a rolling speed of 5 m/s (giving an area of contact ratio of 0.53) at a slip ratio

of 0.3 are typical. The contribution to the friction coefficient from the valleys was found to be 0.0002, 0.005 and 0.020 at pressures of 230, 645 and 1510 MPa respectively. These must be added to the asperity contact contributions, which were 0.0015, 0.014 and 0.03 for hydrodynamic lubrication, or 0.007, 0.007 and 0.019 for boundary lubrication at the respective pressures. The hydrodynamic components of friction are rather lower than most quoted values because of the lower viscosity of the oil used in rolling aluminium foil than that used in other rolling processes. The boundary components are also lower than generally quoted values because the shear strength of the boundary layers, taken from [12], is smaller than that normally assumed.

Chapter 5 describes a set of experiments on an experimental rolling mill to measure oil film thicknesses and area of contact ratios for thicker strip. Lead, soft and harder aluminium were rolled with a range of inlet strip thicknesses and speeds, to investigate the effect of the variables found from the theory to be important. The mean film thickness was measured both by finding the amount that an oil drop spread out on rolling and from the profile of the crushed roughness when rough strip was rolled with smooth rolls. These profile measurements were also used to find the area of contact ratio. It was found that the film thickness measurements did not agree with the simple theory where the roughness was much less than the film thickness, with measured films up to half that predicted. After investigating both experimentally and theoretically a number of hypotheses to explain this discrepancy, it was concluded that the uneven lubrication conditions of the experiments, in which only one side of the strip was lubricated, were causing the foil to deflect in the inlet region thereby reducing the effectiveness of the inlet in generating an oil film. After taking this into account experimental measurements with rough surfaces were found to agree reasonably with the theoretical mean films, although the scatter in individual results was fairly large. The large influence of Λ expected theoretically was clearly shown in the experiments. There was some evidence in the experiments of the small effect of strip thickness and yield stress predicted from theory.

Finally, measurements were made in a disc machine to study the effect of the Λ ratio on traction in the mixed lubrication regime. The details of the dependence of friction on Λ will be different in the cases of elastic disc contacts and metal rolling friction.

Nevertheless, the measurements in the disc machine can be explained by applying the approach also used to estimate traction in metal rolling.

- i) Asperity film thicknesses can be estimated using hydrodynamic theory, including the effect of oil side leakage in the inlet on the pressure buildup there.
- ii) Traction forces can be deduced from the calculated film geometry using the rheological properties of the oil at the pressures and strain rates under the contacts and in the valleys.

The apparent thinning of the asperity films in these disc experiments with increased sliding was attributed to side leakage of oil in the nip, enhanced by the non-Newtonian properties of the oil. In metal rolling the pressures in the valleys rise to the asperity pressures close to the front of the contact, so that this thinning should not occur.

In summary, the theoretical model of rolling allows the film thicknesses under the valleys, the area of close contact under the asperities and the film thickness under these contacts to be estimated. The rheological measurements of chapter 2, or similar ones, can then be used to determine traction curves for mixed lubrication rolling. The valley film thickness and area of contact ratio analysis is supported by rolling experiments while the method suggested of using hydrodynamic theory to calculate the asperity films and using the rheological properties to calculate traction curves is supported by the experiments in the disc machine.

7.1 Recommendations for future work

7.1.1 Thermal analysis

A thermal analysis was used in the inlet zone but thermal effects in the work zone were not included in this dissertation. Because the region determining the film thickness and area of contact ratio is small compared with the length of the bite, results obtained for the film thickness and area of contact ratio will not be affected by this omission. However, the traction predictions would be changed by changes in the temperature in the nip. Section 1.3.3 outlines some of the factors that would have to be included in a full thermal analysis..

7.1.2 The geometry of rolls with thin foil

The application of the lubrication theory to foil rolling was limited by the number of roll shape solutions available. When more solutions are found it will be possible to determine friction for a greater variety of foil rolling conditions. Section 4.7 outlines how the smooth film thicknesses can be derived simply by approximating the film shape in the inlet as a straight line. If there is little change in the slope of the roll between the inlet and the beginning of the work zone, the results given in chapter 4 can be used to deduce film thicknesses, the area of contact ratios and traction curves.

7.1.3 Breakdown of lubrication

The transition between full film and boundary lubrication does not seem to be well defined. Although additives clearly play a rôle in friction in metal working, their importance in determining the friction force in foil rolling is not proven. Experiments (for example those of chapter 6) show that full film lubrication can be effective with film thicknesses only slightly greater than the molecular length of the lubricant. On the other hand where there is a range of asperity wavelengths, the analysis of section 4.6 shows that the film thickness under the sharper contacts can be expected to be more severe and it may be that these contacts are protected by the additives.

Experiments, which could be on a disc machine, should attempt to reproduce the asperity films expected in industry and to measure the friction force with and without additives as the conditions become more severe. It might be useful to use a simple flattened geometry similar to those of chapter 6, perhaps generated from random rough surfaces, where the area of contact ratio can be estimated with confidence. These traction forces could be compared with those expected from hydrodynamic or boundary lubrication measurements to identify the changeover between these regimes.

7.1.4 Measurements of friction in rolling

This thesis has attempted to concentrate on the mechanisms of lubrication and friction. Much of the work in friction is hampered by attempts to deduce laws from a number of friction measurements without a sufficiently clear understanding of the mechanisms underlying these gross friction measurements. While friction measurements on a rolling situation would clearly be desirable it is important that conditions are well controlled and an attempt is made to understand fully the processes involved to avoid over-simplifying the process. The experiments of chapter 5 demonstrate that it is possible to deduce asperity contact areas from measurements of the mean film thickness with reasonable confidence where there is significant asperity contact and, indeed, the results of the theory or experiments could be used to estimate these area of contact ratios. The film thickness in the valleys could be estimated with a reasonable amount of confidence where the mean film thickness is known and the friction contribution from these areas estimated. If the total friction is measured, the contribution from the asperity contacts could then be inferred. It would be necessary to use a real ground finish (or a smooth surface) on the roll and the strip. As it is suggested that the contact on the asperities may be due to hydrodynamic friction, measurements of friction using pressure pin transducers cannot be expected to give reasonable results without interfering with the asperity film thicknesses. Deposited pressure transducers may be sufficiently small to avoid interfering with the lubrication process and, if homogeneous deformation is assumed, the change in pressure through the bite could be used to infer friction conditions there.

Although it would be desirable to use the same lubricants as found industrially, with the lower speeds of experimental mills this would generally result in different mechanisms of lubrication in the experiments compared with industrial practice, unless special care was taken to adjust the roughness length scales accordingly.

APPENDIX A

ASPERITY CRUSHING CALCULATIONS FOR THE NEW VELOCITY FIELD

An upper bound on the load required for bulk deformation with longitudinal roughness is to be deduced for the geometry of figure 3.12. Consider the power per half indenter spacing c , down to a depth d_0 (greater than the depth d of any local perturbed fields), per unit length in the z direction. Take real surface tractions T_i , and a compatible virtual velocity field with velocities u_i^* on the surfaces, strain rates $\dot{\epsilon}_{ij}^*$ and velocity discontinuities $[v_i^*]$. By using the concept of a plastic potential and knowing that the shear stress along velocity discontinuities is less than or equal to the shear yield stress k , it can be shown [44] that

$$\int_{\text{Surface}} T_i u_i^* \leq \int_{\text{Volume}} \sigma_{ij} \dot{\epsilon}_{ij}^* + \int_{\text{Disc}} k [v_i^*] \quad \{\text{A.1}\}$$

where σ_{ij}^* are the internal stresses associated with the virtual velocity field. Taking P_d as the work dissipated due to the assumed virtual field for the volume comprising $OPRS$ and of unit length, and evaluating the integral on the left hand side, using volume conservation,

$$c\bar{p}(v_f^*(1-A) + \dot{\epsilon}_z^* d_0) + \sigma_b \dot{\epsilon}_z^* d_0 c + F \dot{\epsilon}_z^* \leq P_d + \bar{p} \dot{\epsilon}_z^* c (d_0 - d) + \sigma_b \dot{\epsilon}_z^* c (d_0 - d) \quad \{\text{A.2}\}$$

Putting $D = d/c$, using $\bar{p}/2k + \sigma_b/2k = 1$ and rearranging, we obtain the upper bound on $F/2kc^2$

$$\frac{F}{2kc^2} \leq \frac{P_d}{2kc^2 \dot{\epsilon}_z^*} - D - \frac{\bar{p}}{2k} W(1-A) \quad \{\text{A.3}\}$$

This is true for any velocity field. $(P_d/2kc^2 \dot{\epsilon}_z^* - D)$ is the redundant work due to inhomogeneous deformation. $(\bar{p}/2k)W(1-A)$ is the work saved by allowing the loaded regions to move in more quickly than the mean surface velocity.

The redundant work $(P_d/2kc^2 \dot{\epsilon}_z^* - D)$ can be found for a given assumed class of velocity fields as a function of the indenter geometry A , the velocity parameter W and the depth of the perturbed field D . P_d is given by the integral

$$P_d = \int_{\text{Vol}} \sigma_{ij}^* \dot{\epsilon}_{ij}^* + \int_{\text{Disc}} k [v_i] \quad \{\text{A.4}\}$$

With the Von Mises yield criterion, this becomes

$$P_d = \int_{\text{Area}} \sqrt{2} k (\dot{\epsilon}_x^2 + \dot{\epsilon}_y^2 + \dot{\epsilon}_z^2 + \frac{1}{2} \dot{\gamma}_{xy}^2)^{1/2} + k \int_{\text{Disc}} [v_i] \quad \{\text{A.5}\}$$

Since $\partial/\partial z = 0$, $\dot{\gamma}_{xz} = \dot{\gamma}_{yz} = 0$. $\dot{\epsilon}_z$ is a constant. Referring to figure 3.12, where $A = 0.5$, by considering volume continuity $u = \dot{\epsilon}_z d$ and using $\dot{\epsilon}_x + \dot{\epsilon}_y + \dot{\epsilon}_z = 0$, the strain rates in regions A, B and C are given by

$$\text{Region A} \quad \dot{\epsilon}_x = \frac{v_f}{2d} \quad \{\text{A.6}\}$$

$$\dot{\epsilon}_y = -\frac{1}{d} \left(\frac{v_f}{2} + \dot{\epsilon}_z d \right) \quad \{\text{A.7}\}$$

$$\dot{\gamma}_{xy} = 0 \quad \{\text{A.8}\}$$

$$\text{Region B} \quad \dot{\epsilon}_x = -\frac{v_f}{2d} \quad \{\text{A.9}\}$$

$$\dot{\epsilon}_y = \frac{1}{d} \left(\frac{v_f}{2} - \dot{\epsilon}_z d \right) \quad \{\text{A.10}\}$$

$$\dot{\gamma}_{xy} = 0 \quad \{\text{A.11}\}$$

$$\text{Region C} \quad \dot{\epsilon}_x = 0 \quad \{\text{A.12}\}$$

$$\dot{\epsilon}_y = -\dot{\epsilon}_z \quad \{\text{A.13}\}$$

$$\dot{\gamma}_{xy} = \frac{v_f a}{d^2} \quad \{\text{A.14}\}$$

The size of the velocity discontinuities between regions A and C and between regions B and C varies linearly from $(v_f/2) \cdot (\sqrt{d^2 + a^2}/d)$ at the surface to zero on OS. Using equations A.6 to A.14, equation A.5 becomes

$$P_d =$$

$$\begin{aligned} &\text{from Region A} \quad \frac{1}{2} da \sqrt{2} k \left(\left(\frac{v_f}{2d} \right)^2 + \left(\frac{v_f}{2d} + \dot{\epsilon}_z \right)^2 + \dot{\epsilon}_z^2 \right)^{1/2} \\ &\text{from Region B} \quad + \frac{1}{2} da \sqrt{2} k \left(\left(\frac{v_f}{2d} \right)^2 + \left(\frac{v_f}{2d} - \dot{\epsilon}_z \right)^2 + \dot{\epsilon}_z^2 \right)^{1/2} \\ &\text{from Region C} \quad + da \sqrt{2} k \left(2\dot{\epsilon}_z^2 + \frac{1}{2} \left(\frac{v_f a}{d^2} \right)^2 \right)^{1/2} \\ &\text{velocity discontinuities} \quad + k \frac{v_f}{2} \left(\frac{d^2 + a^2}{d} \right) \end{aligned} \quad \{\text{A.15}\}$$

Using dimensionless groups, with $A = 0.5$

$$\begin{aligned}\frac{P_d}{2kc^2\dot{\epsilon}_z} &= \frac{D}{4\sqrt{2}} \left(\left(\frac{W}{2D} \right)^2 + \left(\frac{W}{2D} + 1 \right)^2 + 1 \right)^{1/2} \\ &\quad + \frac{D}{4\sqrt{2}} \left(\left(\frac{W}{2D} \right)^2 + \left(\frac{W}{2D} - 1 \right)^2 + 1 \right)^{1/2} \\ &\quad + \frac{D}{2\sqrt{2}} \left(2 + \frac{1}{2} \left(\frac{W}{2D^2} \right)^2 \right)^{1/2} \\ &\quad + \frac{W}{4} \left(D + \frac{1}{4D} \right)\end{aligned}\tag{A.16}$$

APPENDIX B

ASPERITY CRUSHING RESULTS WITH WILSON AND SHEU'S VELOCITY FIELD

Consider the geometry of figure 3.12 where a block is discretely loaded and undergoes a longitudinal bulk strain. Upper bounds on the change in end force F which will allow bulk yielding to occur are to be deduced from Wilson and Sheu's calculations for their velocity field with no velocity discontinuities [86].

Wilson and Sheu consider a block loaded with pressures p_0 and p_b on the 'loaded' and 'unloaded' parts of the surface. The average pressure on the surface \bar{p} is assumed equal to the plane strain yield stress $2k$.

$$\text{i.e.} \quad (ap_0 + (c - a)p_b)/c = 2k \quad \{\text{B.1}\}$$

They take the end force F as zero. With these stress boundary conditions, considering the power down to a depth d , the virtual work equation A.1 becomes

$$ap_0 (\dot{\epsilon}_z d + v_f (1 - a/c)) + (c - a)p_b (\dot{\epsilon}_z d - v_f (a/c)) \leq P_d \quad \{\text{B.2}\}$$

In dimensionless form, after a little algebra, using equation B.1, this becomes

$$\left(\frac{p_0 - p_b}{k} \right) \leq \frac{2}{WA(1 - A)} \left(\frac{P_d}{2kc^2\dot{\epsilon}_z} - D \right) \quad \{\text{B.3}\}$$

Wilson and Sheu then find the minimum value of hardness $(p_0 - p_b)/k$ for their velocity field for given values of W and A by varying D . Hence the minimum amount of redundant work $(P_d/2kc^2\dot{\epsilon}_z - D)$ as a function of W and A can easily be deduced from their values of minimum hardness using equation B.3. The corresponding curves of upper bounds on $F/2kc^2$ as a function of W are then given by equation A.3.

APPENDIX C

ESTIMATING THE AREA OF CONTACT RATIO IN THE TRACTION EXPERIMENTS FOR $\Lambda \leq 0.88$

To estimate the contact area the situation is idealised as consisting of an array of asperities with constant tangential and circumferential curvatures. As a first approximation the Hertz calculation for individual point contacts can be used (see [51]). For the $0.5\mu\text{m}$ disc, the calculated major and minor semi-axes of the dry contact ellipse are $213\mu\text{m}$ and $28\mu\text{m}$ respectively. This will overestimate the contact area, since the presence of neighbouring asperities restricts the contact growth.

Greenwood [39] considers the problem of an array of such asperities each loaded with Hertzian ellipsoidal pressure distributions. He integrates the appropriate elastic equations to find the deflections on the asperity surface and then identifies a contact patch by considering the effect of these deflections on the original profile. In order to flatten the contact patch the deflections in this region must have the same constant curvature transversely and circumferentially as the original undeformed asperity. Although this is found to be true of the transverse deflections, the circumferential curvature of the deflection calculated is not found to be constant along the contact with the assumed ellipsoidal pressure distribution. The calculation of the contact length from this integration is then uncertain. For the $0.5\mu\text{m}$ disc the semi-length and width of the contact are found from this calculation to be $220\mu\text{m}$ and $25\mu\text{m}$. This length can be compared with the semi-length for line contacts of $171\mu\text{m}$.

In addition to obtaining an estimate of the contact length directly from the integration of the elastic deflection equations, Greenwood suggests an alternative approach. By considering the extent to which the ellipsoidal pressure distribution is more dispersed away from the centre line than the equivalent elliptical line contact pressure distribution, he produces an estimate of the semi-contact length for heavily loaded contacts (where the asperities are well squashed down) which for the $0.5\mu\text{m}$ disc gives a semi-length of $190\mu\text{m}$.

APPENDIX D

EFFECT OF NON-NEWTONIAN FLOW ON OIL SIDE LEAKAGE

The effect of Eyring viscous behaviour on the enhancement of side leakage is to be investigated. x and y axes are taken in the entraining and transverse directions respectively with corresponding velocities u and v . z is normal to these axes and the velocity in this direction will be assumed to be zero. The constitutive relationship for Eyring fluids is then

$$\left(\frac{\partial v}{\partial z}\right)^2 + \dot{\Gamma}^2 = \frac{\tau_0^2}{\eta^2} \sinh^2 \sqrt{\left(\frac{\tau_{yz}^2 + T^2}{\tau_0^2}\right)} \quad \{\text{D.1}\}$$

where $T = \tau_{zx}$ and $\dot{\Gamma} = \partial u / \partial z$. The shear stress T and strain rate $\dot{\Gamma}$ in the entraining direction (where sliding is also taking place) are then assumed to be much greater than the shear stress τ_{yz} and strain rate $\partial v / \partial z$ in the transverse direction. The total shear stress is also assumed to be much greater than the Eyring shear stress, so that $\sinh(\tau/\tau_0) \approx \frac{1}{2} \exp(\tau/\tau_0)$.

In addition, the direction of the shear stress must be in the direction of the resultant strain rate

i.e.
$$\frac{\dot{\Gamma}}{\partial v / \partial z} = \frac{T}{\tau_{yz}} \quad \{\text{D.2}\}$$

Taking only first order terms, equations D.1 and D.2 become

$$\frac{\partial v}{\partial z} = \frac{\tau_{yz} \tau_0}{\eta 2T} \exp\left(\frac{T}{\tau_0}\right) \quad \{\text{D.3}\}$$

For Newtonian flow

$$\frac{\partial v}{\partial z} = \frac{\tau_{yz}}{\eta}$$

Hence the effect of the non-Newtonian behaviour is to reduce the effective viscosity resisting side flow in the transverse y direction, when compared with Newtonian flow, by a factor $2T / (\tau_0 \exp(T/\tau_0))$. This is the same factor by which the effective viscosity is reduced in the entraining direction due to non-Newtonian flow.

APPENDIX E

CENTRAL FILM THICKNESSES IN ELLIPTICAL CONTACTS

In order to help estimate film thicknesses in lubricated line and circular point contacts, Johnson [49] has identified four regimes determining the film thickness. These regimes are rigid isoviscous, rigid piezoviscous, elastic isoviscous and elastic piezoviscous.

Several authors have constructed regime charts for line contacts [47, 49], but the corresponding charts for elliptical contacts have only been constructed where the major axis is in the transverse direction [41]. It is the purpose of this appendix to quantify the transition between the rigid and elastic piezoviscous regimes for elliptical contacts, since this is the region in which the disc experiments of chapter 6 lie. It is then possible to estimate film thicknesses in the transition regime using results derived for the elastic regime.

Three approaches to the determination of film thicknesses in elliptical contacts have been used. Kapitza [54] solves the hydrodynamic equations for rigid elliptical contacts analytically. Semi-analytical solutions have been derived by Archard and Cowking [2], Hooke [46, 47] and Cheng [14] in the elastic regions by making some simplifying assumptions (generally assuming a Hertzian film shape). Finally, several authors have solved the coupled elastic and hydrodynamic equations numerically for particular cases. Numerical results have been presented by Chittenden *et al.* [17] and by Mostofi and Gohar [68] in circular contacts and in elliptical contacts for ψ both greater and less than 1, where $\psi = b/a$, the ratio of the Hertz contact semi-axes in the transverse and the entraining directions. Hamrock and Dowson [42] have calculated film thicknesses for elliptical contacts where $\psi > 1$ and Evans, Snidle and co-workers [24, 55, 57, 25, 26] have calculated film thickness for circular contacts and for elliptical contacts with $\psi < 1$.

Hooke's analysis for elastic contacts is the most detailed semi-analytical solution and is here used as a convenient reference solution. He deduces film thicknesses for

the elastic isoviscous and elastic piezoviscous regimes for line and elliptical contacts for incompressible fluids. If the contact is sufficiently far into the elastic regime, then the dimensions of the region in which significant hydrodynamic buildup of oil pressure occurs are much less than the size of the flattened Hertz contact. The oil film thickness will also be much less than the elastic deflection, so that the film thickness will be nearly constant under the contact with an almost Hertzian pressure distribution. For highly elastic contacts the shape in the inlet is first approximated by Hooke by a power law expansion of the Hertzian profile given by the pressures in the conjunction. He then shows that the shape of the inlet and the front of the Hertz flat is significantly altered by the hydrodynamic pressure in the inlet sweep. As the contact changes from isoviscous to piezoviscous, the hydrodynamic oil pressure generated in the inlet is shown to have less effect on the shape of the inlet and in the piezoviscous limit, has no effect at all. This transition between elastic isoviscous and elastic piezoviscous behaviour is found to depend on a group c . For elliptical contacts, this group is

$$c = \frac{3}{2a_1} (\pi\psi)^{-2/5} (G^4 U)^{1/5} (G^3 W)^{1/15} \quad \{\text{E.1}\}$$

where $G = \alpha E'$, $U = \bar{u}\eta_0/(E'R'_e)$ and $W = w/(E'R'_e{}^2)$. α is the pressure viscosity coefficient in the Barus equation, E' the effective elastic modulus, u the mean entraining velocity, η_0 the viscosity at ambient pressure, R'_e the equivalent entraining radius and w the load. a_1 is a constant depending on the ellipticity ratio, defined in [48], which satisfies the relationship $a/R'_e = a_1 W^{1/3}$. For $c \gg 1$, the oil pressure buildup is piezoviscous, for $c \ll 1$ it is isoviscous.

Taking a dimensionless film thickness H , given by

$$H = \frac{h}{(\alpha\eta_0 u)^{2/3} R'_e{}^{1/3}}$$

where h is the central film thickness, Hooke's analysis gives a central film thickness H_h in the elastic piezoviscous regime for elliptical contacts

$$H_h = \lambda\psi^{0.5} a_1^{5/4} (G^3 W)^{-1/12} (G^4 U)^{1/12} \quad \{\text{E.2}\}$$

The numerical factor λ in equation 5.2 varies with the value of c and for values of $1/c$ between 0 and 1 may be approximated by

$$\lambda = 1.794 \left(1 + \frac{0.97}{c} \right) \quad \{\text{E.3}\}$$

Similarly he finds a distance n to characterise the distance in which a significant pressure buildup occurs. For the elastic piezoviscous regime this is taken arbitrarily as the distance from the edge of the Hertzian flat to the point of inflection in the reduced pressure buildup curve for $c \rightarrow \infty$. In the piezoviscous limit, the final 22% rise in the reduced pressure before the Hertz flat occurs over a distance n and the final 70% over a distance $3.2n$. For finite c , the transition between the inlet and the Hertz flat is less well defined, but Hooke shows that the length scale of the critical region where the film thickness is determined is still of the same order. For elliptical contacts this distance n is given by

$$\frac{n}{b} = 0.63a_1^{3/2}(G^4U)^{1/2}(G^3W)^{-1/2} \quad \{\text{E.4}\}$$

Cheng has calculated the central film thicknesses in elliptical contacts by assuming a Hertzian profile in the inlet. He solved the two dimensional hydrodynamic equation numerically with this prescribed inlet shape and with suitable boundary conditions on the centre lines of the contact. In Hooke's analysis for large values of c well into the piezoviscous region, the effect of the hydrodynamic pressure on the inlet shape becomes small so that his analysis will then have the same inlet shape as Cheng's. Differences in the two analyses may still arise, however, because of the oil side leakage considered in Cheng's analysis and neglected in that of Hooke.

Numerical calculations combining the elastic and hydrodynamic equations for circular contacts cover a wide range of conditions, but results for elliptical contacts in the piezoviscous regime with $\psi < 1$ are less extensive.

Mostofi and Gohar's results, which were interpreted assuming a glass/steel pair, are close to the isoviscous boundary, with values of c between 2.1 and 3.3.

Chittenden *et al.* give a formula for the central film thickness for contacts with $\psi < 1$ which is based on four points at each of eight ellipticity ratios between 0.3 and 1.0. These points are in the transition region between elastic and rigid and also between piezoviscous and isoviscous so that trends found from the four points at each ellipticity ratio will not in general be appropriate for conditions outside the region of the calculations. In many cases use of the formula will involve extrapolation into a region for which it was not formulated, both in terms of the position on a regime map and for smaller values of the ellipticity ψ .

Chittenden *et al.* used between 15 and 20 nodes per Hertz semi-axis length a .

Because the values of n/a are smallest for the results with smaller ellipticity ratios, the mesh will be less accurate for these calculations. With typical values of n/a of around 0.07 for the results with $\psi = 0.3$, the distance between nodes is 1.4 times the length n characterising the pressure buildup length in the inlet. For circular contacts values of n/a are larger and the mesh will not be as coarse in the critical region.

The inverse method used by Snidle and co-workers in [24, 25, 26, 55, 57] is able to solve the equations well into the elastic regime, although it is rather expensive in computer time and only a few results are available. In addition to an early result by Evans and Snidle and a calculation for an array of contacts by Karami *et al.*¹, recent unpublished results by Evans and Snidle [25] for $\psi = 0.24$ and Evans [26] for $\psi = 0.3$ considerably augment the number of solutions found.

E.1 Comparison of different calculations with Hooke's analysis

In order to quantify the transition between elastic piezoviscous and rigid piezoviscous contacts it is useful to compare how the various calculations for point and line contacts approach Hooke's asymptote as n/a and n/b decrease. Line contact calculations by Dowson and Higginson for incompressible oils and by Dowson, Higginson and Whitaker (taken from [22]) for compressible oils have been used. Hooke's formulae for H and n/a (where a is the semi-width of the contact) for line contacts are given in [48].

For each set of results the computed film thickness was compared with Hooke's asymptotic film thickness and the value of the parameters n/a and n/b found from equation 5.4. The ratio of the central film thickness to Hooke's asymptotic result H/H_h is then plotted against the parameters n/a or n/b in figures E.1 and E.2². The film thickness given by Hooke's formula was calculated for each point taking into account

¹ This paper dealt with an array of circumferential asperities. However one of the results had negligible oil pressure in the valleys between the asperities, so becoming an isolated point contact except for the alteration in the inlet profile due to the adjacent asperities. Since the pressure buildup is close to the edge of the Hertzian contact this should cause only a small change in film thickness.

² The MPFS theoretical curve and the results from Karami *et al.* when the contacts are *not* isolated in figure E.2 are not relevant at this stage. Their significance is explained elsewhere.

the change in the numerical factor λ in equation 5.2 with c .

Cheng expresses his results, which are appropriate for $c \rightarrow \infty$, as the dependence of a dimensionless film thickness on a group closely related to n/b . Although, in general, a second independent group (for example Hooke's group c) is needed to define the position on a regime chart, and determine the film thickness, it was found that the ratio of Cheng's and Hooke's film thicknesses was independent of c . This may be expected, since the effect of c is to change the film shape in the inlet due to hydrodynamic pressure — an effect that Cheng's analysis does not include. The calculations of Cheng for ellipticity ratios ψ of 0.5, 1 and 2 are included in figures E.1 and E.2.

For point contacts Kweh *et al.* find that introducing compressibility reduces the calculated central film thickness roughly in proportion to the inverse of the factor by which the density of oil under the centre of the contact is increased by compression. This reflects the fact that the amount of oil drawn in is controlled in the inlet region where compressibility is generally small. Where compressibility was included in the numerical calculations, its effect on the central film thickness was estimated using this observation. Knowing the compressibility laws and peak pressures used in each calculation, the ratio of the density of the oil under the contact to its density at ambient pressure was calculated to deduce an equivalent incompressible result. This derived incompressible result was then compared with Hooke's analysis, which does not include compression of the oil.

Where n/b and n/a are small the contact is elastic and Hooke's approximations will be good. Where they are large conditions will be closer to Kapitza's for rigid contacts. Figures E.1 and E.2 show how accurate Hooke's asymptotic result for highly elastic contacts is as n/a and n/b increase and conditions change from elastic to rigid. An alternative measure of the transition, taking the ratio of the film thickness deduced by Kapitza to the amount of elastic flattening for dry contacts $a^2/(2R'_e)$ gives the same combination of the parameters G , U and W as n/a or n/b . As well as depending on n/a or n/b , this transition between elastic and rigid can also be expected to depend on the ellipticity ψ and c , the parameter determining how piezoviscous the contact is.

Hooke's theory assumes that the pressure buildup length is small compared with the size of the Hertz contact dimensions and that the film thickness is much less than the elastic deflections in the contact. For line contacts deviations from this asymptotic

result can occur for three reasons as n/a increases.

- i) Errors in taking a power law approximation to the initial Hertzian profile will grow as n/a increases and the buildup of pressure occurs further away from the elastic contact area. For large enough n/a , the shape of the inlet region will be better approximated as rigid.
- ii) In Hooke's analysis for highly elastic contacts it is assumed that the amount of oil entrained is determined in the inlet and that, because the elastic deflections in the contact are much greater than the film thickness, the film thickness under the contact is effectively constant. The pressure under the contact is then close to Hertzian. This assumption of a constant film under the contact will not always be good. If n/a is large the film thickness becomes comparable with the size of elastic deflections, the pressure will not be close to Hertzian and the film thickness will not be constant under the contact.
- iii) Hooke's analysis does not include compression of the oil under the contact, while most of the numerical calculations do. The difference between calculations with and without compression of the oil has been estimated from the change in density of the oil under the contact. This may not always be accurate. However, where identical calculations have been done with and without compressibility, this estimate of the effect of compression on the central film thickness is close to that in fact found.

Compressibility will only affect the volume of oil entrained in the elastic regimes if the change in density of the oil is significant in the inlet region. A position towards the end of the inlet region may be estimated by the the inflection point in the reduced pressure curve. For values of c of 2, 3 and ∞ the values of αp in Hooke's analysis at the inflection point are 0.88, 0.96 and 1.4 respectively. With the compressibility relation used in all the numerical calculations, compression of the oil is under 10% for pressures below 0.24 GPa. If compressibility is going to make a significant difference to the amount of oil entrained, then $\alpha \times 0.24\text{GPa}$ must be below say 2. Hence α must be below $8.3 \times 10^{-9} \text{m}^2/\text{N}$, which is at the lower limit for most mineral oils. The results of Kweh *et al.* with small values of c were calculated with $\alpha = 6.8 \times 10^{-9} \text{m}^2/\text{N}$, so that compression of the oil may change the oil entrainment in the inlet and give rise to the difference between these

calculations and Hooke's formula for small n/a .

Results for line contacts suggest that it is the deviation of the film shape and pressure distribution under the contact from Hertzian which is producing the fall in film thickness ratio at large values of n/a . The line contact result with $n/a = 0.59$ corresponds to a higher value of c of 35 and has an almost Hertzian pressure distribution over the contact. Hooke's analysis agrees well with this calculation. The other line contact results with $n/a > 0.4$ do not approach a Hertzian pressure distribution and Hooke's formula does not give such a good approximation to the calculated film thickness. The good agreement between Hooke's formula and the calculation with $c = 35$ show that the power law approximation to the inlet shape is adequate even at quite large values of n/a .

Of the calculations for elliptical contacts, results by Hamrock and Dowson with large values of n/a and small values of c do not have a Hertzian pressure profile in the conjunction. The film thickness under the contact is not uniform and changes rather more than would be expected from the compression of the oil. This non-uniform film thickness explains the difference between Hooke's approximate analysis and the actual film thickness calculated. Other available elliptical contact pressure distributions from the results of Evans and Snidle and Karami *et al.* are close to Hertzian under the contact.

For elliptical contacts there are two further reasons for differences between Hooke's asymptotic formula and the full numerical calculations.

- iv) Hooke assumes plane strain conditions in the inlet to calculate the effect of the hydrodynamic loading on the film shape. This will become less valid as n/b increases, although this effect will be less important for larger values of c , where the elastic deflections due to the hydrodynamic loading become insignificant.
- v) Side leakage of oil in the inlet, which is neglected in Hooke's analysis, will become important when n/b is not small. As n/b becomes small pressure gradients in the entraining direction become much larger than gradients in the transverse direction and the side leakage of oil in the inlet can be neglected. Where n/b is no longer small, then differences between the asymptotic film thickness and actual film thickness will arise due to side leakage of oil in the inlet zone. The ratio n/b is a measure of the ratio of the entraining pressure gradient to the transverse

pressure gradient.

Results by Cheng have a Hertzian contact, as does Hooke's calculation in the limit where $c \rightarrow \infty$, so that the only significant difference between these results and Hooke's formula is due to side leakage of oil. The effect of side leakage highlighted by Cheng's results for $\psi = 1$ is in good agreement with the difference between Hooke's formula and the calculations of Kweh *et al.*. This shows that side leakage is the dominant reason for the drop in the film thickness with increasing n/b in these calculations too and that the other effects detailed above are small by comparison. In fact Kweh's results are closer to Cheng's calculations with $\psi = 0.5$, but the difference between Cheng's results with $\psi = 0.5$ and 1 is small. Chittenden's results for $\psi > 0.5$ are in good agreement with the calculations of Kweh *et al.* and Cheng. The points significantly below the results of Kweh *et al.* are for smaller ellipticity ratios of 0.5 and 0.6.

Of the calculations with ellipticities less than 0.5, the film thickness ratio calculated from the results of Evans and Snidle varies with the side leakage parameter in a similar way to the results for the circular contacts. For the calculations by Evans and Snidle, the published result of [24] with $\psi = 0.24$ has the largest value of n/b , while the other results with this value of ψ are taken from [25]. The effect of the parameter c appears to be small both in these results and for those of Kweh *et al.* with $\psi = 1$. The calculation using the results of Karami *et al.* for an array of contacts gives a slightly higher film thickness ratio than an extrapolation of the results for $\psi = 0.24$. Results presented by Mostofi and Gohar are slightly lower than this extrapolation; this may be explained by the small values of c in Mostofi and Gohar's calculations, indicating that they are not well into the piezoviscous regime. The length scale of the pressure buildup n is appropriate for piezoviscous contacts and may not be a good measure of the pressure buildup length and hence side leakage as the contact becomes isoviscous.

The film thickness ratios calculated from Chittenden *et al.* with $\psi = 0.3$ and 0.4 are significantly lower than the results from Evans and Snidle's work with $\psi = 0.24$, although the trend from other results is for larger values of ψ to have larger film thickness ratios. The scatter in these results of Chittenden *et al.* is also greater than the scatter for their calculations with larger values of ψ . The calculation by Evans with $\psi = 0.3$ and $c = 3.8$ has conditions very close to that of Chittenden for $\psi = 0.3$ with the smallest film thickness ratio, where $c = 4.08$. Evans' calculation, with a film

thickness ratio 26% greater than that of Chittenden *et al.*, seems to fit in well with results at other ellipticity ratios.

In the papers of Chittenden *et al.* and Dowson and Hamrock, the viscosity is assumed to follow a more complicated Roelands law than the simple Barus exponential rise assumed in the analysis of Hooke and the calculation of Evans. This relationship includes the reduction in pressure viscosity index α with pressure found in mineral oils. The value of G quoted in their paper and used here to calculate the theoretical film thickness of Hooke is based on an averaged value of α with pressure. The actual value of viscosity used in their calculations and the value using a Barus relationship with this averaged pressure viscosity index agree for $\alpha p \approx 2$. At lower pressures the Barus law will underestimate the actual viscosity, while at higher values it will have a higher viscosity than that used in the calculations with the Roelands relationship. With Evans' calculation, the reduced pressure has reached 86% of its final value when $\alpha p = 2$, so that the film thickness is essentially determined for $\alpha p < 2$. If anything, the effect of the reduction in Roelands viscosity below the assumed Barus law relationship close to the end of the inlet with $\alpha p > 2$ will be less than the effect of the increased viscosity for values of $\alpha p < 2$. The Roelands viscosity relationship would then be expected to generate *larger* films than the equivalent Barus relationship.

It may be that the difference between the Roelands relationship used in the calculations of Chittenden *et al.* and the Barus law used in other calculations is the cause of the smaller film thickness ratios found from the calculations of Chittenden *et al.* with $\psi = 0.3$ and 0.4 , although the good agreement between the results of Chittenden *et al.* using the Roelands law and Kweh *et al.* using the Barus relationship for $\psi = 1$ suggest that this effect is not significant. It seems more probable that these calculations underestimate the actual central film thicknesses because the mesh was not sufficiently fine for the small values of n/a in these calculations.

For the purposes of calculating the film thickness, the film thickness ratio H/H_h may be approximated by the relationship

$$\frac{H}{H_h} = 1 + (0.61 - 0.32\psi) \left(\left(\frac{n}{b} \right)^2 - 2.2 \frac{n}{b} \right) \quad \{\text{E.5}\}$$

for $0.24 \leq \psi \leq 1$ and $0 \leq n/b \leq 1.0$.

The effect of side leakage of oil in the inlet can also be estimated by using a modification of Tønder's program to calculate the hydrodynamic pressure rise in the

inlet sweep. The shape of the inlet is approximated by the line contact Hertz shape in the entraining direction and triangular ridges in the circumferential direction, truncated to give a flat on the top of the ridge half the width of the asperity spacing. The film thickness is then determined by finding the separation that gives a reduced pressure of $1/\alpha$ at the front of the Hertz flat. This can be compared with the line contact film found using the same calculation method. Although the actual value of the film thickness deduced must be treated with caution because of the inaccuracy of the inlet shape assumed, the difference between calculations with and without side leakage may still be reasonable. The ratio of the line contact film thickness to the side leakage calculations using this geometry are also included on figure E.2 (shown as the MPFS calculations — the y axis is not, in this case, the ratio of the film thickness to Hooke's film thickness). Because the inlet shape is assumed to be constant, these calculations correspond, like Cheng's, to large values of c , with the disc experiment geometry which has an ellipticity ratio ψ of about 0.13. This set of calculations agrees well with the results of Evans and Snidle.

E.2 Deducing film thicknesses for the disc experiments

Various calculations of central film thicknesses in elliptical contacts have been compared with film thicknesses deduced by Hooke appropriate for conditions well into the elastic regime.

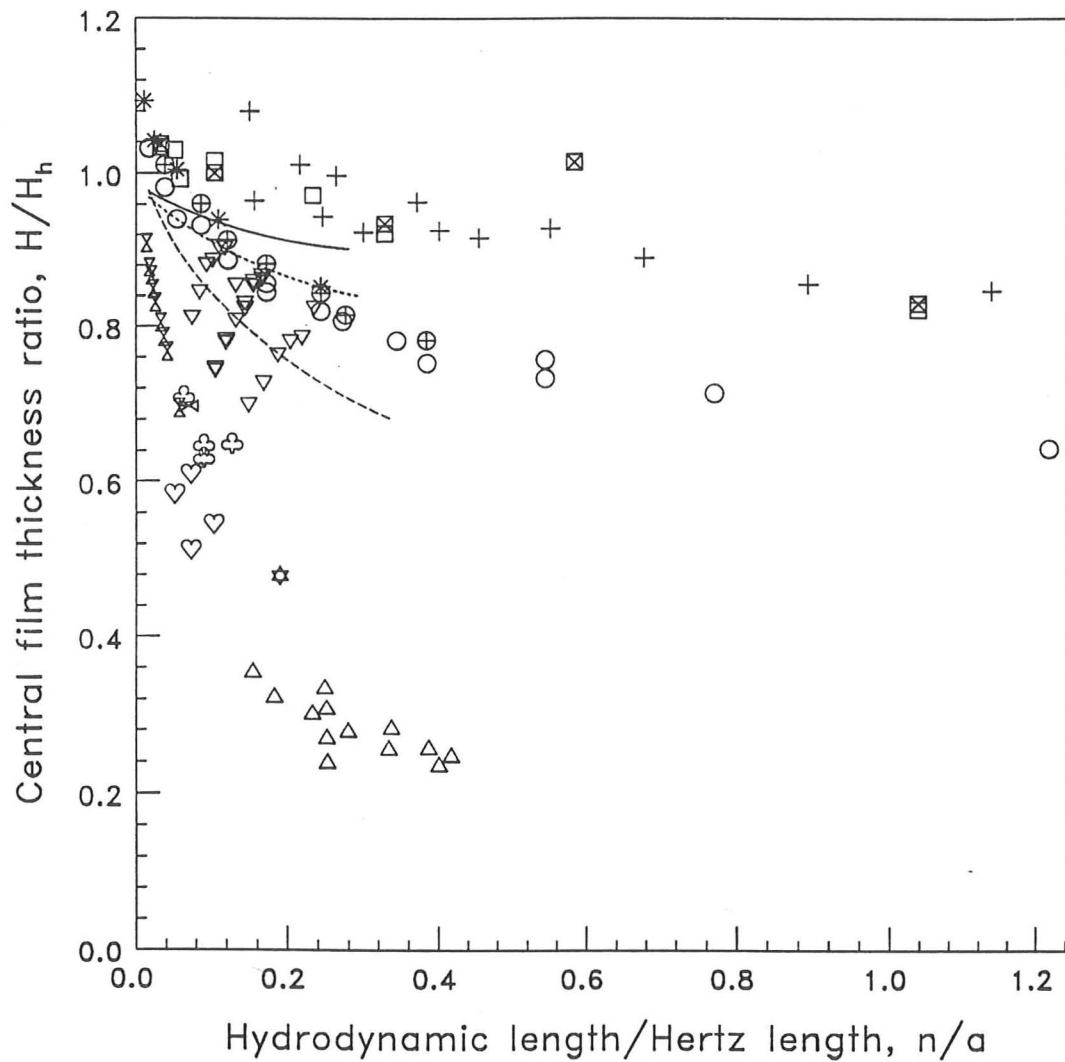
For piezoviscous contacts with ellipticity ratios less than 1, the parameter n/b describes the effect of oil side leakage on the entrained central film thickness as conditions change from elastic to rigid. Other differences between Hooke's analysis and the true conditions in these circumstances appear to have a relatively small effect on the film thickness.

This appendix has identified a way of estimating central film thicknesses for elliptical contacts with entrainment along the major axis in the transition between the piezoviscous elastic and rigid regimes with $n/b \leq 1$. The result of Karami *et al.* supports the proposition that an array of elliptical contacts behave in a similar way to isolated point contacts if there is negligible pressure between the asperities.

Hooke's analysis should first be used to calculate a film thickness ignoring the

effect of side leakage using equations E.1, E.2 and E.3. The effect of side leakage is governed by the parameter n/b given in equation E.4. The factor by which Hooke's film thickness is reduced due to side-leakage is then found from equation E.5. Finally, the reduction in the central film thickness due to compression of the oil may be estimated by the ratio of the oil's density at the peak Hertzian pressure under the contact to its density at ambient pressure.

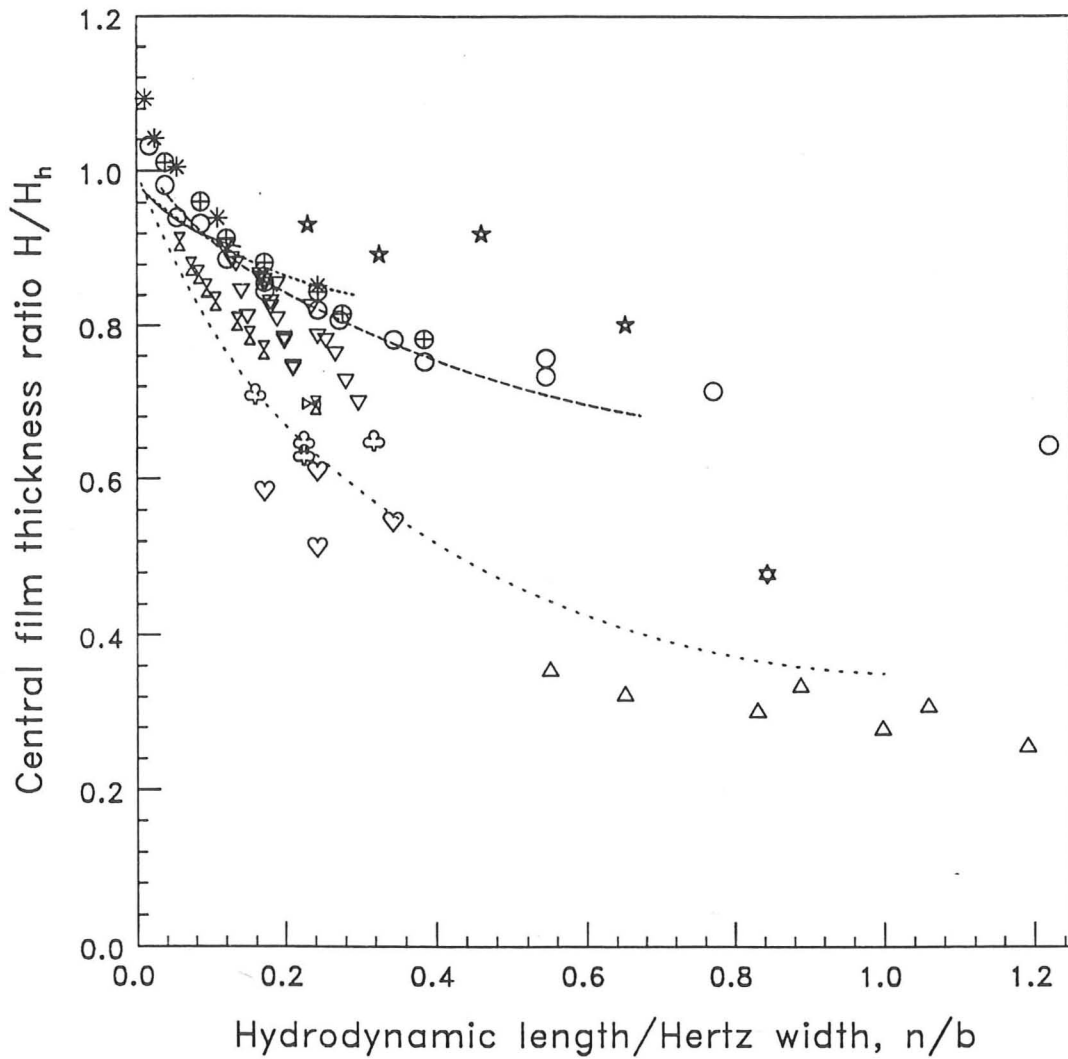
For the disc experiments with an ellipticity ratio ψ of about 0.13, the effect of side leakage on the ratio of the actual film thickness to Hooke's theory is assumed to be given by the 'MPFS' curve of figure E.2. Calculations were made for values of n/b less than one.



KEY

- * Kweh *et al.*, $c=1.7-3.9$, $\psi=1$
- o Kweh *et al.* (compressible), $c=6.4-51$, $\psi=1$
- ⊕ Kweh *et al.* (incompressible), $c=6.4-51$, $\psi=1$
- ▽ Chittenden *et al.*, $c=2.7-3.7$, $\psi=0.5-1$
- ⊕ Chittenden *et al.*, $c=3.2-3.8$, $\psi=0.4$
- ◇ Chittenden *et al.*, $c=3.4-4.1$, $\psi=0.3$
- ⊗ Evans, $c=3.8$, $\psi=0.3$
- ⊗ Evans and Snidle, $c=4.9-9.7$, $\psi=0.24$
- * Karami *et al.*, $c=6.1$, $\psi=0.23$
- △ Mostofi and Gohar, $c=2.1-3.3$, $\psi=0.16-0.28$
- + Dowson & Hamrock, $c=4.6-10.5$, $\psi=6$
- Dowson & Higginson line contact (incompressible), $c>4.4$
- ⊗ Dowson *et al.* line contact (compressible), $c>4.4$
- Cheng, $\psi=2$
- ⋯ Cheng, $\psi=1$
- - - Cheng, $\psi=0.5$

Figure E.1 The effect of the parameter n/a on the ratio of the central film thickness to Hooke's analysis, H/H_h .



KEY

- * Kweh *et al.*, $c=1.7-3.9$, $\psi=1$
- Kweh *et al.* (compressible), $c=6.4-51$, $\psi=1$
- ⊕ Kweh *et al.* (incompressible), $c=6.4-51$, $\psi=1$
- ▽ Chittenden *et al.*, $c=2.7-3.7$, $\psi=0.5-1$
- ⊕ Chittenden *et al.*, $c=3.2-3.8$, $\psi=0.4$
- ♥ Chittenden *et al.*, $c=3.4-4.1$, $\psi=0.3$
- × Evans, $c=3.8$, $\psi=0.3$
- ⋈ Evans and Snidle, $c=4.9-9.7$, $\psi=0.24$
- * Karami *et al.*, $c=6.1$, $\psi=0.23$
- △ Mostofi and Gohar, $c=2.1-3.3$, $\psi=0.24-0.28$
- Cheng, $\psi=2$
- - - Cheng, $\psi=1$
- ⋯ Cheng, $\psi=0.5$
- · - · - MPFS estimates of film thicknesses ($\psi=0.13$)
- * Karami *et al.*, not isolated contacts (see text), $c=5$, $\psi=0.57$

Figure E.2 The effect of the parameter n/b on the ratio of the central film thickness to Hooke's formula, H/H_h .

REFERENCES

- [1] Al-Salehi, F.A.R., Firkbank, T.C and Lancaster, P.R. An experimental determination of the roll pressure distributions in cold rolling. *Int. J. Mech. Sci.* **15**, 693-710 (1973)
- [2] Archard, J.F. and Cowking, E.W. Elastohydrodynamic lubrication at point contacts. *Proc. Instn. Mech. Engrs.* **180**, Part 3B, 47-55 (1965-1966)
- [3] Atkins, A.G. Hydrodynamic lubrication in cold rolling. *Int. J. Mech. Sci.* **16**, 1-29 (1974)
- [4] Azushima, A. Characteristics of lubrication in cold sheet rolling. *Proc. First Int. Conf. on Lubrication challenges in metalworking and processing.* I.I.T.R.I., Chicago. (1978)
- [5] Baglin, K.P. Elastohydrodynamic pressure rippling in cylinders finished with a circumferential lay. *Proc. Instn. Mech. Engrs.* **200(C5)**, 335-347 (1986)
- [6] Bair, S. and Winer, W.O. Some observations in high pressure rheology of lubricants. *J. Lubr. Tech.* **104**, 357-364 (1982)
- [7] Bair, S. and Winer, W.O. Shear strength measurements of lubricants at high pressure. *J. Lubr. Tech.* **101**, 251-257 (1979)
- [8] Bair, S. and Winer, W.O. Regimes of traction in concentrated contact lubrication. *J. Lubr. Tech.* **104**, 382-391 (1982)
- [9] Bay, N. and Wanheim, T. Real area of contact and friction stress at high pressure sliding contact. *Wear* **38**, 201-209 (1976)
- [10] Blok, H. The flash temperature concept. *Wear* **6**, 483-494 (1963)
- [11] Bowden, F.P. and Tabor, D. *The friction and lubrication of solids.* Vol. 1, Oxford Clarendon Press. (1953)
- [12] Briscoe, B.J., Scruton, B. and Willis, F.R. The shear strength of thin lubricant films. *Proc. Roy. Soc. Lond.* **A333**, 99-114 (1973)
- [13] Chambat, F., Lashermes, M. and Hendricks, H. Organometallic compounds produced during aluminium cold rolling. *Lubr. Engng.* **43**, 522-527 (1987)
- [14] Cheng, H.S. A numerical solution of the elastohydrodynamic film thickness in an elliptical contact. *J. Lubr. Tech.* **93**, 155-162 (1970)
- [15] Cheng, G.K. Functions of lubricant in aluminium-foil rolling. *Lubr. Engng.* **39**, 87-92 (1983)
- [16] Childs, T.H.C. The persistence of roughness between surfaces in static contact. *Proc. Roy. Soc. Lond.* **A353**, 35-53 (1977)
- [17] Chittenden, R.J., Dowson, D., Dunn, J.F. and Taylor, C.M. A theoretical analysis of the isothermal elastohydrodynamic lubrication of concentrated contacts. I Lubricant entrainment along major axis. *Proc. Roy. Soc. Lond.* **A397**, 245-269 (1985)

- [18] Christensen, H. Stochastic models for hydrodynamic lubrication of rough surfaces. *Proc. Instn. Mech. Engrs.* **184**, 1013–1022 (1969–70)
- [19] Dare-Edwards, M.P. *Private communication.* (1986)
- [20] Dow, T.A., Kannel, J.W and Bupara, S.S. A hydrodynamic lubrication theory for strip rolling including thermal effects. *J. Lubr. Tech.* **97**, 4–13 (1975)
- [21] Dowd, J.D. Herringbone formation in sheet and foil rolling. *Proc. of Aluminium Technology '86.* 258–263, Inst. Metals. (1986)
- [22] Dowson, D. and Toyoda, S. A central film thickness formula for elastohydrodynamic line contacts. *Proc. 5th. Leeds-Lyon Symp. on Elastohydrodynamics and Related Topics.* 60–65, Instn. Mech. Engrs. (1979)
- [23] Dowson, D. and Higginson, G.R. *Elasto-hydrodynamic lubrication.* Pergamon Press, Oxford. (1977)
- [24] Evans, H.P. and Snidle, R.W. Analysis of elastohydrodynamic lubrication of elliptical contacts with rolling along the major axis. *Proc. Instn. Mech. Engrs.* **197C**, 209–211 (1983)
- [25] Evans, H.P. and Snidle, R.W. *Private communication.* (1989)
- [26] Evans, H.P. *Private communication.* (1989)
- [27] Evans, C.R and Johnson, K.L. Regimes of traction in elastohydrodynamic lubrication. *Proc. Instn. Mech. Engrs.* **200(C5)**, 313–324 (1986)
- [28] Evans, C.R and Johnson, K.L. The rheological properties of elastohydrodynamic lubricants. *Proc. Instn. Mech. Engrs.* **200(C5)**, 303–312 (1986)
- [29] Evans, C.R and Johnson, K.L. The influence of surface roughness on elastohydrodynamic traction. *Instn. Mech. Engrs.* **201(C2)**, 145–150 (1987)
- [30] Evans, C.R. The measurement and mapping of the rheological properties of elastohydrodynamic lubricants. Ph.D. Thesis. Cambridge Univ. (1983)
- [31] Ewing, D.J.F. A series-method for constructing plastic slipline fields *J. Mech. Phys. Solids* **15**, 105–114 (1967)
- [32] Felder, E. Interaction between friction, lubrication and surface roughness in metal working. *Proc. 4th. Leeds-Lyon Symp. on Surface roughness effects in lubrication.* 308–312, Inst. Mech. Engrs. (1978)
- [33] Fleck, N.A and Johnson, K.L. Towards a new theory of cold rolling thin foil. *Int. J. Mech. Sci.* **29**, 507–524 (1987)
- [34] Fogg, B. A preliminary study of the influence of stress and deformation in the substrate on junction growth and friction. *Proc. Conf. on Properties and metrology of surfaces.* Instn. Mech. Engrs. (1968)
- [35] Ford, H. *Advanced mechanics of materials.* Longmans, London (1960)

- [36] Fowles, P.E. The application of E.H.D lubrication theory to individual asperity-asperity collisions. *J. Lubr. Tech.* **93**, 213-215 (1971)
- [37] Green, A.P. A theoretical investigation of the compression of a ductile material between smooth flat plates. *Phil. Mag.* **42**, 900-918 (1951)
- [38] Greenwood, J.A. and Rowe, G.W. Deformation of surface asperities during bulk plastic flow. *J. Appl. Phys.* **36**, 667-668 (1965)
- [39] Greenwood, J.A. Deflections due to a row of Hertz contacts. *Private communication.*
- [40] Halling, J., Arnell, R.D and Nuri, K.A. The elastic-plastic contact of rough surfaces and its relevance in the study of wear. *Proc. Instn. Mech. Engrs.* **202(C4)**, 269-274 (1988)
- [41] Hamrock, B.J. and Dowson, D. *Ball Bearing Lubrication.* John Wiley, New York (1980)
- [42] Hamrock, B.J. and Dowson, D. Isothermal elastohydrodynamic lubrication of point contacts. III Fully flooded results. *J. Lubr. Tech.* **99**, 264-276 (1977)
- [43] Higginson, J.G. The failure of elastohydrodynamic lubrication. Ph.D. Thesis. Cambridge Univ. (1984)
- [44] Hill, R. *The mathematical theory of plasticity.* Oxford Clarendon Press (1950)
- [45] Hirst, W. and Moore, A.J. Elastohydrodynamic lubrication at high pressures. II Non-Newtonian behaviour. *Proc. Roy. Soc. Lond.* **A365**, 537-565 (1979)
- [46] Hooke, C.J. The elastohydrodynamic lubrication of heavily loaded point contacts. *J. Mech. Engng. Sci.* **22**, 183-187 (1980)
- [47] Hooke, C.J. The elastohydrodynamic lubrication of heavily loaded contacts. *J. Mech. Engng. Sci.* **19**, 149-156 (1977)
- [48] Hooke, C.J. Minimum film thicknesses in lubricated point contacts operating in the elastic piezoviscous regime. *Proc. Instn. Mech. Engrs.* **202C**, 73-84 (1988)
- [49] Johnson, K.L. Regimes of elastohydrodynamic lubrication. *J. Mech. Engng. Sci.* **12**, 9-16 (1970)
- [50] Johnson, K.L and Higginson, J.G. A non-Newtonian effect of sliding in micro-E.H.L. *Wear* **128**, 249-264 (1988)
- [51] Johnson, K.L. *Contact mechanics.* Cambridge Univ. Press. (1985)
- [52] Kaneta, M. and Cameron, A. Effects of asperities in elastohydrodynamic lubrication. *J. Lubr. Tech.* **102**, 374-379 (1980)
- [53] Kannel, J.W. and Dow, T.A. The evolution of surface pressure and temperature measurement techniques for use in the study of lubrication in metal rolling. *J. Lubr. Tech.* **96**, 611-616 (1974)
- [54] Kapitza, P.L. Hydrodynamic theory of lubrication during rolling. *Zh. Tekh. Phys.* **25**, 759-775 (1955)

- [55] Karami, G., Evans, H.P. and Snidle, R.W. Elastohydrodynamic lubrication of circumferentially finished rollers having sinusoidal roughness. *Proc. Instn. Mech. Engrs.* **201C**, 29–36 (1987)
- [56] Kudo, H and Azushima, A. Interaction of surface microstructure and lubricant in metal forming tribology. *Proc. Conf. on Advanced technology of plasticity.* 373–384, Tokyo (1984)
- [57] Kweh, C.C., Evans, H.P. and Snidle, R.W. Elastohydrodynamic lubrication of heavily loaded circular contacts. *Proc. Instn. Mech. Engrs.* **203C**, 133–148 (1989)
- [58] Lahoti, G.D., Subramanian, T.L and Altan, T. Computer-aided prediction of metal flow, temperatures and forming load in selected metal-forming processes. *Proc. Conf. on Num. Methods in metal forming.* 183–195, A.S.M.E. (1978)
- [59] Lenard, J.G. Prog. Rep. A.I.S.I. Project. 53–459, American Iron and Steel Inst. (1983)
- [60] Lu, S.S and Chuang, Y.H. Effects of surface roughness on lubrication on cold rolling of metals. *J. Trib.* **107**, 522–526 (1985)
- [61] Mahdavian, S.M and Wilson, W.R.D. Lubricant flow in a plastrohydrodynamic work zone. *J. Lubr. Tech.* **98**, 16–21 (1976)
- [62] Makinouchi, A., Ike, H., Murakawa, M., Koga, N. and Ciupik, L.F. Finite element analysis of flattening of surface asperities by rigid dies in metal working processes. *Proc. 2nd. Int. Conf. Technol. of Plasticity.* 59–66, Stuttgart (1987)
- [63] McFarlane, J.S. and Tabor, D. Junction growth in metallic crystals. *Proc. R. Soc. Lond.* **A202**, 244–253 (1950)
- [64] Mear, M. and Zhang, L.C. *Private communication.* (1989)
- [65] Mizuno, T., Matsubara, K. and Kimura, H. Friction and lubrication in the cold rolling of thin sheet metals. *Bull. of J.S.M.E.* **12**, 359–367 (1969)
- [66] Mizuno, T. and Hasegawa, K. Effects of die surface roughness on lubricating conditions in the sheet metal compression-friction test. *J. Lubr. Tech.* **104**, 23–28 (1982)
- [67] Mizuno, T. and Okamoto, M. Effects of lubricant viscosity at pressure and sliding velocity on lubrication conditions in the compression-friction test on sheet metals. *J. Lubr. Tech.* **104**, 53–59 (1982)
- [68] Mostofi, A. and Gohar, R. Oil film thickness and pressure distribution in elastohydrodynamic point contacts. *J. Mech. Engng. Sci.* **24**, 173–182 (1982)
- [69] Parsons, M.W. and Pascoe, K.J. Development of the Cambridge University biaxial fatigue rig. *Report No. C.U.E.D. - Mat/T.R2* Cambridge (1970)
- [70] Patir, N. and Cheng, H.S. Effect of surface roughness orientation on the central film thickness in E.H.D. contacts. *Proc. 5th. Leeds-Lyon Symp. on Elastohydrodynamics and Related Topics,* Instn. Mech. Engrs. (1979)
- [71] Patir, N. and Cheng, H.S. An average flow model determining effects of three-dimensional roughness in partial hydrodynamic lubrication. *J. Lubr. Tech.* **100**, 12–17 (1978)

- [72] Patula, E.J. Steady-state temperature distribution in a rotating roll subject to surface heat fluxes and convective cooling. *J. Heat Transfer*. **103**, 36-41 (1981)
- [73] Rashid, M. and Seifrig, A. Heat partition and transient temperature distribution in layered concentrated contacts. Part I Theoretical model. *J. Trib.* **109**, 487-495 (1987)
- [74] Rashid, M. and Seifrig, A. Heat partition and transient temperature distribution in layered concentrated contacts. Part II Dimensionless relationships and numerical results. *J. Trib.* **109**, 496-502 (1987)
- [75] Ratnagar, D.D., Cheng, H.S and Schey, J.A. The surface deformation of aluminium compressed with viscous lubricants. *J. Lubr. Tech.* **94**, 591-594 (1974)
- [76] Reid, J.R and Schey, J.A. Full fluid lubrication in aluminium strip rolling. *A.S.L.E. Trans.* **21**, 191-200 (1978)
- [77] Richmond, J., Nilsson, O. and Sandberg, O. Thermal properties of some lubricants under high pressure. *J. Appl. Phys.* **55**, 2065-2067 (1984)
- [78] Roelands, C.J.A., Vlugter, J.C. and Waterman, H.I. The viscosity-temperature-pressure relationship of lubricating oils and its correlation with chemical constitution. *J. Basic Engng* **85**, 601-607 (1963)
- [79] Rowe, G.W. *Principles of industrial metalworking processes*. Edward Arnold, London (1977)
- [80] Sargent, L.B and Tsao, Y.H. Surface roughness considerations in metalworking. *A.S.L.E. Trans.* **23**, 70-76 (1980)
- [81] Schey, J.A. Surface roughness effects in metalworking lubrication. *Lubr. Engng*. **39**, 376-382 (1983)
- [82] Schey, J.A. *Metal deformation processes: friction and lubrication*. Dekker (1970)
- [83] Schipper, D.J. Transitions in the lubrication of concentrated contacts. Ph.D. Thesis. Twente Univ., Netherlands (1987)
- [84] Seabra, J. and Berthe, D. Elastohydrodynamic point contact Part II: influence of surface speeds, surface waviness and load on the contact behaviour. *Wear* **130**, 319-335 (1989)
- [85] Sengupta, A.K., Fogg, B and, Ghosh, S.K. On the mechanism behind the punch-blank surface conformation in stretch-forming and deep-drawing. *J. Mech. Working Tech.* **5**, 181-210 (1981)
- [86] Sheu, S. and Wilson, W.R.D. Flattening of workpiece surface asperities in metalforming. *Proc. XI. N.A.M.R.C.*, 172-178 (1983)
- [87] Sheu, S. and Wilson, W.R.D. Viscoplastic lubrication of asperities. *J. Lubr. Tech.* **104**, 568-574 (1982)
- [88] Sheu, S. Mixed lubrication in bulk metal forming processes. Ph.D. Thesis. Northwestern Univ., Illinois. (1985)

- [89] Sinha, P., Kennedy, J.S., Rodkiewicz, C.M., Chandra, P., Sharma, R. and Prasad, K.R. Effects of surface roughness and additives in lubrication: generalized Reynolds equation and its application to elastohydrodynamic films. *Proc. Instn. Mech. Engrs.* **210**(C1), 1-9 (1987)
- [90] Stephenson, D.A. Friction in cold strip rolling. *Wear* **92**, 293-311 (1983)
- [91] Tønder, K. Hydrodynamic bearings. Arbitrary film shapes. S.I.N.T.E.F Rep. No. 18/71-50 (1971)
- [92] Tønder, K. and Christensen, H. Waviness and roughness in hydrodynamic lubrication. *Proc. Instn. Mech. Engrs.* **186**, 807-812 (1972)
- [93] Tabor, D. *The hardness of metals*. Oxford Clarendon Press (1953)
- [94] Tanner, R.I and Johnson, W. Temperature distribution in some fast metal-working operations. *Int. J. Mech. Sci.* **1**, 28-44 (1969)
- [95] Tevaarwerk, J. L. *The shear of elastohydrodynamic films*. Ph.D. Thesis, Cambridge Univ. (1976)
- [96] Thomson, P.F. The influence of texture on the surface character of rolled strip. *J. Australian Inst. Metals.* **15**, 34-46 (1970)
- [97] Tsao, Y.H. and Sargent, L.E. A mixed lubrication model for cold rolling of metals. *A.S.L.E. Trans.* **20**, 55-63 (1977)
- [98] Tsao, Y.H. and Tong, K.N. A model for mixed lubrication. *A.S.L.E. Trans.* **18**, 90-96 (1975)
- [99] Tsao, Y.H and Sargent, L.B. Friction and slip in the cold rolling of metals. *A.S.L.E. Trans.* **21**, 20-24 (1978)
- [100] Tsao, P. and Wilson, W.R.D. Entrainment of lubricant in the cold rolling of steel and aluminium. *Proc. Int. Conf. on Steel rolling.* 49-64 (The Iron and Steel Inst.of Japan) (1981)
- [101] Van Rooyen, G.T and Backofen, W.A. *J. Iron Steel Instn. Lond.* **186**, 235-244 (1957)
- [102] Von Stebut, J. Modification of a surface profile's height parameters during strip drawing. *Wear* **109**, 145-155 (1986)
- [103] Von Stebut, J. Modification of a surface profile's horizontal spacing during strip drawing. *Wear* **118**, 329-340 (1987)
- [104] Wanheim, T. Friction at high normal pressures. *Wear* **25**, 225-244 (1973)
- [105] Wilson, W.R.D. and Sheu, S. Real area of contact and boundary friction in metal forming. *Int. J. Mech. Sci.* **30**, 847-868 (1988)
- [106] Wilson, W.R.D and Sheu, S. Influence of surface topography in viscoplastic asperity lubrication. *Wear* **124**, 311-326 (1988)
- [107] Wilson, W.R.D and Walowit, J.A. An isothermal hydrodynamic lubrication theory for strip rolling with front and back tension. *Proc. 1971 Tribology convention.* 164-172, Instn. Mech. Engrs. (1972)

- [108] Wilson, W.R.D and Murch, L.E. A refined model for the hydrodynamic lubrication of strip rolling. *J. Lubr. Tech.* **98**, 426-432 (1976)
- [109] Wilson, W.R.D and Mahdavian, S.M. A thermal Reynolds equation and its application in the analysis of plasto-hydrodynamic inlet zones. *J. Lubr. Tech.* **96**, 572-578 (1974)
- [110] Wilson, W.R.D and Mahdavian, S.M. Hydrodynamic lubrication of hydrostatic extrusion. *J. Lubr. Tech.* **98**, 27-31 (1976)
- [111] Wilson, W.R.D. Friction models for metalforming in the boundary lubrication regime. *To be published by A.S.M.E.*
- [112] Wilson W.R.D. Workpiece surface roughening in a hydrodynamically lubricated metal forming process. *J. Lubr. Tech.* **99**, 10-14 (1977)